Particle-in-cell – Monte Carlo Collisions Simulations for a Direct Current Planar Magnetron Discharge

Proefschrift voorgelegd tot het behalen van de graad van Doctor in de Wetenschappen aan de Universiteit Antwerpen te verdedigen door

Ivan Kolev

Faculteit Wetenschappen
Departement Chemie

Antwerpen 2007

Promotor
Prof. Dr. Annemie Bogaerts

Co-Promotor
Prof. Dr. Renaat Gijbels

PLASMANT
Plasma, Laser Ablation & Surface Modelling
Antwerp

Universiteit Antwerpen

Universiteit Antwerpen

Faculteit Wetenschappen

Departement Chemie

Particle-in-cell – Monte Carlo collisions simulations for a direct current planar magnetron discharge

"Particle-in-cell – Monte Carlo collisions" simulaties voor een gelijkstroom planaire magnetron ontlading

Proefschrift voorgelegd tot het behalen van de graad van
Doctor in the Wetenschappen aan de Universiteit Antwerpen,
te verdedigen door

Ivan KOLEV

Promotor: Prof. Dr. Annemie Bogaerts

Co-Promotor: Prof. Dr. Renaat Gijbels

Antwerpen **2007**

PLASMANT
Plasma Laser Ablation & Surface Modelling
Antwerp

In the beginning was the Word ...

John 1:1

... but we still need numbers to determine when was the beginning.

An unknown Simulator

Contents

Chapter Three

Chapter Four

Acknowledgements

Finishing my work on the doctoral thesis, I have realized that I never even would have been able to start it, if several persons had not helped me to become a physicist well before the beginning of my doctorate study. It is not possible to mention all of them, but to a few, I want to express my deepest gratitude. In a chronological order, I must start with Prof. Maria Moldovanova – a founder of the Semiconductors Department of the Faculty of physics at Sofia University, who gave me an entirely new perception for physics. She was also who inspired me to study semiconductors physics. My "semiconductors period" successfully led me to a M. Sc. degree, for which I am in debt to my promoters Prof. Nellie Zheleva and Prof. Deyan Kushev for their guidance and advises. I cannot miss Prof. Ivan Ivanov as well as the rest of the staff in the Laboratory of Thermodynamics and Physicochemical Hydrodynamics at Sofia University. Although my stay there was only a year, it influenced me profoundly. Finally, I would like to thank Prof. Krikor Ozanyan from the School of Electrical and Electronic Engineering at Manchester University for his support and valuable advises dating back to my school years. To all these persons is my sincerest gratitude.

As a Ph. D. student in the Research Group PLASMANT at Antwerp University, I had the chance to have two supervisors – Prof. Annemie Bogaerts and Prof. Renaat Gijbels. To both of them, I want to express my big gratitude for everything they did to help me throughout past years.

In addition, I want to acknowledge Prof. Gijbels for his unsurpassed ability to see always in the core of the problem. Each discussion with him was always helping me to see where was I at the moment, and how realistic were my scientific ideas and results. His words of wisdom in difficult moments I appreciate greatly.

To Prof. Bogaerts, I want to thank for her permanent encouragement, numerous discussions, and strong support. Annemie, this journey could never have

successfully ended without your enthusiasm and understanding. Thank you for your belief in me, even in times when it has not been so straightforward to do.

To both my supervisors, I am also grateful for all the work they did to improve this manuscript, as well as my other publications.

I had the "luck" to have to develop a numerical model almost from scratch. This could have been a very solitary journey, if there were not a number of fellow researchers who shared their knowledge and experience with me. Again in a chronological order, the first one I need to thank is Prof. Wim Goedheer from the FOM Institute for Plasma Physics Rijnhuizen in The Netherlands. Thank you, Wim, for all your consultations, which were so valuable for me in the beginning of my research.

Special thanks to the people from Ghent University – Dr. Guy Buyle, Prof. Roger De Gryse, and Prof. Diederik Depla. To them I owe a lot. They made me familiar with the "real magnetrons". My discussions with them contributed largely to tuning up my model. Without the magnetic field measurements done by Guy, many of my results would never appear. I am also using the possibility, to thank Prof. De Gryse for serving in my doctoral committee and in my jury.

I want to thank the former member of our group Dr. Andriy Okhrimovskyy, the person with whom I was able to discuss for three years on a daily basis almost all scientific problems I was facing. Спасибо Андрюха!

To other former member of the group, Dr. Upendra Bhandarkar, I am grateful for the useful discussions about introducing an external circuit to my model. Thank you Upendra for this and for all the great time we had.

Very valuable was the help from Dr. Neyda Baguer from our group concerning the introduction of the sputtered particles in my model. Neyda, thank you for that and for all the other help you never refused me.

I want to thank also Dr. Violeta Georgieva for the discussions we had about the PIC method.

Special thanks go to Dr. Erik Neyts and Evi Bultinck for translating in Dutch my summary. Erik, I want to thank you also for your kindness and for that you were helping me with so many formalities throughout these years.

I want to thank also all my former and present colleagues from the group for their support and friendship. Thank you Dieter, Min Yan, Velislava, Chen, Myriam,

Kathleen, Liu, Tom, and David. I am especially grateful to Dieter, who was attached to me when I first arrived in the group. Dieter, without your help in the beginning, I would not have adapted so quickly.

I had also many interesting discussions with Dr. Adam Cenian, Dr Andrey Chernukho, and Dr. Alexei Migoun during their visiting our group, for which I am grateful.

I want to thank also Prof. Kenichi Nanbu from the Institute of Fluid Science in Tohoku University for his kindly answering all my questions related to the art of kinetic simulations.

There are two persons that I cannot miss. These are the former and the present system administrators of our group – Koen De Couwsemaeker and Luc Van't dack. They were the ones that made all the computers to run smoothly, without which no computer simulation could happen.

On numerous occasions, I was helped by our secretary staff. Nelly, Tania, and Ingrid, thank you for always having been so kind to me and helping me to solve my problems in no time.

As a foreign student, I am deeply in debt to Martine Depauw, who was always taking care for all kind of formalities and problems that go with the foreign students. Here I also want to thank Suzanne Wouters.

Special thank to Dr. Eric Mathieu, the coordinator of the doctoral program in the University, who was always doing his best to assist.

Very valuable assistance during the printing of this manuscript I received from Dr. Kontozova and Dr. Deutch. Villy and Felix, thank you for your hospitality.

Besides the people from my scientific life, I want to thank all my friends who were there for me throughout these years. Without them, I never would succeed. On a first place, I want to thank Venko – one of my best friends with whom we have been sharing so many things already for 26 years. Cheers, Venko! Special thanks to his wife Emi as well. Next to him was Stancho, with whom we had not one or two critical situations in the mountains. Stancho, thanks for everything.

I want to give my big thanks to Violin and Daniela. I know, sometimes I was asking too much and now is the moment to say how much I appreciate you. I cannot omit Toshko and Titi – my compulsory stop always when I am back in Bulgaria.

Very special thanks go to Zlatan and Ana. It is difficult to imagine how I would sort out so many difficult issues without them. Thank you also for the finest moments we had.

I am particularly grateful to Lilly Marinova for what she did for me in a crucial moment of my life.

Many of my friends from LTPH are now in different countries after obtaining their doctoral grades. Here, I want to thank all of them: Georgi Marinov (UK), Reni and Marko (NL), Lubo and Beni (NL), Rumi (D), Tanja (BE), Drago (USA), Nikolina (NZ), Krasi and Nadya (NL), Peshko (NL), and Aneliya (UK).

Special thanks to Dr. Peter Petrov from Procter&Gamble for helping me with everything in the beginning of my stay in Belgium. Pesho, I really appreciate what you did for me.

Many thanks to my old friends Radostina and Veso.

I appriciate the nice time that my Maastricht friends gave me. Thank you Desi and Iliya, Silvena and Dencho, Nadya and Svetljo, Polly and Evgeni, Katya and Nic, Brigitte and Serve.

I am grateful to my parents for always encouraging my interest in science. I am also very grateful to my grandparents for all their love, understanding, and support.

Last, but definitely not least, I want to thank Nikoleta for her love and for making me so happy. She is to whom I mostly owe the successful ending of my thesis.

Chapter One

Introduction

1.1 Motivation

Thin films of metals or insulators play a central role in many key technologies, including fabrication of semiconductor chips, computer hard disks, and high performance optical coatings. Magnetron sputtering is the most widely used method for vacuum thin film deposition [1]. The basic principle of sputter magnetrons was discovered as early as 1936 by Penning [2]. However, the intensive use of magnetrons as a sputtering source begins in the early 1970's [3]. Currently, around 90 % of the industrial sputtering is realized by magnetrons. This wide use motivates the permanent high interest in studying magnetron discharges. The main practical interest is towards better utilization of the sputtering source (the target) and the homogeneity of the deposited film. The key to achieve these two "simple" tasks is to understand and to control the numerous physical processes taking place inside the magnetron chamber. What makes this understanding much more complex than it is in the case of the non-magnetized discharges is the existence of the applied magnetic field, especially when this field is multidimensional and not constant, as in the planar magnetrons. This complexity is primarily a result of the complicated trajectory, which an electron follows in combined spatially inhomogeneous electric and magnetic fields crossed at arbitrary angles. Consequently, it is rather difficult to build a simple analytical model that can describe satisfactorily the magnetrons without two many simplifications. Experiments can reveal interesting aspects of the magnetron operation, but cannot show the entire picture. A typical illustration of that statement is the electrical probe measurements. The latter are widely applied in discharge diagnostics, providing information about the plasma potential, charge density, and electron temperature. Probe measurements, however, are limited to the plasma region located away from the cathode. At the same time, almost all important

processes in the magnetrons occur in the sheath, which can be as thin as 1 mm. This is ten times less than the closest to the cathode, reported probe measurement [4]. On the other hand, numerical models are not restricted to a particular region of the discharge and can offer a detailed picture of the processes at given operating conditions as well as the trends of the parameters with the change of one or another operating condition (e.g., applied voltage, pressure, and magnet configuration). The results of the models should always be checked against experimentally well-established facts and compared to benchmark theoretical results. Their accuracy is a function of the initial assumptions and simplifications made. The exponential growth of the computer productivity, in terms of speed and memory restrictions, in the last two decades created the possibility for developing realistic numerical models, based on first principles and capable of simulating real (not idealized) systems.

In this work, a two-dimensional computer model is developed to describe a commercially available planar sputter magnetron discharge operated in direct current (dc) regime. The model is fully kinetic, based on the *particle-in-cell-Monte Carlo collision* (PIC-MCC) technique. It is expanded beyond the standard PIC-MCC algorithm, including the effects of the gas heating and the transport of the sputtered atoms and energetic gas neutrals.

The *overall goal of this research* has been to develop a numerical model of a dc planar magnetron:

based on as little as possible approximations and assumptions;
including as many as possible plasma species;
accounting for all important processes occurring in the discharge;
being as general as possible.

1.2 Plasma, glow discharges, and magnetrons

1.2.1 Definition and classification of plasma

Plasma is a quasineutral gas of charged and neutral particles, which exhibits collective behavior.

Formally, the quasineutrality means that almost all positive charges in the plasma are compensated by negative charges; that is $n = n_e = n_i$, where n is a

common density called the *plasma density*, n_e is the electron density, and n_i is the positive ion density♦. This is fulfilled in a volume, occupied by plasma, the characteristic size of which, L, is greater than some parameter, called *Debye length*, λ_D. The Debye length represents the fundamental characteristic of the behavior of plasma – to shield out electrical potentials that are applied to it. If some potential, Φ_0, is introduced in plasma at position x_0 then λ_D is the distance from x_0 at which the potential, Φ, is e times weaker than Φ_0, where the number e is the base of the natural logarithms. λ_D is connected to the plasma density and temperature by [5]:

$$\lambda_D = \left(\frac{\varepsilon_0 k T_e}{n e^2} \right)^{1/2}, \tag{1.1}$$

where ε_0 is the permittivity of free space, k is the Boltzmann's constant, e is the elementary charge, and T_e is the electron temperature, related to the average kinetic energy of the electrons, $E_{av} = (3/2)kT_e$. The very fact of introducing a temperature implies a statistical approach, *i.e.*, the concept of shielding is correct when there are enough particles to form a statistically representative ensemble. By using (1.1), the number of particles in a *Debye sphere* (a sphere with a radius λ_D) can be defined as [5], $N_D = (4/3)\pi n \lambda_D^3$.

The concept of collective behavior originates from the nature of the forces acting on the plasma species. When charged particles move, the information for their movement is relayed to the rest of the system in two different ways. The first way is a short-ranged, when they collide binary with other particles. This is not different from the collisions in an ensemble of neutrals. The second mechanism is long-ranged. When charges move, they generate local concentrations of positive or negative charges, which give rise to electric fields. Motion of charges also generates currents, and hence magnetic fields. These fields affect the motion of other charged particles far away. For the collective behavior to be dominant, the long-ranged collisions should prevail over the collisions between the charged particles and the neutrals, characterized by the mean collision time, τ. A merit for the long-ranged interactions in plasma is the plasma oscillation frequency, ω, commonly referred to

♦ In the present study, an electropositive plasma is examined. Hence, ions are only positive and n_i represents always positive charge density.

as *plasma frequency*. The nature of this oscillation is the following. If the electrons in plasma are displaced from a uniform background of ions, electric fields will be built up in such a direction as to restore the neutrality of the plasma by pulling the electrons back to their original positions. However, being inert, the electrons will overshoot and oscillate around their equilibrium positions with the plasma frequency.

Thus, for an ionized gas to be considered as plasma, three conditions must be satisfied [5]:

$$\lambda_D \ll L$$

$$N_D \gg 1$$

$$\omega\tau > 1.$$

Although the guiding equations describing plasma are the same regardless of the type of plasma, useful particular solutions can be deduced based on approximations, which are a function of the values of base plasma parameters, such as the plasma density, n, and the plasma temperature, T. Such division reflects as well the fact that different physical phenomena are dominant at different ranges of n and T, which can vary within broad limits. Generally, electrons and ions in plasma can have rather different temperatures. However, since many plasma properties are dependent on the electron temperature, T_e (being normally the higher), the plasma classification is based on it. Such classification is shown in Figure 1.1[6].

An additional important parameter, besides plasma density and temperature, is the degree of ionization, *i.e.*, what fraction of the neutral gas is ionized. Although related to the plasma density, the degree of ionization should be considered separately, because plasmas with the same density can have a different degree of ionization. It can vary largely from as low as 10^{-4} in weakly ionized plasmas to almost 1 in high-temperature fusion plasmas. For the purposes of numerical simulations, the degree of ionization determines whether Coulomb interactions should be included in a model or whether they can be disregarded.

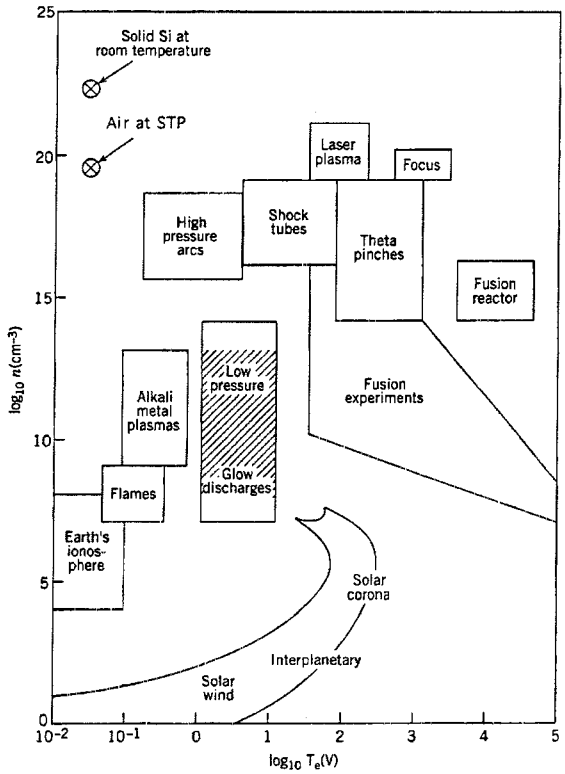

Figure 1.1 Classification of plasmas based on plasma density and temperature. Reproduced from [5].

1.2.2 Glow discharges

At normal conditions, almost any gas is partially ionized. The degree of this natural ionization, however, is very low and is caused mainly by cosmic rays. The low degree of ionization means that the gas is practically an insulator. However, when a significant electric potential drop is applied across a region of such partially ionized gas, the gas turns into a conductor – an effect known as *breakdown*. It is caused by the production of charges as a result of mainly electron-impact ionization of the gas. The process is avalanche-like and is schematically shown in Figure 1.2.

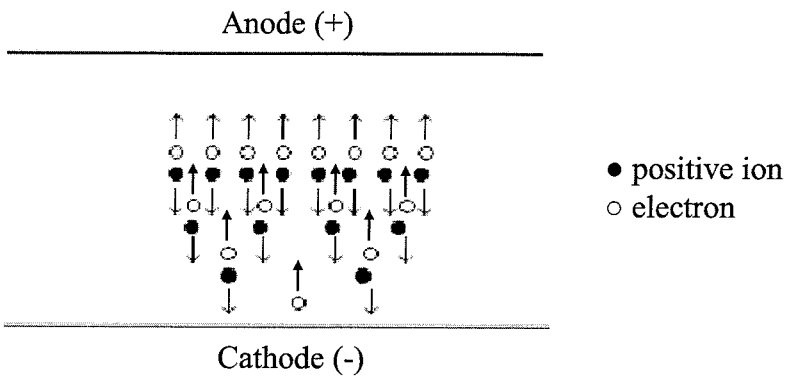

Figure 1.2. Scheme of an electron avalanche.

The primary ionization electrons cause electron avalanches to form: the accelerating electric field is high enough to impart to the electrons, generated by the primary ionization in the gas, an energy higher than the first ionization potential of the gas. These electrons then produce ion-electron pairs while continuing along their path; the secondary electrons may, in turn, form further pairs, and so on. Eventually, the freed electrons drift towards the anode. The ions collide with the cathode and, as a result, electrons are knocked out from the cathode surface. This process is known as secondary electron emission and is characterized by the secondary electron emission coefficient (SEEC), γ. The SEEC is defined as the number of electrons produced by a single ion striking the cathode. There is some ambiguity in the literature about the term "secondary" when applied to an electron. It is used for both the electron, created in an ionization process, to distinguish it from the primary electron that caused the ionization and for an electron released at the cathode by a bombarding (primary) ion or atom. The SEEC depends strongly on the condition of the surface. For clean surfaces, γ is energy independent in the range of the typical ionic energies in this study (up to 500 eV) [7].

The ionization efficiency of an electron moving in a gas is given by the *first Townsend coefficient, α.* It is the number of the electrons generated per unit length by a primary electron during ionization. There are several empirical forms for the relation that expresses α in terms of the gas pressure, p, and the electric field, E. One of the most commonly used reads [8]

$$\frac{\alpha}{p} = A\exp\left(-\frac{Bp}{E}\right), \tag{1.2}$$

where A and B are gas-dependent constants.

The critical value of the potential needed for breakdown to happen, known as *breakdown voltage*, V_t, depends on the distance between the electrodes, d, surface state of the cathode area, configuration of the electrodes, gas pressure, p, and weakly on gas temperature [9, 10]. The most important factors are the pressure and the interelectrode distance. For a wide range of pressures, V_t = f (pd); an empirical relation known as Paschen's law [11].

As the breakdown voltage is reached across the electrodes, a *self-sustained discharge* is formed. In the idealized case, the current tends to infinity due to the avalanche. In a real circuit, there is always an ohmic resistance, Ω. This can be a specially introduced resistor or just the resistance of the wires of the power source, which is never zero. This resistance sets a maximum value of the current for a given electromotive force (e.m.f), $\mathcal{E}$, produced by the power supply unit. If a closed circuit, with a power source, $\mathcal{E}$, and a resistance, Ω, is connected to the discharge gap in Figure 1.2, the equation of the voltage (Kirchoff's voltage loop law) is

$$\mathcal{E} = V + i\Omega, \tag{1.3}$$

where V is the voltage drop between the electrodes and i is the discharge current. Plotted as a straight line in V vs. i coordinates, (1.3) is known as the *load line*. It is plotted in Figure 1.3, where the $V - i$ characteristic of a discharge between electrodes is shown [12].

As follows from Figure 1.3, it is the discharge current that determines what type of discharge is formed for a given value of V. The region of operation of the discharge is where the load line crosses the $V - i$ curve, or with other words, the circuit realizes those values of V *and* i that correspond to the intersection of the load line and the $V - i$ curve. For fixed $\mathcal{E}$ (*i.e.*, for a given constant voltage source), the steepness of the load line and consequently the region of operation are determined by the resistance, Ω. Therefore, the desired mode of operation of a discharge can be

set by properly choosing the value of Ω. This basic fact is of great importance for the numerical models as well, as it will be illustrated in Chapter Five.

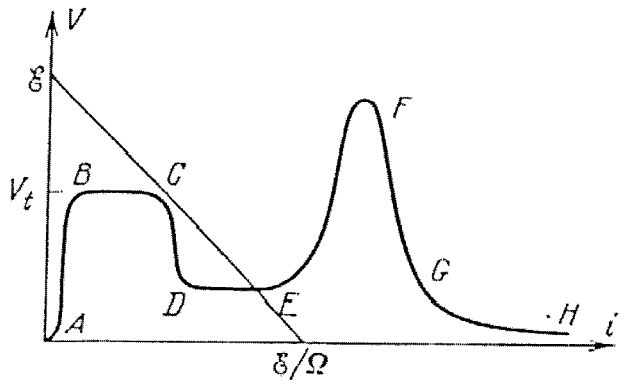

Figure 1.3 ***V – i*** **characteristic of a discharge between electrodes for a wide range of currents: (A) region of non self-sustaining discharge; (BC) Townsend dark discharge; (DE) normal glow discharge; (EF) abnormal glow discharge; (FG) transition to arcing; and (GH) arc. The straight line is the loading line (Eq. (1.3)). Reproduced from [12].**

Magnetrons are generally operated in the glow discharge region. After breakdown, it can be achieved by gradually increasing the current. This can be done by either reducing the load resistance, Ω, or by increasing the e.m.f., $\mathcal{E}$. The glow discharge (Figure 1.4[12]) is a *self-sustaining* discharge with a cold cathode emitting electrons due to secondary electron emission mostly due to positive ion bombardment. The self-sustainment can be defined in terms of α and γ. In the one-dimensional steady-state approach, the current densities, as a function of the distance from the cathode, x, are

$$\frac{\partial j_e}{\partial x} = \alpha j_e; \quad \frac{\partial j_+}{\partial x} = -\alpha j_e; \quad j_e + j_+ = j = const \tag{1.4}$$

The boundary conditions at the cathode (x = 0) and the anode (x = L) describe the secondary electron emission and the absence of ionic emission at the anode:

$$j_e\big|_{x=0} = \gamma j_+\big|_{x=0} = \frac{\gamma}{1+\gamma} j; \quad j_+\big|_{x=L} = 0; \quad j_e\big|_{x=L} = j$$

If (1.4) is integrated, starting at the cathode and assuming $\alpha[E(x)] = const$, the electronic current density is

$$j_e = \frac{\gamma}{1+\gamma} j e^{\alpha x}$$

This solution obeys the boundary condition at the anode only, if

$$\alpha L = \ln(1+1/\gamma).$$

This is known as the *criterion of self-sustainment.* For the case of a variable α, it has the form [12]

$$\int_0^L \alpha\left[E(x)\right] dx = \ln(1+1/\gamma). \tag{1.5}$$

A distinctive feature of the glow discharge is a layer of large positive space charge in front of the cathode with a significant potential drop of 100-1000 V [13]. This drop is known as *cathode fall*, and its thickness is inversely proportional to the gas density. If the interelectrode separation is sufficiently large, an electrically neutral plasma region with a weak field is formed between the cathode layer and the anode. Its relatively homogeneous middle part is called *positive column* and it is separated from the anode by the *anode layer*. The positive column of a direct current (dc) glow discharge is the best-pronounced and most widespread example of weakly ionized nonequilibrium plasma sustained by an electric field [12]. Its presence, however, is not vital for the existence of a glow discharge. No such column is formed, if the cathode layer fills the interelectrode gap. As it will become clear in Chapter Five, no positive column is formed in magnetrons, either, but for reasons related to the magnetic field.

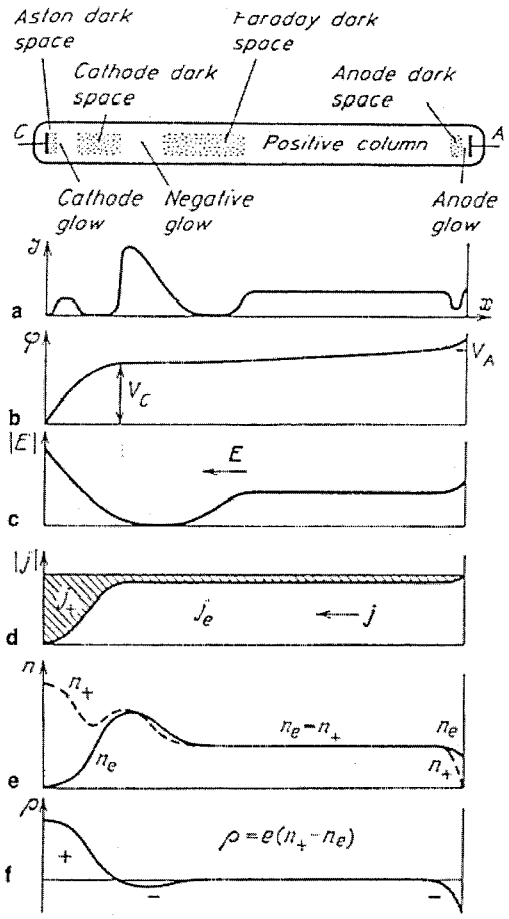

Figure 1.4 Structure of a glow discharge in a tube: (a) glow intensity; (b) potential, φ; (c) longitudinal field, E; (d) electronic, ionic and total current densities j_e, j_+ and j; (e) electronic and ionic densities n_e and n_+; and (f) space charge $\rho = q(n_e + n_+)$. Reproduced from [12].

1.2.3 Magnetrons

Magnetrons are magnetically enhanced glow discharges. This means that an external magnetic field, $\boldsymbol{B}$, is imposed on a glow discharge. The configuration and the magnitude of this field may largely vary, but the purpose is always the same – to entrap the electrons released from the cathode in a region close to it, and to obstruct their traversing the discharge toward the anode. This is done in order to allow the stable operation of a glow discharge at much lower pressures, which is needed for effective sputter deposition. The lower pressure is desired, in order to increase the sputtered flux arriving at the substrate by decreasing the collision rate of the

sputtered atoms. However, from (1.2) it follows that a decrease of p leads to a decrease of α. The latter can extinguish the discharge, if (1.5) is not any longer satisfied. Note that it is the left-hand side integral in (1.5) that matters and not just the under-integral quantity. The integral is taken along the path that the electron travels from the cathode to the anode. Hence, the longer the path, the bigger the integral. The role, played by the magnetic field in magnetrons, is precisely this – to prolong this path. (The principles of electron motion in electric and magnetic fields will be given in Section 2.2.) Thus the left-hand side of (1.5) is bigger in magnetrons than in conventional glow discharges for a given α. Consequently, according to (1.2) a lower operating pressure is possible.

The magnetrons can be classified according to two characteristics. The first one is the operational regime. It can be direct current (dc), radio frequency (rf) or pulsed. DC magnetrons are usually operated in argon at pressures 1-100 mtorr and at cathode potentials 200-800 V. Under these conditions, current densities can vary from 4 to 60 mA/cm^2 [14]. When used for sputter deposition of insulating materials (e.g. oxides and nitrides), dc magnetrons exhibit two major weaknesses. The first one is the *target poisoning* (the target covering with insulating material, e.g. oxides or nitrides), which leads to accumulation of positive charge on the target surface and consequently to arcing. The second weakness is the maximum power loading of the target (normally, up to several tens of W/cm2), which is limited by the target overheating due to ionic bombardment.

Magnetrons with an rf potential at the cathode (usually 13.56 or 27 MHz) enable the use of nonconductive materials as targets and allow direct or reactive deposition of dielectric films in the same manner as conventional rf sputtering. Magnetron rf sputtering shows similarities with dc magnetron sputtering. These include achievement of low plasma impedance and high power density at low applied rf potentials. For example, at a power density of 2 W/cm^2 the dc self-bias on the target is about 360 V for rf magnetron sputtering compared to about 3500 V for conventional rf sputtering [15]. RF magnetrons, however, have a relatively low deposition rate of insulating films, in comparison to the dc operated magnetrons.

A best-of-both-worlds solution for deposition of high quality insulating thin films is the pulsed (actually dc-pulsed) magnetron. In a single magnetron configuration, during the long-term operation for deposition of dielectric materials, eventually all surfaces become coated with insulating layer. This causes the effect of

anode disappearing [16]. A remedy for that problem is a scheme with two, instead of one magnetron, often called *dual magnetron* [17]. In this case, each magnetron acts alternatively as an anode and a cathode during the pulse cycle, providing very long-term process stability. The application of a pulsed power waveform has commonly taken two forms: the unipolar and bipolar modes. Both operate typically at frequencies between 10 and 350 kHz [18] and at pressures lower than 0.3 Pa. In unipolar pulsing, the discharge voltage returns to zero during the "pulse-off" period. The bipolar mode, on the other hand, is characterized by an overshoot in the target cathode voltage, V, where V becomes positive by a pre-set average value, typically 10-20% of the full bias. In both cases, the sputtering takes place from the target during the negative pulse and discharging of the target occurs during the positive pulse. Since no overheating of the target happens, high instantaneous power densities are achieved – several kW/cm^2. The high power density makes it possible to use pulsed magnetrons in applications where an ionized sputtered flux is sought.

The second main characteristic of the magnetrons is their geometry and the shape of the cathode. The two main groups here are *cylindrical* and *planar* magnetrons. In the first group, the discharge vessel is cylindrical. Different existing configurations of cylindrical magnetrons are shown in Figure 1.5 [19]. Among them, the post-cathode magnetron [Figure 1.5 (e)] is the most used. The discharge there is formed between two coaxial cylindrical surfaces, acting as anode and cathode. The magnetic filed is normally quasi one-dimensional, oriented parallel to the axis of the cylinders. Quasi means that the field is one-dimensional in the majority of the discharge, with appearance of a second component only at the ends of the cylinder. The magnetic field and the cathode form an electron trap of such geometry that the $\boldsymbol{E} \times \boldsymbol{B}$ electron drift currents (see Section 2.2.2) close on themselves. With its sufficiently uniform magnetic field distribution, the cylindrical post-magnetrons provide uniform sputtering over the whole cathode surface. This fact has been verified in experiments [1, 20, 21] by measuring the erosion of the target after intensive sputtering. A large amount of coating material can be stored in the cylindrical target and used efficiently. The plasma, however, is not prevented from leaking in the axial direction, thus lower plasma density can be achieved in comparison to planar configurations. Current densities are typically from 50 to 500 A/m^2 with erosion rates of 33 nm/s. However, several times higher current densities and erosion rates are also possible. Post-cathodes can be scaled to big sizes (more

than 2 m) permitting large areas to be uniformly coated. A schematic representation of the electron transport in the post-cathode magnetron is shown in Figure 1.6 [19].

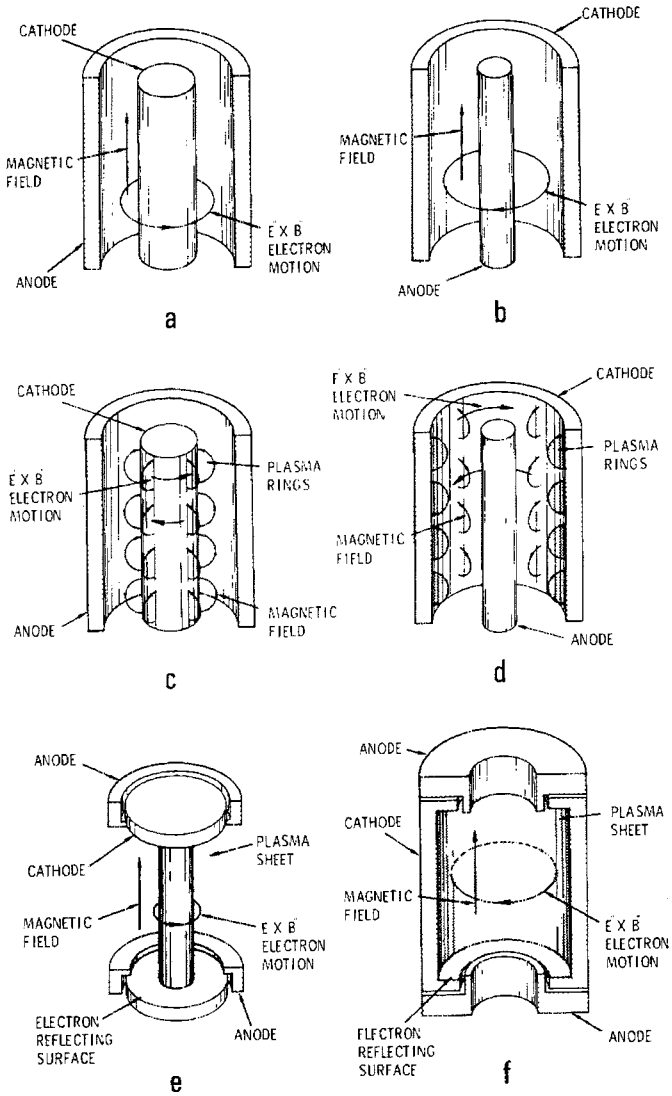

Figure 1.5 The configuration of various cylindrical magnetron sputtering sources. (a) and (b) have general magnetron configurations, but do not operate in magnetron mode, because of end (axial) losses. (b), (d), and (f) are called inverted magnetrons or hollow cathodes. (e) is known as cylindrical post-magnetron, and (f) as a cylindrical hollow magnetron. Reproduced form [19].

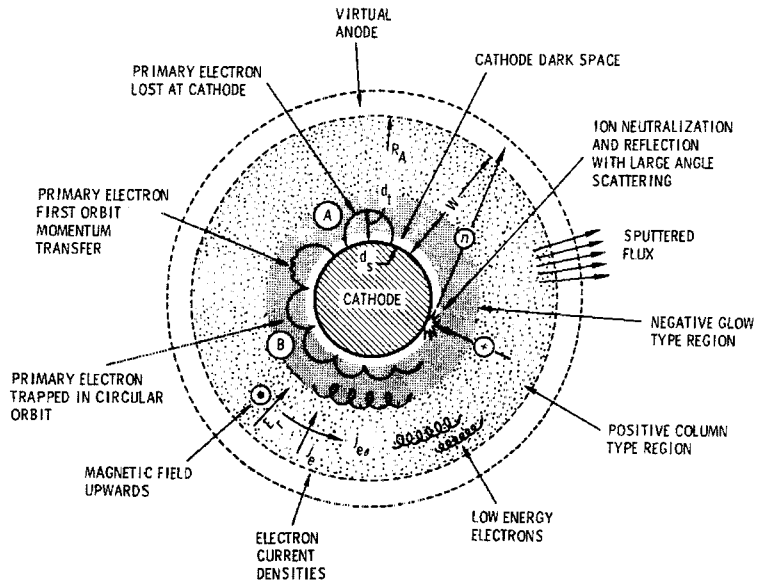

Figure 1.6 Schematic representation of electron transport processes in the magnetron of Figure 1.5 (e) in a uniform axial magnetic field. Reproduced from [19].

The second group are the planar magnetrons, which are magnetron discharges sustained between two planar parallel electrodes. The magnetic field source (usually permanent magnets) is located behind the cathode and forms magnetic field lines that originate at the cathode surface. The field lines may end completely or partially at the cathode. In the first case, the resulting configuration is known as *balanced magnetron* and the latter as *unbalanced magnetron*. The magnets are arrayed so that there is at least one region in front of the cathode surface where the locus of the magnetic field lines parallel to the cathode surface is a closed path. The magnetic field can be supplied by electromagnets, but at the loss of simplicity. It is never one-dimensional or spatially homogeneous. In fact, its geometry is rather complex with strong gradients. The magnetic field strength can exceed 0.1 T (1000 G) in the region between magnetic poles immediately before the cathode (target), although the threshold flux density for the magnetron discharge may be as low as 80 – 90 G [22], whilst at the anode (substrate) it can be lower than 0.005 T (50 G). Two common designs exist. The first one is with a disc-shaped cathode [23, 24] and is called *circular planar magnetron*. A characteristic property of this arrangement is the axisymmetric magnetic field. The symmetry axis is perpendicular to the cathode and passes through its center. The second one is with rectangular or oval cathode in

conjunction with a means whereby the substrates are moved continuously in a direction perpendicular to the cathode width during the deposition. The plasma region has a toroidal shape in the first design, whilst in the second it is in the shape of an elongated ring. The two configurations are shown in Figure 1.7 [3].

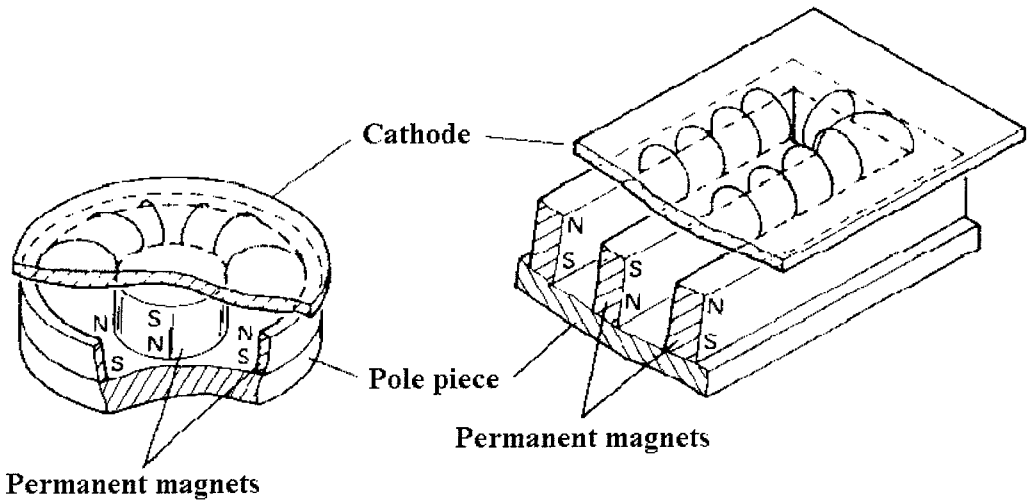

Figure 1.7 Circular (left) and rectangular (right) planar magnetrons. The curved lines represent magnetic field lines. Reproduced from [3].

1.3 Overview of the numerical models for magnetrons

Since the beginning of the intensive use of magnetrons as a sputtering tool in the early 1970's [3], constant attempts to improve the understanding of the physical processes occurring during the sputtering process have been made. An important part of these attempts belongs to the numerical modeling, which use begins in the middle 1980's and nowadays is very intensive.

The term numerical modeling refers to the process of finding approximate numerical solutions to a system of proper physical equations that adequately describe the system of interest. In a slightly broader aspect, in this category fall also analytical models based rather on simplifications of globally valid, but complicated, physical equations than on numerical solutions of these globally valid equations. The choice of the proper set of equations is normally based on the given operating conditions. In other words, certain physical approximations are assumed already priory to the process of numerical solving, which in its turn introduces mathematical

(numerical) approximations. The overall goal is always to obtain maximum useful results at the lowest possible computational price.

A complete numerical model of a sputter magnetron must include the magnetron plasma and its interactions with (some of) the solid surfaces that surround it. There are two surfaces that cannot be omitted in a model. These are the cathode (also known as target) and the substrate (the plate where the sputtered material is deposited as a thin film). In many cases, the substrate is grounded, and therefore, acts as an anode. An intrinsic part of the operation of the magnetron is the effective electric field that results from the external power source and the movement of the plasma charged particles. Therefore, a procedure that calculates this field should also be a part of the model. Such a procedure will be shown in Section 3.2.4. When the calculation of the resultant electric field is included in the model, the model is called self-consistent. It should be mentioned that for real self-consistency, some external electrical circuit should be coupled to the magnetron plasma [25 - 28]. However, in the literature, it is common to use the term self-consistent even when no external circuit is included.

The existing numerical models of magnetrons can be classified in several ways. The first division was already mentioned. It is between analytically based models and "purely" numerical. The analytical models usually approximate the magnetron chamber with a one-dimensional domain in the coordinate space, where the electric and magnetic forces are perpendicular to each other and the electron transport is considered in the direction parallel to the electric field and perpendicular to the magnetic field. In addition, the magnetic field is considered constant. Such a picture results in a particularly simple form of the electron transport coefficients. Namely, only the diagonal elements of the tensors of mobility and diffusion are non zero and can be regarded as permutations of the mobility and diffusion, referring to the non-magnetized case [5]. In such an analysis, classical diffusion is considered. Examples for a numerical study of this type are the works [29 - 33]. In [29], a scaling between the sheath width and the applied voltage and magnetic field strength has been given. In [30], two different models for the movement of the electrons in a cylindrical magnetron have been proposed and compared with experimental data. In [31 - 33], a particularly interesting result has been the prediction of the appearance of a negative space charge region due to the highly restricted electron mobility at strong magnetic fields and low pressures. This result has been later on validated by

more realistic particle simulations for both cylindrical [34] and planar magnetrons [26].

Analytical models have been also used intensively by Bradley and coworkers, who in a series of papers have investigated different parts of the magnetron discharge, such as the cathode fall [35], the pre-sheath [36], and the bulk plasma [37]. All these works are based on an earlier work by the same author [38], which is a one-dimensional fluid description. In [35,36], the classical diffusion has been replaced by Bohm diffusion and the results have indicated that the later is more realistic mechanism for the electron transport across the magnetic force lines. Recently, an analytical model has been proposed for an RF sputtering system [39]. The analytical models, like the above stated works, have proved to be an important step in the understanding of the magnetron discharges and a base for developing of more complex models. Their main advantages are the relative simplicity, the ability to produce fast results, and the fact that the results are intuitively easy for understanding. They are particularly suitable in situations where the main purpose of the model is to be seen whether a given phenomenon is important or it is negligible. Such an example is the electron recapture at the cathode, which has been studied by simple semi analytical model [40, 41]. The model has shown undoubtedly the principal importance of the electron recapture. The results have been later confirmed and extended by a much more complex and accurate particle model [26].

The general disadvantage of the analytical models is that they are unable to describe quantitatively the complex electron motion in the multidimensional electric and magnetic fields crossed at arbitrary angles that are typical for the real sputter magnetrons, especially for the planar ones.

The purely numerical models can be split into two groups depending on how plasma is treated. In the first group, plasma is considered a fluid with one or two components. The fluid methods are well developed mainly because of their extensive application in the field of aerodynamics. Magnetrons, however, cannot be so easily considered as a fluid. The main reason is the relatively low pressure (normally several millitorr) at which they are operated. At such low pressure, the main assumptions of the fluid theory are not necessarily valid. An additional difficulty comes from the complicated forms of the equations of magnetohydrodynamics, which describe a magnetized fluid. If these equations are applied to arbitrarily magnetic and electric fields, they require elaborated

discretization, resulting in long computational times. Moreover, here comes the issue of the validity of the classical diffusion at high ratios of the magnetic field and the gas pressure. At relatively weak magnetic fields and relatively high gas pressure, fluid models with simplified transport coefficients can be employed. This has been done in [42], where the bulk plasma in an RF cylindrical magnetron has been simulated and the results have been compared to a particle simulation. Fluid description has been used also to develop a theory of the cathode sheath in magnetrons [43]. A two-dimensional fluid model using the drift-diffusion theory has been reported [44]. However, it is applied for conditions not used in sputtered magnetrons – a pressure of several torr and a magnetic field weaker than 100 G.

An attempt to overcome the complicity of the full magnetohydrodynamics equations of the electron transport [45] was proposed in [46]. There, the presence of the magnetic field is included as a perturbation to the flux equations, valid in the unmagnetized case, and by assuming a classical transport. The criticism here comes from the fact that the electrons are so strongly magnetized that this fact cannot be represented in their transport by a perturbation. The very condition for applying the perturbation formalism is thus violated.

While electrons are heavily magnetized, the ions, due to their big masses, can be considered practically unmagnetized and therefore can be well described by the classical fluid approximation. This assumption lies in the foundation of the so-called *hybrid models*. The hybrid models are combination between fluid and particle models. In the simulations of non-magnetized glow discharges [47], the ions and the bulk electrons are regarded as a fluid, while the energetic (beam-like) electrons, normally emitted from the cathode or generated in the sheath, are simulated as particles, *i.e.*, kinetically. This approach combines the precision of the kinetic models with the relatively higher speed of the fluid codes, and successfully overcomes the low-pressure restrictions. Simulations based on the hybrid model are [48 - 54]. These simulations provide thorough pictures of the magnetron discharge. They are performed in (r, z) cylindrical geometry that corresponds to the planar circular magnetrons. The limits of validity of the hybrid models are discussed in [54]. The main uncertainties come from three directions. The first is the uncertainty of the electron transport coefficients. This problem has been partially overcome by using the data provided by a parametric study performed by numerical solution of Boltzmann equation for given sets of reduced electric and magnetic fields [55].

The second is the fact that the ions are not at all with a Maxwellian distribution as it will be shown in Chapter Four (see Figure 4.22). This questions their description as a fluid.

The third is related to the criterion of selecting which electron can be considered slow. In the nonmagnetized situation [47], the discharge is in a positive space charge mode. Then, once the electron has left the sheath and has energy less than some threshold, it can be transferred to the slow group. In magnetrons, depending on the reduced magnetic field, there can be a negative space charge mode. This means that even if the electron energy is less than the threshold at a given moment, the electron still can become fast. This is definitely the situation at high reduced magnetic fields. This situation has led to a modification of the classical hybrid scheme, where all the electrons are treated kinetically, whereas only the ions are described as a continuum [56]. In this way, the first and the third uncertainties are eliminated, but the computational cost approaches that of a particle model. At the same time the limitations of the fluid approximation for the ions remain.

Another disadvantage of the hybrid models is that they cannot provide the energy distribution of the incident ions at the cathode, which is essential for a self-consistent calculation of the erosion profile and the sputtered flux.

The maximum information with minimum assumptions about the discharge can be obtained by the kinetic models. These are divided into two groups. The first group is based on numerical solving of the Boltzmann equation with a volumetric force term corresponding to the Lorentz force. The direct solving of the Boltzmann equation has been a popular tool for plasma modeling for many years. Adding the Lorentz force term, however, complicates significantly the solver and makes it impractical in two and three dimensions and arbitrary magnetic fields. There is one situation where it can and has been successfully used in magnetrons. This is the simulation of the cylindrical magnetrons, where in a large part of the discharge the magnetic field is one-dimensional and constant, which simplifies the Boltzmann equation. Such simulations are [57 - 64].

The second type of kinetic simulations consists of the Direct Monte Carlo (DMCS or just MC) and Particle-In-Cell/Monte Carlo collisions (PIC/MCC) simulations. In the MC simulations, computational test particles that represent a large number of real plasma particles are followed. Their movement is a subject of the applied forces and the collisions of the particles are included by using

probabilities and random numbers. This technique is relatively easy to implement and fast to compute. Its main disadvantage is that the forces must be an input, *i.e.*, the simulation is not self-consistent. There are many MC simulations of different types of magnetrons reported in the literature. Among them are [65 - 72], which have contributed largely to the understanding of the transport and collision properties of the charged particles in magnetron discharges. Of particular importance has been [65], where by following the electron trajectories, it has been shown that the electron transport across the magnetic lines is mainly due to collisions and not due to field instabilities causing turbulence.

Although non self-consistent, and therefore, limited in their predictions, MC model are still a valuable tool for simulating large-scale magnetrons, where PIC/MCC models are restricted by the size. An example is the modeling of the cross-corner effect in rectangular magnetrons [73, 74].

Another application of the MC models is the simulation of the sputtered transport. These are normally non-self consistent trajectory calculations of the sputtered particles with included collisions with the background gas atoms. In this way, the spatial distribution of the sputtered atoms and their energy and angular distribution at the substrate are calculated. This allows accurate predictions for the quality of the deposited film. Possible effects of the spatial location of the target and the substrate can be easily studied. The drawback is the needed input for the starting positions of the sputtered atoms at the cathode. It is usually taken either from an experimentally measured erosion profiles or from a calculated erosion profile by a particle model. Reported works include, among others, [75 - 85].

When the calculation of the electric field produced by the external power source and the spatial distribution of the plasma charged particles is added to a MC simulation, the whole simulation becomes self-consistent. It is commonly referred to as PIC/MCC. Full description of this technique will be given throughout Chapter Three. The PIC/MCC simulations are the most powerful numerical tool for investigation of magnetrons. They can cope with the low operating pressures and the strongly inhomogeneous field and density distributions typical for the sputtered magnetrons. In addition, they are capable of providing the full picture about the processes occurring in the discharge chamber as it will be shown in Chapters Three through Seven. The disadvantage of the PIC/MCC simulations is their extensive computational load. This is especially valid when two- and three- dimensional

simulations are needed and when DC magnetrons are simulated. The latter is related to the long characteristic times (typically longer than 10^{-5} s) for achieving a steady state. Simulations of cylindrical magnetrons have been performed in 1D [25, 34]. Planar magnetrons cannot be simulated with one-dimensional codes. Fully three-dimensional PIC/MCC model of a planar magnetron has been reported in [86, 87]. It has shown the lack of angular dependence in the axisymmetrical planar magnetrons. This result has traced the path for simulating this type of magnetrons by performing two-dimensional simulations in cylindrical coordinates. The first very thorough work of that kind has been [88] followed by [89]. These codes, though, do not include an external circuit and the question about their convergence is open. The convergence issue will be discussed in Section 3.2.

The PIC/MCC method has been also applied to an RF sputter magnetron as well [90].

A two-dimensional survey of the velocity distributions in a magnetron sputter has been performed in [91] also without showing that the simulation has converged. The convergence with respect to the external circuit has been discussed and illustrated in [26] and will be presented in Chapter Four.

The results of a PIC/MCC simulation have been used to fit the erosion profile of a DC sputter magnetron with a Gaussian, in order to investigate the erosion [92].

Recently, a complete model based on the PIC/MCC technique, accounting for the gas heating and including the sputtered atom transport and collisions has been reported [27]. The model will be explained in detail in Chapter Six, and the results of it will be presented in Chapter Six and Chapter Seven.

The influence of the dielectric target in an RF sputtered magnetron has been investigated in [93].

A hybrid PIC/MCC – ion relaxation model has been reported also recently [94]. Here, the electrons are resolved in a standard PIC/MCC algorithm, whereas the ionic distribution is calculated by a continuum relaxation model in order to achieve a speedup.

Chapter Two

Fundamental processes in planar dc magnetrons

2.1 Introduction

In this chapter an overview of all important processes in a dc magnetron is given. Since argon is the most frequently used feeding gas, this study describes a dc magnetron operated in argon. Consequently, the included collision processes are those specific for argon. Because the specific phenomena in magnetrons are related to the particularities of the motion of the charged particles in electric and magnetic fields, the basic concepts of this motion will also be discussed. Although these concepts refer to a single particle motion and, as it has been explained in Chapter One, plasma manifests collective behavior, they are of great importance. That is so, because kinetic models are based on the description of the motion of a single particle.

2.2 Charged particle motion in electric and magnetic field

When a particle with a charge q and mass m is influenced by an electric field, $\boldsymbol{E}$, and a magnetic field, $\boldsymbol{B}$, its equation of motion is [95]

$$m\frac{d\boldsymbol{v}}{dt} = q\left(\boldsymbol{E} + \boldsymbol{v}\times\boldsymbol{B}\right), \tag{2.1}$$

where $\boldsymbol{v}$ is its velocity. The right-hand side of (2.1) is commonly known as Lorentz force. Strictly speaking, (2.1) is valid in the non-relativistic case only. For the typical forces in magnetrons, the electrons accelerate to speeds of maximum 10^7 m/s, which is well below the speed of light in vacuum. Consequently, (2.1) is accurate enough for a correct description of the single-particle motion in magnetrons. The $\boldsymbol{v}\times\boldsymbol{B}$ term leads to the following particularity. Even if a given component of both $\boldsymbol{E}$ and $\boldsymbol{B}$ is zero there is still a non zero force acting in the direction of the missing component.

This fact directly affects the dimensionality of the models of magnetrons, *i.e.*, the models must be three-dimensional at least in the velocity space.

The most important aspect of the motion caused by (2.1) is the so-called gyration. It has a particularly simple form in two cases, described in 2.2.1 and 2.2.2.

2.2.1 Motion in uniform B (E = 0)

In a Cartesian coordinate system with $\boldsymbol{B}$ chosen as $\boldsymbol{B}(0,\ 0,\ B_z)$, the components of (2.1) are

$$m\dot{v}_x = qBv_y \qquad m\dot{v}_y = -qBv_x \qquad m\dot{v}_z = 0$$

$$\ddot{v}_x = \frac{qB}{m}\dot{v}_y = -\left(\frac{qB}{m}\right)^2 v_x \tag{2.2}$$

$$\ddot{v}_y = -\frac{qB}{m}\dot{v}_x = -\left(\frac{qB}{m}\right)^2 v_y$$

As it is known from theoretical mechanics [96], (2.2) describes a simple harmonic oscillator with a frequency,

$$\omega_c \equiv \frac{|q|B}{m}, \tag{2.3}$$

which is known as *cyclotron* or *gyro frequency*. By convention, it is always positive; however, the gyration of positive and negative charges is in the opposite direction, as it is illustrated in Figure 2.1 [5].

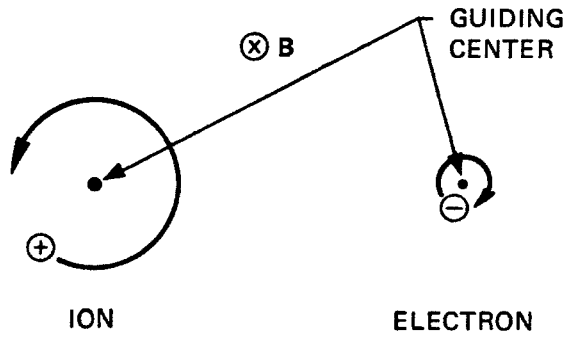

Figure 2.1 Gyration of an electron and an ion in the plane perpendicular to a uniform magnetic field *B*.

The centers of the orbits are known as *guiding centers*. Their mathematical definition comes after the solution of (2.2)

$$v_{x,y} = v_{\perp} \exp\left(\pm i\omega_c t + i\delta_{x,y}\right). \tag{2.4}$$

The ± denotes the polarity of the charge and $v_{\perp}$ is a positive constant representing the speed in the plane perpendicular to $\boldsymbol{B}$. Then after two subsequent integrations and proper choosing of the phase, δ, the coordinates of the charges as function of time become [5]

$$x - x_0 = r_L \sin\left(\omega_c t\right) \qquad y - y_0 = \pm r_L \cos\left(\omega_c t\right). \tag{2.5}$$

Equation (2.5) is a parametric equation of a circle, the center of which (the guiding center) is fixed and has coordinates x_0 and y_0. The radius

$$r_L \equiv \frac{v_{\perp}}{\omega_c} = \frac{mv_{\perp}}{|q|B}$$

is known as *Larmor* or *gyro radius*. It is a constant only in the case of a uniform $\boldsymbol{B}$. Otherwise the gyro radius is spatially dependent. It is an important parameter in the description of magnetrons, because it gives a quantitative merit for the degree of magnetization of the plasma. From (2.2) it follows that the magnetic field does not affect the motion in the direction parallel to the field. However, since there is

practically always some initial velocity in that direction, the actual motion of a charged particle in a uniform magnetic field is helical, rather than circular.

2.2.2 Motion in crossed E and B (uniform fields)

When $\boldsymbol{E} \neq 0$ is chosen to lie in the x-z plane and, as in the previous subsection, $\boldsymbol{B}$ is oriented in z-direction, the components of (2.1) are

$$\dot{v}_y = \pm\omega_c v_y \qquad \dot{v}_x = \frac{q}{m}E_x \pm \omega_c v_y \qquad \dot{v}_z = \frac{q}{m}E_z$$

The third component can be integrated directly to produce

$$v_z = \frac{qE_z}{m}t + v_{z0}. \tag{2.6}$$

This is acceleration along $\boldsymbol{B}$. The two components, transverse with respect to $\boldsymbol{B}$, can be differentiated to produce

$$\ddot{v}_x = -\omega_c^2 v_x \qquad \ddot{v}_y = \mp\omega_c\left(\frac{q}{m}E_x \pm \omega_c v_y\right) = -\omega_c^2\left(v_y + \frac{E_x}{B}\right).$$

Since $\boldsymbol{E}$ and $\boldsymbol{B}$ are constant with time, v_y can be replaced by $\left(v_y + E_x/B\right)$ in the above equation. Then the result of the integration is a replacement of (2.4) with

$$v_x = v_\perp \mathrm{e}^{i\omega_c t} \qquad v_y = \pm i v_\perp \mathrm{e}^{i\omega_c t} - \frac{E_x}{B} \tag{2.7}$$

Equations (2.6) and (2.7) define a motion identical to the motion described in 2.2.1 except for the superimposed drift of the guiding center in $-y$ direction (for $E_x > 0$), v_{gc} (Figure 2.2).

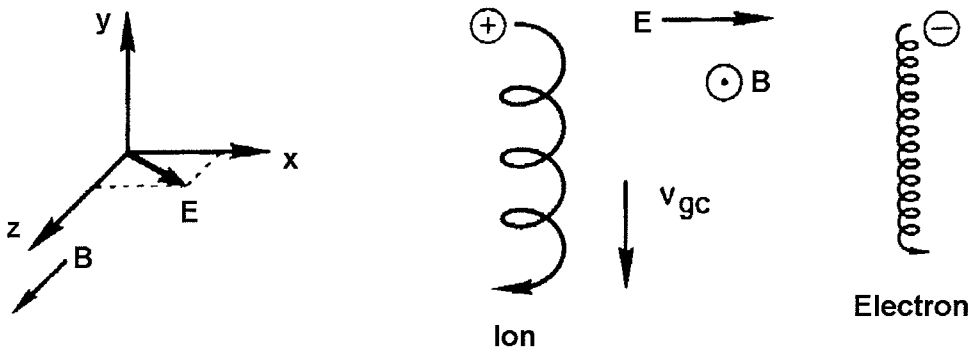

Figure 2.2 Charged particle drifts in crossed electric and magnetic fields.

By solving (2.1) in vector form [95], the transverse component of the velocity of the guiding center in the general case is

$$\boldsymbol{v}_{\perp gc} = \boldsymbol{E} \times \boldsymbol{B} / B^2 \equiv \boldsymbol{v}_E. \tag{2.8}$$

The velocity, $\boldsymbol{v}_E$, is called *electric field drift* of the guiding center. It is independent from q, m, and $v_\perp$ and is always directed perpendicularly to the plane $\boldsymbol{B}$ and $\boldsymbol{E}$ lie in. In principle, in the above analysis the electric field can be substituted by any general force (e.g. gravitational) to produce its drift. In the description of magnetrons, gravitational forces can be omitted, because their magnitude is much weaker than the magnitude of the electro-magnetic force for typical operating conditions.

2.2.3 Nonuniform fields

When $\boldsymbol{E}$, $\boldsymbol{B}$, or both are nonuniform, there is no exact solution of (2.1). The guiding center theory can be approximated, by expanding in the small ratio r_L/L, where L is the scale length of the inhomogeneity. This approach is known as *orbit theory*. With its help, simplified cases of charged particle motion in nonuniform fields can be described and visualized. With aspect to magnetrons, the following drifts are particularly relevant.

2.2.3.1 Gradient B Drift ($\nabla B \perp B$)

This is the situation, where $\boldsymbol{B}$ is one-dimensional, but with different strength in direction perpendicular to the direction of the field (the magnetic lines are straight and parallel, but with different density).

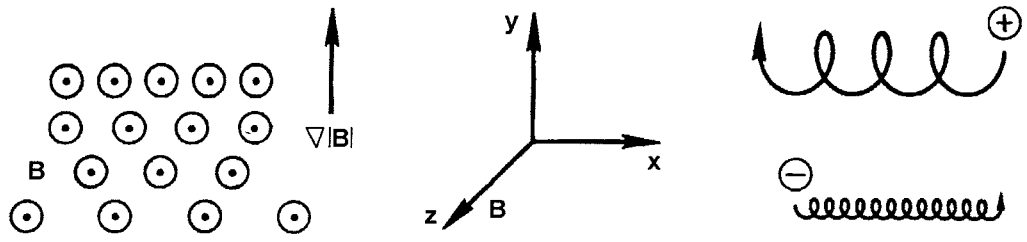

Figure 2.3 Gradient B drift.

Such configuration (Figure 2.3) causes the change in the gyro radius during one gyro period. The radius is larger when the particle is from the side of the lower density of the magnetic lines. The field strength experienced by a particle changes periodically as it circulates with frequency ω_c. Thus, a drift is created perpendicular to both $\boldsymbol{B}$ and $\nabla\boldsymbol{B}$. The direction of this drift depends on the sense in which the particle is rotated, and is therefore opposite for electrons and ions. Then expanding the orbits at the case of uniform $\boldsymbol{B}$ [given by (2.5)] in Taylor series towards $\boldsymbol{B}(y)$ and averaging over a gyro period, an expression for the guiding center can be obtained [5]

$$\boldsymbol{v}_{\nabla B} = \pm\frac{1}{2} v_{\perp} r_L \frac{\boldsymbol{B}\times\nabla B}{B^2}. \tag{2.9}$$

2.2.3.2 Curvature drift (Curved B)

If a magnetic configuration characterized by constant magnitude and curved force lines with an equal curvature can be realized,♦ (Figure 2.4 [5]) a guiding center drift arises from the centrifugal force, $\boldsymbol{F}_{cf}$, felt by the charged particle as it moves along the field line. Then, as it has been mentioned in 2.2.2, (2.8) can be used with $\boldsymbol{F}_{cf}$ instead of $\boldsymbol{E}$ to produce the *curvature drift*

$$\boldsymbol{v}_R = \frac{1}{q}\frac{\boldsymbol{F}_{cf}\times\boldsymbol{B}}{B^2} = \frac{mv_{\parallel}^2}{qB^2}\frac{\boldsymbol{R}_c\times\boldsymbol{B}}{R_c^2},$$

♦ Such a field does not obey Maxwell's equations in vacuum.

where $v_{\|}$ denotes the velocity in the direction of $\boldsymbol{B}$. In reality, there is always a dependence of $\boldsymbol{B}$ on the radius. To account for this dependence, the grad$\boldsymbol{B}$ drift must be added to the curvature drift. For the case of Figure 2.4, $\nabla \boldsymbol{B}$ has only a radial component. At the same time in vacuum $\Delta \times \boldsymbol{B} = 0$ and only the z-component of the rotor does not equal zero. Then (2.9) takes the form [5, 95]

$$\boldsymbol{v}_{\nabla B} = \frac{m}{2q} v_{\perp}^2 \frac{\boldsymbol{R}_c \times \boldsymbol{B}}{R_c^2 B^2}$$

Consequently, the combined drift in curved vacuum magnetic field can be approximated with

$$\boldsymbol{v}_R + \boldsymbol{v}_{\nabla B} = \frac{m}{q} \frac{\boldsymbol{R}_c \times \boldsymbol{B}}{R_c^2 B^2} \left(v_{\|}^2 + \frac{1}{2} v_{\perp}^2 \right) = \pm \frac{r_L}{R_c} v_{th} \hat{\mathbf{e}} .$$

The second equality holds for a Maxwellian distribution with v_{th} being the thermal speed and $\hat{\mathbf{e}}$ the unit vector in a direction of $\boldsymbol{R}_c \times \boldsymbol{B}$.

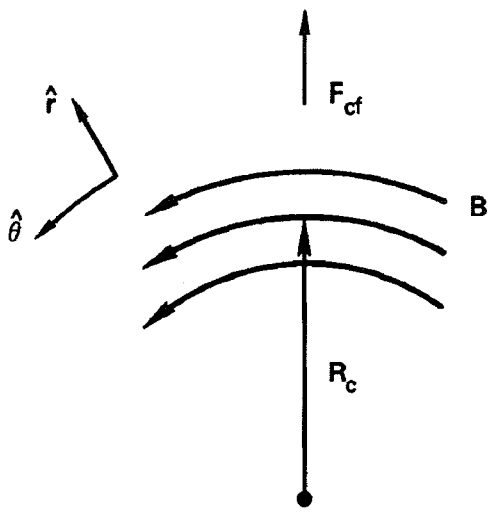

Figure 2.4 Curved magnetic field with constant radius R_c and magnitude B

2.2.3.3 Magnetic mirrors $\nabla B \parallel B$

When the magnetic field is pointed primarily in the z-direction and its magnitude varies in the z-direction (Figure 2.5 [5]) a magnetic trap can be formed. This trap is known as *magnetic mirror*. In case of an axisymmetric $\boldsymbol{B}$, there is always a non-vanishing radial component, B_r, which could be obtained from the Maxwell's equation $\nabla \cdot \boldsymbol{B} = 0$. If $\partial B_z/\partial z$ is given at $r = 0$ and does not vary significantly with z, then [97]

$$B_r \approx -\frac{1}{2} r \left[\frac{\partial B_z}{\partial z}\right]_{r=0}.$$

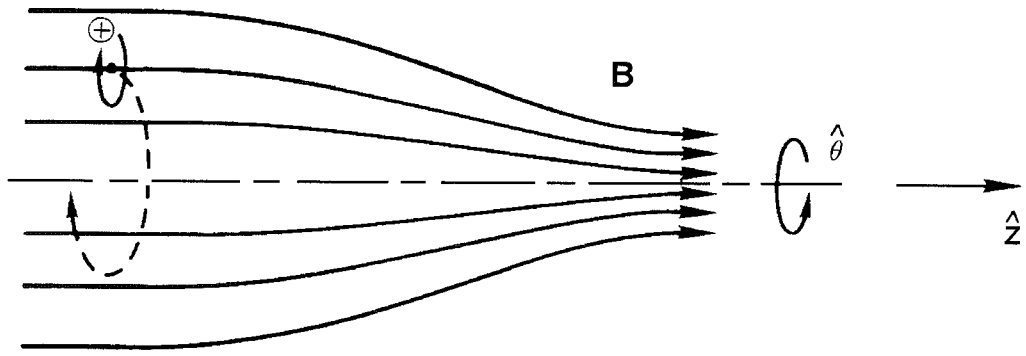

Figure 2.5 Drift of a charged particle in a magnetic mirror field.

This variation of the magnitude of $\boldsymbol{B}$ with r causes a grad-$\boldsymbol{B}$ drift of guiding centers about the axis of symmetry, without a radial grad-$\boldsymbol{B}$ drift ($\partial B/\partial\theta = 0$). By substituting the above expression for B_r in the Lorentz force, a non-zero z-component of the force appears

$$F_z = \frac{1}{2} q v_\vartheta r \left(\frac{\partial B_z}{\partial z}\right).$$

After averaging over one gyro period and choosing for simplicity a particle whose guiding center lies on the symmetry axis (v_θ = const = $v_\perp$)

$$F_z = -\frac{1}{2}\frac{mv_\perp^2}{B}\frac{\partial B_z}{\partial z}.$$

The quantity

$$\mu \equiv mv_\perp^2/2B$$

is called the *magnetic moment* of the guiding center. It is a very important parameter, because it is an invariant, as could be shown [98]. The conservation of the magnetic moment and the kinetic energy of a charged particle moving in a magnetic field like that of Figure 2.5 leads to the following phenomenon. As such a particle moves from a weak-field region to a strong-field region, it sees an increasing $\boldsymbol{B}$, and thereafter its $v_\perp$ must increase in order to keep μ constant. But to satisfy the total energy conservation, $v||$ must necessarily decrease. At some critical value of $\boldsymbol{B}$, $v_{||}$ will actually pass through zero and reverse its direction. This is why this drift is called magnetic mirror. It should be noted that the effect works on both ions and electrons, but is not perfect. First, because a particle with $v_\perp = 0$ has no magnetic moment, and therefore cannot be trapped. Second, because there is a critical value of $\boldsymbol{B}$ dependent on the ratio $v_\perp/v_{||}$, which is needed for the velocity reversal to take place.

The magnetic mirror effect is of big importance for planar magnetrons. It affects the behavior of the electrons returning at the cathode. More detail about that will be given in Chapter Five.

2.2.3.4 Nonuniform E field

If the magnetic field is uniform and the electric field is not, the charged particle experiences again a drift (Figure 2.6 [5]).

If for simplicity $\boldsymbol{E}$ is chosen to have only a sinusoidally varying x-component, $\boldsymbol{E} \equiv E_0(\cos kx)\hat{\boldsymbol{e}}_x$, the particle's equation of motion is

$$m(\partial \boldsymbol{v}/\partial t) = q\left[\boldsymbol{E}(x) + \boldsymbol{v}\times\boldsymbol{B}\right].$$

The transverse components of the equation of motion are

$$\dot{v}_x = \frac{qB}{m} v_y + \frac{q}{m} E_x(x) \qquad \dot{v}_y = -\frac{qB}{m} v_x$$

$$\ddot{v}_x = -\omega_c^2 v_x \pm \omega_c \frac{E_x}{B} \qquad \ddot{v}_y = -\omega_c^2 v_y - \omega_c^2 \frac{E_x(x)}{B}$$

In the above set of equations, E_x is needed in a position x, which is also unknown.

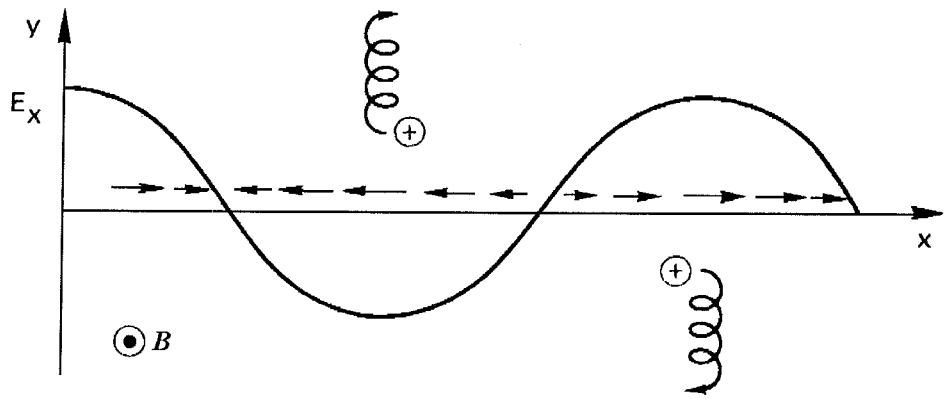

Figure 2.6 Drift of a gyrating particle in a nonuniform electric field.

An approximation based on the perturbation theory may be used, if the electric field is weak. Then as a first approximation, the undisturbed orbit [(2.5) left] may be used. Further, after averaging over one cycle and subsequent canceling of the oscillating terms [5, 97, 98], only the y-component of the velocity has an average value different from zero

$$\overline{v}_y = -\frac{E(x_0)}{B}\left(1 - \frac{1}{4}k^2 r_L^2\right).$$

As it can be expected, this defines a drift that can be thought as a perturbation of the standard $\boldsymbol{E} \times \boldsymbol{B}$ drift. In invariant form the above equality reeds [5]

$$\boldsymbol{v}_E = \left(1 + \frac{1}{4} r_L^2 \nabla^2\right) \frac{\boldsymbol{E} \times \boldsymbol{B}}{B^2}.$$

The second term is called the *finite-Larmor-radius* effect. The significance of this correction is that it makes the otherwise species-non-selective $\boldsymbol{E} \times \boldsymbol{B}$ drift to act differently upon electrons and ions. The reason for that is the dependence of the correction on the gyro radius, r_L.

2.2.3.5 Time varying E field: Polarization drift

This drift has a marginal importance for the present study, because the study is devoted to dc magnetrons, whilst the drift appears only in time varying electric fields. For sake of completeness, however, it is mentioned here without particular detail. When a charged particle is under the influence of spatially uniform $\boldsymbol{B}$ and $\boldsymbol{E}$, but $\boldsymbol{E}$ only is time-dependent, the guiding center experiences a new drift in the direction of $\boldsymbol{E}$. This drift, known as *polarization drift*, follows the momentous orientation of the electric field and is given by [5]

$$\boldsymbol{v}_p = \pm \frac{1}{\omega_c B} \frac{d\boldsymbol{E}}{dt}.$$

2.2.3.6 Orbit theory and magnetron modeling

It is very important to understand that the orbit theory is only an approximation, which can shed some light on important phenomena, but barely could be used for quantitative description. As it has been illustrated in the previous subsections, the drifts represent idealistic situations. Furthermore, often a perturbation theory is used to obtain the mathematically simple expressions. However, the perturbation theory is useful, as far as the described phenomenon is really only a perturbation in comparison to the unperturbed state. As an example, the ratio $\nabla \cdot \boldsymbol{B}/\boldsymbol{B}$ must be small enough for results to be physical. The same holds for the electric field. This is not the case in the planar magnetrons, where the gradients in front of the target do not obey this condition. Another problem arises for the electrons located near the cathode. Since their interaction with the cathode can strongly influence the discharge (see Chapter Four), their exact location is important, and not the location of their guiding centers. Finally, the configuration of the fields in the planar magnetrons provokes the manifestation of all of the discussed drifts

(except the polarization drift). But the formulae that describe these drifts have been deduced on the assumption that only one or two drifts are present. Generally, as far as the processes require kinetic description the guiding centers approximation cannot be used. But it still can form a qualitative picture.

2.3 Collision events in an argon plasma

The plasma in a magnetron is collisional. This means that a model of a magnetron cannot only include the motion of the plasma species in electric and magnetic fields, but should also account for the different collisions that these species encounter in the discharge chamber. These are basically two sorts: collisions among species (different or alike) and collisions between the species and the walls of the discharge vessel. Here an overview of the first sort follows for the case of a discharge, operated in argon with a copper cathode. The included processes are those with significant importance to the operation of magnetrons, and which are hence incorporated in the model discussed in Chapter Four. In Section 2.4, the plasma-wall interactions will be described.

2.3.1 Electron collisions with argon atoms

The collisions of electrons with the argon atoms are the most important processes in the magnetrons. The electrons themselves are the most magnetized species in the discharge, *i.e.*, they are the species that give the magnetrons their unique properties. These collisions not only sustain the discharge, but also determine its conductivity.

2.3.1.1 Elastic scattering

The process of elastic scattering of electrons from argon atoms is one of the best-studied collision processes in argon [99]. It has the highest collision frequency among all collisions involving electrons. Although the energy transfer in a single collision is very small due to the vast disparity in the masses of the electrons and argon atoms, it plays a very important role in magnetrons. This is so, firstly because an average electron suffers a big number of elastic collisions during its lifetime. This is in contrast to the situation in nonmagnetized discharges and is a consequence of the electron entrapment. Secondly, during elastic collisions the electron changes its momentum. This is a very important effect, because via this abrupt change in the

velocity, the electrons can jump over magnetic field lines. Therefore, the collisions actually contribute to the electrical conductivity, as opposed to the situation in normal gas discharges, where more elastic collisions mean a lower drift velocity, *i.e.*, higher resistance.

The electron scattering from argon is highly anisotropic. Both experimental measurements [100] and theoretical calculations [101] confirm this fact. The anisotropy is a function of the electron energy.

2.3.1.2 Inelastic processes

In the inelastic processes, the total kinetic energy of the participants is not preserved. The "missing" part of the energy is transferred in internal energy of the argon atom. This means that the internal state of the atomic system changes as a result of the collision. When a new particle is created, part of the initial energy can be transferred to create an initial kinetic energy of the new particle.

2.3.1.2.1 Electron-impact ionization

Similar to the elastic scattering, the electron-impact ionization is a very-well studied phenomenon. Its importance is crucial for the self-sustainment of the discharge, as it has already been discussed in Section 1.2.2. Ionization can be single or multiple. The argon atom can be in ground state or in an excited state. The single ionization from the ground state is known to have a threshold energy of 15.76 eV and is represented by

$$e^- + Ar \rightarrow 2e^- + Ar^+ .$$

The cross section for the process has a broad maximum at app. 80 eV, equal to $3\times10^{-20}\,\mathrm{m}^{-2}$. After the maximum, the cross section gradually decreases with the energy. The ionization of the excited argon atoms requires a smaller threshold energy of 4.2 eV. At typical operating conditions, the ground state ionization is the dominant ionization mechanism, because the density of the excited argon atoms is much lower than that of the atoms in ground state.

All sorts of ionization, as well as the other collision processes, are quantum processes. From quantum mechanical point of view, the ionizing electron after the ionization and the electron that is a product of this ionization are undistinguishable.

However, it is not statistically the same, how the energy is divided between them. The possible effect of energy partition upon energy distribution functions of electrons has been demonstrated elsewhere [102].

Multiple ionization is statistically an unimportant process, because of its high threshold energy compared to the typical electron energies and is therefore not considered here.

2.3.1.2.2 Electron-impact excitation

The argon atom has a complicated structure of excited levels [103]. Different levels have rather different probability for being populated. Both transfers from ground state to a higher energy level and transfers between two levels other then the ground level are possible. Statistically, the most important are the transitions from the ground level to some of the higher levels. The cross sections for these processes have very similar thresholds, the lowest of which is equal to 11.55 eV. A special case of excitation is the excitation to the so-called *metastable levels*. These are states characterized by long lifetimes. The argon metastable atoms play an important role in the ionization of the sputtered atoms. Since the discrete argon levels are very closely located to each other, they can be combined in a single excited state in a model, providing the model disregards the metastable atoms. Electron-impact excitation and ionization are competing processes. Their cross sections show similar trend and magnitude, differing slightly in the threshold energy.

2.3.2 Electron collisions with the sputtered atoms

Electron collisions with sputtered (target) atoms are also important. As in the case of argon atoms, elastic and inelastic collisions take place. The data for electron-copper collisions, however, are much scarcer in the literature than those for electron-argon collisions. In the present study, only two collision mechanisms are considered.

2.3.2.1 Elastic scattering

Elastic scattering of electrons from copper atoms is characterized by a cross section with a maximum of 9.1×10^{-19} m^2, corresponding to an electron energy of 10 eV. [104, 105]. This maximum is about 4 times higher than the maximum of the cross section for elastic scattering of electrons from argon ions (2.3×10^{-19} m^{-2}, corresponding to an electron energy of 14 eV [101]). In front of the cathode, the

copper density can approach 10^{19} m^{-3}. Therefore, the influence of the process on the electron velocity distribution should be considered.

2.3.2.2 Copper ionization

The ionization of the copper atoms is an important process with respect to sputtering applications of magnetrons. The copper ions contribute to the charge distribution on the discharge and can cause *self-sputtering*. Electron-impact ionization is one of the significant mechanisms for ionization of the copper ions. Its cross section has a maximum of 2×10^{-20} m^2, corresponding to electron energies of approximately 55 eV. [106] The threshold energy for the process is 7.72 eV.

2.3.3 Electron collisions with argon metastable atoms

When electrons collide with argon metastable atoms, the result is the transition of the metastable state in a resonant, higher-energy excited or ionic state. All three processes are loss mechanisms with respect to the metastable atoms. Their influence on the electron velocity distribution is a function of the relative density of the metastable atoms compared to the argon ground state atom density. This ratio depends on the operating conditions, mostly the pressure. The process of argon ionization out of a metastable level is interesting because it has lower threshold energy (4.2 eV [107]) in comparison to the ionization from the ground state. Thus, it can occur in regions of the discharge, where the mean electron energy is not sufficient for direct ionization.

2.3.4 Argon ions collisions

The argon ions are the main carriers of the positive electric charge. Thus, their collisions directly affect the charge distribution in the discharge. Their collisions with the cathode are responsible for the maintenance of the discharge (see Section 1.2.2) and for the main application of the magnetrons: sputtering (see Chapter Seven). In contrast to the electron collisions, ion collisions lead to significant energy transfer due to the similar masses of the argon ions and target particles (argon atoms and sputtered atoms).

2.3.4.1 Collisions with argon atoms

The Ar^+ - Ar collisions can be elastic and inelastic in the same way as the electron-argon atom collisions.

2.3.4.1.1 Inelastic scattering

The thresholds for the inelastic processes are identical to the corresponding electron-impact collisions. However, the cross sections for the ion-induced excitation and ionization reach their maxima at much higher energies – around and above 100 eV. [108] The reason for that is the possibility for effective exchange of kinetic energy during the collision. This means that part of the kinetic energy of the incident ion is transferred in kinetic energy of the target atom. In other words, only a fraction of the ion energy is available for changing the electron structure of the atom. Excitation to a metastable state is one of the mechanisms for creation of metastable atoms. Due to the shifting of the ionization maximum to higher impact energies and moderate voltages in magnetrons, the relative role of ion-impact ionization is not very significant.

2.3.4.1.2 Elastic scattering and charge transfer

In the course of a collision between an argon ion and its parent atom, an electron can leave the atom and neutralize the ion. The process is elastic, since the total energy of the system ion-atom is unchanged. It is known as s*ymmetric charge exchange*. After the collision, the ion becomes a neutral and the neutral is ionized. Both particles keep their precollision velocities.

Besides this mechanism, a classical elastic scattering is also possible. When this is the case, the scattering is mostly isotropic. The probability that determines which of the two cases is realized is energy dependent. At lower energies isotropic scattering dominates, whilst at higher energies it is much less pronounced. [109]

Charge transfer leads to creation of energetic atoms in the cathode fall, which bombard the cathode and contribute to the sputtering (see Chapter Seven). These fast neutrals play an important role for the gas heating as well (see Section 6.3.2).

2.3.4.2 Collisions with sputtered atoms

Argon ions can collide with copper atoms. One possible mechanism is *asymmetric charge transfer*. The result is the transfer of an electron from the copper atom to the argon ion in a similar fashion as in the symmetric charge transfer. In principle, the probability for asymmetric charge transfer depends on the difference in the energy levels of the free states in the outer electron shells of the two colliding particles. The smaller the difference, the higher the probability. In case of copper, the energy difference is relatively small and the process is expected to be an effective source for copper ionization. This statement has been confirmed numerically for higher pressures (above 500 mtorr) in analytical discharges. [110] The problem with inclusion of this collision in the model is the relative uncertainty for its cross section in the literature. [110]

2.3.5 Collisions of argon metastable atoms, sputtered atoms and ions, and argon ground state atoms

2.3.5.1 Collisions of argon metastable atoms

The collisions of argon metastable atoms with themselves and with argon ground state atoms lead to destroying the metastable state

$Ar_m^* + Ar_m^* \rightarrow Ar^0 + Ar^+ + e^-$ – metastable - metastable collision

$Ar_m^* + Ar^0 \rightarrow Ar^0 + Ar^0$ – two - body collision

$Ar_m^* + 2Ar^0 \rightarrow Ar_2^* + Ar^0$ – three - body collision

For all the three processes, the rate constants are known. [111 - 113]

2.3.5.2 Penning ionization

For copper, the Penning ionization is given by

$$Cu^0 + Ar_m^* \rightarrow Cu^+ + Ar^0 + e^- .$$

In this type of collision, the energy of the argon metastable level is enough to ionize the copper atom, because it is higher than the ionization potential of copper. The

process is at the same time a loss mechanism for the metastables and the third important path for ionizing the sputtered atoms besides electron-impact ionization and asymmetric charge transfer. Although Penning ionization is known for a long time, there is a lack of cross section data, based on sound measurements or theoretical calculation. It is estimated that the cross section of Penning ionization for the most of the metals by argon metastable atoms is of the order of 5×10^{-21} m^2 [111,114]. For copper, in particular, a value of 4.87×10^{-21} m^2 has been adopted [110].

2.3.5.3 Collisions of the sputtered ions and atoms

Except to be ionized, the copper atoms can collide with the background argon atoms. Those are elastic collisions with considerable energy transfer. They are the main mechanism for thermalization of the sputtered atoms. To some extent, it is a desired effect, in order to homogenize the sputtered flux at the substrate. On the other hand, if the rate of these collisions is too high, it will lead to an insufficient flux at the substrate, as it will be shown in Section 7.3.

The energy transfer, resulting in the creation of energetic argon atoms is one of the important mechanisms for gas heating. In some cases, the effect is very strong, leading to a significant reduction of the gas density; an effect known as *sputtering wind* [115].

The ions of the sputtered atoms can be elastically scattered by the argon atoms in the same way as the copper atoms. This process is included, because it influences the spatial and the energy distributions of the copper ions. The former contributes to the charge distribution and the latter to the sputtering efficiency. These collisions also generate fast neutrals and therefore affect the gas heating.

2.3.5.4 Collisions of the energetic (fast) argon atoms

Fast argon atoms are defined as having an energy above several times the thermal energy ($\cong$ 0.03 eV). More explanation about this division will be given in Section 6.2.2. Fast argon atoms can be generated in symmetric and asymmetric charge transfer, and in Penning ionization collisions. The first type of collisions is the most effective. Fast argon atoms are included in the model, mainly because they play the most important role in the gas heating and for their contribution to the sputtering. Other processes where they participate are atom-impact ionization and

excitation to the metastable level of the thermal argon atoms. They add little to the ionization, however, since the process is effective at high energies, requiring stronger voltages than those usually applied in magnetrons. Thus, the most important collision process involving them is elastic scattering from the thermal argon atoms

$$Ar^{f} + Ar^{th} \rightarrow Ar^{f(th)} + Ar^{f(th)}.$$

In the course of a single such a collision, the initial fast atom loses part of its energy. The result can be that at the end both atoms are thermalized, both are fast, or one of them is fast and the other is thermalized.

2.3.6 Coulomb collisions

So far, binary[♦] collisions have been discussed only. Charged particles, however, can interact with each other driven by electrical forces. In this case, their trajectories are influenced by the presence of other charges inside a certain radius. In fact, these are not collisions at all, but gradual deviations of the trajectories. Nevertheless, they could be thought of as collisions, which are a result of a large number of small deviations in the trajectory. In other words, after some distance, the velocity vector of the "colliding" particle is changed by some amount, as a result of the influences of the many "collision partners". Thus on macro level, the process can be described in terms of collisions. They are commonly known as *Coulomb collisions*. It should be said that since the electrical (Coulomb) force is long-ranged, the whole interaction is a long-ranged one. This means that a single, moving, charged particle experiences simultaneously the influence of many other charged particles.

Generally, Coulomb collisions are important when the degree of ionization is relatively high. In magnetrons, they should not be disregarded, even at moderate degree of ionization, because they contribute to the electron mobility. The change in the velocity vector of the electrons is a way to escape the magnetic trap.

[♦] with the exception of the three-body collision of the argon metastable atoms.

2.4 Plasma-wall interactions

Plasma species can collide and interact with the walls of the discharge vessel (*i.e.*, the magnetron chamber, with the substrate and with the cathode). In fact, some of the plasma species are created or lost there. Hereafter, a review of the interactions included in the model follows.

2.4.1 Ion- and atom- induced secondary electron emission

When ions or energetic atoms strike the cathode, one of the possible outcomes is the ejection of an electron off the cathode surface. At low energies (less than app. 600 eV), the process is much more efficient for the ions [99] . Ion-induced secondary electron emission is the primary mechanism for sustaining the magnetron discharge. The SEEC (see Section 1.2.2) for most of the metals is believed to be around 0.1 for argon ions with energies of up to 1000 eV [116]. Experimental determination of SEEC is usually made in swarm experiments. This means that a clean metal surface is bombarded by a monoenergetic swarm of ions approaching normally to the surface [117]. The condition of the surface, however, can largely affect the SEEC. It has been shown that the results for clean and dirty metal surfaces can differ significantly [7]. Another factor is the topography of the surface. In magnetrons, the active part of the cathode is not a plane. The region of maximum cathode erosion has a depth in the millimeter range. The SEEC is dependent on the crystallographic orientation of the surface, if any. Finally, the cathode could be heated by the bombarding plasma particles. All these effects introduce a considerable uncertainty about the value of the SEEC. At the same time, the whole behavior of the magnetron is very sensitive to this value.

All phenomena mentioned above are valid for all metal surfaces that surround the magnetron discharge. The discussion has been made for the cathode, since most of the magnetron discharge is localized in front of the cathode, and the secondary electron emission from the other surfaces is unimportant for the operation of the magnetrons.

2.4.2 Electron interaction with the walls

When an electron strikes a metal surface, it can be absorbed, reflected elastically, or reflected inelastically (with a change in the kinetic energy). The incident electron can also cause the emission of a secondary electron from the

surface. All these processes are probabilistic and dependent on the type of the surface and mostly on the energy of the incident electron. In magnetrons, electron interactions with the walls, other than the cathode, have little influence. This is so, because the electrons, which have already managed to escape the magnetic trap and have approached these walls, can be considered lost for the discharge. Moreover, their number is small compared to the number of the electrons confined in front of the cathode. The situation at the cathode, however, is very different. The electrons that have returned there are 100% primary electrons, directly responsible for sustaining the entire discharge. Hence, their reflection or absorption has deep influence on the operation of the discharge. Chapter Five is devoted to the study of this effect.

2.4.3 Sputtering

Sputtering is the erosion of a target material under energetic atom or ion bombardment. It was observed for the first time in the middle of the nineteenth century [118, 119]. However, its understanding becomes satisfactory with the development of the *collision cascades theory* in the 1960's. Bombarding energies under which sputtering occurs vary in large limits. For metals, and particularly for copper, the sputtering threshold is about 13 eV for argon bombardment. Ions are the main type of bombarding particles, because they can be easily accelerated in electric fields. In the present study, they are two sorts of ions: argon and copper. As it will be shown later (see Chapter Seven) the main sputtering source are the argon ions. Sputtering is the main application of the magnetron discharges and therefore a magnetron model must include and treat this phenomenon properly.

Recoil atoms from collisions between the penetrating particle and atoms of the target will, if sufficiently energetic, create secondary and higher generation recoils and thus a collision cascade is formed. Sputtering occurs if such moving atoms reach the surface of the target and can overcome the surface binding forces. For these processes leading to sputtering, three regimes can be distinguished [120]. They are schematically shown in figure 2.7 [120] and briefly explained in its caption.

In magnetrons, the energies of the bombarding particles (ions and atoms) are always less than 1 keV, because the applied voltages normally do not exceed 500 V. In this case, the spike regime cannot be realized. The most likely regime is the linear

cascade regime, but the single knock-on regime can also be expected. The linear cascade regime is most often described by *Sigmund's linear collision cascade theory* [120, 121]. According to it, the sputtering caused by an energetic ion consists of three subprocesses: slowing down and energy dissipation of the ion, development of the collision cascade itself, and passage of atoms through the surface, which then become sputtered particles.

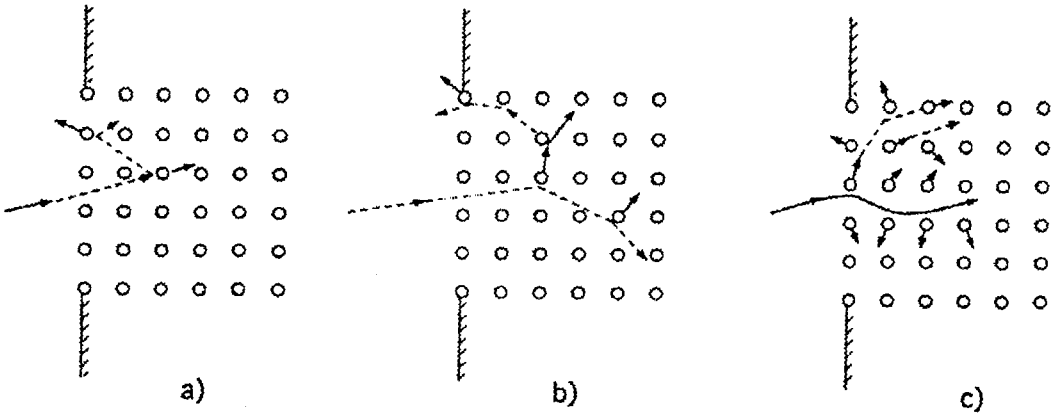

Figure 2.7 The regimes of sputtering: (a) The single knock-on regime. Recoil atoms from the target collisions receive enough energy to be emitted, but not enough atoms are set in motion to generate a recoil (collision) cascade; (b) The linear cascade regime. Recoil atoms from ion-target collisions receive enough energy to generate a recoil cascade. The density of the moving atoms is sufficiently low, so that collisions between the moving atoms can be neglected; (c) The spike regime. The density of the atoms in the recoil cascade is so high that most of the atoms within a certain volume (spike volume) are in motion.

An integral characteristic of the sputtering is the *sputtering yield, Y*, defined as the number of sputtered atoms produced by a single incident ion (atom). The sputtering yield depends on the energy and the incidence angle of the bombarding particle. It is specific for each couple bombarding particle-target atom. For Ar-Cu, Y grows with energy in the range of operation of the sputter magnetrons.

The Sigmund sputtering yield is incompatible with the finite value of the mean energy of sputtered atoms [122]. Different corrections have been made to cope with that [123, 124]. However, there is no solution of the problem valid for the whole energy range so far. A commonly accepted approach is to use the semi

empirical formula for the sputtering yield as a function of the incident energy [125], commonly referred to as the *Matsunami formula*. It is derived based on *Lindhard's range theory* [126] and a compilation of numerous experimental results. This approximation, however, disregards the angular dependence of the sputtering yield. Indeed, it is a well-established fact that the sputtering of copper is maximal at incident angles between 60 and 80 degrees with respect to the surface normal for the energy range in discussion [127]. The Matsunami formula reads

$$Y(E) = 0.42 \frac{\alpha^* Q K s_n(\varepsilon)}{U_s \left[1 + 0.35 U_s s_e(\varepsilon)\right]} \left[1 - \left(E_{th}/E\right)^{1/2}\right]^{2.8}. \tag{2.10}$$

In (2.10), the participating quantities are as follows:

E - the incident energy expressed in eV

ε - the reduced energy

$$\varepsilon = \frac{0.03255}{Z_1 Z_2 \left(Z_1^{2/3} + Z_2^{2/3}\right)^{1/2}} \frac{M_2}{M_1 + M_2} E$$

where Z_1 and Z_2 are the atomic numbers of the incident ion and the target atoms, and M_1 and M_2 are their mass numbers, respectively.

U_s – the sublimation energy of the cathode material

E_{th} – an empirical parameter, dependent on the target material, representing the fact that sputtering requires a threshold energy

$$E_{th} = \left(1.9 + 3.8\left(M_2/M_1\right)^{-1} + 0.134\left(M_2/M_1\right)^{1.24}\right) U_s$$

α^* - an empirical parameter, function of the mass ratio

$$\alpha^* = 0.008 + 0.164\left(M_2/M_1\right)^{0.4} + 0.0145\left(M_2/M_1\right)^{1.29}$$

Q - an empirical parameter, dependent on the target material

s_e - Lindhard's inelastic reduced cross section [126]

$$s_e(\varepsilon) = 0.079 \frac{(M_1 + M_2)^{3/2}}{M_1^{3/2} M_2^{1/2}} \frac{Z_1^{2/3} Z_2^{1/2}}{(Z_1 + Z_2)^{3/4}} \varepsilon^{1/2}$$

s_n - Lindhard's elastic reduced cross section [126]

$$s_n = \frac{3.441\sqrt{\varepsilon}\ln(\varepsilon + 2.718)}{1 + 6.355\sqrt{\varepsilon} + \varepsilon(6.882\sqrt{\varepsilon} - 1.708)}$$

K - a conversion factor, related to the different systems of units used above

$$K = 8.478 \frac{Z_1 Z_2}{(Z_1^{2/3} + Z_2^{2/3})^{1/2}} \frac{M_1}{M_1 + M_2}.$$

Formula (2.10) is used in our model, because it: (i) captures most main features of the sputtering; (ii) is easy to implement; (iii) can handle different incident ions; and (iv) is suitable for kinetic models, because it represents a single collision event, rather than dealing with group properties as fluxes, for example.

2.4.4 Reflection, neutralization and deexcitation

When heavy particles collide with some of the walls, they can be reflected or absorbed. The probability that an incident particle will remain at the surface of the wall is given by the *sticking coefficient.* For magnetron modeling, sticking coefficients are important when the aim is to determine the properties of the film deposited onto the substrate.

In terms of energy, reflection can be elastic or inelastic. In the former, the incident particle is reflected without change in its velocity magnitude. The postcollision velocity, $\boldsymbol{c}$, in this case is given in terms of the precollision speed, $c = |\boldsymbol{c}|$

$$c_z = \sqrt{1 - U_1}, \qquad c_x = c\sqrt{U_1}\sin(2\pi U_2), \qquad c_y = c\sqrt{U_1}\cos(2\pi U_2). \quad (2.11)$$

Here, U_1 and U_2 are independent, homogeneously distributed random numbers in the interval [0,1], c_z is the velocity component normal to the wall, and c_x and c_y are the velocity components parallel to the wall. Equations (2.11) represent the cosine distribution law.

The inelastic reflection is also called *thermal accommodation*. In this case, the incident particle thermalizes during the collision. When reflected, its energy is equal to the energy that corresponds to the temperature of the wall. If T_w is the wall temperature the postcollision velocity is [128]

$$c_z = \sqrt{\frac{-2k_B T_w \ln U_1}{M}}, \quad c_x = c_r \cos\varphi, \quad c_y = c_r \sin\varphi$$
$$c_r = \sqrt{\frac{-2k_B T_w \ln U_2}{M}}, \quad \varphi = 2\pi U_3. \tag{2.12}$$

Here, M is the mass of the incident particle, and U_1, U_2 and U_3 are independent random numbers.

Which of the two mechanisms takes place is determined by a parameter called *thermal accommodation coefficient*. The thermal accommodation coefficient is subject to considerable uncertainty. There are no sufficient data in the literature. At the same time, its value influences the calculation of the gas temperature [129].

Argon metastable atoms are considered to undergo deexcitation at the walls. Afterwards, they are reflected as neutrals. Thus, this is a loss mechanism for them.

Argon ions are neutralized when colliding with the walls and can be reflected, turning into fast neutrals.

Chapter Three

Particle-in-Cell/Monte Carlo Collision method and its application to modeling of sputter magnetrons

3.1 Introduction

Contemporary physics defines four fundamental interactions in the universe: gravitational, electromagnetic, nuclear (strong), and weak. Theoretically, based on their laws plus the formalisms of quantum mechanics and relativity theory, all physical and chemical phenomena can be described. However, the mathematical apparatus, needed for obtaining exact solutions is in most of the cases still missing. In other words, the analytical solutions, able to give answers to specific problems are extremely rare. The description of a "relatively simple" system like the molecules of two chemically interacting substances in a cubic centimeter requires a simultaneous solution of huge number of equations that give the forces acting upon each molecule. An additional complication is the duality that not only the properties of the molecules are a function of the forces, but also that the forces themselves depend on the positions and the states of the molecules. Because of this, the idea of describing and predicting the behavior of a real system of molecules by direct solution of the force equations of its members is practically impossible for now.

An alternative approach is to describe the system on macro level. This means to ascribe collective properties to the whole system, rather than to deal with the individual properties of its members. This approach is additionally motivated by the fact, that the everyday quantities we deal with, like pressure, temperature, power, electric current strength and so on are collective or macroscopic parameters. Of course, every macroscopic parameter can be defined in terms of microscopic forces. However, macroscopic parameters are averaged quantities. And as it is well known from statistics, averaging makes sense only when it is performed over a large

ensemble. Only then, the fluctuations (local or temporal deviations from the mean value) are negligible in comparison to the averaged (macroscopic) value.

Macro description is often referred to as *continuum approach* or *continuum mechanics*. One of its most prominent and mature subfields is fluid dynamics. Although very powerful, fluid dynamics has its natural limit. It works correctly upon systems, whose *Knudsen number* [130]

$$K_n = \frac{\lambda}{L} = \frac{k_B T}{\sqrt{2}\pi d^2 pL} \leq 0.01,$$

where λ is the mean free path of the particles, L is the characteristic size of the system, d is the diameter of the particles and p is the pressure.

At typical operating conditions for sputtering magnetrons (T = 300 K, p = 1 – 100 mtorr, L = 2 – 10 cm) in argon ($d \approx$ 200 pm), K_n >20. This means that the continuum (fluid) approximation of plasma is invalid. In that case, the individual properties of the particles, forming the plasma should be taken into account. Therefore, a *particle model* is required for proper description of sputtering magnetrons.

Particle models is a generic term for the class of simulation models where the discrete representation of physical phenomena involves the use of interacting particles. The name "particles" is used, because in most applications the particles may be identified directly with physical objects. Each particle in the model has a set of properties, such as mass, momentum, charge, velocity and position in space. The key feature of particle models is that the state of the real (physical) system is defined in terms of the attributes of the finite ensemble of particles. The evolution of the system is determined by the laws of interactions of the particles. As it has been mentioned above, computing of the interactions of all real particles that constitute a physical system is not feasible. However, doing the same for a limited ensemble of particles is a task that contemporary computers can cope with. An additional advantage is that in the foundation of the particle models are basic physical laws of interaction. This makes the modeling intuitively clear and sound. In principle, physical phenomena, which are adequately described by classical or pseudo-classical theory, can be simulated by means of particle models. In reality, the

question of the time scales is always open. This means that when significantly different times characterize the phenomena in the same physical system, particle models have their limitation. A typical example is the gas heating in magnetrons (see Chapter Six). It is a much slower process than the formation of the space charge or the establishment of a steady state collision rate, for example. The adequate modeling of the last require a sampling of the system properties in very short intervals, a fraction of the collision frequency. For such short times, heating cannot evolve. On the contrary, if the model is oriented to capture the long-term effects, it can produce a false picture due to the incorrect representation of the short-term effects. Despite these limitations, the particle models are a powerful tool for studying low-pressure gas discharges and magnetrons in particular.

They are three types of particle models that have been developed [131]:

- particle-particle (PP) model;
- particle-mesh (PM) model;
- particle-particle – particle-mesh (PPPM) model.

A PP model is computationally and conceptually the simplest of the three. The system is described by the knowledge of the coordinates and velocities of all particles at a given time. The time evolution is achieved by solving the forces of interaction and equations of motion in discrete moments of time, known as *time steps*. It is obvious that the PP models can have only limited practical applications – for systems consisting of small number of particles or for systems for which a very short temporal evolution is of interest.

The PM models determine the potential only on a discrete mesh of points in the computational domain. Later the particles are advanced, based on a force interpolated to their locations from the potentials known exactly only at the nodes of the mesh. This allows significant speeding at the cost of loss of accuracy. Due to the limited resolution of the mesh, PM models cannot handle correlated systems, *i.e.* systems where the interaction forces are not smoothly varying.

The PPPM models are a hybrid between first two types of models. They split the interaction force in two components – short-ranged and long-ranged. The long-ranged component is treated with the PM model, while the short-ranged with the PP model, where interactions within only a certain radius (usually of the order of a mesh cell) count.

Finally, the limited ensemble can be constructed in two different ways. The first one is to take a very small part of the physical system and to "promote" it to be representative for the whole system. Then each model particle stands for an identical real particle with the same mass, charge, position, and velocity. The representativeness is additionally reinforced by setting periodic boundary conditions. The most widely used example is *molecular dynamics.*

The second one is to create a substitute system, consisting of particles, each of which is representative for a large number of real particles. In this case, however, there is no one-to-one correspondence between a computer and a real particle, although the computer particles still retain much of the identity of the real ones. This approach is commonly used when modeling dilute plasmas, galaxies and semiconductor devises.

In plasma physics, particle-mesh models realized in the second way (see above) have become known as *particle-in-cell* or *PIC* models.

3.2 Particle-in-cell (PIC) model

The PIC model is a numerical model describing an ensemble of collisionless charged particles, which can be, but not necessarily, under the influence of an external electromagnetic force. The constituents of the ensemble are not real physical subjects. They are artificial objects, representing the main physical properties of the real particles, such as charge, mass, and momentum. These computational particles are referred to as *superparticles* (SP's). Each SP represents a large number of real particles. This number is called *weight* and is in the order 10^6 – 10^9. Thus, the first approximation of PIC is the replacement of the real particles in a physical system with artificial superparticles. The second approximation is the discretization of time. This means that the simulated system jumps from one temporary state to another, in contrast to the real system, where the time-evolution is continuous. The third approximation is the space discretization. As it has been mentioned in the introduction of this chapter, a mathematical spatial grid is imposed. The electrostatic field that results from the position of all simulated particles at a given moment of time is calculated on the grid only. In the same fashion, the external field, if any, is calculated. The particles advance is then made by interpolating the forces resulting from these fields from the grid to the particle locations. All this is repeated until convergence is reached. The convergence is

always conditional. This means that the level of numerical noise, naturally introduced by the discretization of time and space, is always an issue. Correspondingly, convergence can be declared when the physical change of the system is lower than this noise. But since the latter cannot be precisely defined, so is the convergence. Thus a PIC simulation is a conditionally repeated loop, called a *computational cycle*, over a time period, Δt equal to the discretization pace in time. An example of such a cycle for the case of an external magnetic field, $\boldsymbol{B}$ and electrostatic field $\boldsymbol{E}$ is shown in Figure 3.1.

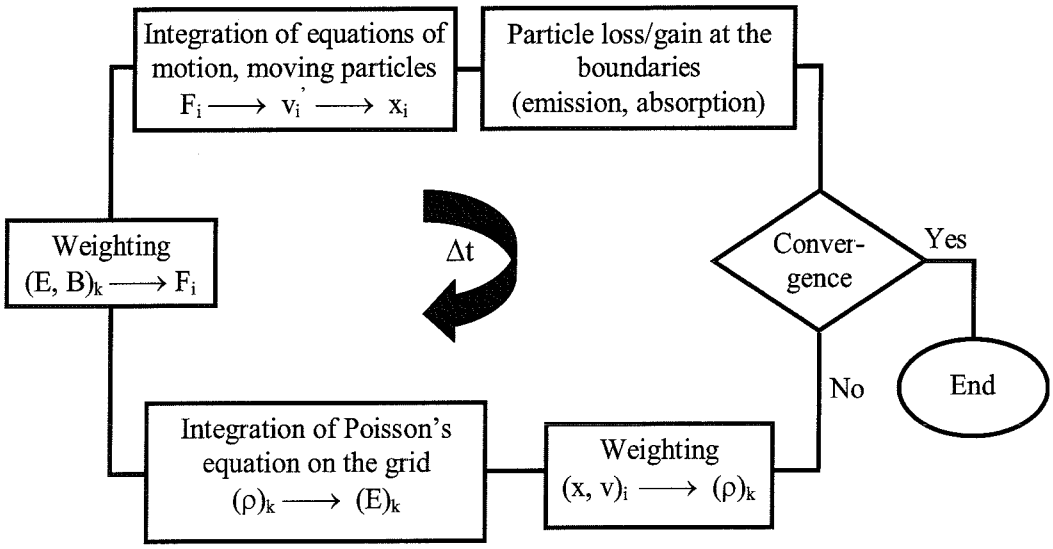

Figure 3.1 A scheme of a PIC cycle for the case of electrostatic field, E, and an external magnetic field, B. Here v represent the velocity of the SP's, x their coordinate, F the force acting upon them, and ρ is the charge density. The index k refers to the grid and the index i to the SP's. The time step of the cycle is Δt.

Before the first execution of the cycle, the initial state of the system need be specified. This includes the initial distributions of the particles in the coordinate and the velocity spaces. In fact, this is the main guess in a PIC simulation, so it must be a physical one.

The detailed explanation of the procedures in the computational cycle follows in the next sections.

3.2.1 Integration of the equation of motion

In a dc magnetron, the force acting on a charged particle has two components: electric and magnetic. The gravitational force is ignored because its magnitude is very low in comparison to the electric and magnetic forces, due to the small masses of the electrons and ions. Further, the magnetic force can be considered external, because the magnetic field that results from the motion of the charges inside the magnetron is only a small perturbation to the magnetic field created by the magnets. Thus the force is

$$\boldsymbol{F} = \boldsymbol{F}_{electric} + \boldsymbol{F}_{magnetic} = q\boldsymbol{E} + q(\boldsymbol{v} \times \boldsymbol{B}), \tag{3.1}$$

leading to equations of motion

$$m\frac{d\boldsymbol{v}}{dt} = q(\boldsymbol{E} + \boldsymbol{v} \times \boldsymbol{B})$$

$$\frac{d\boldsymbol{x}}{dt} = \boldsymbol{v}$$

where $\boldsymbol{x}$ denotes the coordinate. This is a system of ordinary differential equations. It is discretized by the method of the *finite differences* [132] using central differences for most stability and accuracy at low computational cost. A standard way to achieve this is to use the *leap-frog algorithm* whose sketch is given in Figure 3.2. The time centering is clearly seen. The application of the leap-frog algorithm leads to the following system of finite differences equations

$$\begin{aligned} \frac{\boldsymbol{v}_{t+\Delta t/2} - \boldsymbol{v}_{t-\Delta t/2}}{\Delta t} &= \frac{q}{m}\left[\boldsymbol{E}_t + \frac{\boldsymbol{v}_{t+\Delta t/2} - \boldsymbol{v}_{t-\Delta t/2}}{\Delta t} \times \boldsymbol{B}\right] \\ \frac{\boldsymbol{x}_{t+\Delta t} - \boldsymbol{x}_t}{\Delta t} &= \boldsymbol{v}_{t+\Delta t/2}. \end{aligned} \tag{3.2}$$

The magnetic field is not indexed, because it is constant with time. The system (3.2) is in vector form. When written in components, it produces in general six scalar equations. Those of them that originate from the first equation are heavily coupled because of the rotation term. This makes the direct solution very complicated and computationally ineffective, because a solution is needed for every particle per each time step.

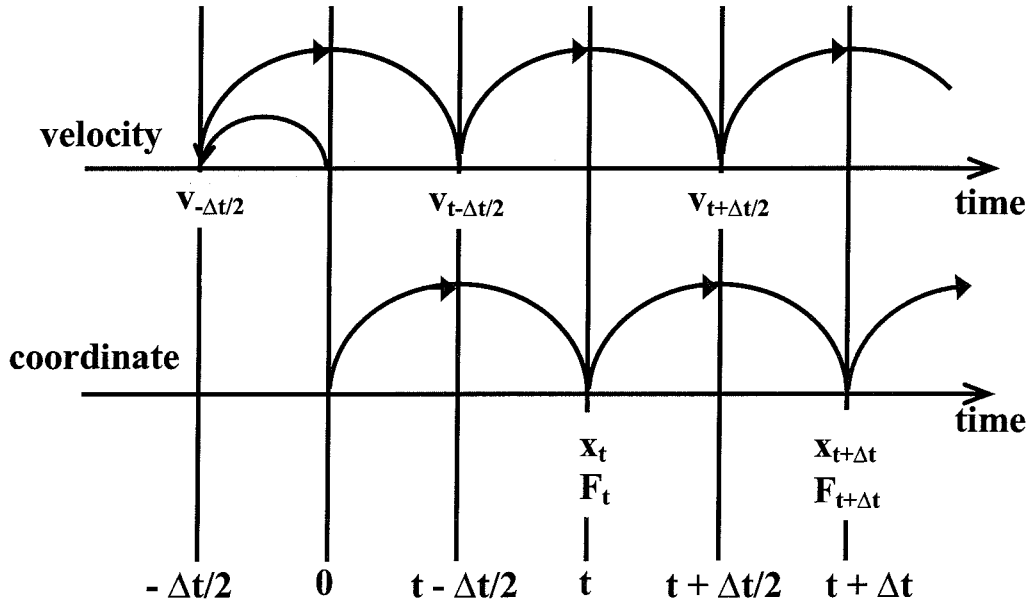

Figure 3.2 Sketch of the leap-frog algorithm. The position of a particle is advanced from a moment t to a moment t + Δt, even though the velocity is not known in neither of the two moments, but in between. This represents the time centering. In time t = 0, the initial conditions are specified at the same time. That is why the velocity is initially returned half a time step back in time.

The problem can be surmounted by noticing that the first term in the right-hand side of the first equation (3.2) is acceleration along the electric field and changes the magnitude of the velocity, while the second term is a rotation of the velocity vector, which does not alter the velocity magnitude. Then the force can be split into pure acceleration and pure rotation. To stick with the time centering, the acceleration can be performed in two stages, each with half of the time step, while the rotation is performed at once, in between the two half-accelerations. In terms of velocities this can be expressed as

$$v_{t-\Delta t/2} \xrightarrow[\Delta t/2]{\text{half acceleration}} v' \xrightarrow[\Delta t]{\text{full rotation}} v'' \xrightarrow[\Delta t/2]{\text{half acceleration}} v_{t+\Delta t/2},$$

where v' and v'' are some dummy velocities. Half-accelerations are trivial for handling since there is no coupling there. The rotation can be handled geometrically, as first suggested by Boris [133]. If $\theta = \omega_c \Delta t$ is the angle of the rotation, then first v' can be incremented to produce some intermediate velocity v^*, perpendicular to both $(v'' - v')$ and B (see Figure 3.3)

$$v^* = v' + v' \times t.$$

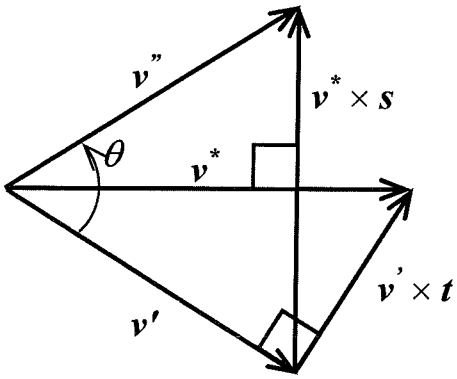

Figure 3.3 Representation of the rotation from v' to v'' in the velocity space. All represented velocity vectors are projectiles of the total velocity in the plane perpendicular to B.

From basic geometric considerations, it is clear that the angle between v^* and v' is precisely $\theta/2$. Then

$$t \equiv \hat{b} \tan\frac{\theta}{2} = \frac{qB\Delta t}{2m},$$

where $\hat{b}$ is the unity vector parallel to B. Since $(v'' - v')$ is parallel to $(v^* \times B)$

$$v'' = v' + v' \times s,$$

where $s \parallel B$, and its magnitude is

$$\boldsymbol{s} = \frac{2\boldsymbol{t}}{1+t^2}$$

and it is obtained by the requirement that the rotation preserves the velocity magnitude - $|v'|^2 = |v''|^2$.

The operations in (3.2) and in the following equations are algebraic, which means they are invariant in all orthonormal coordinate systems. Therefore, only trivial changes are necessary when changing from rectangular to cylindrical coordinate system, for example. Thus for the case of axisymmetric fields, the components of the vectors $\boldsymbol{t}$ and $\boldsymbol{s}$ are

$$t_r = \lambda B_r \qquad t_\theta = 0 \qquad t_z = \lambda B_z$$

$$s_r = \frac{\lambda B_r}{1+\lambda^2\left(B_r^2 + B_z^2\right)} \qquad s_\theta = 0 \qquad s_z = \frac{\lambda B_z}{1+\lambda^2\left(B_r^2 + B_z^2\right)} \tag{3.3}$$

$$\lambda \equiv \frac{q\Delta t}{2m}$$

The parameter, λ, is specific for each type of particles (due to the charge and mass dependence), but is otherwise constant, providing the time step is also constant. Therefore, it can be precalculated to improve the efficiency of the algorithm.

Then the calculation of the rotation passes in two steps. First the dummy velocity, $\boldsymbol{v}^*$, is calculated

$$v_r^* = v_r' + v_\theta' t_z \qquad v_\theta^* = v_\theta' + v_z' t_r - v_r' t_z \qquad v_z^* = v_z' - v_\theta' t_r$$

then the postrotation velocity, $\boldsymbol{v}''$

$$v_r'' = v_r' + v_\theta^* s_z \qquad v_\theta^* = v_\theta' + v_z^* s_r - v_r' s_z \qquad v_z'' = v_z' - v_\theta^* s_r$$

with t_r, t_z, s_r and s_z given by (3.3).

After performing the rotation, the second half of the acceleration is done to obtain the velocity, $\boldsymbol{v}_{t+\Delta t/2}$. Afterwards, the particle is advanced using the second equation (3.2). This last step finalizes the integration of the equation of motion and the advance of the particles.

3.2.2 Charge assignment

Once the particles' positions are calculated (see the previous section), the charge density, ρ, at the grid must be obtained. This procedure is called *charge assignment.* It is done, by ascribing fractions of each point charge to the neighboring grid points. To account for the charge conservation, the sum of all fractions must be equal to the point charge. The resulting charge, assigned to a given grid point, is the sum of all fractions assigned to that grid point. The charge density then is the grid charge divided by some specified volume around it. Each of these physical volumes must be used for only one grid point, *i.e.*, one volume – one grid point.

The function, which determines what fraction of the point charge is to be assigned to a given grid point is called *weighting function* or *shape factor*, *S*. The latter term comes from the way the grid sees the particles. There are different ways to construct the weighting function. The choice is always a compromise between more accurate physics incorporated and higher computational costs. The simplest scheme for charge assignment is the so-called *nearest grid point* (NGP) scheme. The NGP scheme assigns the whole point charge to the nearest grid point. It is computationally very attractive, but is seldom used, because of its coarseness that can introduce fatal numerical instabilities. The NGP scheme is of zeroth order. The first order scheme is the so-called *cloud-in-cell* (CIS) scheme, first introduced by Birdsall and Fuss [134] for one-dimensional plasma simulations. The CIS scheme uses linear interpolation to assign the charge to the nearest grid points. It is much more accurate than the NGP scheme and in addition smoother. When more smoothness or accuracy is desired, higher order schemes can be used. Then a point charge is assigned to not only the closest grid points, but also to one or more distant grid points. The interpolation function then is of second or higher order. The fact that is not linear anymore, leads to often unacceptable computational intensification. That is why the CIS scheme is the most commonly used scheme. In two dimensions, the linear weighting may be performed in two ways. The first one is a complete

analogue of the CIS scheme. The second one is area weighting, also known as *bilinear weighting*. When axisymmetric systems are modeled, the usual choice of coordinate system is cylindrical (r-z). Although formally two-dimensional, it in fact describes a volume. To represent this correctly in the charge assignment, the weighting is to be volumetric (r^2, z), rather than area weighting. The way it is done is shown and explained in Figure 3.4.

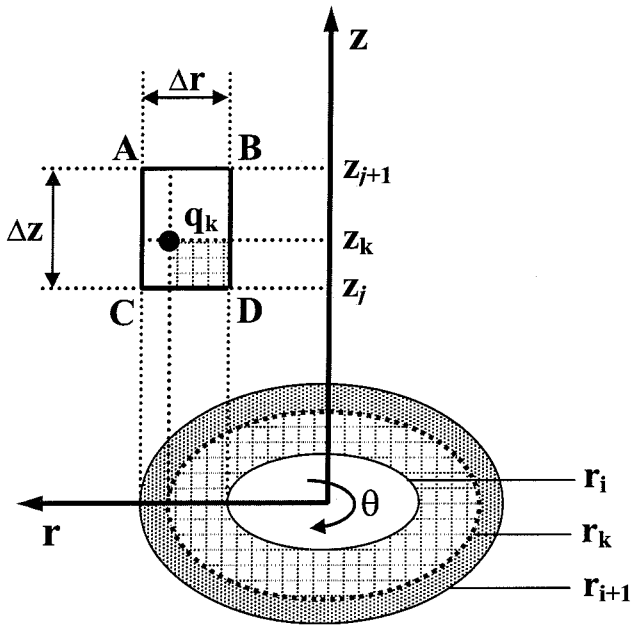

Figure 3.4 Illustration of the charge assignment in cylindrical (r, z) coordinates according to the volumetric weighting. The charge q_k, located at point (r_k, z_k), is distributed among the four grid nodes A, B, C, and D of the grid cell it is located in. The fraction of q_k that is assigned to A, for example, is equal to the product of q_k and the ratio of the volumes: 1) obtained by full rotation of the shaded area of the grid cell ABCD around the z-axis and 2) obtained by full rotation of the whole grid cell ABCD around the z-axis. Δr and Δz are the grid sizes in r and z direction, respectively.

3.2.3 Integration of Poisson's equation on the grid

The charge distribution, characterized by the charge density, ρ, creates an electrical potential, V, given by Poisson's equation, which in cylindrical (r, z) coordinates reads

$$\frac{1}{r}\frac{\partial}{\partial r}r\frac{\partial V(r,z)}{dr}+\frac{\partial}{\partial z}\frac{\partial V(r,z)}{\partial z}=-\frac{\rho(r,z)}{\varepsilon_0}$$

$$\rho(r,z)=q\left(n_i(r,z)-n_e(r,z)\right) \tag{3.4}$$

where n_i and n_e represent the ionic and electronic number density, respectively.

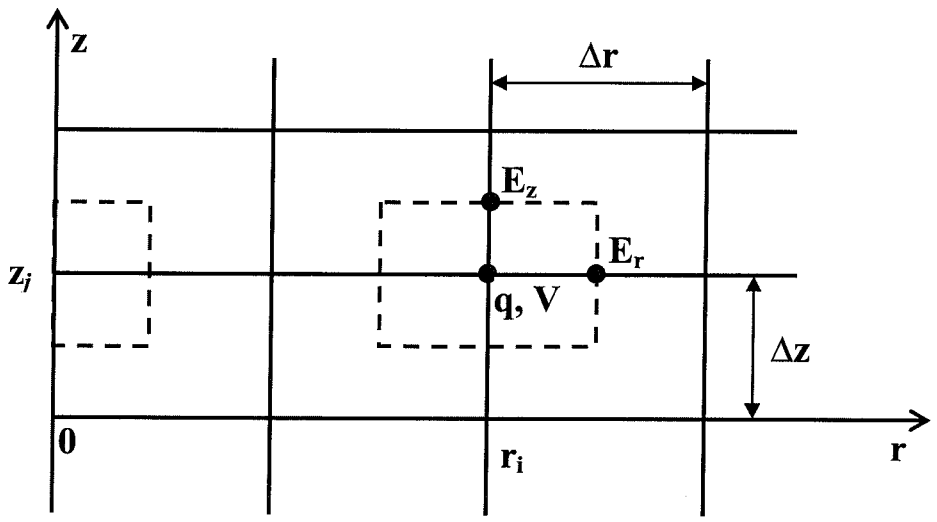

Figure 3.5 A sketch of the computational grid with grid separations Δr and Δz. The dashed line centered on the grid point (r_i, z_j) represents the surface on which the Gauss' theorem is applied. The discrete values of the charge , q, and the potential, V, are known in the grid nodes, whereas the components of the electric field, E_r and E_z, are defined on the Gauss' surface. The surfaces allocated at the origin, r = 0, (left dashed box) are half the size of those located in the volume.

The discretized form of (3.4) is obtained by applying the Gauss' law for the dashed volume, centered on a grid node (r_i, z_j) [Figure 3.5]

$$\frac{q_{i,j}}{\varepsilon_0}=2\pi r_{i+1/2}\Delta z E_{r\,i+1/2,j}-2\pi r_{i-1/2}\Delta z E_{r\,i-1/2,j}+\pi\left(r_{i+1/2}^2-r_{i-1/2}^2\right)\left(E_{z\,i,j+1/2}-E_{z\,j,i-1/2}\right),$$

where the geometric factors are defined as follows

$$\Delta r_{i+1/2} \equiv r_{i+1} - r_i$$

$$\left(\Delta r^2\right)_i \equiv r_{i+1/2}^2 - r_{i-1/2}^2$$

$$\left(\Delta r^2\right)_0 \equiv r_{1/2}^2.$$

Then, employing single cell finite differencing

$$E_{r\,i+1/2,j} = \frac{V_{i+1,j} - V_{i,j}}{\Delta r_{j+1/2}} \qquad E_{z\,i,j+1/2} = \frac{V_{i,j+1} - V_{i,j}}{\Delta z}$$

and using a standard five-point stencil [132], the discretized form of (3.4) becomes

$$\frac{2r_{i+1/2}}{\left(\Delta r^2\right)_i \Delta r_{i+1/2}}\left(V_{i+1,j} - V_{i,j}\right) - \frac{2r_{i-1/2}}{\left(\Delta r^2\right)_i \Delta r_{i-1/2}}\left(V_{i,j} - V_{i-1,j}\right) + \frac{1}{\Delta z^2}\left(V_{i,j+1} - 2V_{i,j} + V_{i,j-1}\right) = \frac{1}{\varepsilon_0}\rho_{i,j} \qquad i > 0 \tag{3.5}$$

$$\frac{2r_{1/2}}{\left(\Delta r^2\right)_0 \Delta r_{1/2}}\left(V_{1,j} - V_{0,j}\right) + \frac{1}{\Delta z^2}\left(V_{0,j+1} - 2V_{0,j} + V_{0,j-1}\right) = \frac{1}{\varepsilon_0}\rho_{0,j} \qquad i = 0$$

The charge density $\rho_{i,j}$ is obtained from $\rho_{i,j} = q_{i,j} / vol_{i,j}$, where

$$vol_{i,j} \equiv \pi\left(\Delta r^2\right)_i \Delta z. \tag{3.6}$$

In the second of the equations (3.5), an implicit boundary condition is implied representing the symmetry around the axis $r = 0$

$$\left.\frac{\partial V}{\partial r}\right|_{r=0} = 0.$$

The other boundary conditions are discussed in Section 3.2.4

Equation (3.4) is an elliptic partial differential equation with separable coefficients. This favors the use of some of the so-called rapid elliptic solvers [131], which are much more efficient than the more frequently used mesh-relaxation methods (MRM's) [135]. Since there is no periodicity in either of the directions, *fast Fourier transform techniques* [136] are inapplicable. Instead, the *cyclic reduction method* (CRM) can be employed [137]. The CRM is more complicated from programmer's viewpoint, but it is the most efficient numerical method for the case of interest. The description of the general CRM and a possible algorithm for its implementation is given in [137].

If an equidistant grid in the z-direction is used, the CRM algorithm is even faster. An additional advantage of the CRM is that as a direct method, it is presumably more accurate than any of the MRM's, which are iterative. That is why, the CRM is used in this work.

3.2.4 External circuit

In Section 1.2.2, the need of a current limiting mechanism in the operation of magnetrons has been discussed (see Figure 1.3). The same problem exists in the modeling of magnetrons and it has been first discussed in [25]. The nature of the problem is that without a current limiting mechanism the simulation current will grow unlimitedly and the charge density will increase correspondingly until the simulation goes unstable. There is also no proof in the literature that two PIC/MCC simulations, one with a current limiting mechanism and one without, evolve in the same way with time. For this reason, even if the simulation without a current limiting mechanism is stopped at an early stage when the electron density approaches some experimentally known value, for example, it is not clear whether the rest of the simulation results are correct.

Such current limiting mechanism can be an external circuit, consisting of a constant voltage source, V_{ext}, and a ballast resistor, R_{ball}, in series with the cathode. It is shown on Figure 3.6 together with a sketch of the planar magnetron considered in the present study.

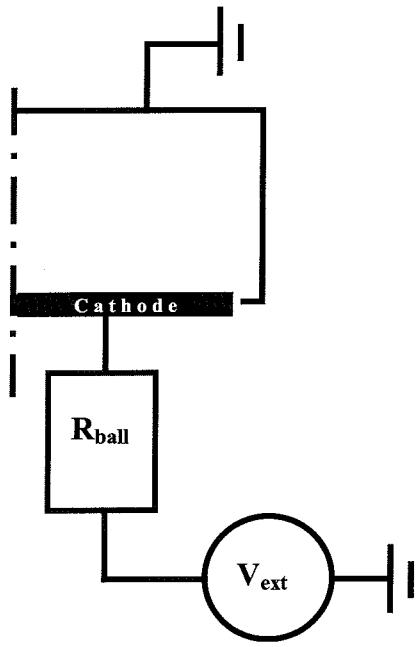

Figure 3.6 An external circuit consisting of a constant voltage source, V_{ext}, and a ballast resistor, R_{ball}, in series with the cathode. The dot-dashed line represents the symmetry axis, r = 0.

The presence of an external circuit leads to the necessity of simultaneous advance in time of the circuit and the discharge. This problem is known as *modeling of bounded plasmas with external circuits* [138]. Its numerical application in 1D has been given in detail in [138 - 140]. A comprehensive procedure for the case of 2D Cartesian coordinates can be found in [141]. For 2D cylindrical (r, z) coordinates, certain modifications in the procedure in [141] are necessary.

The coupling between the circuit and the discharge is maintained through satisfying the charge conservation at the cathode

$$A\frac{d\sigma}{dt} = I_{ext}(t) + Q_{disch} \tag{3.7}$$

where σ is the total surface charge density at the cathode, I_{ext} is the external circuit current, A is the cathode surface, and Q_{disch} is the charge deposited from the discharge on the cathode during a period, dt. The total surface charge can be determined independently of (3.7) by applying Gauss's theorem on a number of

boxes, closely surrounding the cathode. This is done in the following manner. The cathode surface is divided into nr_1 boxes, as shown in Figure 3.7.

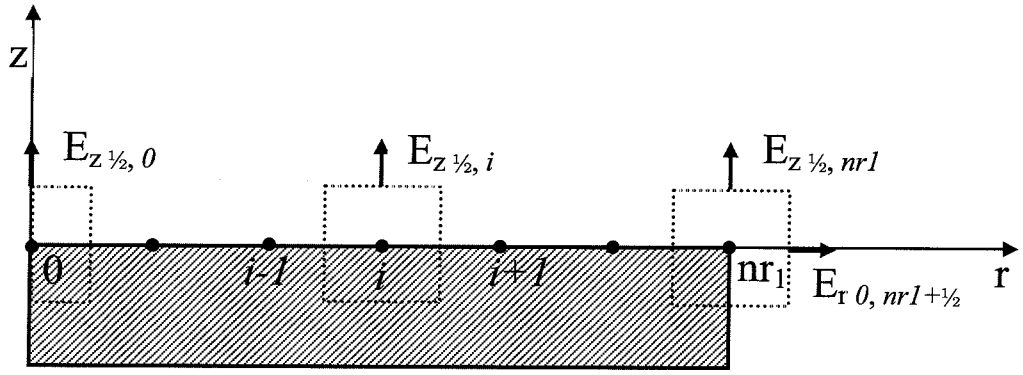

Figure 3.7 The cathode surface (z = 0, r ∈ [0; r_{nr1}]) is enclosed by nr_1 boxes. For each of them, the Gauss' law is applied. For all boxes, except the one centered on r = nr_1, the flux of the electric field through the boxes' surfaces is non-zero only in +z-direction. For the box centered on r = r_{nr1}, there is also a non-zero flux in r-direction.

For the i-th box Gauss' law is

$$\oint_{S_i} \varepsilon_0 \boldsymbol{E} \cdot \boldsymbol{ds} = Q_i$$

where S_i is the surface of the i-th box, $\boldsymbol{ds}$ is the surface element, and Q_i is the total charge inside the box. The total charge, Q_i, is a sum of the surface charge, caused by the charging of the cathode by the discharge and the external circuit, and the volume charge that comes from the charged plasma particles, which are weighted to the grid point i[♦] in the radial direction. Then Gauss' law takes the form

$$\oint_{S_i} \varepsilon_0 \boldsymbol{E} \cdot \boldsymbol{ds} = Q_i = \oint_{S_i} \sigma_i ds + \int_{Vol_i} \rho_i dV,$$

where σ_i is the surface charge density at point i, ρ_i is the charge density in the same point, and Vol_i is the volume of the box. This is equivalent to

♦ The grid point is actually (0, i), but the first index is omitted for simplicity, hence i refers to the r-coordinate.

$$\varepsilon E_{z\,i,1/2} = \frac{1}{2}\rho_i Vol_i + \sigma_i \tag{3.8}$$

By use of finite differences, $E_{z\,i,1/2}$ can be expressed as $\left(\Phi_0 - V_{i,1}\right)/\Delta z$, where Φ_0 is the cathode potential. In this case, the cathode is assumed an ideal conductor, hence there is no radial dependence of the cathode potential. Then (3.8) can be rewritten for σ_i

$$\sigma_i = \frac{\varepsilon_0}{\Delta z}\Phi_0 - \frac{\varepsilon_0}{\Delta z}V_{i,1} - \frac{\Delta z}{2}\rho_i, \qquad i \in [0, nr_1 - 1]$$

$$\sigma_{nr1} = -\frac{\varepsilon_0}{\Delta z}C_1 V_{nr_1,1} + \left(\frac{\varepsilon_0}{\Delta z}C_1 + \varepsilon_0 C_2\right)\Phi_0 - C_3\rho_{nr_1,0}$$

where the constants C_1, C_2, and C_3 are

$$C_1 = \frac{r_{nr_1+1/2}^2 - r_{nr_1-1/2}^2}{r_{nr_1}^2 - r_{nr_1-1/2}^2 + r_{nr_1}\Delta z}$$

$$C_2 = \frac{1}{r_{rn_1+1/2} - r_{rn_1-1/2}}\frac{r_{nr_1+1} - r_{nr_1}}{r_{nr_2} - r_{nr_1}}$$

$$C_3 = \frac{\Delta z}{2}\frac{2r_{nr_1+1/2}^2 - r_{nr_1}^2 - r_{nr_1-1/2}^2}{r_{nr_1}^2 - r_{nr_1-1/2}^2 + r_{nr_1}\Delta z}$$

The total surface charge density on the cathode is

$$\sigma_T = \sum_{i=0}^{nr_1}\sigma_i = \sum_{i=0}^{nr_1-1}\sigma_i + \sigma_{nr_1}$$

$$\sigma_T = a_1\Phi_0 + a_2\sum_{i=0}^{nr_1-1}V_{i,1} + a_3 V_{nr_1,1} + a_4\sum_{i=0}^{nr_1-1}\rho_{i,0} + a_5\rho_{nr_1,0}, \tag{3.9}$$

where the a's are

$$a_1 = nr_1 \frac{\varepsilon_0}{\Delta z} + \varepsilon_0 C_1 + \varepsilon_0 C_2$$

$$a_2 = -\frac{\varepsilon_0}{\Delta z}$$

$$a_3 = a_2 C_1$$

$$a_4 = -\frac{\Delta z}{2}$$

$$a_5 = -C_3.$$

Equation (3.7) can be discretized with backward finite differences

$$A\left(\sigma_T^t - \sigma_T^{t-1}\right) = \left[I_{ext}(t) - I_{disch}\right]\Delta t \tag{3.10}$$

Then according to Kirchhoff's voltage loop law, the cathode potential, $\Phi_0 = V_{ext} - R_{ext} I_{ext}$. Expressing from there I_{ext} and introducing it to (3.10) produces

$$\sigma_T^t = \frac{1}{A}\left[\left(V_{ext} - \Phi_0\right)\frac{\Delta t}{R_{ext}} + Q_{disch}^t\right] + \sigma_T^{t-1} \tag{3.11}$$

Equations (3.9) and (3.11) can be combined in a single equation for Φ_0 as a function of the potentials, $V_{i,1}$, and charge densities, $\rho_{i,0}$, both taken in time, t, and the total surface charge density at time $(t - 1)$. The problem here is that such an equation is at the same time a boundary condition for the Poisson's equation (3.5). This leads to the necessity (3.5) to be solved iteratively until the boundary condition

is fulfilled, which is extremely inefficient in computational sense. Alternatively, the potential, $V_{i,j}$, can be expressed as a superposition of two other potentials

$$V_{i,j} = V_{i,j}^{P} + \Phi_0 V_{i,j}^{L}. \tag{3.12}$$

The potential, $V_{i,j}^{P}$, is a result solely of the presence of charges inside the magnetron. Thus it is a solution of (3.5) with boundary conditions $V_{i,0}^{P} = V_{i,nz}^{P} = V_{nr,j}^{P} = 0$, where *nr* and *nz* represent the grid nodes located at the walls of the magnetron. The dimensionless potential, $V_{i,j}^{L}$, accounts for the influence of the cathode potential and is a solution of the Laplace equation $\Delta V_{i,j}^{L} = 0$ with boundary conditions $V_{i \le nr_1,0}^{L} = 1$ and $V^{L} = 0$ at the walls. In the gap between the cathode and the grounded wall at r = 0, V^{L} is assumed linearly decaying with the distance from the cathode.

Combining (3.9) and (3.11) and replacing $V_{i,j}$ with (3.12) yields

$$\Phi_0 = \frac{-a_2 \sum_{i=0}^{nr_1-1} V_{i,1}^{P} - a_3 V_{nr_1,1}^{P} - a_4 \sum_{i=0}^{nr_1-1} \rho_{i,0} - a_5 \rho_{nr_1,0} + \frac{Q_{disch}^{t}}{A} + a_6 V_{ext} + \sigma_T^{t-1}}{a_7}, \tag{3.13}$$

where a_6 and a_7 are

$$a_6 = \frac{\Delta t}{R_{ext} A}$$

$$a_7 = a_1 + a_2 \sum_{i=0}^{nr_1-1} V_{i,1}^{L} + a_3 V_{nr_1,1}^{L} + a_6.$$

In this way, Φ_0 at time, *t*, can be calculated only from known quantities at the same time. Then the overall procedure for simultaneous advance of the circuit and the discharge in time is as follows. In the beginning of the simulation, the Laplace equation is solved to determine $V_{i,j}^{L}$. Next, the coefficients, a_1 through a_7, are calculated. These two steps are performed only once. Then at each time step,

(3.5) is solved with zero boundary conditions to obtain $V_{i,j}^{P}$. With $V_{i,j}^{L}$ and $V_{i,j}^{P}$ known, (3.13) is solved for Φ_0. Afterwards, (3.12) is used to produce the discrete potential distribution in the discharge, V_{ij}. Finally, (3.11) is solved to get σ_T^t, which is going to be used in (3.13) during the next time step.

Once the potential, V_{ij}, is known, the electric field, $\boldsymbol{E}$, is calculated from

$$\boldsymbol{E} = -\nabla V ,$$

which is performed by central finite differences inside the computational domain

$$E_{r\,i,j} = \frac{V_{i-1,j} - V_{i+1,j}}{r_{j+1} - r_{j-1}}$$

$$E_{z\,i,j} = \frac{V_{i,j-1} - V_{i,j+1}}{2\Delta z}. \tag{3.14}$$

On the boundaries, the central differences are replaced by backward or forward differences. To keep the same second order of accuracy as inside the domain, schemes with three points [132] are implemented on the boundaries

$$E_{r\,0,j} = 0$$

$$E_{r\,nr,j} = \frac{(r_{nr-2} - r_{nr})^2 V_{nr-1,j} - (r_{nr-1} - r_{nr})^2 V_{nr-2,j} + \left[(r_{nr-1} - r_{nr})^2 - (r_{nr-2} - r_{nr})^2\right] V_{nr,j}}{(r_{nr-1} - r_{nr})(r_{nr-2} - r_{nr})^2 - (r_{nr-2} - r_{nr})(r_{nr-1} - r_{nr})^2}$$

$$E_{z\,i,0} = \frac{3V_{i,0} - 4V_{i,1} + V_{i,2}}{2\Delta z} \tag{3.15}$$

$$E_{z\,i,nz} = \frac{-3V_{i,nz} + 4V_{i,nz-1} - V_{i,nz-2}}{2\Delta z}.$$

3.2.5 Force interpolation and smoothing

With $\boldsymbol{E}_{i,j}$ calculated from (3.14) and (3.15), the force, $\boldsymbol{F}_{i,j}$, needs to be interpolated to the particle locations. This operation is known as *force interpolation* and is inversely identical to the charge assignment (see Section 3.2.2). What is important is that the same shape factor must be used in both charge assignment and force interpolation. Not doing so usually results in a non-physical self-force, *i.e.*, a particle experiences a "force" caused by the particle itself [131, 139]. Using the same shape factor secures the total momentum conservation of the simulated system.

The procedure of weighting (charge assignment and force interpolation) introduces naturally fluctuations of the grid quantities. The amplitude and the density of the fluctuations are reversely proportional to the number of superparticles per grid cell. In magnetrons, the charge distribution is very inhomogeneous (see Chapter Four). This results in a situation where in some grid cells the number of SP's is very small, which can cause strong fluctuations. These fluctuations can evolve in instabilities that can terminate the simulation or bring it to a non-physical solution. To prevent that from happening, *digital filtering* or *smoothing* is needed. The smoothing can be described as substitution of the grid quantities at every grid node with some averaged (smoothed) values received by averaging the grid quantities at the adjacent grid nodes. Different methods exist for that. In the current simulation, after the charge assignment is finished the charge density is smoothed before being used for calculation of the potential.

There are many digital filters that in principle can be used [142, 143]. However, the filter must be isotropic in order to represent correctly the physical reality. Additionally, it must be computationally efficient, because the filtering is performed at each time step. The filter, adopted here, uses the unfiltered values of the closest neighboring grid points (9-point filtering) [139]. It can be represented by the following transformation

$$\rho_{i,j}^{filtered} \leftarrow \frac{4\rho_{i,j}^{raw} + 2\left(\rho_{i-1,j}^{raw} + \rho_{i+1,j}^{raw} + \rho_{i,j-1}^{raw} + \rho_{i,j+1}^{raw}\right) + \rho_{i-1,j-1}^{raw} + \rho_{i-1,j+1}^{raw} + \rho_{i+1,j+1}^{raw} + \rho_{i+1,j-1}^{raw}}{16}.$$

3.2.6 Stability and accuracy of the PIC model

The PIC model is a discrete approximation of the continuous physical picture. As such, it always introduces a numerical noise. The magnitude of this noise reaches zero only when the number of superparticles per grid cell approaches the number of real particles in the same grid cell. Therefore, all particle simulations are always noisy in contrast to fluid models. The noise however should be kept under certain maximum level in order to have meaningful results. More importantly, the error introduced by the noise must not be allowed to grow with the simulation. Several factors influence directly the noise. These include the time step, the number of SP's per grid cell, the shape factor, and the grid size. The specific mechanism through which this influence is manifested depends on the type of the numerical integrator of the equation of motion. Since the leap-frog integrator is implemented in the present study (see Section 3.2.1), a quantitative analysis for it is given for the one-dimensional case. For that purpose, a harmonic oscillator is chosen, because its equation of motion has an analytical solution, which can be compared to the numerical one.

A 1-d harmonic oscillator with an angular frequency, ω_0, has an equation of motion [96]

$$\frac{d^2x}{dt^2} = -\omega_0{}^2 x, \tag{3.16}$$

which exact solution is

$$x(t) = A(t_0)\cos\omega_0 t + B(t_0)\sin\omega_0 t\,. \tag{3.17}$$

The discrete form of (3.16) with respect to the leap-frog algorithm is

$$\frac{x^{t+\Delta t} - 2x^t + x^{t-\Delta t}}{\Delta t^2} = -\omega_0{}^2 x^t\,. \tag{3.18}$$

It must have the same type of solution as (3.16) has. Having that in mind the solution of (3.18) is

$$x^t = Ae^{-i\omega t}, \tag{3.19}$$

where A is an initial value and ω is unknown. Expressing $x^{t-\Delta t}$ from (3.19) by replacing t with $t - \Delta t$ and substituting it together with x^t, taken also from (3.19), in (3.18) yields

$$\sin\left(\omega\frac{\Delta t}{2}\right) = \pm\omega_0\frac{\Delta t}{2}. \tag{3.20}$$

In order (3.18) to be a physically correct representation of (3.16), $\omega \approx \omega_0$. According to (3.20), it is fulfilled for $\omega_0\Delta t \ll 2$. By plotting (3.20) as a solution for ω in terms of ω_0, it is easily seen [139] that for $\omega_0\Delta t > 2$, the solution becomes complex with growing and decaying roots. This is a typical manifestation of numerical instabilities. The accuracy of the leap-frog algorithm can also be obtained from (3.20). Assuming $\omega_0\Delta t \ll 1$ and expanding ω in Taylor series in terms of the small parameter $\omega_0 t$ produces [139]

$$\omega\frac{\Delta t}{2} \approx \omega_0\frac{\Delta t}{2}\left[1+\frac{1}{6}\left(\omega_0\frac{\Delta t}{2}\right)^2+\ldots\right],$$

which means that the leap-frog algorithm has a quadratic error term for $\omega_0\Delta t \ll 1$. It should be emphasized that the error is cumulative with the number of time steps. This means that the longer the simulation is run, the bigger the overall error is. Consequently, the following paradox exists. Setting the tolerable error too small limits the number of time steps. Allowing a large number of time steps increases the error as the cube of the time step [139]. In the literature [131], a common compromise has been set

$$\omega_0\Delta t \approx 0.2. \tag{3.21}$$

In magnetrons, the standard leap-frog algorithm is expanded to deal with the magnetic field and the rotation caused by that field. Thus, it is important to keep the calculated rotational angle reasonably close to the real one. An analysis of this problem can be found in [131]. It shows that for magnetic field strengths of interest the condition (3.21) secures that the rotation term of the equation of motion, when treated as described in Section 3.2.1 , is calculated with an error not exceeding that of the general leap-frog algorithm. The exact condition is

$$\omega_0 \Delta t < 0.35 \tag{3.22}$$

Comparing (3.21) and (3.22) launches the question for specifying ω_0. In the above analysis, ω_0 was the frequency of the harmonic oscillator. In plasma simulations, it has to be replaced by the characteristic frequency in the simulated system. In dc magnetrons, the two highest frequencies are the electron plasma frequency

$$\omega_{pe} = \sqrt{n_e q_e^2 / \varepsilon_0 m_e}$$

and the electron gyro frequency, ω_{ce}, given by (2.3). Hence, $\omega_0 = max\{\omega_{pe}, \omega_{ce}\}$.

Generally, in two and three dimensions, the discussion for the stability and accuracy is much more complex. However, when one of the dimensions is dominant and the stability is achieved for it, it can be accepted that the whole simulation is stable. Typically, the dominant dimension is in the direction of the strongest gradient of the electric field. For the current simulation, it is the z-direction. In line with that, the *Courant criterion* [144], is

$$v_k \Delta t_k / \Delta z \le 1, \tag{3.23}$$

where v_k is the characteristic velocity of the k-th type of SP's and Δt_k is its time step. The meaning is that, if (3.23) is violated, too many SP's are jumping over field variations, which leads to numerical heating. Thus for a Δt given by (3.22), the

relation (3.23) sets a bottom limit for the grid size, Δz. At the same time, the grid must be fine enough to resolve the sheath. This leads to the upper limit for Δz

$$\Delta z \leq \lambda_D, \tag{3.24}$$

where λ_D is the Debye length defined in (1.1).

Relations (3.21), (3.23) and (3.24) define the stability and accuracy domain in terms of time step and grid size for the standard PIC simulation. Adding to that MCC brings some additional conditions. More detail about that is given at the end of the next Section. Modifications of the stability criteria with respect to speeding up the procedure are presented in Section 3.5.2.

3.3 Monte Carlo collision (MCC) method

The PIC method has been originally designed to model collisionless plasmas. In magnetrons, as in other types of glow discharges, collisions sustain the discharge. Therefore, a numerical model must be able to incorporate them. This can be achieved by coupling the PIC model with a *Monte Carlo collision* (MCC) model. This means that at a certain moment of the time step the SP's should be checked for collisions. The coupling is not just a numerical trick made to account somehow for the collisions. It has sound physical grounds, which follow from the Boltzmann equation, which for electrons that collide only with neutrals (with a differential cross section $\sigma_{e\text{-}N}$), can be written as [145]

$$\frac{\partial f^{e^-}}{\partial t} + v_i \frac{\partial f^{e^-}}{\partial x_i} + \frac{1}{m_{e^-}} \frac{\partial f^{e^-}}{\partial v_i}\left(F_i f^{e^-}\right) = \iiint \left[f^{e^-}(\boldsymbol{v}') f^N(\boldsymbol{u}') - f^{e^-}(\boldsymbol{v}) f^N(\boldsymbol{u}) \right] g \sigma_{e^-N} d\Omega du, \tag{3.25}$$

where f^{e^-} and f^N are the velocity distribution functions of the electrons and neutrals respectively, $\boldsymbol{v}$ and $\boldsymbol{u}$ are their precollision velocities, $\boldsymbol{v}'$ and $\boldsymbol{u}'$ are their postcollision velocities, $g = |\boldsymbol{v} - \boldsymbol{u}|$ is the relative speed, dΩ is the solid angle, the force, $\boldsymbol{F}$, is given by (3.1), and summation over the repeating index, i, is imposed.

If a method that produces $f^{e^-}(\boldsymbol{v},\boldsymbol{x},t+\Delta t)$ from $f^{e^-}(\boldsymbol{v},\boldsymbol{x},t)$ exists, the solution of (3.25) at any time can be computed step-by-step starting from the initial velocity distribution. For a small enough Δt the solution can be expanded

$$f^{e^-}(\boldsymbol{v},\boldsymbol{x},t+\Delta t)=f^{e^-}(\boldsymbol{v},\boldsymbol{x},t)+\left.\frac{\partial f^{e^-}}{\partial t}\right|_t \tag{3.26}$$

Combining (3.25) and (3.26) allows the distribution function to be expressed as

$$f^{e^-}(\boldsymbol{v},\boldsymbol{x},t+\Delta t)=(1+\Delta tC)(1+\Delta tD)f^{e^-}(\boldsymbol{v},\boldsymbol{x},t), \tag{3.27}$$

where C and D can be interpreted as collisional and noncollisional operators, respectively

$$C(f^{e^-})=\iint\left[f^{e^-}(\boldsymbol{v}')f^N(\boldsymbol{u}')-f^{e^-}(\boldsymbol{v})f^N(\boldsymbol{u})\right]g\sigma_{e^-N}d\Omega d\boldsymbol{u} \tag{3.28}$$

$$D\left(f^{e^-}\right)=-v_i\frac{\partial f^{e^-}}{\partial x_i}-\frac{1}{m_{e^-}}\frac{\partial f^{e^-}}{\partial v_i}\left(F_i f^{e^-}\right). \tag{3.29}$$

Equation (3.27) effectively decouples collisional and noncollisional parts of the motion. It is identical to (3.26) if the quadratic terms with respect to Δt can be neglected. It has been proven [146, 147] that this can be done when $\Delta t \ll \tau_c$, where τ_c is the mean collision time. Then a procedure to solve the Boltzmann equation is given in [146]. First, obtain

$$f_1^{e^-}\equiv[1+\Delta tD]f^{e^-}(t). \tag{3.30}$$

Next, calculate

$$f^{e^-}(t+\Delta t)\equiv[1+\Delta tC]f_*^{e^-}. \tag{3.31}$$

Equation (3.30) is equivalent to the PIC method. Thus, the PIC method is a solution of the collisionless Boltzmann equation. Equation (3.31) requires solving the double integral in the right-hand side of (3.28). It is usually done by the numerical method known as *Monte Carlo* [148].The nature of the PIC method though, namely that it treats the whole particle ensemble particle by particle, requires a different approach. Note that (3.30) and (3.31) yield the integral velocity distribution of the whole system, while in the PIC method the discrete properties of the particles are examined. Correspondingly, the collision probability for each particle is needed. After some lengthy manipulations [149], it can be proven that the probability, P_i, for the i-th electron (for example) to collide binary with any of the particles of type g (gas atom, for example) during time, Δt, calculated from (3.28), agrees with the probability received from the elementary free-path theory [130]. That is

$$P_i = \nu \Delta t,$$

where ν is the collision rate given by $\nu = n_g \bar{g} \sigma_T$ with n_g being the target density, $\bar{g}$ the average relative speed between the i-th electron and the target particles, and σ_T the total cross section. In case of big disparity between the speed of the colliding particle, v_i, and the mean speed of the target particles, a common approximation is $\bar{g} \approx v_i$.

The cross section and therefore the collision rate are generally energy dependent. Since the velocities of the particles change with time, the collision rate is also time dependent. The probability, Q, that an electron started at time $t = 0$ does not collide in the interval $(0, t + \Delta t)$ is

$$Q(t + \Delta t) = Q(t)\left[1 - \nu(t\Delta t)\right],$$

where the term in the square brackets is the probability for no collision in the interval $(t, t + \Delta t)$. When $\Delta t \to 0$, this equation becomes

$$\frac{dQ}{dt} = -\nu(t)Q(t)$$

with a solution

$$Q(t) = \exp\left[-\int_0^t \nu(t)dt\right]. \tag{3.32}$$

If the collision occurs in time T_c and the probability density function of this event is $f_c(t)$, the probability for collision

$$\mathrm{Prob}\{T_c < t_c\} = \int_0^{t_c} f_c(t)dt = 1 - Q(t_c).$$

The general rule for making a random sample of a probability density function $f_c(t)$ is [150]

$$\int_0^{t_c} f_c(t)dt = 1 - Q(t_c) = U, \tag{3.33}$$

where U is a random number uniformly distributed in the interval [0.1]. Once U is generated, the time, t_c can be calculated from (3.32) and (3.33), and thereafter the collision in $t = t_c$. This constitutes the general Monte Carlo procedure for determining whether a collision happens. However, it is impractical, unless the collision rate is constant.

Instead, the *null-collision method,* first introduced by Scullerud [151], can be used. Its main feature is the introduction of a constant maximum collision frequency, ν_{max}, that is always higher than $\nu(t)$ for any t. Then when (3.32) and (3.33) are solved with ν_{max} in place of ν, the solution is

$$t_c' = -\nu_{\max}^{-1} \ln U. \tag{3.34}$$

To find a relation between t_c and t_c', the same U should be used. Then according to (3.33), $t_c' < t_c$. The collision probabilities for ν and ν_{max} respectively at time, $t = t_c'$, are

$$P_c = 1 - \exp\left[-\int_0^{t_c'} \nu(t)\,dt\right]$$
$$(P_c)_{\max} = 1 - \exp\left(-\nu_{\max} t_c'\right). \tag{3.35}$$

Then the probability that a collision is regarded real, *i.e.*, it really happens in the model, is equal to $P_c/(P_c)_{\max}$. Note that the condition, $P_c < (P_c)_{\max}$, is always fulfilled. The efficiency of the method comes from the fact that there is no need to calculate the actual collision time, t_c, in (3.33). If t_c' is small enough, which is always true if the time step of PIC is used, the collision rate can be approximated with a quadratic polynomial. Then the integral in the first of the equations (3.35) becomes [146]

$$\int_0^{t_c'} \nu(t)dt = \frac{t_c'}{6}\left[\nu(0) + 4\nu\left(t_c'/2\right) + \nu\left(t_c'\right)\right]. \tag{3.36}$$

Equation (3.36) can be used to determine the probability for collision from (3.35).

So far, the total probability of collision, P_T, has been discussed. When there are m types of collisions, all possible in the time interval of interest, the probability for the k-th type of collision ($0 < k \le m$), characterized by a collision rate ν_k is

$$P_k = 1 - \exp\left[-\int_0^{t_c'} \nu_k(t)\,dt\right],$$

and

$$P_T = \sum_{k=1}^{m} P_k. \tag{3.37}$$

Then the sampling of the k-th collisional event is made with a probability of P_k / P_T.

The drawbacks of the null-collision method are connected to the implicit condition that the particles in the ensemble have the same collision rates. Or, what is equivalent, that their mean collision path is the same. Such situation is easily realized in a uniform electric field, for example. That is why the method is especially efficient in swarm calculations. Its application to PIC simulations has been introduced by Vahedi and Surendra [152]. However, no theoretical analysis has been carried out to determine what strength of the gradients of the electric field may severely trespass the stability domain of the null-collision method. In magnetrons, strong gradients in both electric and magnetic fields exist, and as it has already been pointed out, the whole magnetron plasma is very inhomogeneous. The amplitude of the electric field gradients is proportional to the strength and geometry of the magnetic field. All this makes the use of the null-collision method in magnetron modeling highly questionable, especially at strong magnetic fields. Additional problem may appear from the selection of the particles (especially the electrons) which are considered for collision in each time step. The procedure of Vahedi and Surendra [152] requires determination of some maximum number of particles eligible for collision. It is intuitively clear that when the particles have a small dispersion in their velocity distribution they can be selected randomly. Unfortunately, that is not the case in magnetrons, where a relatively small number of electrons are responsible for the main processes that sustain the discharge. Consequently, if the colliding electrons are selected purely on random basis it can lead to underestimation of the collisions of the "important" group of electrons.

The above discussion motivates the introduction of a collision sampling procedure, both capable of dealing with strongly inhomogeneous velocity and spatial distributions and computationally effective. Such a procedure has been developed by Nanbu [153]. It makes it possible, by using a single random number, to determine not only whether a collision occurs, but also what type of collision takes place. In this way, the computational efficiency is significantly improved. The checking is done on per particle basis, which ensures the equal treatment of all particles. For the

case of electron-neutral collisions, where the speed of the neutrals is neglected and they are considered homogeneously distributed in space with a density, n_g, the procedure is as follows.

The total probability of collision is given by (3.37), where

$$P_k = n_g v \sigma_k \Delta t. \tag{3.38}$$

Here, v is the electron speed. Equation (3.37) can be rewritten as

$$1 = P_T + (1 - P_T) = \left[\sum_{k=1}^{m} P_k + \left(\frac{1}{m} - P_k \right) \right],$$

which is visualized in Figure 3.8.

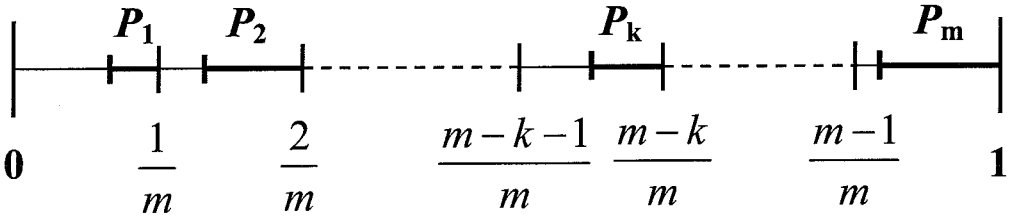

Figure 3.8 Visualization of Nanbu's method [153] for sampling a collisional event. The right-hand side of the k-th interval (represented by ticker line) represents the probability of the k-th type of collision. The sum of the left-hand sides of all intervals (represented by thinner line) is equal to the probability of no collision. The sum of the right-hand sides equals the total collision probability, P_T.

The unit length is divided into m equal intervals. Each interval has two parts. In the k-th interval, e.g., the left part has a length equal to $1/m - P_k$ and the right side is P_k. The sum of the right parts of all m intervals equals the total collision probability, P_T, and the sum of the left parts gives the probability of no collision, $1 - P_T$. The procedure is to generate a uniformly distributed random number $U \in [0,1]$. The integral part of $mU + 1$ specifies the k-th interval corresponding to the k-th collisional event, *i.e.*, $k = \text{int}[mU + 1]$. Then only P_k needs to be calculated,

which is a significant speed-up in case of big m. Finally, the same U is checked to see in which part of the k-th interval it falls. If

$$U > \frac{k}{m} - P_k$$

holds, the k-th collisional event occurs. If not, no collision takes place.

In all Monte Carlo collision algorithms, the collisional time step, Δt_c must be small enough in order not to miss a real collision. This condition comes from the fact that for one time step, the colliding particle is allowed to undergo maximum one collision. For Nanbu's method, this condition is $P_k < 1/m$ for all m, for all electron energies. The electron energies in dc magnetrons are restricted approximately to the energy equivalent of the applied voltage. Then some $P_{\max}$ can be estimated, that corresponds to the biggest cross section, $\sigma_{\max}$, of all the included processes for all the possible energies. Then the maximum allowed Δt_c can be obtained from (3.38) with σ_k replaced by $\sigma_{\max}$ and $P_k = 1/m$. This is practically not a limitation at all, when the method is used in PIC simulation, because the general time step limitation of PIC (3.22) is more restrictive.

The coupling of the collision check with the PIC cycle can be done in different moments inside the time step. Our choice is to check for a collision in the middle of the time step. This choice has been dictated by the time centering of the leap-frog integrator (see Section 3.2.1, and especially Figure 3.2). At this moment, the positions of the particles are exactly known. At the same time, only half of the acceleration is applied. The rotation may be, or may not be calculated. It does not matter, because the rotation does not change the speed and hence the energy of the colliding particle. Therefore, the energy is also known at the middle of the time step, though the velocity is unknown.

The inclusion of the MCC module to the PIC method is shown schematically in Figure 3.9. In case of collisions, the precollision velocity of the colliding particle is replaced by its postcollision velocity (see next Section); otherwise it remains unaltered.

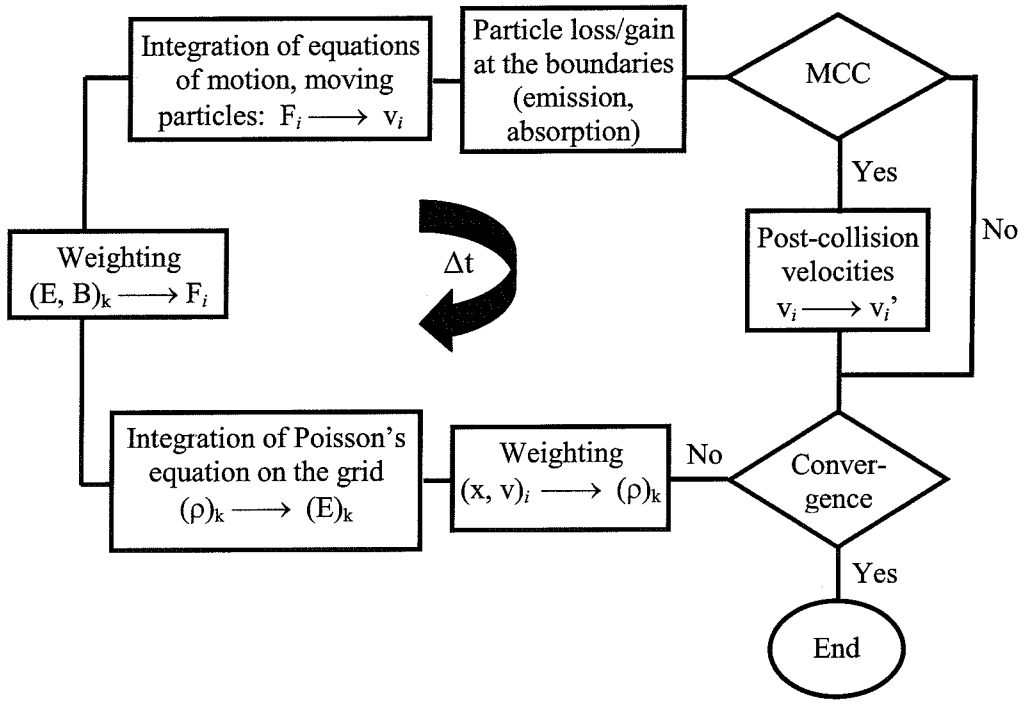

Figure 3.9 Scheme of a PIC - MCC cycle. The collision check is performed at time $t+(1/2)\ t$. The notation, v_i', refers to the postcollision velocity of the *i*-th particle. All other symbols are as in Figure 3.1.

3.4 Post-collision velocities

When a binary collision occurs, the velocities of the colliding particles change. Obtaining the postcollision velocities is based on the fundamental laws of conservation of energy and momentum plus geometrical considerations related to the particle's orientation before the collision. A key assumption is that of a spherical shape of the particles, which leads to spherical symmetry of the interparticle potential. The conservation of the total momentum, *i.e.*, the momentum of both particles, makes it convenient to represent the collisional event in a *center of mass* (c.m.) coordinate system moving with constant velocity, $\boldsymbol{w}$, with respect to the laboratory frame

$$\boldsymbol{w} = \frac{m\boldsymbol{v} + M\boldsymbol{V}}{m+M}, \tag{3.39}$$

m and $\boldsymbol{v}$ are the mass and the precollision velocity of the first particle and M and $\boldsymbol{V}$ are the same quantities but for the second particle. The precollision velocities in the c.m. frame, $\tilde{\boldsymbol{v}}$ and $\tilde{\boldsymbol{V}}$, are then

$$\tilde{\boldsymbol{v}} = \boldsymbol{v} - \boldsymbol{w} = \frac{M}{m+M}\boldsymbol{g}$$
$$\tilde{\boldsymbol{V}} = \boldsymbol{V} - \boldsymbol{w} = \frac{m}{m+M}\boldsymbol{g}. \tag{3.40}$$

Here, $\boldsymbol{g}$ is the relative velocity, $\boldsymbol{g} \equiv \boldsymbol{V} - \boldsymbol{v}$. With introducing the reduced mass

$$\mu = \frac{mM}{m+M},$$

the precollision momenta of the two particles can be expressed from (3.40) as

$$m\tilde{\boldsymbol{v}} = -\mu\boldsymbol{g}$$
$$M\tilde{\boldsymbol{V}} = \mu\boldsymbol{g}. \tag{3.41}$$

Equations (3.40) state that the velocities of the two colliding particles in the c.m. reference frame are parallel. The initial momenta are also parallel in that frame according to (3.41). Furthermore, the force acting on each particle is equal in magnitude and opposite in direction at every instant. All that leads to the conclusion that the final momenta are also equal and opposite. Consequently, the particles' velocities remain parallel throughout the course of the collision. Thus in the c.m. reference frame, the whole collision process happens in a plane. This plane and all related quantities are shown in Figure 3.10.

If the unit apse vector $\boldsymbol{k}$ is introduced (unit vector parallel to the symmetry line of both trajectories), the velocity and momentum components perpendicular to it do not change by the collision, whereas the parallel components reverse their direction. Taking into account this fact and some geometrical transformations leads

to a relation for the postcollision velocities in the laboratory reference frame in terms of the precollision velocities in the laboratory reference frame, the deflection angle in the c.m. reference frame and the components of the vector $\boldsymbol{k}_\perp$ ($\boldsymbol{k}_\perp$ is received by resolving $\boldsymbol{k}$ in components parallel and perpendicular to $\boldsymbol{g}$ [see Figure 3.10]) [154]

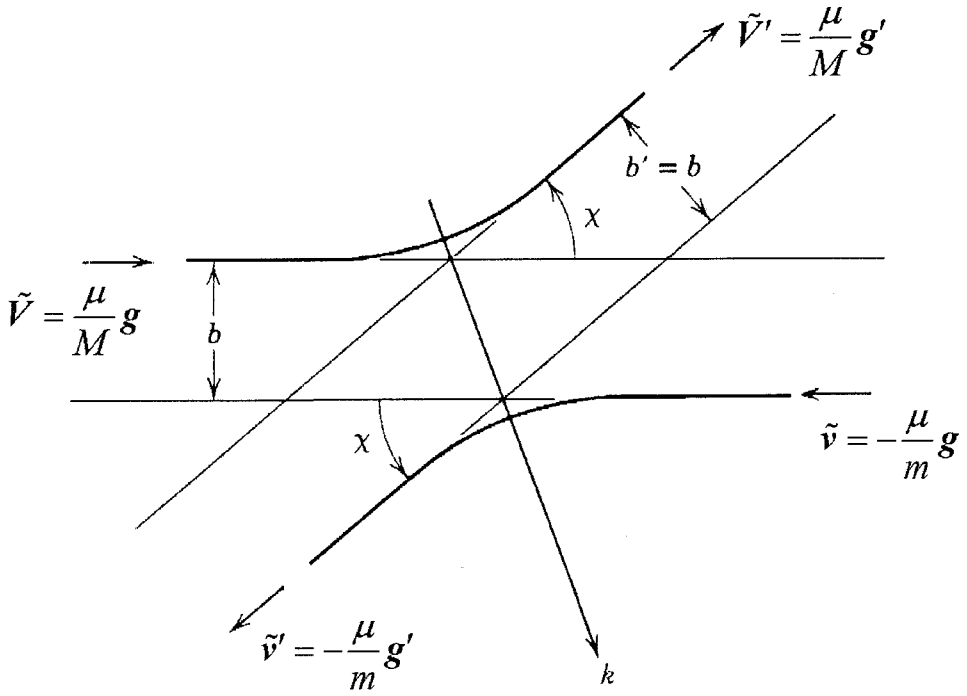

Figure 3.10 Trajectories of the colliding particles in the c.m. reference frame. The angle, χ, is the deflection (scattering) angle. Symbol b is the impact parameter – the closest separation between the centers of the particles during the collision. The vector k is the apse vector.

$$\boldsymbol{v}' = \boldsymbol{v} + \frac{2M}{m+M}\sin\left(\frac{\chi}{2}\right)\left(\boldsymbol{g}\sin\left(\frac{\chi}{2}\right) + |\boldsymbol{g}|\boldsymbol{k}_\perp\right)$$

$$\boldsymbol{V}' = \boldsymbol{V} - \frac{2m}{m+M}\sin\left(\frac{\chi}{2}\right)\left(\boldsymbol{g}\sin\left(\frac{\chi}{2}\right) + |\boldsymbol{g}|\boldsymbol{k}_\perp\right). \qquad (3.42)$$

To obtain the components of $\boldsymbol{k}_\perp$, the collision plane of Figure 3.10 should be specified in the laboratory reference frame. This is done by introducing the angle, φ,

giving the inclination of the collision plane to the axis l_1 of the laboratory reference frame specified by its basis (l_1, l_2, l_3) as shown in Figure 3.11.

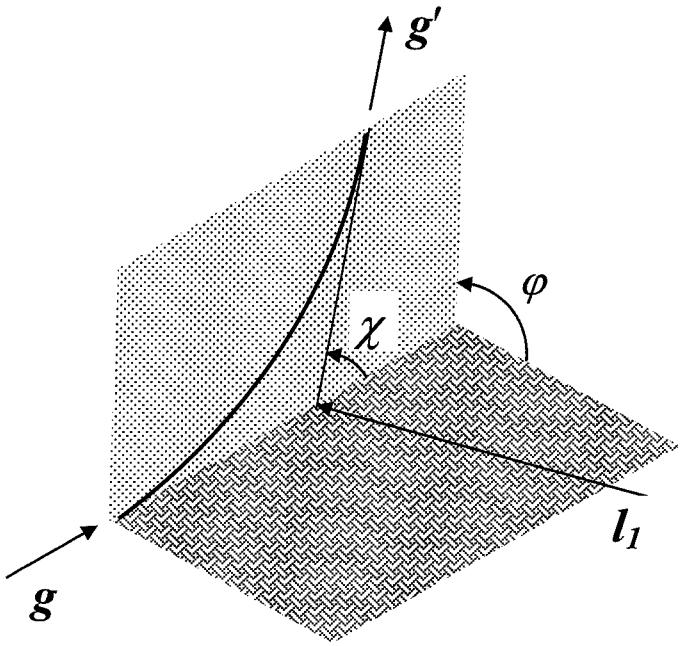

Figure 3.11 Specification of the angle, φ. The plane holding g and g' is the plane of Figure 3.10.

If $g = |\boldsymbol{g}|$ is the norm of the relative velocity vector and g_1, g_2, and g_3 are its components, then by solely geometrical consideration, the components of $\boldsymbol{k}_\perp$ are [155]

$$
\begin{aligned}
k_{\perp 1} &= \cos\left(\frac{\chi}{2}\right)\cos(\varphi)\sqrt{1-g_1^{\,2}/g^2} \\
k_{\perp 2} &= -\cos\left(\frac{\chi}{2}\right)\left(\frac{g_1 g_2\cos(\varphi)+g g_3\sin(\varphi)}{g\sqrt{g^2-g_1^{\,2}}}\right) \\
k_{\perp 2} &= -\cos\left(\frac{\chi}{2}\right)\left(\frac{g_1 g_3\cos(\varphi)+g g_2\sin(\varphi)}{g\sqrt{g^2-g_1^{\,2}}}\right).
\end{aligned}
\tag{3.43}
$$

Thus (3.42) and (3.43) define the postcollision velocities of two colliding particles as a function of the angles, φ and χ. The first angle is arbitrary, as it brings no physics to the dynamics of the collision. That is why it can be randomly sampled

$$\varphi = 2\pi U, \qquad U \in [0,1]. \tag{3.44}$$

The scattering angle, however, contains the whole information for the nature of the interaction that has caused the collision. Formally, χ can be function only of the impact parameter, b (defined in Figure 3.10) and the relative velocity, $\boldsymbol{g}$. They can be specified if the interaction potential and the initial state (pre-interaction state) of the colliding particles are both known. In practice, what is often known by experiments or calculations is the cross section for a given type of collision. The cross section is an integral quantity and as such is averaged. So, when applied to binary events samples of its distribution are needed, unless the cross section is constant. The connection between the cross section and the deflection angle can be deduced from the following discussion.

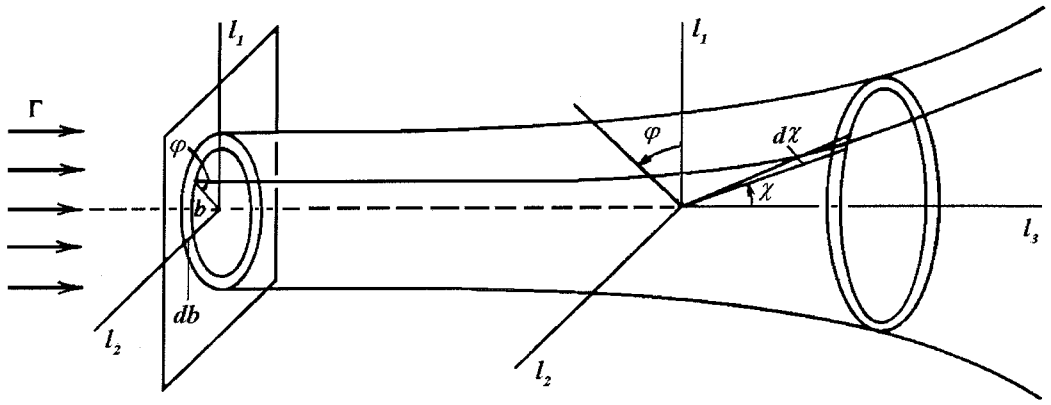

Figure 3.12 Illustration of the scattering of a flux of particles, Γ, passing through an annulus with a radius *b* and a thickness *db*. The meaning of φ is the same as in Figure 3.11.

Let a beam of particles with a flux density, $\Gamma = n\boldsymbol{g}$, where n is the density of the particles and $\boldsymbol{g}$ their average velocity, approach a surface perpendicular to the flux as shown in Figure 3.12. The fraction of the beam, which passes through an annulus with a radius b and a thickness db, is scattered into a solid angle

$$d\Omega = 2\pi \sin\chi \, \mathrm{d}\chi. \tag{3.45}$$

The meaning of b and χ is the same as in Figure 3.10. Then the flux conservation requires

$$\Gamma 2\pi b \, \mathrm{d}b = -\Gamma \sigma(g,\chi) 2\pi \sin\chi \, \mathrm{d}\chi. \tag{3.46}$$

Here the quantity $\sigma(g,\chi)$, which has the dimensionality of area per steradian, is known as *differential cross section*. It is related to the probability for a particle with a velocity, $\boldsymbol{g}$, relative to the target to be elastically scattered into a solid angle $\mathrm{d}\Omega$. From (3.46) it is equal to

$$\sigma(g,\chi) = \frac{-b}{\sin\chi}\frac{\partial b}{\partial \chi}, \tag{3.47}$$

where the minus sign represents that when b is increased, χ is decreased. The partial differentiation indicates that the derivative is taken when g is held fixed. The total cross section (integrated over angles) as a function of the speed g is then

$$\sigma_T(g) = 2\pi \int_0^{\pi} \sigma(g,\chi) \sin\chi \, \mathrm{d}\chi. \tag{3.48}$$

From (3.47) and (3.48), it is clear that the probability, P, that a particle with a relative velocity $\boldsymbol{g}$ has its postcollision velocity $\boldsymbol{v}'$ inside a solid angle, $\mathrm{d}\Omega$, given by (3.45) after being elastically scattered is

$$P(g,\chi) = \frac{\sigma(g,\chi)\sin\chi \, \mathrm{d}\chi \, \mathrm{d}\varphi}{\sigma_T(g)}. \tag{3.49}$$

Then taking into account (3.44), the probability density function of χ is equal to $2\pi\sigma(g,\chi)\sin\chi/\sigma_T(g)$, from which a random sample of χ can be taken from [146]

$$\frac{2\pi}{\sigma_T(g)}\int_0^{\chi}\sigma(g,\chi')\sin\chi'\,\mathrm{d}\chi' = U. \tag{3.50}$$

Thus, the task to calculate the postcollision velocities is reduced to the knowledge of the differential cross section of the process. This knowledge can come from direct measurements or by evaluation of the interparticle force by either classical or wave mechanism. An example for classical evaluation is the determination of the differential cross section for the case of electron collisions with monatomic gases, discussed in the following section.

3.4.1 Electron-neutral collisions

In this case, the electron-atom potential can be approximated to the screened Coulomb potential [95]. This leads to an expression for the differential cross section [156]

$$\sigma(\varepsilon,\chi) = \frac{1}{4\pi}\frac{1+8\varepsilon}{(1+4\varepsilon-4\varepsilon\cos\chi)^2}, \tag{3.51}$$

where $\varepsilon = E/E_0$ is dimensionless energy, $E = mg^2/2$ is the electron energy and $E_0 = 27.21\text{eV}$ is the atomic unit of energy. Then substituting (3.51) in (3.50) leads to a random sample of χ [156]

$$\chi = \arccos\left[1-\frac{2U}{1+8\varepsilon(1-U)}\right]. \tag{3.52}$$

In this way, the electron-argon elastic collisions are treated in the following way. At the middle of the time step, each electron is checked for collision according to (3.38) and the mechanism represented in Figure 3.8. If an elastic collision occurs, the energy, ε, is calculated from the precollision electron speed, v (*i.e.*, due to the big disparity between electron and argon speeds, the relative speed, g, is approximated to v). Next, χ is determined from (3.52). Finally, the postcollision electron velocity

is computed from the first of the equations (3.42) with $\boldsymbol{g} = -\boldsymbol{v}$ and (3.43). The mass, M, is the argon atom mass in this case and $V \approx 0$ is the atom speed.

The above procedure allows electron-impact ionization and excitation of the argon atom to be treated similarly to the elastic scattering. In an excitation event with threshold energy, E_{th}^{exc}, the electron with energy, E, leaves the collision with postcollision energy, $E - E_{th}^{exc}$. Hence, the postcollision speed is

$$v' = v\sqrt{1 - E_{th}^{exc}/E} \tag{3.53}$$

The postcollision electron velocity, however, cannot be determined strictly from classical considerations only. A reasonable approximation, suggested by Nanbu and Uchida [157] is to replace the precollision speed of the incident electron with its postcollision speed (3.53) keeping the direction of the precollision velocity and then to scatter the electron elastically. This approach has been checked [87] by comparing the calculated drift velocity to measured data [158]. Both data agree well, but the comparison has been made for reduced electric fields not exceeding 100 Td (the experimental results do not spread further). In magnetrons, the reduced electric field can be orders of magnitude stronger, so the validation of this approach remains open.

When the excited argon atoms are to be followed in the model, the initial velocity of the excited argon atom, $\boldsymbol{V}'$, is sampled from a Maxwellian distribution with thermal energy.

In case of ionization of a neutral atom, the change of the momentum of the atom can be ignored due to the much smaller electronic mass in comparison to the atomic mass. Thus, the velocity of the newborn ion is the precollision velocity of the colliding atom. The latter is again sampled from a Maxwellian distribution as in the case of excitation. This assumption leads to rewriting of the energy balance, which is

$$m\boldsymbol{v}^2 = m\boldsymbol{v}'^2 + m\boldsymbol{v}_{ej}'^2 + 2E_{th}^{ion}, \tag{3.54}$$

where v_{ej}' is the initial velocity of the newly created electron and E_{th}^{ion} is the ionization potential of the atom. Equation (3.54) does not specify the post collision velocities. It only says what their sum must be. The exact probability for a given energy partition is given by quantum mechanics. An alternative, but yet physical approach [159] is discussed next.

Based on experimental and/or theoretical data the energy partition is made between the scattered ionizing electron and the ejected electron. Let the energy of the ejected one be E_{ej}. Then (3.54) is rewritten for the speed. v'

$$|\boldsymbol{v}'| = |\boldsymbol{v}|\sqrt{1-\frac{E_{th}^{ion}+E_{ej}}{E_{inc}}}, \tag{3.55}$$

where E_{inc} stands for the precollision energy of the incident electron. Next, the original velocity of the incident electron is reduced by a factor of $\sqrt{1-\left(E_{th}^{ion}+E_{ej}\right)/E_{inc}}$ and with this velocity, the electron is scattered elastically to obtain $\boldsymbol{v}'$. To the ejected electron, a precollision velocity with magnitude, v_{ej}', and direction parallel to $\boldsymbol{v}$ is assigned. With the so-constructed velocity, the ejected electron is also scattered elastically and his postcollision velocity, $\boldsymbol{v}_{ej}'$, is determined. What remains to be specified is the postcollision speed, v_{ej}'. Detailed measurements of the energy partition for a number of gases in the energy range 4 – 200 eV for the secondary electrons and impact energies of up to 500 eV have been reported by Opal and coworkers [159]. Their data has been numerically fitted and an analytical expression for the energy of the progeny has been suggested for argon [160]

$$E_{ej} = a_0 + a_1 \tan\left[U\left(\arctan\left(\frac{a_1}{b}\right)+\arctan\left(\frac{a_0}{b}\right)\right)-\arctan\left(\frac{a_0}{b}\right)\right]. \tag{3.56}$$

The parameters in (3.56) are

$$a_0 = 2 - \frac{100}{E_{inc} + 10}$$

$$a_1 = \frac{E_{inc} - E_{th}^{ion}}{2} - a_0$$

$$b = 10.3.$$

In the case of electron-copper atom collisions, the formulae (3.52) remain valid. Since there is no information in the literature for the energy partition during copper ionization, the combined energy of the scattered primary electron and the progeny is randomly distributed between them.

3.4.2 Ion-neutral collisions

The main ion-neutral collisions in the model are those between argon ions and argon atoms. Both elastic and inelastic scattering is considered. Ions participate in a symmetric ion - atom scattering. This scattering can be considered as consisting of two components [109]: (*i*) isotropic and (*ii*) a well expressed backward component, which at high energies coincides with symmetric charge transfer, but at low energies its magnitude differs from that of the symmetric charge transfer as calculated from quantum mechanics considerations [161]. There is a lack of separate cross-section data for elastic scattering and symmetric charge transfer in the literature. In [109], Phelps gives analytical expressions for the isotropic and backwards components of the symmetric ion atom scattering, which are adopted here.

The postcollision velocities are determined as follows. In the case of isotropic scattering, (3.42) is used with χ determined from

$$\cos\chi = U_1, \tag{3.57}$$

where $U_1 \in [-1,1]$ is a uniformly distributed random number. In the case of backward scattering, the ion obtains the atom velocity, determined from sampling a

Maxwellian distribution of a temperature of 300 K. The azimuthal scattering angle in a c.m. system is again given by (3.44).

The inelastic scattering of argon ions from their parent atoms includes ion-induced excitation and ionization. In the course of the collision, the precollision velocity of the incident ion is reduced with the amount corresponding to the threshold energies for excitation and ionization, respectively. The initial velocity of the colliding atom is sampled from a Maxwellian distribution at a given temperature. With those velocities, the two particles are scattered elastically as described above. After the collision, the atom turns into an ion or excited atom. The excited atom is traced further only if it is in metastable state. The initial velocity of the newborn ion or metastable atom is the postcollision velocity of the colliding atom. The created electron in case of ionization is given the same initial velocity as that of the created ion.

Except with its parent atoms, the argon ions can collide with the sputtered copper atoms. Simple elastic collisions of that type are not included here, because there is no data about the cross sections in the literature and because the process is expected to be marginal in comparison to the argon ion – argon atom scattering. Asymmetric charge exchange (see Section 2.3.5.3) however is included. It is treated in the same way as the symmetric charge transfer.

Copper ions are the second type of ions in the model. Their collisions with the copper atoms are disregarded, because of the significant difference in the densities of the argon atoms and copper atoms. The collisions between copper ions and argon atoms, however, are important for the charge distribution and for creation of fast argon atoms, which contribute to both sputtering and gas heating. Only elastic collisions are considered. Since there is a lack of data in the literature regarding the cross section of this process, it is treated in the same way as the collisions between copper atoms and argon atoms. The procedure is explained in the next section.

3.4.3 Neutral - neutral collisions

Two sorts of neutral – neutral collisions are included. The first one is the Ar – Ar collision between a fast argon atom and a cold background argon atom. In this case, based on cross sections, elastic scattering, atom-induced excitation, or atom-induced ionization can occur. In the first case, the process is considered isotropic. The scattering angle is given by (3.57). The precollision velocity of the background

argon atom is sampled from a local Maxwellian distribution and the postcollision velocities are calculated from (3.42). In the case of an inelastic process, the same procedure is followed as for ion-induced excitation and ionization.

The second type of neutral – neutral collision is between the sputtered copper atoms and the background argon atoms. Note that the fast argon atoms are neglected, as they are only a tiny fraction of the whole argon atom population. This process is of great importance for the sputtering flux distribution at the substrate. Therefore, it should be dealt with carefully.

Due to a lack of information about experimental cross sections for elastic collisions between Cu and Ar atoms, the cross section adopted in the model has been obtained from theoretical considerations. As a starting point the range concept [126] is used with the interaction potential, V, as a function of the interatom distance, r, in the form

$$V(r) = Z_{Cu} Z_{Ar} q^2 a_s^{n-1} \frac{r^n}{n}, \tag{3.58}$$

where a_s is a parameter known as screening length (to be defined) and Z_{Cu} and Z_{Ar} are the atomic numbers of Cu and Ar. The power, n, specifies the nature of the interaction. In particular, $n = 1$ corresponds to Coulomb interaction. As shown in [126], (3.58) leads to a differential cross section for an energy transfer, T

$$d\sigma = \pi a_s^2 \frac{dt}{2t^{3/2}} f(t) \tag{3.59}$$

with $t = \left(\frac{a_s}{b}\right)^2 \frac{T}{T_M}$ and $f(t) = \beta_n t^{\frac{1}{2}-\frac{1}{n}}$, where T_M is the maximum allowed energy transfer, b is the collision diameter given by $b = 2Z_{Cu}Z_{Ar}q^2 / M_0 v_{Cu}$, $M_0 = M_{Cu}M_{Ar}/(M_{Cu}+M_{Ar})$, v_{Cu} is the precollision speed of the Cu atom, and $\beta_n = \frac{3n-1}{8n^2}$. Simplifying (3.59) and changing the integral variable from t to T produces

$$d\sigma = \frac{\pi}{2}\beta_n \left(a_s^{2n-2} b^2 T_M\right) T^{-(1+1/n)} dT \tag{3.60}$$

To obtain the integral cross section, (3.60) is integrated over all possible transfer energies. That is

$$\sigma(E,\chi) = \int_{T'}^{T_M} \frac{\pi}{2}\beta_n^{1/n} \left(a_s^{2n-2} b^2 T_M\right)^{1/n} T^{-(1+1/n)} dT = n\beta_n^{1/n} \left(a_s^{2n-2} b^2\right)^{1/n} \left[\left(\frac{T_M}{T}\right)^{1/n} - 1\right] \tag{3.61}$$

In the case of elastic scattering, which is of relevance here, the transferred energy, T, is related to the scattering angle in the c.m reference frame

$$T = T_M \sin^2\left(\frac{\chi}{2}\right). \tag{3.62}$$

Substituting (3.62) in (3.61) and integrating over all angles leads to

$$\sigma(E) = \int_0^{\pi} \sigma(E,\chi)\sin\chi d\chi = \frac{\pi}{2}\beta_n^{1/n} \left(a_s^{2n-2} b^2\right)^{1/n} \left[\int_{-1}^{1} \frac{2^{1/n}}{(1-\cos\chi)^{1/n}} d\cos\chi - \int_{-1}^{1} d\cos\chi\right].$$

Finally, performing the integration yields

$$\sigma(E) = \frac{2\pi}{n-1}\left(b^2 a_s^{2(n-1)}\right)^{1/n} \beta_n^{1/n}. \tag{3.63}$$

If the reduced energy, ε, is defined as

$$\varepsilon = \frac{a_s M_{Ar}}{Z_{Cu} Z_{Ar} q^2 \left(M_{Cu} + M_{Ar}\right)} E, \tag{3.64}$$

where $E = m_{Cu} v_{Cu}^2 / 2$ is the Cu atom precollision energy, (3.63) becomes

$$\sigma(E)=\frac{2\pi}{n-1}a_s^2\beta_n^{1/n}\varepsilon^{-2/n}. \tag{3.65}$$

Equation (3.65) is analytical and universally valid. For practical applications however, the power, n, must be specified as well as the screening length, a_s. Sielanko [162] proposes a numerical fit of n as a function of the reduced energy, ε. This fit is based on the exact value of the scattering angle obtained from numerical evaluation of the classical scattering integral for the Molier potential [163]. It reads [162]

$$n(\varepsilon)=1+4\exp\left(-1.9\varepsilon^{0.1}\right). \tag{3.66}$$

The screening length is taken in the Firsov's approximation [164]

$$a_s=\frac{0.8853a_0}{\left(Z_{Cu}^{1/2}+Z_{Ar}^{1/2}\right)^{2/3}}, \tag{3.67}$$

where the number 0.8853 is the evaluation of the Thomas-Fermi constant, which exact value is $\left(9\pi^2\right)^{1/3}2^{-7/3}$ and $a_0=0.529\mathring{A}$ is the Bohr radius.

It should be taken into consideration that (3.58) and consequently (3.65) are not in SI, but in SGS units. Thus for numerical calculations, the elementary charge, q, should be taken equal to 4.81×10^{-10} cgs. The energy in (3.66) is in ergs. Since the convenient unit for calculations is eV, a conversion factor must be used. This factor is $1\,\text{erg}=6.242\times10^{-11}\,\text{eV}$. In addition, the screening length in (3.66) is in centimeters. In this way, the reduced energy is evaluated as

$$\varepsilon=6.92446\times10^6\frac{a_s[\text{cm}]M_{Ar}}{Z_{Cu}Z_{Ar}\left(M_{Cu}+M_{Ar}\right)}E[\text{eV}]. \tag{3.68}$$

Thus, the cross section for an elastic collision between a Cu atom with incident energy, E, and an Ar atom at rest is given by (3.65), with ε computed from

(3.68) and n calculated in (3.66). The dimensionality of the so-calculated cross section is square centimeters.

The above approach allows determining the scattering angle as well. If (3.60) is integrated from some energy transfer, T' to the maximum energy transfer, T_M, its left hand side gives the cross section for the energy transfer, T'. Since for a given precollision energy, E, the transfer, T', defines an unique scattering angle, χ', this is effectively the differential cross section $\sigma(E,\chi') = 2\pi b_\chi db_\chi$, where b_χ is the impact parameter corresponding to scattering at angle χ'. Then after performing the integration and by using (3.62), the following relation for the scattering angle is obtained [162]

$$\sin^2\left(\frac{\chi'}{2}\right) = \left[1+\frac{b_\chi^2\varepsilon^{2/n}}{a_s^2\beta_n^{1/n}}\right]^{-n},$$

from where

$$\cos\chi' = 1-2\left[1+\frac{b_\chi^2\varepsilon^{2/n}}{a_s^2\beta_n^{1/n}}\right]^{-n}. \tag{3.69}$$

To determine the impact parameter in (3.69), the total elastic cross section is presented as $\sigma(E) = \pi b_0^2$, where b_0 is the maximum value of the impact parameter. This approach has been proposed by Wronski [165]. Then a random sampling is performed

$$U = \int_0^{b_\chi} \frac{2\pi b'}{\pi b_0^2} db', \qquad U \in [0,1],$$

resulting in

$$b_\chi = \sqrt{\frac{U\sigma(E)}{\pi}} \tag{3.70}$$

with $\sigma(E)$ calculated from (3.65).

The postcollision velocities of the copper atom and the argon atom are determined from (3.42). If the postcollision energy of the argon atom is above the threshold energy, it is transferred to the group of the fast argon atoms. If the postcollision energy of the copper atom is less than the thermalization threshold it is excluded from the group of the fast copper atoms and is counted in the source term of the diffusion equation for the slow copper atoms (see Section 6.2.2).

3.4.4 Coulomb collisions

Coulomb collisions in plasmas, also known as *Rutherford scattering*, are different from isolated binary collisions. This difference originates from the fact that the Coulomb force, which is responsible for the collisions, is long-ranged. This means that a moving charged particle receives action from all other charged particles situated within a distance of the Debye length, *i.e.*, the Coulomb collision in plasma is a many-body collision. To include such many-body collision in a PIC simulation requires a special treatment. There are two approaches, each with numerous modifications. The first one is to identify all charged particles inside a Debye sphere, centered on the test charged particle, then to calculate the effective force, with which all charged particles inside the sphere act upon the test particle, using the superposition principle. Then the test particle is advanced as a result of two forces: the smoothly varying mesh force and the Coulomb force. This approach has been developed by Hockney and Eastwood [166-168]. It is computationally intensive, because the magnetron plasma is very well confined, which leads to a very high number of charged particles situated in a Debye sphere.

An alternative approach is to treat the many-body collision as a succession of small-angle binary collisions. This idea has been initially explored by Rosenbluth *et al.* [169] for deriving the Landau-Fokker-Planck equation for an arbitrary velocity distribution from the Boltzmann equation. Later on, it has been implemented in Monte Carlo and PIC codes [170, 171], but with some limitations concerning the velocity distribution function. An additional disadvantage of the above-mentioned works is that all binary collisions have been calculated one by one. This drawback has been overcome by Nanbu [172, 173], who proposed a different formulation for the cumulative property of the Coulomb collisions in plasmas. He determined the probability distribution for a cumulative deflection angle resulting from many small-

angle collisions. The Nanbu scheme is computationally very efficient and has been applied in our model. The full details of the scheme can be found in [146, 172, 173]. Below, it is only summarized.

For a plasma consisting of s charged species, the evolution of the velocity distribution of the species α is [172]

$$f_\alpha(\boldsymbol{v},t+\Delta t)=\frac{1}{n}\sum_{\beta=1}^{s}\int_{R^3\times S^2} d\omega d\omega D\left(\frac{\boldsymbol{g}\cdot\boldsymbol{\omega}}{g}A_{\alpha\beta}\frac{\Delta t}{g^3}\right)f_\alpha(\boldsymbol{v}'_{\alpha\beta},t)f_\alpha(\omega'_{\alpha\beta},t), \quad (3.71)$$

where n is the total number density of all charged species, R^3 is 3d Euclidean space, S^2 is a unit sphere in R^3, $\boldsymbol{g}=\boldsymbol{v}-\boldsymbol{\omega}$, $\boldsymbol{v}'_{\alpha\beta}$ and $\omega'_{\alpha\beta}$ are the postcollision velocities

$$\boldsymbol{v}'_{\alpha\beta}=\boldsymbol{W}+\frac{\mu_{\alpha\beta}}{m_\beta}g\omega, \qquad \boldsymbol{\omega}'_{\alpha\beta}=\boldsymbol{W}-\frac{\mu_{\alpha\beta}}{m_\beta}g\omega \quad (3.72)$$

$\boldsymbol{W}=(m_\alpha\boldsymbol{v}+m_\beta\boldsymbol{\omega})/(m_\alpha+m_\beta)$ is the c.m. velocity, $\mu_{\alpha\beta}=(m_\alpha m_\beta)/(m_\alpha+m_\beta)$ is the reduced mass, $g\omega=\boldsymbol{v}_{\alpha\beta}-\boldsymbol{\omega}_{\alpha\beta}$ is the relative postcollision velocity, and

$$A_{\alpha\beta}=\frac{n}{4\pi}\left(\frac{q_\alpha q_\beta}{\varepsilon_0\mu_{\alpha\beta}}\right)^2\ln\Lambda_{\alpha\beta}. \quad (3.73)$$

Here q represents the charge of the particle and $\Lambda_{\alpha\beta}$ is given by

$$\Lambda_{\alpha\beta}=\frac{4\pi\varepsilon_0\mu_{\alpha\beta}\langle g_{\alpha\beta}^2\rangle\lambda_D}{|q_\alpha q_\beta|}, \quad (3.74)$$

where λ_D is chosen to be the electron Debye length for any α and β. The weak dependence of the Coulomb logarithm, $\ln\Lambda_{\alpha\beta}$, on $g_{\alpha\beta}$ allows the mean square

relative velocity, $\left\langle g_{\alpha\beta}^2 \right\rangle$ to be approximated by adopting the Maxwellian distribution for species α and β

$$\left\langle g_{\alpha\beta}^2 \right\rangle = \frac{3k_B T_\alpha}{m_\alpha} + \frac{3k_B T_\beta}{m_\beta} + \left(\left\langle \boldsymbol{v}_\alpha \right\rangle - \left\langle \boldsymbol{v}_\beta \right\rangle \right)^2 . \tag{3.75}$$

Here, T is temperature and $\boldsymbol{v}$ is flow velocity. The kernel D in (3.71) is given by

$$D(\mu,\tau) = \sum \frac{2l+1}{4\pi} P_l(\mu) \exp\left[-\frac{1}{2} l(l+1)\tau \right], \tag{3.76}$$

where $P_l(\mu)$ is the Legendre polynomial and

$$\tau = A_{\alpha\beta} \Delta t / g^3 \tag{3.77}$$

If χ is the deflection angle in the c.m. reference frame, from (3.72) and the definition of $g\omega$, it follows that $\mu = \boldsymbol{g} \cdot \omega / g = \cos\chi$. From (3.76) it follows

$$2\pi \int_{-1}^{1} P_l(\mu) D(\mu,\tau) d\mu = \exp\left[-\frac{1}{2} l(l+1)\tau \right]. \tag{3.78}$$

For $l = 0$ $\left[P_{l=0}(\mu) = 1 \right]$, (3.78) reads

$$\int_0^{2\pi} d\psi \int_0^{\pi} D(\cos\chi,\tau) \sin\chi d\chi = 1, \tag{3.79}$$

from where the meaning of $D(\cos\chi,\tau)$ as the probability that $g\omega$ is directed into $\sin\chi d\chi d\psi$ is clearly seen. The complicated form of (3.76) makes it difficult to make a random sample of $D(\cos\chi,\tau)$. This problem has been overcome by realizing that it is enough accurate for plasma simulations to use an approximate

function $D^*(\cos\chi,\tau)$ that satisfies (3.78) only for $l=0$ and $l=1$ [146]. Such function is [172]

$$D^*(\cos\chi,\tau)=\frac{A}{4\pi\sinh A}\exp(\mu A) \tag{3.80}$$

with A given by

$$\coth A - A^{-1} = e^{\tau}. \tag{3.81}$$

A random sample, μ, of (3.80) is

$$\begin{aligned}&\cos\chi=[A(\tau)]^{-1}\ln\left(e^{-A(\tau)}+2U\sinh A(\tau)\right), \qquad U\in[0,1]\\ &\sin\chi=+\left(1-\cos^2\chi\right)^{1/2}\end{aligned} \tag{3.82}$$

It should be said that regardless of how small the time step, Δt, might be, Coulomb collisions always occur. This is in contrast to the normal binary collisions, where Δt determines the collision probability. The meaning of Δt for the Coulomb collisions is through the dependence $\tau(\Delta t)$ (3.77), which affects the deflection angle. Thus for longer Δt, the cumulative deflection angle is simply bigger. In the limit of $\Delta t\to 0$, $\chi\to 0$ as it should be.

To facilitate the calculations, $A(\tau)$ is approximated as

$$\begin{aligned}&A(\tau)=\tau^{-1} \qquad \tau<0.003\\ &A(\tau)=3e^{-\tau} \qquad \tau>3\end{aligned} \tag{3.83}$$

In the interval, $\tau \in [0.003, 3]$, (3.81) has been numerically solved using Newton's method [148] and $A(\tau)$ tabulated with step 0.001 for τ. The exact values of $A(\tau)$ are obtained by linear interpolation from the two nearest tabulated values.

Having in mind that the overall limitations for the grid density of the PIC method require the cell size to be of the order of the Debye length, the Coulomb collisions are calculated on per cell basis. This means that all the charged particles within a given grid cell feel each other, but are not influenced by and do not influence the charged particles from the other cells. Then for two types of charged superparticles (e.g., electrons and argon ions) with weights, W_α and W_β, which number is N_α and N_β, respectively, the number densities are $n_\alpha = W_\alpha N_\alpha / V_{cell}$, $n_\beta = W_\beta N_\beta / V_{cell}$ and $n = n_\alpha + n_\beta$, where V_{cell} is the volume of the cell into consideration. For particles with equal weight, $W = W_\alpha = W_\beta$, the probability that a particle α has a collision partner among particles α is n_α / n, and among particles β is n_β / n. Therefore, the mean number of particles α colliding with particles β is

$$N'_\alpha = \frac{N_\alpha n_\beta}{n}. \tag{3.84}$$

Since all the particles collide, the remainder,

$$N''_\alpha = N_\alpha - N'_\alpha = \frac{N_\alpha n_\alpha}{n}, \tag{3.85}$$

is the mean number of particles α colliding with particles α. Similar expressions hold for particles β

$$N'_\beta = \frac{N_\beta n_\alpha}{n}. \tag{3.86}$$

and $N''_\beta = N_\beta n_\beta / n$, where N'_β is the mean number of particles β colliding with particles α and N''_β is the mean number of particles β colliding with particles β. The equal weight of the particles leads to $N'_\alpha = N'_\beta$. Because each particle collides only once per time step, either with a like or with an unlike partner, the postcollision velocities of all particles are obtained as follows.

First, $N'_\alpha = N'_\beta$ collisions between particles α and particles β are calculated. This is done by choosing randomly, without repetitions the collision partners. If two collision partners are α_i and β_j, τ is calculated from (3.77) with $g^3 = \left|\boldsymbol{v}_{\alpha i} - \boldsymbol{v}_{\beta j}\right|^3$. Next, $\cos\chi$ and $\sin\chi$ are calculated from (3.82) and used in (3.42) to get the postcollision velocities $\boldsymbol{v}'_{\alpha i}$ and $\boldsymbol{v}'_{\beta j}$.

Second, the collisions $\alpha - \alpha$, which are N''_α in number, are calculated. This is done by making randomly $N''_\alpha / 2$ pairs of particles α selected among those particles that have not participated in the $\alpha - \beta$ collisions. Afterwards, the procedure is the same as with the $\alpha - \beta$ collisions. Just the velocity, $\boldsymbol{v}'_{\beta j}$, is replaced by $\boldsymbol{v}'_{\alpha j}$.

Third, the collisions $\beta - \beta$, which number is N''_β, are handled analogously to $\alpha - \alpha$ collisions forming $N''_\beta / 2$ collision pairs and replacing $\boldsymbol{v}'_{\alpha i}$ with $\boldsymbol{v}'_{\beta j}$.

In the last two steps, it has been assumed implicitly that N''_α and N''_β are both even numbers. In case this is not true, the algorithm is modified [174]. It will be illustrated for N''_α. Let $N''_\alpha = 2m+1$, where m is an integer. The collision partners are (α_1, α_2), $(\alpha_3, \alpha_4) \ldots (\alpha_{2m-1}, \alpha_{2m})$, $\left(\alpha_1', \alpha_{2m+1}\right)$, where α_1' denotes the second collision of the particle α_1, *i.e.*, the precollision velocity of α_1 in $\left(\alpha_1', \alpha_{2m+1}\right)$ is the postcollision velocity of α_1 in (α_1, α_2). Constructing in such a way the collision pairs, however, brings discrepancy between the time increments in the physical system and in the calculated one. It is visible from the following discussion. The time increment for each colliding particle is Δt. For an odd N''_α, the collision pairs are $\left(N''_\alpha + 1\right)/2$. The average time increment then is

$$\Delta t_{sys} = 2\Delta t \times \left[\left(N''_{\alpha} + 1 \right) / 2 \right] / N''_{\alpha} = \left(N''_{\alpha} + 1 \right) \Delta t / N''_{\alpha} \tag{3.87}$$

Thus the average time increment, Δt_{sys}, which is the time increment of a physical system of particles, disagrees with Δt in (3.77) for $\beta = \alpha$. To compensate for this disagreement, the time in (3.77) must be shortened with the factor from (3.87). That is

$$\tau = \frac{A_{\alpha\alpha}}{\left| \boldsymbol{v}_{\alpha i} - \boldsymbol{v}_{\alpha j} \right|^3} \frac{N''_{\alpha}}{N''_{\alpha} + 1} \Delta t_{sys}. \tag{3.88}$$

Hence for the case of odd N''_{α}, (3.88) should be used instead of (3.77). The same holds for odd N''_{β}, after replacing α with β.

In the above procedure for calculating the postcollision velocities in Coulomb collisions, the flow velocity and the temperature in (3.75) are calculated as

$$\left\langle v_{\alpha} \right\rangle = \frac{1}{N_{\alpha}} \sum_{i=1}^{N_{\alpha}} v_{\alpha i},, \tag{3.89}$$

$$T_{\alpha} = \frac{m_{\alpha}}{3k_B} \left(\left\langle v_{\alpha}^2 \right\rangle - \left\langle \boldsymbol{v}_{\alpha} \right\rangle^2 \right), \tag{3.90}$$

where $\left\langle v_{\alpha}^2 \right\rangle$ is the mean of $v_{\alpha 1}, v_{\alpha 2}, ..., v_{\alpha N_{\alpha}}$. It should be realized that the temperature is an averaged collective quantity. Equation (3.90) also represents this fact. Therefore, it can be expected that if averaging is performed when the number of the particles is too small, it may be not physical. For this reason, calculation of the temperature is performed only if the number of the particles in the given cell is larger than ten. This number has been determined by the method of trial and error. When there are less than ten particles, the temperature is set to the averaged value of the nearest neighbor cells.

Due to the cumulative nature of the algorithm, it is not necessary to calculate Coulomb collisions in each time step of the PIC/MCC cycle. Instead, Coulomb

collisions are calculated once per several thousand PIC/MCC cycles. The maximum allowed time step for Coulomb collisions is determined from the condition [174]

$$\tau\left(\Delta t_{\max}\right) < 5. \tag{3.91}$$

The implementation of the procedure requires the knowledge which charged particles are located in the given grid cell. This is achieved by performing a sorting of the particles. The exact procedure is explained in Section 3.5.4.

3.4.5 Sputtering

The process of sputtering has been described in Section 2.4.3. Here, the initial velocity distribution of the sputtered atoms is discussed, as it can also be considered as a postcollision velocity. Therefore, it is treated in this section.

As it has been stated in Section 2.4.3, the magnetron sputtering, characterized by energies of the bombarding ions and atoms less than 1 keV, is best described by the linear collision cascade theory [120, 121]. The theory predicts a cosine angular distribution of the sputtered flux, Φ

$$\frac{d\Phi}{d\Omega} \propto \cos^n \Theta, \qquad 1 \le n \le 2,$$

where Θ is the polar angle of the emitted particles with respect to the surface normal. The distribution should be independent of the angle of incidence. When it is chosen that $n = 1$, the result is the so-called *Sigmund – Thompson differential distribution* [120, 121, 175] for the sputtered flux

$$\frac{d^3\Phi}{dEd^2\Omega} \propto \frac{E}{\left(E+U_b\right)^{3-2m}} \cos\Theta,$$

where E is the energy of the sputtered atom and U_b is the surface binding energy, which is the energy needed to remove an atom from the surface of a solid. Its value has been widely discussed in the literature [176 - 178]. Typically, U_b is taken to be equal to the heat of sublimation. The energy needed to remove an atom from an

ideal crystal surface normally to the surface is about 30-40% greater than the heat of sublimation [176, 178], which suggests that U_b should be taken greater than the heat of sublimation. However, this result holds for perfect surfaces only. The cathode in the magnetrons is heavily bombarded, which makes the surface rough. In addition, the target is normally polycrystalline or amorphous. Consequently, it has been accepted in this model that U_b equals the heat of sublimation.

The value of m is an energy-related parameter in the differential cross section used for a screened Coulomb potential and varies from $m = 0.5$ at incident energies around 100 keV for Ar-Cu down to $m = 0$ for low energies [121]. Thus, $m = 0$ is a good approximation for the problem of interest (*i.e.*, typical incident energies of a few hundred eV at maximum).

The validity of the Sigmund – Thompson distribution is limited to sputtered particles with energies small in comparison to the energy transferred in an elastic head-on collision given by

$$E_{\max} = \frac{4M_{inc}M_{sp}}{\left(M_{inc}+M_{sp}\right)^2}E_{inc}. \tag{3.92}$$

Here, M_{inc} and M_{sp} stand for the masses of the incident ion and sputtered atom, respectively, and E_{inc} is the energy of the bombarding ion.

The velocity of the sputtered atoms is then obtained by performing a random sampling from the Sigmund-Thompson distribution with $m = 0$

$$U_1 = 4\int_0^{\infty}\frac{U_b E}{\left(E+U_b\right)}\mathrm{d}E\int_0^{\Theta}\sin\Theta'\cos\Theta'\mathrm{d}\Theta' \tag{3.93}$$

$$U_2 = 4\int_0^{E}\frac{U_b E'}{\left(E+U_b\right)}\mathrm{d}E'\int_0^{\pi/2}\sin\Theta\cos\Theta\mathrm{d}\Theta \tag{3.94}$$

Here U_1 and U_2 are independent random numbers, homogeneously distributed between zero and one. Equation (3.93) gives the direction of the initial velocity, by means of the inclination, Θ, from the normal to the cathode surface

$$\cos\Theta = \sqrt{1-U_1}$$
$$\sin\Theta = \sqrt{U_1}. \tag{3.95}$$

Equation (3.94), which determines the initial energy of the sputtered atom, leads to a quadratic equation for E

$$E^2(1-U_2) - 2EU_bU_2 - U_b^2U_2 = 0, \tag{3.96}$$

whose roots are

$$E_{1,2} = \frac{U_b\left(U_2 \pm \sqrt{U_2}\right)}{1-U_2}.$$

While the denominator here is always non-negative, the dividend is positive only if the "+" sign is taken. Since the energy cannot be negative, the physical solution is

$$E = \frac{U_b\sqrt{U_2}}{\left(1-\sqrt{U_2}\right)}. \tag{3.97}$$

The energy, calculated in (3.97) is compared to the maximum allowed energy, E_{max}, given by (3.92). If $E > E_{max}$ holds, E is rejected and a new U_2 is generated. The procedure is repeated until E is accepted. Then the initial speed of the sputtered atoms, c, is obtained from $c = \sqrt{2E/M_{sp}}$.

3.5 Methods for speeding up the calculations

PIC/MCC simulations of dc magnetrons are very time consuming. For full convergence in three dimensions and with a million superparticles per type, the simulation may run for three months on a contemporary supercomputer. This is caused by two main factors. The first one is the relatively high plasma density leading to a large number of superparticles that need to be simulated. The second

one is the time needed for convergence to be achieved. The simulation should be run for at least 10^{-5} seconds, which is the relaxation time in a dc glow discharge [12]. The high plasma density shortens the allowed time step, which leads to a large number of time steps (computational cycles) that should be performed in order to reach the 10^{-5} second limit. All this motivates the incorporation of computational techniques and physical approximations that can alleviate the computational load. Here, an overview of the methods, used to achieve this goal, is given.

3.5.1 Subcycling

Subcycling [144] is the partial advance of the simulated system. This means that different parts of the system are advanced with different time steps. The fast evolving components are normally advanced a fixed number of times per one evolution of the slow components. If the system time step and therefore the main cycle are those of the slower components, then the fast ones are moved several times within the main cycle. Or with other words, they are subcycled. The fast particles that require the smallest time step (see Section 3.2.6) are the electrons. Ions are roughly 2000 times heavier than electrons and hardly move during an electron time step. This allows, according to the stability and accuracy criteria of the PIC method, they to be advanced safely once per 20 to 50 electron time steps. The electric field though is recalculated after each electron time step. In this sense, the term subcycling is to some extent a misnomer in the present study.

The applying of subcycling shortens the calculations by factor of 2-6 in our model. Bigger speedup cannot be obtained, because an essential part of the machine time is devoted to calculation of the electric field. The accelerating varies, because the number of the superparticles throughout the simulation also changes.

3.5.2 Variable time step

The initial density, loaded in the beginning of the simulation is much lower than the density in a steady state. The time step restriction, (3.22), must be obeyed at any time. Since the plasma density changes, so can the time step.

The classical approach is to fix the time step to obey (3.22) for the maximum expected density. This is a simple and safe decision from a programmer's point of view, but is computationally ineffective, because unnecessary small time steps are used in the initial stage of the simulation when the discharge is being built and the

plasma density is low. Alternatively, we choose to use a variable time step. This is done in the following way. At the beginning, the time step is set to satisfy (3.22) for the initial electron density. Afterwards, at every 5000 time steps the maximum electron density in the discharge is found and if (3.22) does not hold for it, the time step is increased by 25%. This is illustrated in Figure 3.13, where the time evolution of the time step in a typical simulation is shown. As it is seen, during a significant part of the simulation, the time step is bigger than the steady state time step. This allows decreasing the necessary number of computational cycles by 30 to 40%.

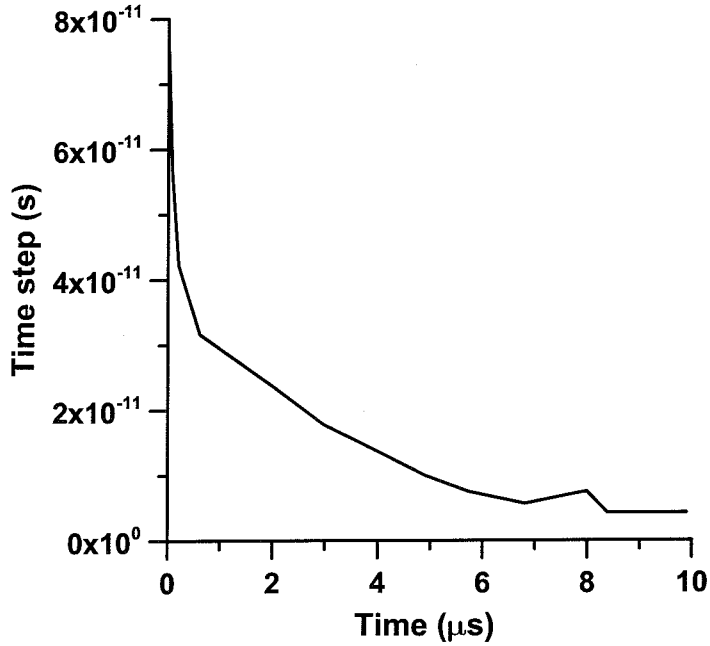

Figure 3.13 Adapting the time step throughout a typical simulation.

3.5.3 Optimization of the weighting

The weighting has been discussed in Sections 3.2.2 and 3.2.5. Each particle should be assigned to the four nearest grid points at every time step. If the coordinates of the particles are stored in physical units for distance, a floating-point division should be performed to determine to which cell the particle belongs. This is computationally very costly. Instead, the coordinates of the particles are stored in terms of grid cells. For example, if the i-th particle has a coordinate, $r = 3.356$ expressed in cell units, rather than in meters, the determination of the cell in which

the particle is located is done by simply taking the integer part of the coordinate. The remainder specifies the location of the particle inside the cell. When the real coordinate of the particle is needed, a multiplication is performed, which is computationally more effective than a division.

3.5.4 Sorting

In the classical form of the PIC method, the simulated particles of a given type are undistinguishable. Each particle is just an element of an array. The position of the particle in this array, *i.e.*, its number, is arbitrary and does not provide any specific information for the particle. This means that there is no correlation between the position of the particle in the array, and the particle's location in the coordinate space. This organization is somehow natural to understand and straightforward to program. The addition of the MCC technique fits into this scheme if the collisions are only between the given type of particles and a background homogeneously distributed in the velocity and coordinate space. Examples for such collisions are the electron-argon atom collisions. In any other type of collisions (e.g., Coulomb collisions), a collision partner must be found, based on its spatial location. One way to do that is to perform a search among all the particles and to find all collision candidates that are in the vicinity of the incident particle. The usual approximation here is to approximate this vicinity to the cell in which the incident particle is. Such procedure is however computationally very inefficient. Alternatively, if the array of the particles is not randomly formed, but ordered in such a way that the number in the array is in direct relation to the cell where the particle is located, finding a collision partner will be very fast. The ordering of the particles in such a way is called *sorting*. It not only facilitates the calculation of collisions, but also has a strong, positive side effect. It speeds up the entire PIC/MCC simulation. This acceleration is in relation with the architecture of the modern computers. This architecture is characterized by the existence of hierarchies to speed up memory accesses. Last in the hierarchy is the main memory, while the first is the processor. In between are caches, labeled L1, L2... The lower the number, the higher the position in the hierarchy. The response to memory transactions of the caches is faster than that of the main memory. Caches usually store the data recently used by the processor. A particularity of this process is that some data are stored in the caches in advance – pre*fetched* in expectation that the processor will soon need

them. When the data requested by the processor are found in the cache, an event known as *cache-hit*, the memory transaction completes quickly. When the data are not in the cache, it is a *cache-miss* and the memory transaction is much slower. In general, caches work poorly for sequences of memory transactions that randomly access large amount of memory. Here, large means that the size of the required data is larger than the cache size. It has been reported [179] that for a 2d3v PIC simulation the calculation time decreases with 40 – 70 % when sorting is implemented. Algorithms for ordering of data can be found in textbooks of numerical methods [148, 180]. Unfortunately, common sorting techniques are very slow at sorting large arrays of particles, which is the case in a PIC/MCC simulation of a dc magnetron. For example, a *quicksort* – an in-place sort algorithm [180] needs to pass through the particles approximately $\log_2 N$ times, where N is the number of particles. This leads to the impressive $8kN\log_2 N$ floating point memory loads and stores for the case of 2d3v PIC/MCC simulation with k types of particles. This inefficiency is a result of the fact that most of the well-known sorting algorithms date from the time when the amount of memory has been the main restriction. Contemporary workstations offer sufficient amount of memory and thus there is no need for in-place algorithms (algorithms that order an array without using auxiliary arrays). The out-of-place sorting algorithm [179] used in our work is explained next.

For simplicity, let there be one type of particles that need to be sorted. If they are N in number, there are five floating point, one-dimensional arrays, each with N elements containing the two coordinates and the three velocities. All five arrays are equally ordered. This means that if the position, m, in the array containing the r-coordinates corresponds to a given particle, the z-coordinate and the three velocities of the same particle are also in the m-th position in the corresponding arrays. Next, let a new integer array be constructed in such a way, that its elements are the positions of the particles in the arrays that contain their coordinates and velocities. This integer array, M, is practically an array of pointers, which point to the locations of the particles in the unsorted floating point arrays. Then, it is enough to sort only the array of pointers, M. It is a huge saving in memory transactions, because the sorting of five floating point arrays is replaced by the sorting of a single integer array. Obviously, there is a need for an additional one-dimensional integer array, K, with $(i-1)\times(j-1)$ elements, where i and j are the numbers of the nodes in

r and z direction. Each element of K contains the position in M of the first pointer corresponding to a given cell. Thus, K is also an array of pointers that point to other pointers. For example, after the sorting is performed, the first l elements of M $\mathrm{M}(1),\mathrm{M}(2),...,\mathrm{M}(l)$ contain the pointers to all particles that are located in the first computational cell $(i=0, j=0)$, the next p elements $\mathrm{M}(l+1),\mathrm{M}(l+2),...,\mathrm{M}(l+p)$ contain the pointers to all particles that are located in the second computational cell $(i=1, j=0)$, and so on, whereas the first element of K is $K(1)=1$, the second is $K(2)=l+1$, and so on. An illustration of the sorting procedure is shown in Figure 3.14.

The above explained sorting is ideal to be incorporated into the structure of a PIC cycle, especially with the optimization described in Section 3.5.3. After each electron time step, charge assignment (see Section 3.2.2) is performed to calculate the electric field. Charge assignment requires one pass through all the particles. This pass is used for the sorting as well. During this pass, it becomes clear how many particles are in each cell. This information is used to fill the array K and in fact does not add any additional computational load. After the calculation of the electric field, a second pass through the particles is made. This time, the array, M, is filled in the following way. Based on the stored information from the first pass, it is already known to which computational cell the particle belongs. The position of this particle in the coordinate and velocity arrays, *i.e.*, its pointer, is recorded in the array, M, at a position given by the corresponding value of the array, K (giving the initial position of all particles belonging to a given grid cell) increased by the number of particles belonging to the same cell and already sorted. This second pass constitutes the additional computational load caused by the sorting.

The sorting is performed at the end of each time step and secures that the particles are ordered before the collision procedure starts, thus allowing for a collision partner in Coulomb collisions (see Section 3.4.4) to be easily picked. The newborn and lost particles during advancing the electrons do not require an extra effort to be sorted, because they appear or disappear before the sorting procedure. The ions and the neutrals, however, are advanced once per several electron time steps (see Section 3.5.1), but after the last electron step is finished, which means after the sorting.

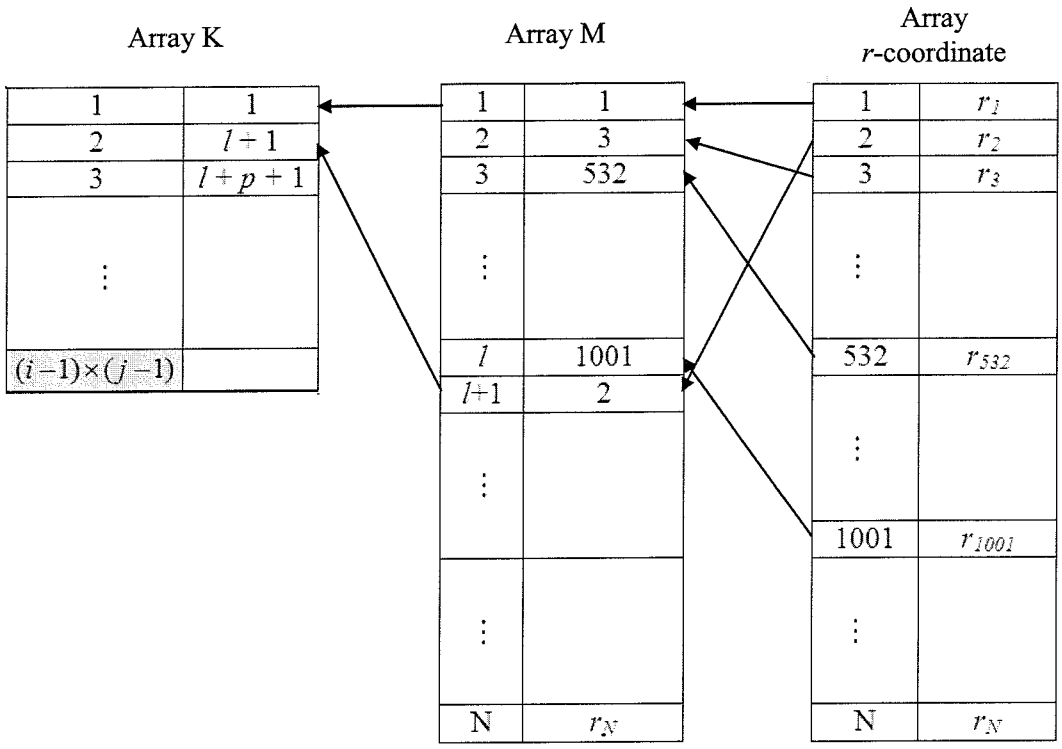

Figure 3.14 Illustration of the sorting procedure. The elements M(1) through M(l) of the array, M, contain the pointers to the particles, which are located in the first computational cell ($i = 0, j = 0$). The next p elements of M, starting with M(l + 1) contain the pointers to the particles located in the second computational cell ($i = 1, j = 0$) and so on. Correspondingly, K(1) contains the pointer of the element of M, where the pointer to the first particle from the first computational cell is stored, K(2) holds the pointer of the element of M, where the pointer to the first particle from the second computational cell is stored and so on. Here i and j are the number of computational nodes in r and z direction, respectively.

Therefore, the electrons that might have appeared or lost by ion and neutral interactions need to be sorted also before the next electron step begins. This is done in a very efficient way. First, all newborn electrons are recorded in an auxiliary array and the pointers of the lost electrons recorded in another auxiliary array. Before the electron time step begins, one pass is made through the array with the lost electrons. For each lost electron, the number, N, of the elements of the coordinate and velocity arrays is decreased by one. Next, the element of the array, K, that corresponds to the cell, next to that where the electron has been lost, is decreased by one. The same is

done with all other elements of K following the so-decreased one. Finally, the array, M, is corrected. The element, corresponding to the lost electron is replaced by the element corresponding to the last electron belonging to the same computational cell as the lost one. The vacant position of the last electron is filled with the last electron of the next cell and the process is repeated until all cells are passed. In this way, the number of the memory swaps equals the number of remaining grid cells after the one from which the electron has been lost. This is in contrast to the classical reordering where all elements above the discarded one are repositioned one by one. In that case, the number of necessary memory swaps is of the order of N.

Once the lost electrons are dealt with, the newborn electrons are added in a manner just opposite to the way in which the lost electrons have been treated.

The implementation of the sorting modifies slightly the computational cycle. The main cycle is still equivalent to one time step. However, inside it, a second loop is built in. This loop passes not through all particles directly, but instead through all computational cells in a consecutive order. In this way not only some of the collisions are properly counted, but the caches are occupied by adjacent data structure, from where an acceleration of the calculations is gained.

3.5.5 Different weights for different types of particles

Depending on the aim of the particular magnetron simulation, different plasma species can be included that can have rather different number densities. For example, while the electrons and argon ions have always similar densities, the density of the sputtered atoms and fast argon atoms is typically one to three orders of magnitude higher. In this case, it is not feasible to use the same weight for the neutrals and for the charged particles. The condition that the minimum number of followed particles must be such that there are at least several superparticles per Debye sphere, combined with the demand for maximal speed of the calculations, determines the weight of the superparticles representing the real type of particles with the lowest density. The weight of the superparticles representing the real particles with higher density is chosen also higher. How much higher is determined from the practical consideration for the number of superparticles from each type to be similar. Using different weights allows us obtaining the necessary statistical representation without paying the price of following an unwantedly large number of superparticles. The implementation of different weights is trivial in a PIC code.

When the MCC method is added, however, there are two cases. The first one is when plasma species collide with the uniformly distributed background gas, or when they collide with other plasma species having the same weight. In this case, the procedure is the same as when all superparticles are equally weighted, because the weight is anyway included in the charge assignment and force interpolation. The second case includes collisions between superparticles with a different weight. This requires an additional treatment. The guiding principle here is that the superparticles represent real particles, and all physical relations among the physical particles must be correctly represented by the superparticles. This refers mainly to the conservation laws. The starting point is the probability for a binary collision (3.38). If there are two particles, A_i and B_j, with velocities, $\boldsymbol{v}_{A_i}$ and $\boldsymbol{v}_{B_j}$, and weights, W_A and W_B, respectively the probability that the particle A_i collides with the particle B_j in a time step, Δt, in a given computational cell with a volume, V_{cell}, is

$$P_{A_i,B_j} = W_B V_{cell}^{-1} g_{A_i,B_j} \sigma_{AB}^T \Delta t. \tag{3.98}$$

At the same time the probability that the particle, B_j, collides with the particle, A_i, is

$$P_{B,A} = W_A V_{cell}^{-1} g_{B_j,A_i} \sigma_{AB}^T \Delta t. \tag{3.99}$$

The relative velocity $g_{A_i,B_j} = g_{B_j,A_i} = \left|\boldsymbol{v}_{A_i} - \boldsymbol{v}_{B_j}\right|$, which means that

$$P_{A_i,B_j} \neq P_{B,A} \tag{3.100}$$

This paradox is easy to understand noting that (3.98) and (3.99) are the probabilities for the collision of two superparticles and not real particles. The inequality (3.100) however is inconvenient, because for the same collision event two different probabilities need to be calculated. This can be avoided by representing (3.98) and (3.99) as [146]

$$P_{A_i,B_j} = \frac{W_B}{\max(W_A,W_B)} q_{ij}^{AB} P_{\max}^{*} \tag{3.101}$$

$$P_{B_j,A_i} = \frac{W_A}{\max(W_A,W_B)} q_{ij}^{AB} P_{\max}^{*}, \tag{3.102}$$

where

$$q_{ij}^{AB} = \frac{g_{A_i,B_j}\sigma_{AB}^{T}\left(g_{A_i,B_j}\right)}{g_{A_i,B_j}^{\max}\sigma_{AB}^{T}\left(g_{A_i,B_j}^{\max}\right)} \tag{3.103}$$

and

$$P_{\max}^{*} = \max(W_A,W_B)V_{cell}^{-1} g_{A_i,B_j}^{\max}\sigma_{AB}^{T}\left(g_{A_i,B_j}^{\max}\right)\Delta t.$$

Here, $P_{\max}^{*}$ is a constant probability, independent of the particles A_i and B_j. The formalism (3.102) allows the following algorithm to be implemented. First, a maximum number of pairs, $N_{\max}^{*}$, that may collide is calculated from

$$N_{\max}^{*} = \sum_{i=1}^{N_A}\sum_{j=1}^{N_B} P_{\max}^{*} = \max(N_A,N_B)N_A N_B V_{cell}^{-1} g_{A_i,B_j}^{\max}\sigma_{AB}^{T}\left(g_{A_i,B_j}^{\max}\right)\Delta t. \tag{3.104}$$

Second, $N_{\max}^{*}$ collision pairs (A_i, B_j) are randomly selected. Third, a random number, U, is generated and compared to the quantity, q_{ij}^{AB}, calculated in (3.103) for each pair. If $U > q_{ij}^{AB}$, the pair does not collide. Otherwise, the precollision velocities, $\boldsymbol{v}_{A_i}$ and $\boldsymbol{v}_{B_j}$, are replaced with postcollision velocities, $\boldsymbol{v}'_{A_i}$ and $\boldsymbol{v}'_{B_j}$ according to (3.42). This replacement, however, is conditional. The transition $\boldsymbol{v}_{A_i} \to \boldsymbol{v}'_{A_i}$ occurs with a probability of $W_B/\max(W_A,W_B)$, whereas $\boldsymbol{v}_{B_i} \to \boldsymbol{v}'_{B_i}$ happens with a probability of $W_A/\max(W_A,W_B)$. This means that the velocity of the

lighter particle changes always in a collision, in contrast to the velocity of the heavier particle, which may as well stay unchanged. The physical meaning of this procedure can be clarified by imagining a collision attempt with $W_A = 1$ and $W_B = 5$, for example. In this case, one real particle of the type A attempts to collide with five real particles of the type B. The collision, however, is binary and therefore one A-particle cannot collide simultaneously with five B-particles. That is why, one B-superparticle, representing five real B-particles, collides with an A-superparticle with a probability of $1/5$.

The momentum and energy conservation are generally violated in a single collision, when the above algorithm is used. However, the overall momentum and energy are conserved in a cell after all collisions are accounted for.

The number, $N^*_{\max}$, should be integer. However, (3.104) produces a real number. To cope with this problem a modification is needed. If the real number that results from (3.104) is denoted as $N^{\mathrm{Re}}_{\max}$,

$$\begin{aligned} N^*_{\max} &= \mathrm{int}\left(N^{\mathrm{Re}}_{\max}\right), \qquad \text{for} \left[N^{\mathrm{Re}}_{\max} - \mathrm{int}\left(N^{\mathrm{Re}}_{\max}\right)\right] < U \\ N^*_{\max} &= \mathrm{int}\left(N^{\mathrm{Re}}_{\max}\right) + 1, \quad \text{for} \left[N^{\mathrm{Re}}_{\max} - \mathrm{int}\left(N^{\mathrm{Re}}_{\max}\right)\right] \geq U. \end{aligned} \tag{3.105}$$

The concept of different weights can be used also to simulate different time scales. This will be explained and illustrated in Section 6.2.2.

Chapter Four

General properties of a dc magnetron – numerical results

4.1 Introduction

In this chapter, the PIC/MCC model described in Chapter Three will be applied to a laboratory magnetron, Von Ardenne PPS 50, operated in argon with a copper cathode. Typical calculation results will be presented. This includes, among others, the discharge potential, the distribution of the electric field, the densities of the plasma species and their energy distribution functions, and the erosion profile as a result of sputtering. The calculated results will be quantitatively compared with existing experimental and numerical data.

4.2 Description of the magnetron

The scheme of the planar magnetron used in the present simulation is shown in Figure 4.1. It is a Von Ardenne PPS 50 magnetron (commercially available), used with plasma shield (the sidewall on the scheme in Figure 4.1). The axisymmetric magnetic field is created by two concentric magnets located under the powered electrode - the cathode. The magnetron is balanced, which means that the majority of the magnetic flux lines originate at and return to the cathode surface without crossing the anode.

All walls, except the cathode, are grounded and act as an anode. The smallest separation between the electrodes is equal to 2 mm and the distance between the cathode and the opposite anode plate, where the substrate is mounted, is 24 mm. The cathode is a copper disk with a thickness of 3 mm and a diameter of 58 mm. The discharge is maintained by a dc power supply, which can be run in a constant current or in a constant voltage mode. The magnetic field used in the simulation has been experimentally measured when the discharge was not operational [181].

In the simulation, the external circuit shown in Figure 3.6 is connected to the cathode.

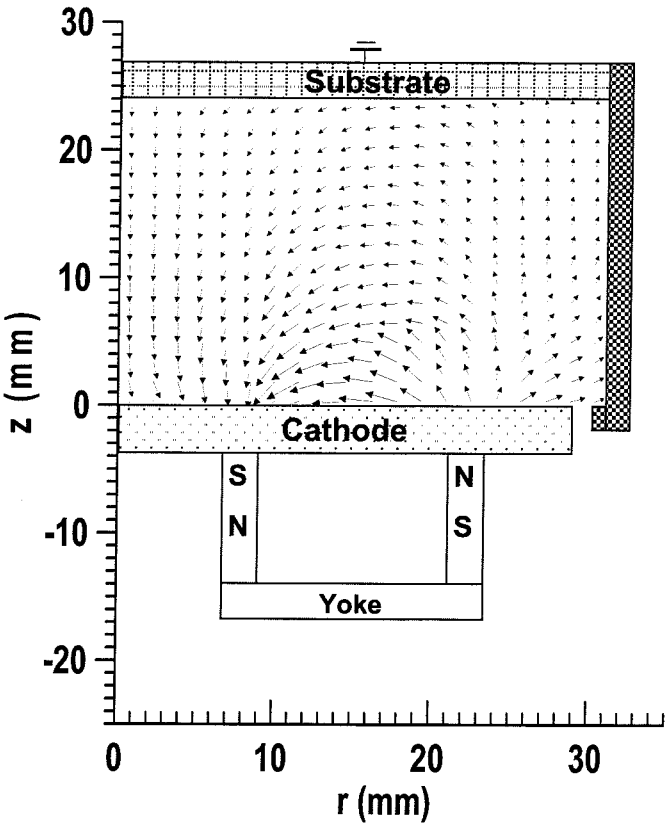

Figure 4.1 Scheme of the Von Ardenne PPS 50 magnetron with the spatial distribution of the magnetic field (measured [181]). The scheme is axisymmetrical relative to the axis, $r = 0$.

4.3 Included collisions in the model and their cross sections

In this numerical study, the magnetron plasma is considered to consist of argon atoms, singly charged argon ions and electrons only. All other plasma species are excluded from the analysis at this moment. In addition, the argon atoms are considered homogeneously distributed at room temperature (300 K). The choice of these plasma species is dictated from the fact that they are the dominant ingredients and play the main role for forming and maintaining the discharge. The influence of

the sputtered atoms and the presence of the nonequilibrium argon atoms will be discussed in the next Chapters.

The collisions that are taken into consideration are electron elastic scattering from the argon atoms, electron- and ion-induced excitation and single ionization of the argon atoms, and elastic scattering of argon ions from their parent atoms. The last process includes isotropic scattering and charge transfer. A description of the electron collisions has been given in Section 2.3.2 and for the collisions involving ions in Section 2.3.4. The way the collisions are implemented in the model has been discussed throughout Sections 3.4.1 and 3.4.2. The created metastable argon atoms are not followed in this simulation. The process of their formation, however, is important for a correct representation of the energy balance. In the case of electrons, it also contributes to the conductivity of the discharge, since the electrons cross the magnetic field lines due to collisions. Because the main excitation levels of the argon atom are very closely located in terms of energy [182] and the metastables are not followed at this stage, all electron-impact excitation processes are grouped into a single collision with an energy loss for the electrons of 11.55 eV. This is done to shorten the computational time.

The cross section of the above mentioned collisions have been adopted from the literature. They are graphically shown in Figure 4.2 and Figure 4.3, and their references are listed in Table 4.1.

Table 4.1 Included collision processes and references to their cross sections

Processes		Cross section	Reference
$e^- + Ar \rightarrow e^- + Ar$	electron elastic scattering	σ(ε)	[183]
$e^- + Ar \rightarrow 2e^- + Ar$	electron-impact ionization	σ(ε)	[7]
$e^- + Ar \rightarrow e^- + Ar^*$	electron-impact excitation	σ(ε)	[182]
$Ar^+ + Ar \rightarrow Ar^+ + Ar$	ion elastic scattering	σ(ε)	[109]
$Ar^+ + Ar \rightarrow 2Ar^+ + e^-$	ion-impact ionization	σ(ε)	[108]
$Ar^+ + Ar \rightarrow Ar^+ + Ar^*$	ion-impact excitation	σ(ε)	[108]

In the code, analytical expressions that fit numerically the cross sections are used. For the electron elastic scattering, the fit as a function of the electron energy, ε, in eV has the form

for $\varepsilon < 0.3889$

$$\sigma_{el}^{e^-}(\varepsilon) = 7.79\times10^{-20}\left[0.57153\exp(-\varepsilon/0.06553)+0.39137\exp(-\varepsilon/0.00855)+0.03715\right]$$

for $0.3889 \le \varepsilon < 3$

$$\sigma_{el}^{e^-}(\varepsilon) = 7.79\times10^{-20}\left[-0.064+0.243\varepsilon+0.005\varepsilon^2\right]$$

for $3 \le \varepsilon < 16$

$$\sigma_{el}^{e^-}(\varepsilon) = 10^{-20}\left[1.568+0.597\varepsilon+0.295\varepsilon^2-0.002\varepsilon^3+0.0003\varepsilon^4\right]$$

for $16 \le \varepsilon < 100$

$$\sigma_{el}^{e^-}(\varepsilon) = 10^{-20}\left[46.583-2.07313\varepsilon+0.045\varepsilon^2-0.0005\varepsilon^3+0.000003\varepsilon^4\right]$$

for $\varepsilon \ge 100$

$$\sigma_{el}^{e^-}(\varepsilon) = 5.9\times10^{-19}\varepsilon^{-0.544327}.$$

For electron-impact ionization, the analytical form of the cross section is adopted from [7] and for the total electron-impact excitation from [182]. The latter has been compared also to the cross section obtained by summing the set of all discrete cross sections for excitation from the ground state to 29 excited states of argon as given in [183]. The difference between the two cross sections does not exceed 7% for energies between the excitation potential and 700 eV.

The analytical expression for the elastic collisions of argon ions and atoms (including symmetric charge transfer) is adopted from [109] and the expressions for ion-impact ionization and excitation from [184].

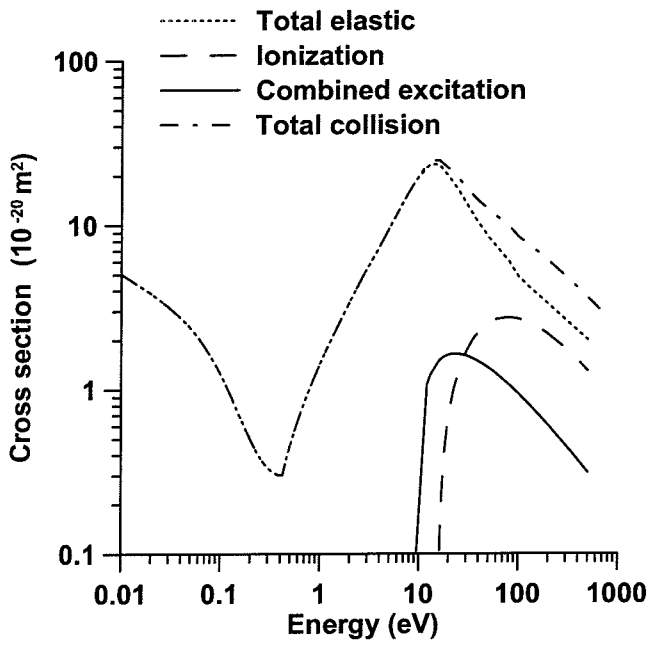

Figure 4.2 Cross sections of the electron collisions with argon atoms included in the model. The references are given in Table 4.1.

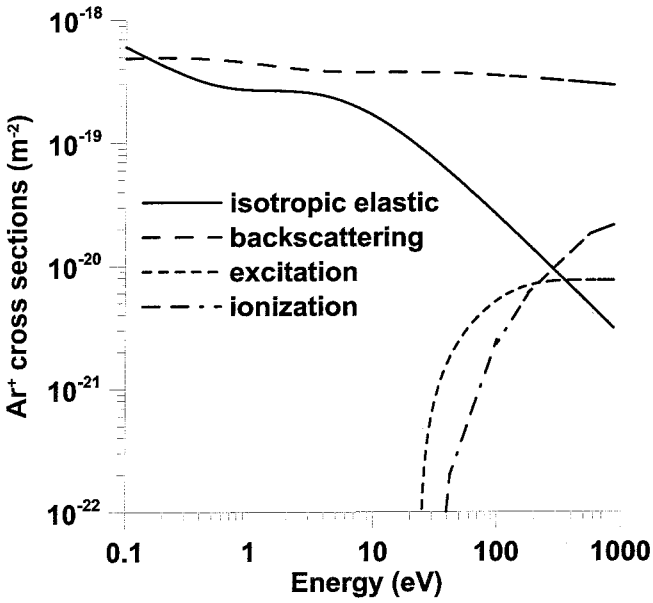

Figure 4.3 Cross sections of the Ar^+ collisions with Ar included in the model. The elastic scattering consists of two components: isotropic and backscattering, which represents the symmetrical charge transfer (see Section 2.3.4.1.2). The references are given in Table 4.1.

4.4 Simulation parameters

The maximum number of the superparticles in this simulation is two millions – one million electrons and one million argon ions. In the beginning of the simulation, they are loaded with uniform density in the coordinate space and with a Maxwellian distribution in the velocity space. The initial density equals 3×10^{14} m^{-3}. The external circuit is set with a resistor of 1200 kΩ and with a constant voltage source of -800 V. The maximum magnetic field is 0.045 T and the gas pressure is set to 5 mtorr. The computational grid has 241 nodes in z-direction and 129 nodes in r-direction. The initial time step is set to 3×10^{-10} s. The number of electronic subcycles per ionic cycle is 25. The simulation is run until convergence is obtained in terms of cathode potential and particles' densities. This is illustrated in Figure 4.4, where the time evolution of the cathode potential, Φ_0, is shown.

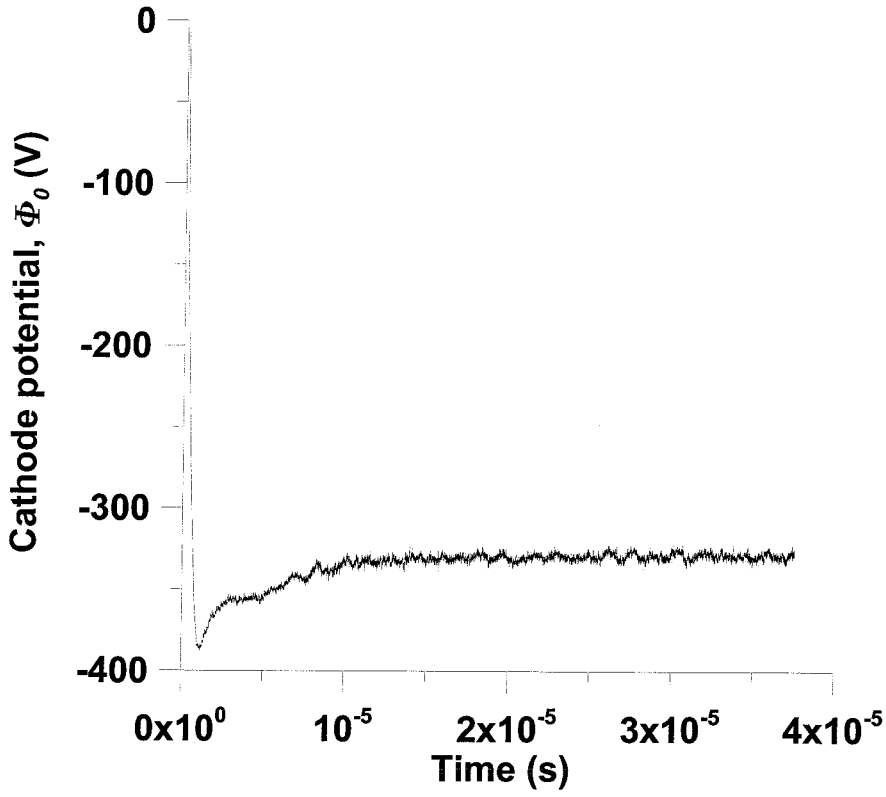

Figure 4.4 Relaxation of the cathode potential, Φ_0, with the physical time of the simulated system. The convergence occurs at time, $t \approx 12\,\mu s$.

4.5 Calculated magnetron characteristics

4.5.1 Discharge potential and electric field

The calculated discharge potential is shown in Figure 4.5. It has a clearly expressed radial dependence, which follows the pattern of the magnetic field. The gradient of the potential is steepest near the cathode at about $r = 18.2$ mm, where the radial component, B_r, of the magnetic field has a maximum. Above the center of the cathode, where the magnetic field lines are perpendicular to the cathode surface (see Figure 4.1), the potential shape is identical to that of a nonmagnetized discharge. As a whole, the plasma potential is negative almost in the entire discharge, *i.e.*, the discharge operates in a negative space charge mode. This is in accordance with analytical models [32], [43], 1d PIC/MCC simulations of a cylindrical post magnetron [25], and experimental measurements at similar operating conditions [4].

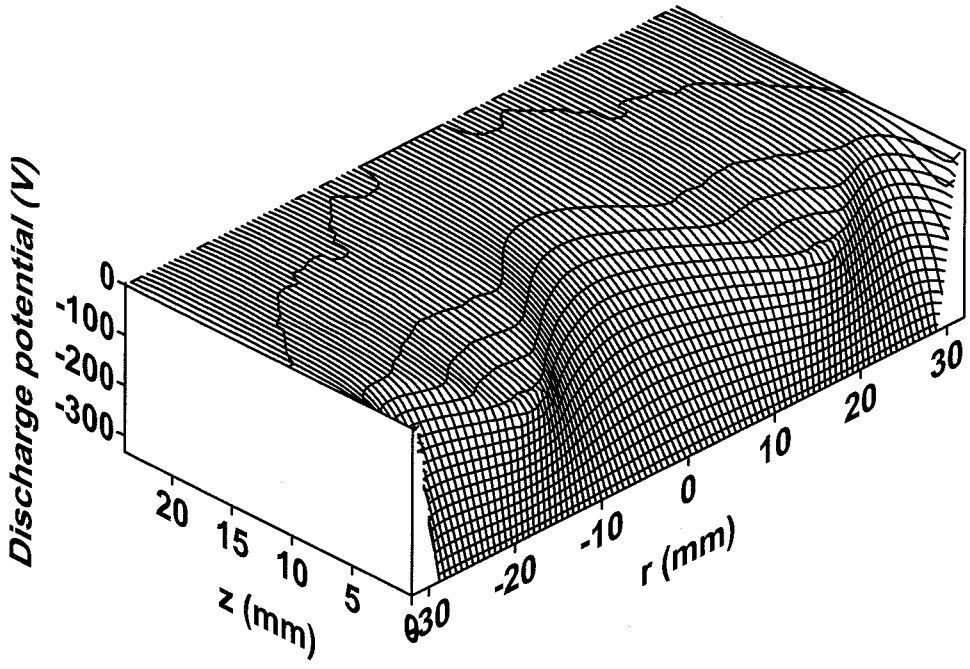

Figure 4.5 Calculated discharge potential.

The sheath architecture can also be seen in Figure 4.5. The sheath itself should be defined differently in the case of magnetrons. In nonmagnetized glow discharges, the sheath boundary is frequently set to lie at the line, which separates

the negative from the positive values of the potential. This definition works well in discharges operated in positive space charge mode. In magnetrons, however, the sheath border should be defined as a line where the potential has a well-pronounced inflexion (see Figure 4.6 and its caption). After the sheath, the next part of the potential can be defined as a presheath. This region is still characterized by a negative space charge and a relatively small electric field, in comparison to the sheath. The reason for appearance of the negative space charge and the presheath is in the restricted mobility of the electrons, due to the magnetic confinement.

The potential from Figure 4.5 creates an electrical field with an axial (Figure 4.6) and a radial (Figure 4.7 and Figure 4.8) components.

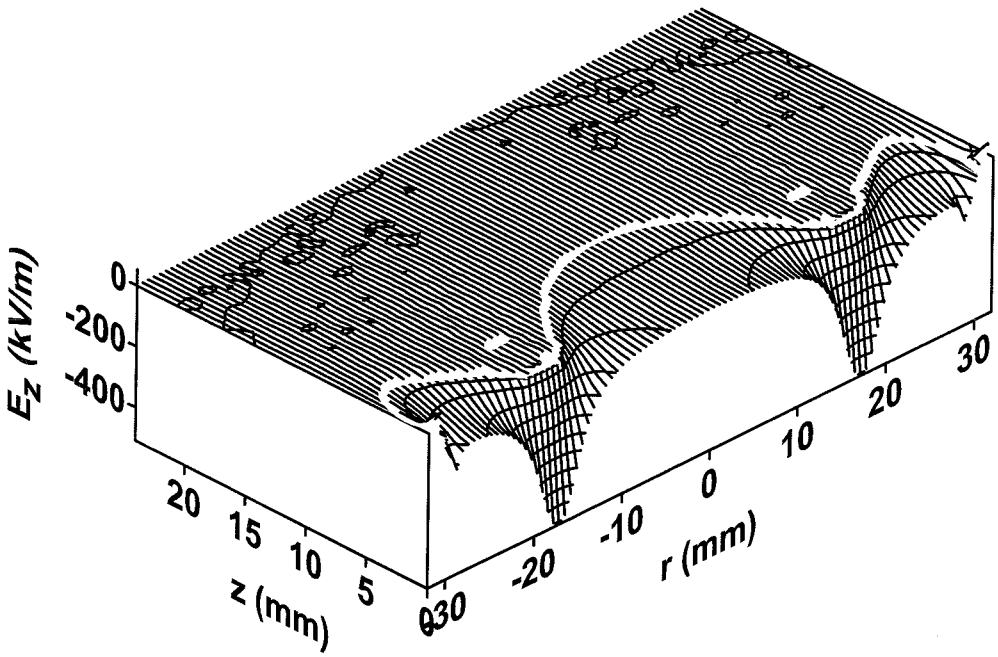

Figure 4.6 Axial component, E_z, of the electric field. The white line corresponds to $E_z = 10\,\mathrm{kV/m}$ and represents the end of the sheath.

The magnitude of the axial field, E_z, is approximately ten times stronger than the magnitude of the radial field, except in the proximity of the gap between the cathode and the sidewall. In the sheath region above the racetrack, E_z approaches 500 kV/m. The sheath border with its strong radial dependence is indicated with the white line in Figure 4.6. Along it, the magnitude of the field is approximately 10 kV/m. The sheath thickness is only 1.6 mm above the racetrack, whereas at $r = 0$ it

is about 13 mm. The sheath is thinnest and E_z stronger exactly in the middle between the magnetic poles ($r = 18.2\,\text{mm}$).

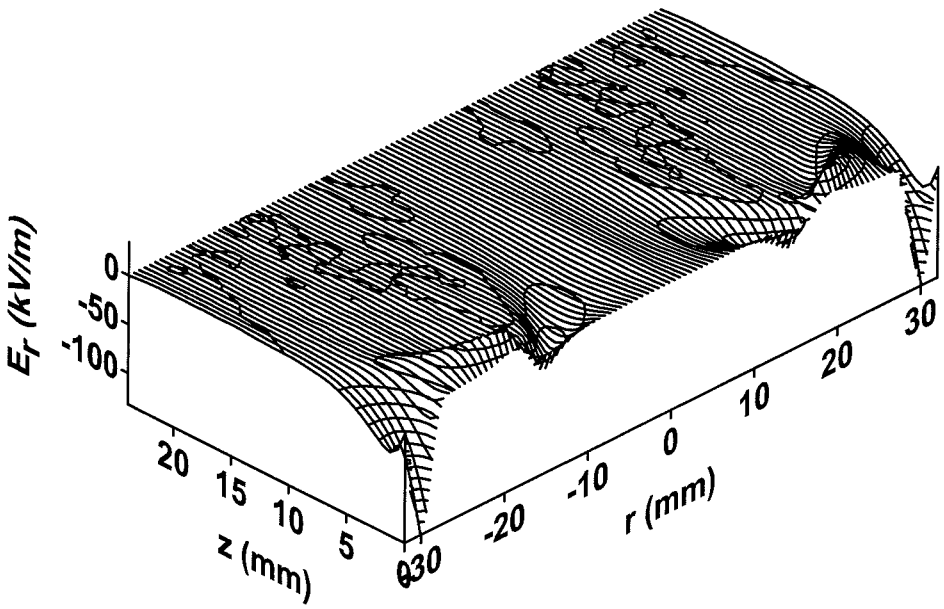

Figure 4.7 Radradial component, E_r, of the electric field.

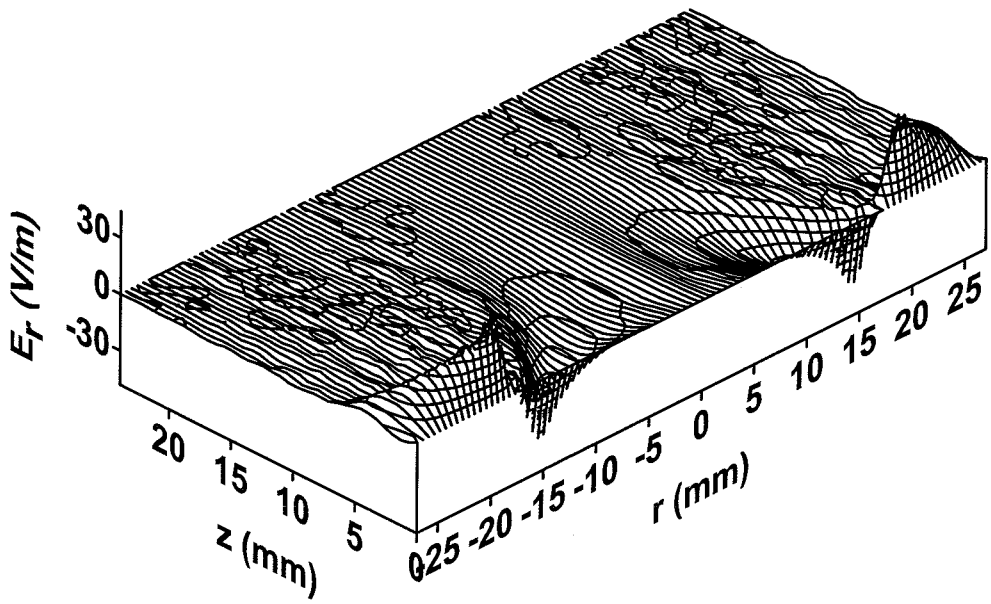

Figure 4.8 Radial component of the electric field, E_r, in the region $r \leq 27\,\text{mm}$.

The radial field, E_r, changes in the axisymmetrical sheath. The field is stronger near $r = r_{max}$, where the gap between the cathode and the grounded sidewall is located. The structure of E_r is such that the region, $E_r > 0$, repels the electrons whereas the region, $E_r < 0$, accelerates the electrons outwards. This has an effect of electrostatic trap, which enhances the magnetic confinement. The "valley – mountain" structure of E_r is more clearly seen in Figure 4.8, where the region of the discharge away from the sidewall is shown.

4.5.2 Electron and Ar^+ densities

Figure 4.9 shows the calculated electron density profile. Most electrons are strongly confined between the magnetic poles. The calculated density profile reproduces satisfactorily the experimental data obtained by Langmuir probe measurements. For example, the calculated peak value at $p = 5$ mtorr is 1.6×10^{17} m^{-3}, whereas in [4] it is 9×10^{16} m^{-3} at $p = 2$ mtorr. The plasma decay with the distance from the cathode, as well as the radial variation of the electron density agree very well with the data reported in [185] for $p = 5$ mtorr. The plasma distribution has a distinctive maximum at $z = 1.2$ mm.

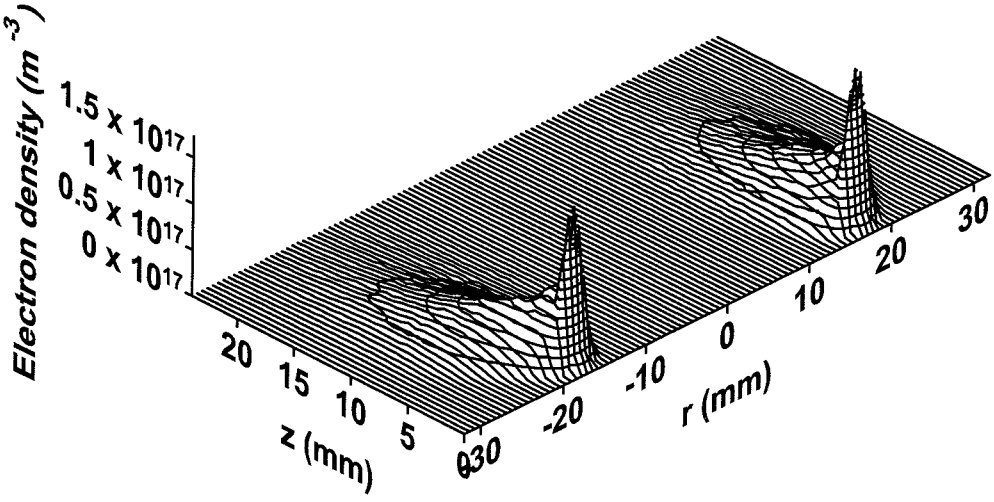

Figure 4.9 Calculated electron density.

Except in the sheath, the Ar^+ density profile (Figure 4.10) is identical to the electron density profile. This is so, because although the ions are not magnetized, and therefore not magnetically trapped, they are electrostatically bound to the electrons. The Ar^+ density profile has a maximum at the same spot as the maximum of the electron density. In the sheath, the Ar^+ density is non-zero, in contrast to the electron density. This gives rise to positive space charge and hence strong gradients in the particle distribution and in the distribution of the axial electric field. The Ar^+ bombarding flux at the cathode is clearly visible.

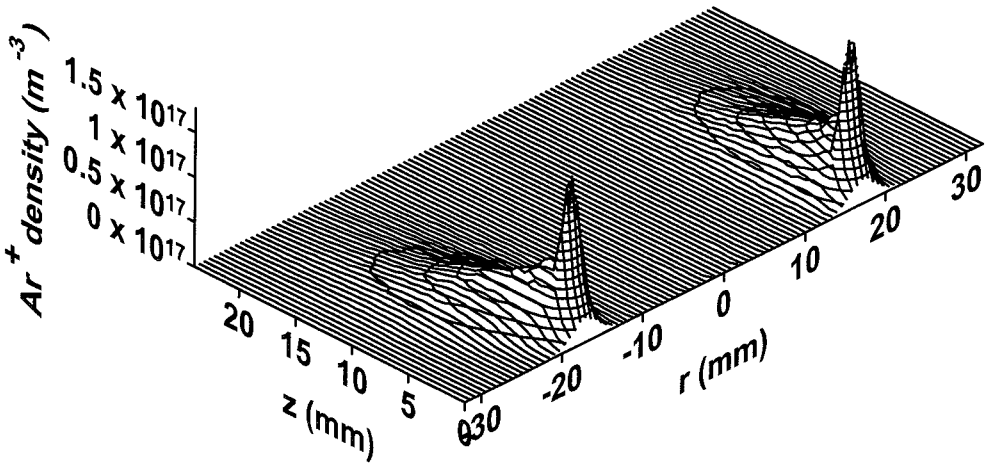

Figure 4.10 Calculated Ar^+ density.

4.5.3 Collision rates

For the sustainment of the discharge, ionization of the argon atoms is crucial. In the present model, ionization is carried out by electrons and Ar^+ ions. The calculated rates of the electron- and Ar^+-impact ionization are shown in Figure 4.11 and Figure 4.12, respectively. Their comparison shows that the main part of the ionization is caused by the electrons. The Ar^+-impact ionization is present only in the sheath where the ions can gain enough energy from the electric field to ionize the atoms. Its peak ($5\times10^{21}\,m^{-3}s^{-1}$) is about 1.5 order of magnitude lower than the peak of the electron-impact ionization ($1.2\times10^{23}\,m^{-3}s^{-1}$). The difference between the ionization rates, integrated over the whole computational domain, is about 800 times in favor of the electron-impact ionization. Therefore, with reasonable accuracy, the

Ar^+-impact ionization can be omitted in models and estimates for the current operating conditions, which is logical for this low voltage across the magnetron.

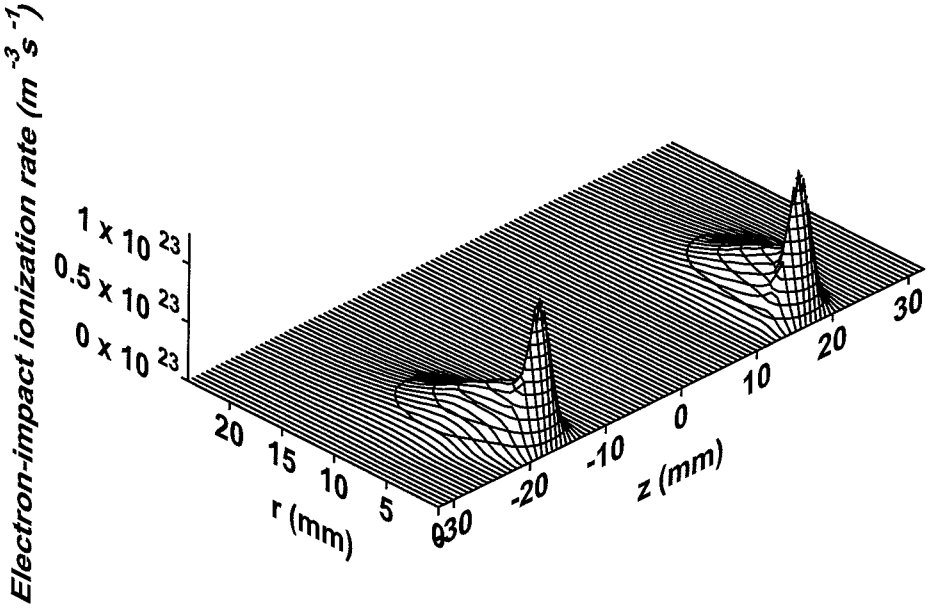

Figure 4.11 Calculated electron-impact ionization.

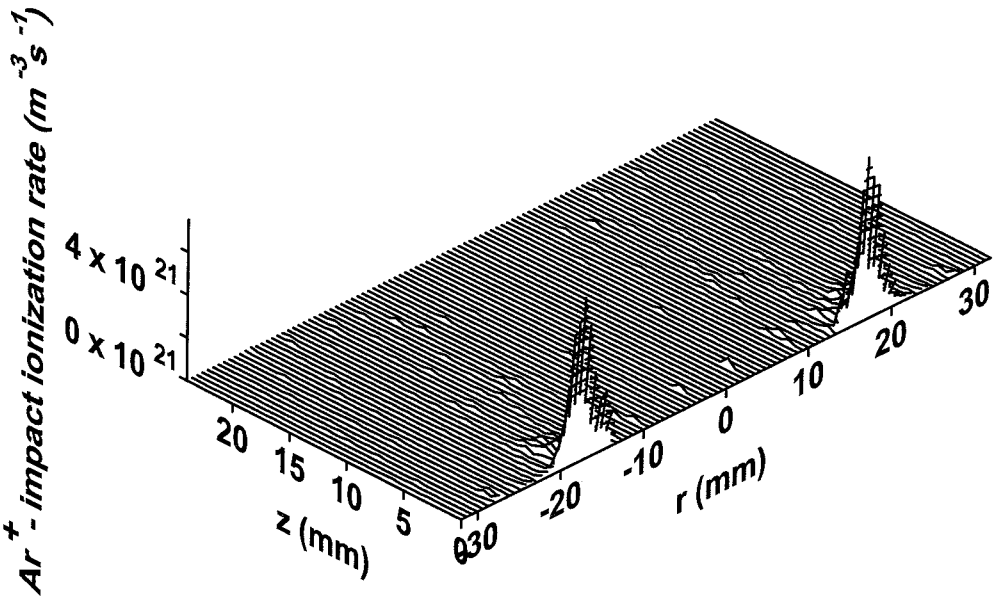

Figure 4.12 Calculated Ar^+-impact ionization.

The axial profile of the electron-impact ionization rate above the racetrack at $r = 18.2\,\text{mm}$, shown in Figure 4.13, has a maximum at $z = 1\,\text{mm}$. It is inside the sheath and its closeness to the cathode can be explained with the magnetic confinement. The Larmor radius (see Section 2.2.1) for electrons with a speed of 10^7 m/s in a magnetic field of 450 G is 1.26 mm. This means that the electrons, ejected from the cathode, stay long enough in a hemisphere, which center is on the cathode and with a diameter equal to the Larmor radius. The electrons have an energy, which is optimal for ionization before reaching the surface of the hemisphere. The shape of the ionization profile shows that most of the ionization is carried out by the primary electrons, originating at the cathode, rather than by secondary electrons, created in ionization collisions. There is nevertheless a significant amount of ionization taking place in the presheath and even in the bulk plasma. The borders of the two regions are reflected in the two inflexion points of the ionization profile at $z \approx 4\,\text{mm}$ and $z \approx 14\,\text{mm}$.

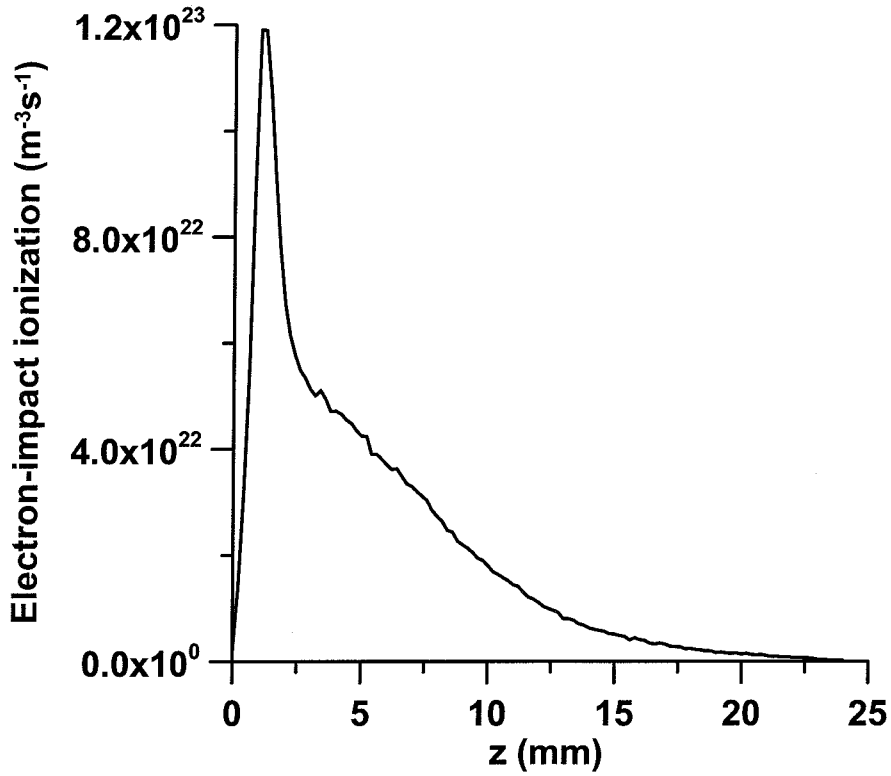

Figure 4.13 Calculated electron-impact ionization rate as a function of the distance from the cathode above the racetrack at $r = 18.2$ mm.

Whereas the ionization processes are responsible for the production of plasma, elastic collisions of the electrons directly determine the conductivity of the discharge, and therefore the discharge current. The calculated rate of the electron elastic collisions with the argon atoms is shown in Figure 4.14. In comparison to the ionization rate, the elastic scattering rate exhibits a second maximum at about $z \approx 2.7\,\text{mm}$. The first maximum corresponds to the spatial location of the maximum of the electron density. The second maximum is related to the mean electron energy and to the maximum of the elastic scattering cross section, which is for energies around 10 eV (see Figure 4.2). The mean electron energy above the racetrack is around 10 eV exactly at $z \approx 2.7\,\text{mm}$. After the second maximum, the rate of the elastic scattering decreases due to the decrease in both the electron density and the electron mean energy.

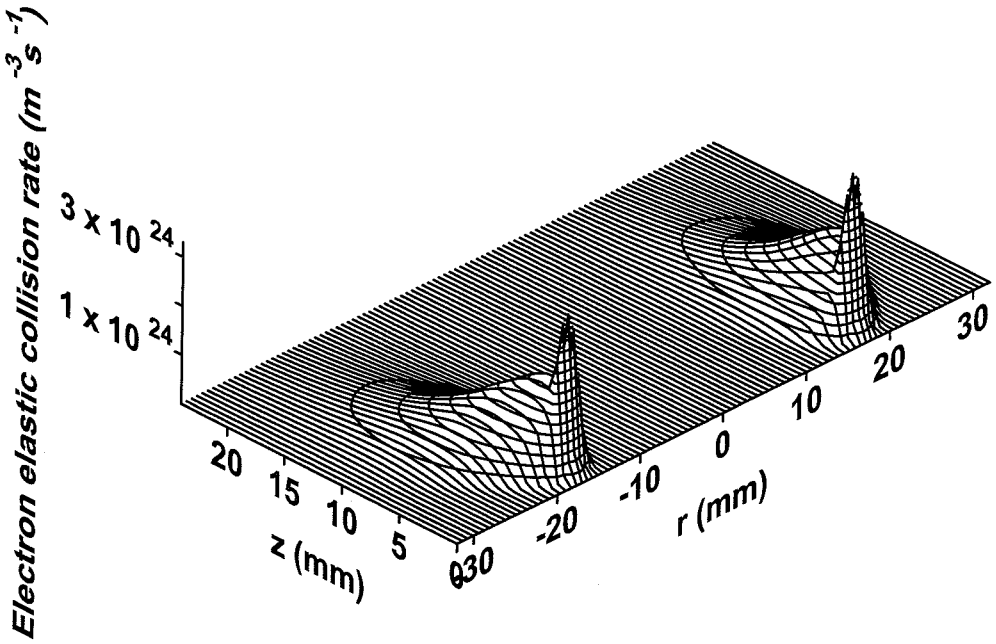

Figure 4.14 Calculated rate of the electron elastic scattering from the argon atoms.

The electron-impact excitation rate is important, because it can be experimentally determined. It has been used as an approximation for the ionization rate in nonmagnetized argon discharges because the cross sections for both excitation and ionization have similar shapes and magnitudes (see Figure 4.2). To

check the validity of this assumption both calculated rates above the racetrack are plotted in Figure 4.15. The locations of the main maxima coincide and their magnitudes are almost equal. Closer to the cathode, preferable is the ionization. This can be explained with the bigger magnitude of the ionization cross section for the energy range of interest. The lower threshold for excitation does not play a role here, because the electrons accelerate faster in comparison to the collision time. At distances further away than two millimeters, however, the excitation rate is up to two times higher than the ionization rate. This can be explained with the relatively low mean energy of the electrons in this region, which favors more the excitation. This region coincides with the presheath, in which the potential is not high enough to accelerate enough the electrons.

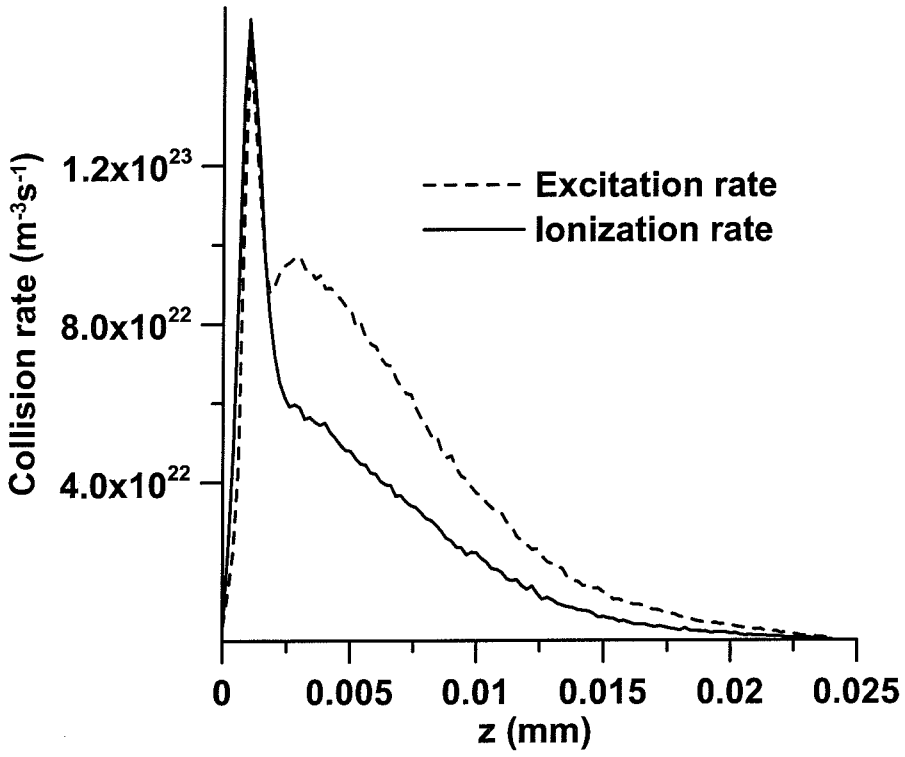

Figure 4.15 Calculated excitation rate (dashed line) and ionization rate (solid line) above the racetrack at $r = 18.2$ mm.

The existence of the second broad maximum in the excitation profile, which is integrally bigger than the first maximum, and the fact, that the first maximum is located only one millimeter away from the cathode, may cause that the experimental

measurements reveal only the second maximum. This and the overall different shape of the excitation and ionization profiles suggest that the use of experimentally obtained excitation rates for evaluation of the ionization in magnetrons or for estimations of the sheath can be rather incorrect.

Elastic collisions of Ar^+ ions, and especially the charge transfer component, play an important role for the energy distribution of the ionic flux at the cathode, which is in direct connection to the secondary electron emission and the sputtering. The calculated collision rates for symmetric charge transfer and isotropic scattering are shown in Figure 4.16 and Figure 4.17, respectively.

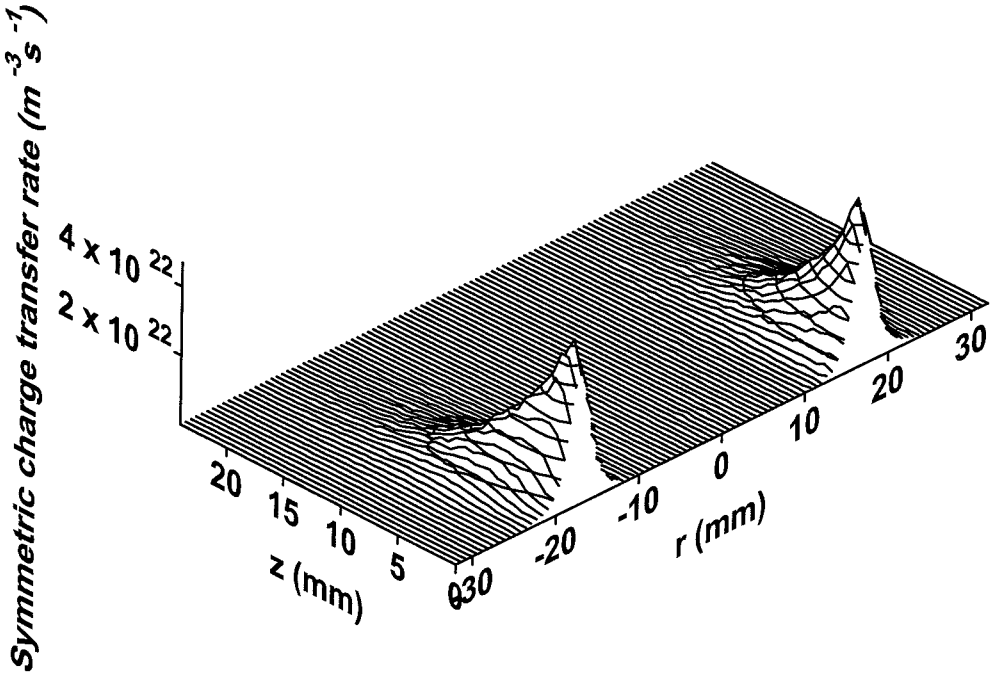

Figure 4.16 Calculated symmetric charge transfer of Ar^+ ions from their parent atoms.

As it can be seen there, both types of collisions exhibit maxima coinciding with the maximum of the Ar^+ ion density. In the sheath, the rate of the charge transfer is close to the maximum, although the density of the ions there is significantly lower than the maximum density. This fact is explained with the rapid acceleration in the sheath. Indeed, the symmetric charge transfer rate, R_{sct}, can be expressed as $R_{sct} = n_{Ar^+} n_{Ar} \overline{v_{Ar^+} \sigma_{sct}(\varepsilon)}$, where n denotes density, $v_{Ar^+} = \left(2\varepsilon / m_{Ar^+}\right)^{1/2}$,

and $\sigma_{sct}(\varepsilon)$ is the cross section for symmetric charge transfer (see Figure 4.3). The cross section is indifferent to the energy range in the sheath, but the speed increases almost as fast as the ionic density decreases.

The ratio between the two components of the elastic scattering is what should be expected from the ratio between their cross sections.

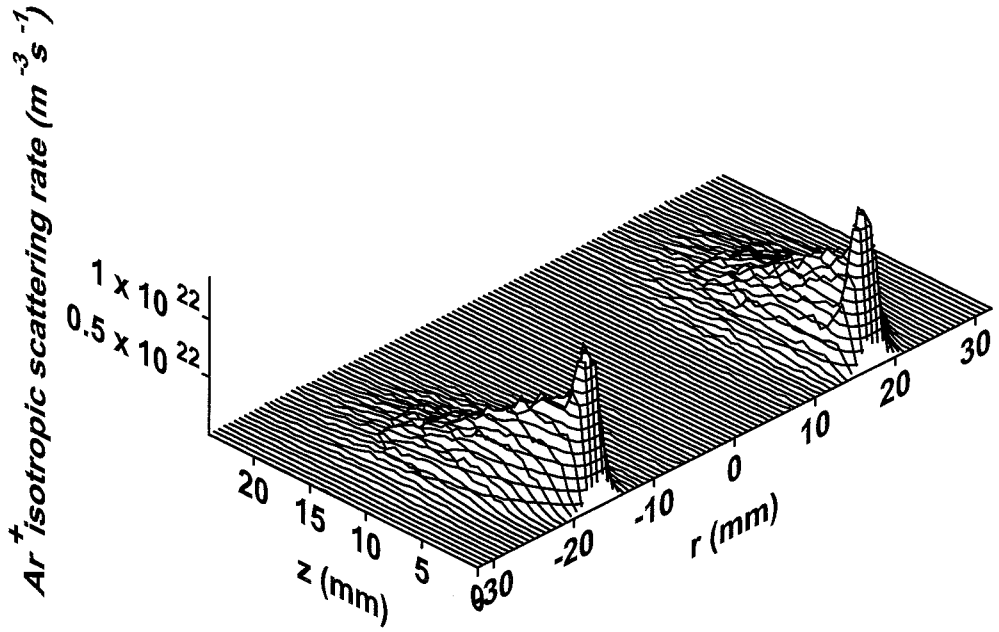

Figure 4.17 Calculated rate of isotropic scattering of Ar^+ ions from their parent atoms.

In the case of isotropic scattering, the cross section (see Figure 4.3) sharply decreases with the increase of the energy above 10 eV, which explains why the profile of the isotropic scattering rate follows that of the Ar^+ ion density.

4.5.4 Mean energy and energy probability function

The collision rates presented in the previous section, together with the distribution of the electric and magnetic field determine the spatial distribution of the mean electron and ion energy and corresponding energy probability functions. The calculated mean energy of the electrons is presented in Figure 4.18. Above the racetrack, where the electrons are strongly magnetized, their mean energy is about 40 eV. With radial displacement from the racetrack, the mean energy increases to

180 eV above the edges of the cathode. This increase is proportional to the weakening of the radial component of the magnetic field away from the centers of the magnets. Those electrons that enter the bulk are mostly with low energies, typically several eV, *i.e.*, below the inelastic threshold. This fact, as well as the sharp transition of the mean energy profile to a plateau, immediately after the sheath illustrates the effectiveness of the magnetrons – the primary electrons are almost entirely utilized in ionization and excitation events before being lost. The region along the symmetry axes is strongly depleted from electrons, which is reflected by the 'valley' in the mean electron energy profile.

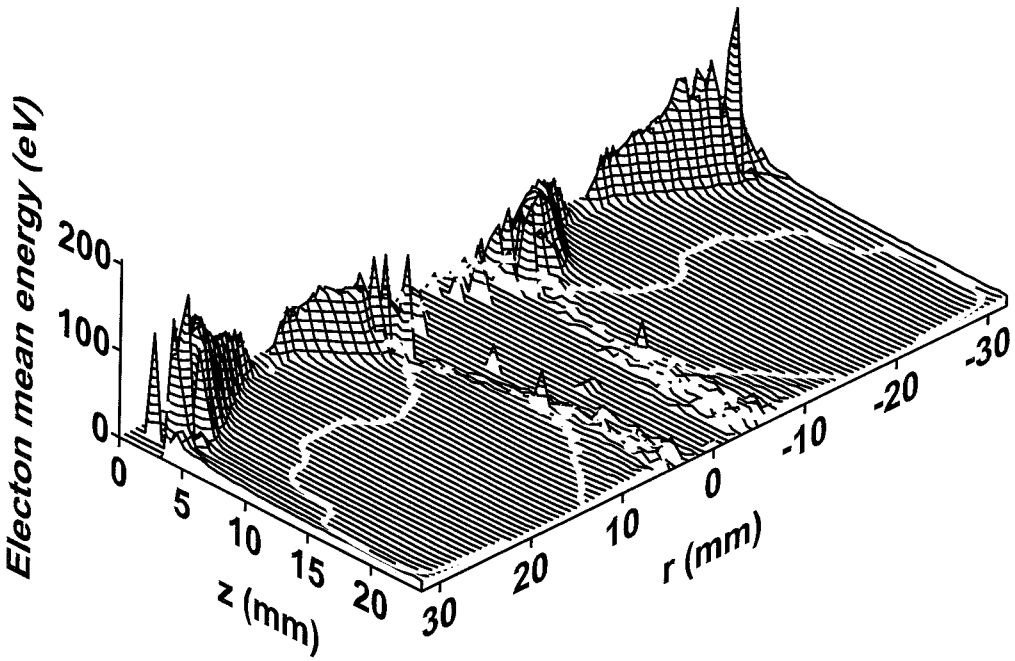

Figure 4.18 Calculated mean energy of the electrons. The cathode is located at $z = 0$. The white line in the bulk corresponds to a mean energy of 10 eV. The figure is turned in opposite way in z-direction (in comparison to the rest of the figures in the Chapter) for more clarity.

The distribution of the Ar^+ ion mean energy (Figure 4.19) follows the potential distribution. As it can be expected, the mean energy is high only in the sheath, with a maximum on the cathode surface. In the bulk, it is low – between 0.2 and 0.6 eV The mean ionic energy in the region between the poles of the magnet is

about 225 eV, which is approximately 70% of the cathode voltage. This ratio is slightly higher than the ratio of 60%, calculated in [88]. The difference can be explained with the broader sheath in [88], which allows the ions to spend more time in the sheath and consequently increases the probability for symmetric charge transfer collisions. These collisions are one of the two factors preventing the ions from obtaining energy values equal to the full cathode potential. The second factor is related to the location of the maximum of the ionization (see Figure 4.); it is between the sheath and the presheath. Thus, most of the produced ions accelerate in a potential difference that is less than the fool interelectrode potential. All this shows that the common assumption of "freely falling ions" is rather inaccurate.

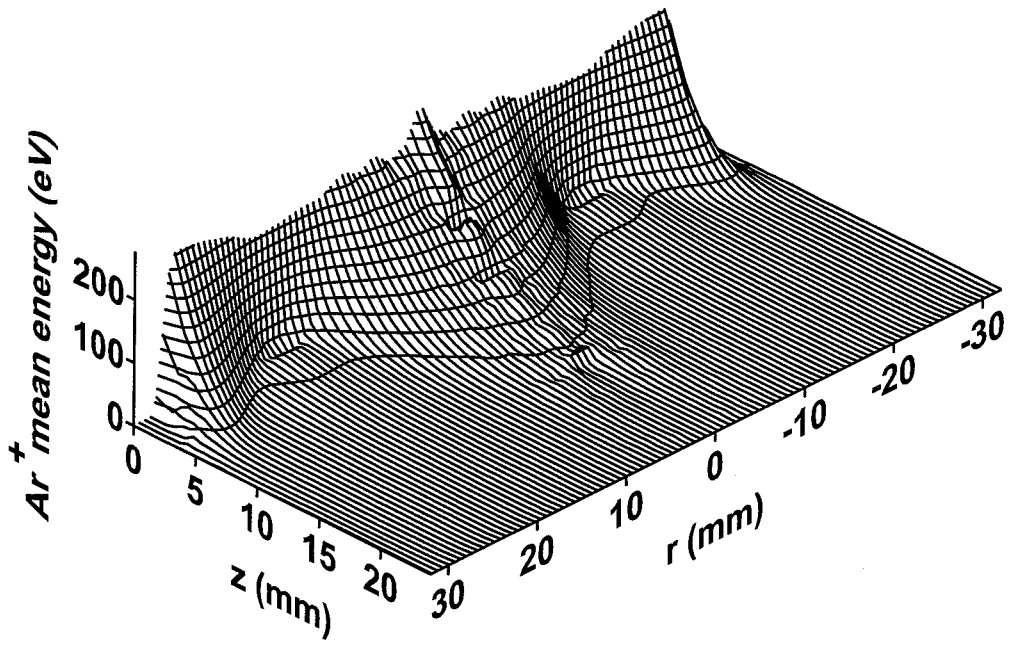

Figure 4.19 Calculated mean Ar^+ ion energy. The cathode is located at $z = 0$.

In contrast to the electron mean energy, the ion mean energy does not have a radial minimum above the racetrack. This is a direct result from the fact that the ions are not magnetized. There is, however, a shallow local minimum in z-direction above the racetrack at $r = 18.2$ mm. It is illustrated in Figure 4.20, where the mean ion energy above the racetrack is shown. The nature of this minimum is related to the maximum of the ionization profile, and the fact that the initial energy of the ions

is that of the thermal argon atoms. To some extent, the minimum represents also the potential well caused by the presence of the confined electrons.

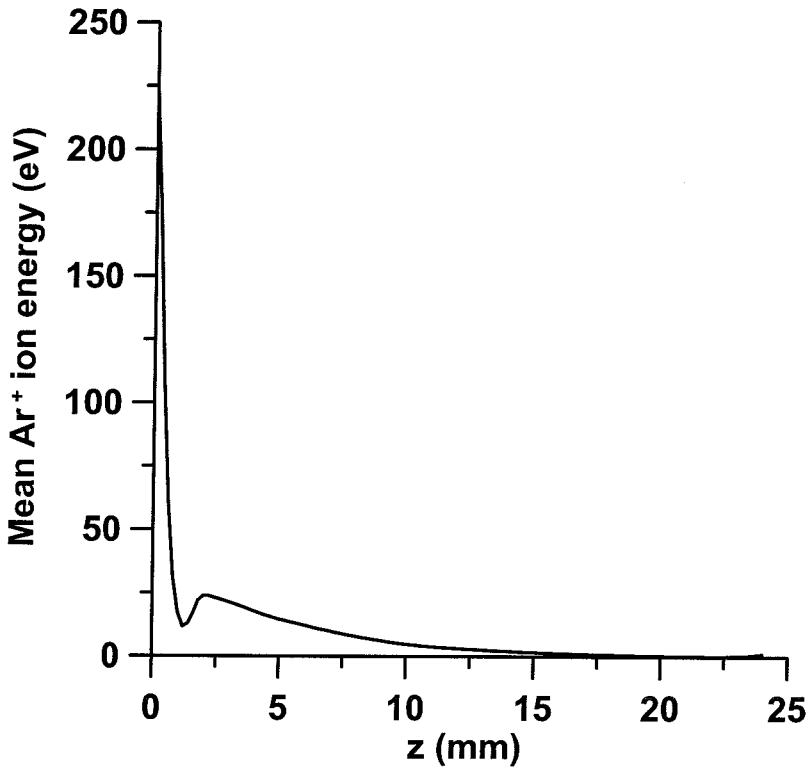

Figure 4.20 Calculated mean Ar^+ ion energy above the racetrack at $r = 18.2$ mm.

The mean energy does not provide information about what is the population in the energy spectrum. Such information is given by the energy probability function (EPF), $f(\varepsilon)$ $(= F(\varepsilon)\varepsilon^{-1/2})$, where $F(\varepsilon)$ is the energy distribution function and ε is the energy. The normalization of the EPF is: $\int f(\varepsilon)\varepsilon^{1/2} d\varepsilon = 1$. The knowledge of the EPF allows also to determine what is the distribution of the velocities and therefore to define a temperature, which allows simulated data to be compared to data received from probe measurements. As it has been already discussed, probe measurements are normally devoted to study of the bulk plasma, because the sheath region compromises the accuracy of the probe readings [186]. For this reason, in order to compare calculated results with experimental data, the quasi-local energy probability function has been sampled in the bulk in the present study. The sampling spot is a volume given by $14\text{mm} < z < 16\text{mm}$ and $16\text{mm} < r < 20\text{mm}$. The

calculated electron energy probability function (EEPF) is shown in Figure 4.21. It represents practically a Maxwellian distribution with a temperature of 6.7 eV. Such value is in good agreement with the spatial survey of magnetron plasma by means of a Langmuir probe [185]. In the latter experiment, for $p = 5\text{mtorr}$, the electron temperature at $z = 3\text{cm}$ is found to be 5 eV and decreases with increase of z ($T_e = 2.5\text{eV}$ at $z = 5\text{cm}$). Therefore, our calculated T_e of 6.7 eV at $z = 1.5\text{cm}$ seams to be consistent with the experiment.

The Maxwellian distribution at such low pressure is a result of the magnetic confinement of the electrons, which secures enough collisions with the argon atoms before the electrons diffuse into the bulk.

They are reports in the literature for existence of two electron populations with different temperatures, which produces a Bi-Maxwellian distribution [187, 188]. More resent work [185], however, fails to confirm such phenomenon. The calculated results in the present work also do not indicate the existence of two electron populations with different temperatures.

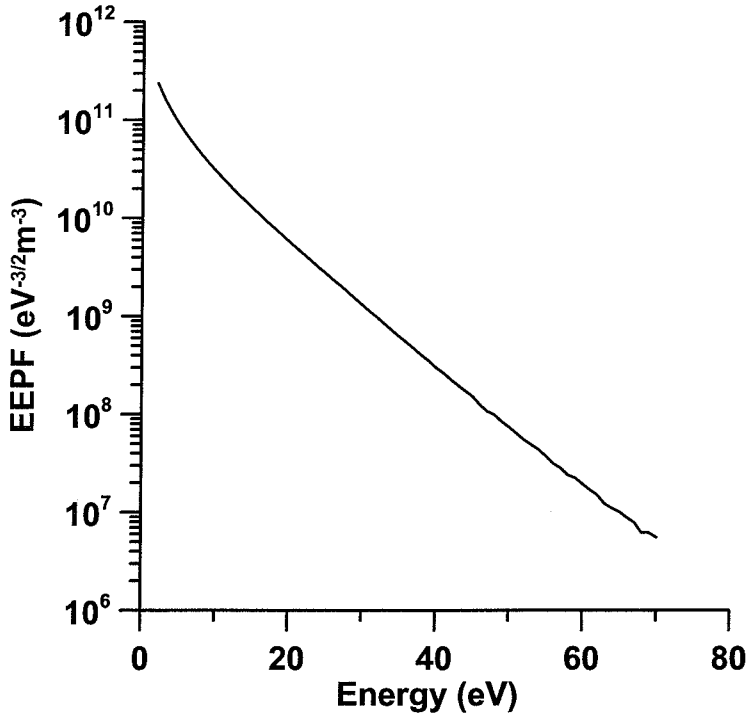

Figure 4.21 Calculated electron energy probability function (EEPF) in the bulk ($14\text{mm} < z < 16\text{mm}$, $16\text{mm} < r < 20\text{mm}$).

The Ar^+ ions behave in a very different way than the electrons. Being practically not magnetized, the ions cannot stay for a long enough time in the discharge. This means they cannot suffer enough collisions for bringing them in equilibrium with the background gas. This is reflected in their EPF, shown in Figure 4.22.

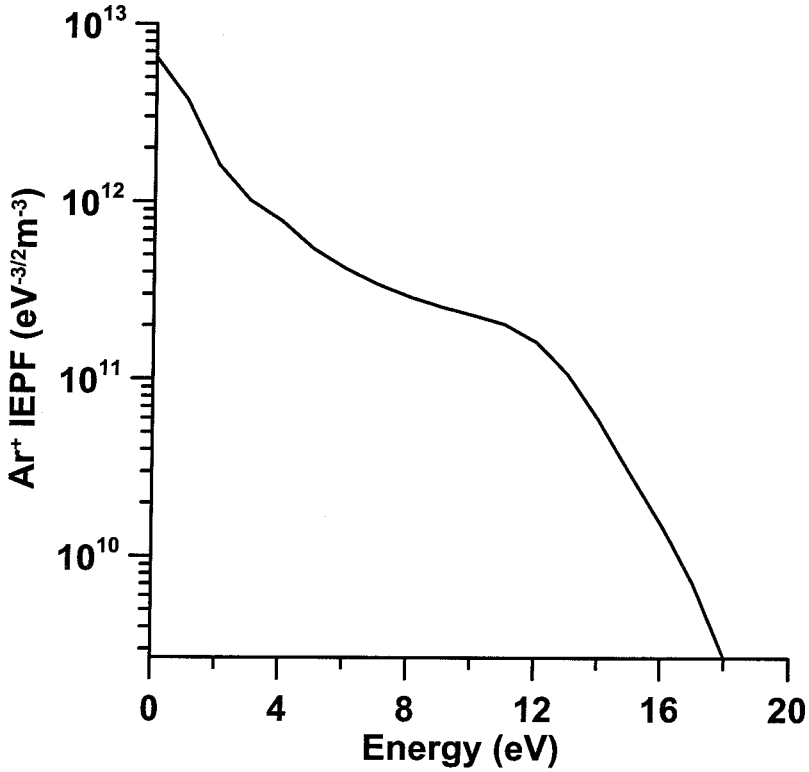

Figure 4.22 Calculated Ar+ ion energy probability function (IEPF) in the bulk ($14\,\text{mm} < z < 16\,\text{mm}$, $16\,\text{mm} < r < 20\,\text{mm}$).

As it is clear from this figure, the energy distribution is far from Maxwellian or other equilibrium distribution. In this case, the use of the temperature as a characteristic of the velocity distribution makes no sense. This result indicates that the use of fluid description for the plasma in dc magnetron discharges operated at standard conditions is incorrect. The same refers to hybrid models [51], where a Maxwellian distribution for the ions is normally assumed and they are treated as a continuum. The IEPF in Figure 4.22 also questions the idea of measuring the ion temperature in dc magnetrons by probe experiments. In a more global aspect, the ion temperature does not bring any valuable information for the state of the plasma in dc

magnetrons. It can only be used as mean ion energy, without providing any further insight for the velocity distribution.

4.5.5 Ion flux at the cathode

The Ar+ ions that reach the sheath region or are created inside the sheath accelerate towards the cathode, which they can bombard. This flux is responsible for the generation of primary electrons that sustain the discharge and for sputtering. The rate of sputtering (see Section 2.4.3) is proportional to the energy density of the bombarding flux. The spatial distribution of this flux at the cathode surface determines the sputtering region – the racetrack. Therefore the knowledge of the flux is important, in order to predict the utilization of the target at given operating conditions. The calculated Ar^+ ion flux at the cathode is presented in Figure 4.23.

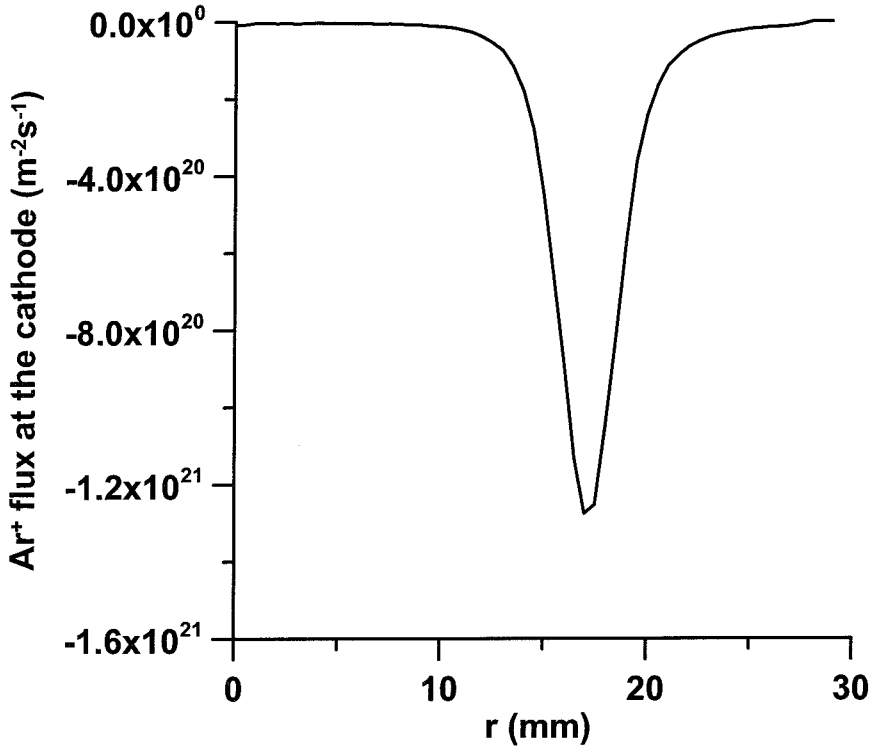

Figure 4.23 Calculated Ar^+ ion flux at the cathode.

The flux is limited to the region between the magnetic poles. This is in accordance with all experimental data. Its amplitude is proportional to the Ar^+ density. The localization of the flux, which follows the localization of the ion

density in the radial direction, is a confirmation of the fact that the ions are practically not magnetized. Therefore, their movement in the sheath can be approximated to a free fall disturbed by the collisions in the sheath.

4.6 Conclusions

In this Chapter, the PIC/MCC model of dc planar magnetron discharge (explained in detail in Chapter Three) has been applied to a laboratory magnetron Von Ardenne PPS 50, operated at a pressure of 5 mtorr in argon. All main characteristics of the magnetron have been calculated and analyzed. The results of the model have been compared to experimental data, where available. The comparison is satisfactory.

- A full quantitative picture of the processes occurring in the magnetron has been obtained. The main results show:
- Presence of a negative space charge region;
- Thin sheath (about 1 mm) with strong radial dependence;
- Electrons are with a Maxwellian distribution, with a temperatures of about several eV;
- Ar^+ ions are with unequilibrium velocity distribution and cannot be described as a fluid;
- Electron and ion density is strongly localized in the close to the cathode above the region where the magnetic field is perpendicular to the cathode;
- The potential is characterized by strong gradients in the z-direction and has strong radial dependence.

Chapter Five

Study of electron recapture at the cathode

5.1 Introduction

In dc magnetrons, the electrons emitted from the cathode may return there due to the applied magnetic field. When that happens, they can be recaptured or reflected back into the discharge, depending on the value of the *reflection coefficient* (*RC*). This phenomenon and the exact way it influences the discharge behavior is one of the sparsely touched problems in the literature. The magnetic confinement allows magnetrons to be operated at pressures of around a few millitorr. Such low pressures lead to long mean free paths, thus allowing a significant number of electrons, ejected from the cathode, to return there during their first gyro-period. Generally, the probability for this process depends on the initial energy of the electrons and on the number of collisions they suffer. Both elastic and inelastic collisions can prevent the electrons from returning to the cathode. The former can change the velocity vector of the electrons and so divert them to another magnetic field line, whereas the latter reduce their energy, so that they cannot overcome the sheath potential and return to the cathode. The initial energy, at which the electrons leave the cathode, in most cases, plays a less important role. The reason is that the initial energy is normally lower than the inelastic threshold of most of the gases used in magnetrons. As it can be seen in [189], the energy distribution of the ejected electrons has a cutoff, given by the empirical relation: $\varepsilon_{cutoff} = \Delta\varepsilon_{ion} - 2W$, where $\Delta\varepsilon_{ion}$ is the ionization potential of the feeding gas and W is the work function of the cathode material. The maximum of the energy distribution is ca. $0.5\varepsilon_{cutoff}$. Therefore, the electron initial energy can change the probability for recapture only for the case of elastic collisions. This statement is valid for all kinds of magnetrons. The specially shaped poloidal magnetic field in planar magnetrons, with magnetic lines of changing density and curvature and crossing the cathode, can create a magnetic mirror (see Section 2.2.3.3). That mirror can cause a sharp turning of an

electron shortly before its reaching the cathode, even though the electron may possess enough energy to strike the target. Taking into account the complexity of the electric and the magnetic fields in planar magnetrons, it is not possible to give a reasonably simple estimate of how much the magnetic mirroring can affect the electron recapture.

The effect of recapture of electrons at the target can interfere with the discharge characteristics in two ways. The more obvious one is that, if an electron is absorbed at the cathode without causing an electron impact ionization of a gas atom, it is, as if it were not emitted at all. This claim is based on the fact that the discharge cannot be sustained without the ionizations caused by the cathode electrons. Therefore, on a macroscopic level, absorption of electrons at the cathode leads to an effective decrease of the secondary electron emission coefficient (SEEC), γ, which gives the number of electrons produced by an ion striking the cathode (see Section 1.2.2). The SEEC is a very important parameter in the operation of dc magnetrons. Small variations of γ cause significant changes in the amount of ionization, plasma density, and sheath architecture at fixed other parameters. The SEEC is energy dependent [7].

The second way the electron recapture influences the discharge is through the cathode potential. The more electrons are absorbed at the cathode, the lower the convective (conductive) discharge current is at the cathode and the more negative the cathode potential is. The latter will be illustrated further. This implies that electron recapture at the cathode may have a complex effect upon the discharge and a detailed investigation is necessary to describe it quantitatively. The results may be of interest to both simulators and experimentalists. In simulations, the reflection of electrons from the cathode surface is a boundary condition: in fluid approach for the electron flux and density and in the kinetic approach as a loss/birth process. In the existing simulation works on dc magnetrons, the value of the reflection coefficient (RC) is frequently not explicitly given [51, 86, 88] or assumed to be zero [190, 191] without argumentation, meaning that all the electrons arriving at the cathode are considered to be absorbed. In the very detailed work on cylindrical magnetrons [25] the authors report using a RC of 0.5 and claim that little change in the discharge characteristics was found when varying the RC between 0.5 and 0.9. Their choice of a $RC = 0.5$ is based on the early work of Thornton [19], where the value of 0.5 for

cylindrical magnetrons is proposed without detailed justification. For planar magnetrons, only recently, a simple model was reported [40], devoted to the influence of the electron recapture on the discharge characteristics. The model is essentially a non self-consistent trajectory calculation, with simplified collision processes and an assumed one-dimensional electric field. Despite its simplicity, it shows clearly the importance of the electron recapture.

Measurements and theoretical calculations [192, 193] of the reflection of low-energy electron beams from metal targets show that for energies up to 20 eV (*i.e.*, more than twice the maximum energy that an electron may have, when returning at the cathode at typical dc magnetron operating conditions) the *RC* is never less than 0.1 (*i.e.*, not equal to zero). Moreover, for energies between 0 and 5 eV it grows very fast with decreasing the energy, approaching a value of 0.55 [measured on Cu (001)] and 0.8 (calculated) [193]. It is necessary to be mentioned, that the electron interaction with the cathode in dc magnetrons involves electrons with energies below or around the work function of the cathode material. This means, that there is no electron multiplication at the cathode, an effect known as *multipactor* [194], which has been intensively studied for many years [195]. Moreover, there are a very limited number of true secondary electrons ejected from the cathode by electron impact. That is why the main mechanisms of interaction between the electrons returning at the cathode and the cathode surface are reflection (elastic or inelastic) and absorption [193, 194].

A lot of attention has been devoted to the investigation of the interaction of electrons with metal surfaces and the probability for electron induced secondary electron emission. The interest in that subject has come mainly from areas such as scanning electron microscopy [196] and cathode emissions from vacuum tubes. However, the characteristic energies of the primary electrons there are from a few hundred eV to a few tens of keV, while the energies of interest in the dc sputtering magnetrons do not exceed a few eV. A relatively recent work to model electron interaction with metal surfaces with improved accuracy for the low energy interval has been reported by Furman and Pivi [197, 198]. It will be discussed in more detail in Section 5.3.6.

The above discussion motivates a detailed investigation of the electron recapture at the cathode in dc magnetrons. The remainder of the chapter is devoted to a PIC/MCC survey that examines the existence and the influence of the electron

recapture at the cathode, and compares different ways of inclusion of this effect in numerical simulations.

5.2 Numerical details

A number of simulations are performed for the magnetron described in the previous chapter. First, a simulation initiated with a homogeneous density, $RC = 0$, and $p = 4$ mtorr has been brought to convergence. Then the results of this run have been used as initial conditions in all following runs, where the RC and/or pressure have been varied. This is done to shorten the time necessary for reaching convergence. This can be seen in Figure 5.1, where the cathode potential evolution with time is shown. As it can be seen in this figure when converged results are used as initial conditions for a new simulation, where only one parameter is changed, the convergence time is shorter. At the same time, the comparison between a simulation started in this way and a simulation with the same operating conditions but started from scratch shows that both simulations produce same results (see Figure 5.1 and its caption).

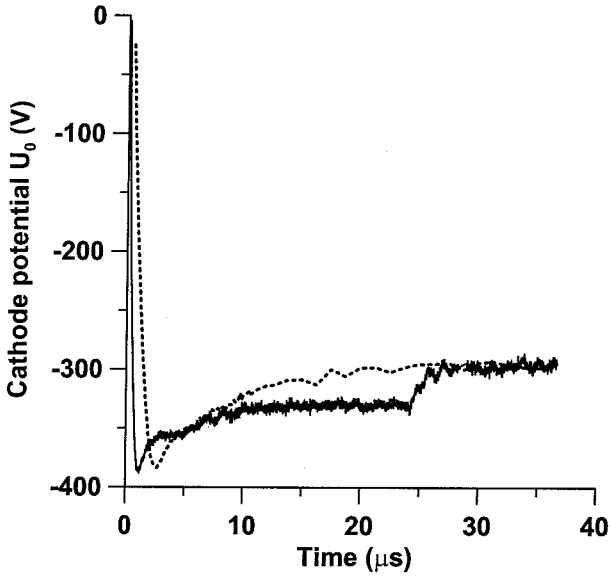

Figure 5.1 Convergence of the cathode potential U_0 for $p = 4$ mtorr and $RC = 0.5$. The dashed line represents a simulation initiated with a homogeneous plasma density. The solid line corresponds to a simulation started with the converged data of a run with $RC = 0$. The transition occurs at $t = 24.2$ μs.

5.3 Results and discussion

5.3.1 Electron trajectories

To visualize the effect of the RC on the discharge on a microscopic level, a sample electron, ejected from the cathode has been traced for the cases of $RC = 0$ (Figure 5.2) and $RC = 1$ (Figure 5.3). For $RC = 0$ the electron returns at the cathode without suffering any collisions, which means its existence remains unseen by the discharge, since no ionization has happened and thus no contribution to the discharge maintenance has occurred. Of course, not all of the electrons, ejected from the cathode, exhibit the same behavior. Some of them manage to collide during this first gyro orbit. A typical particularity of the electron motion in complex electric and magnetic fields can be seen at the turning point at $r \approx 17.7$ mm. At that moment, the electron possesses enough energy to overcome the sheath potential, but nonetheless, it is turned back just immediately before the cathode due to a turn caused by the local magnetic field. Figure 5.2 confirms fully the estimate made in Section 4.5.3 about the radius of the gyro orbit. The estimated radius is 1.26 mm; an exact match to the highest with respect to z points of the trajectory in Figure 5.2. This is another indirect proof for the consistency of the model.

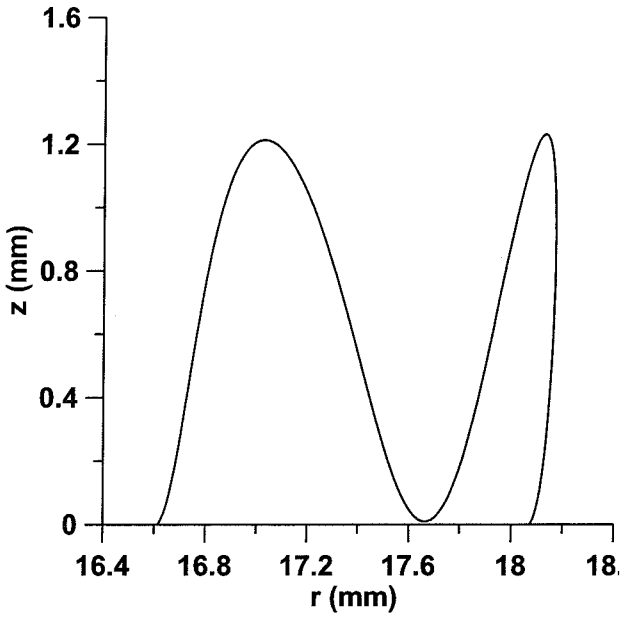

Figure 5.2 Trajectory of a sample electron emitted from the cathode for $RC = 0$.

A rather different picture can be seen in Figure 5.3. Being allowed full reflection, the sample electron stays in the discharge for significantly longer time and eventually manages to ionize an argon atom. In fact, setting $RC = 1$ leads to almost 100% probability that an electron, released from the cathode, will produce ionization. This is so, because the electron needs many elastic collisions to escape the magnetic trap, so the path traveled during its lifetime becomes longer than the mean ionization path.

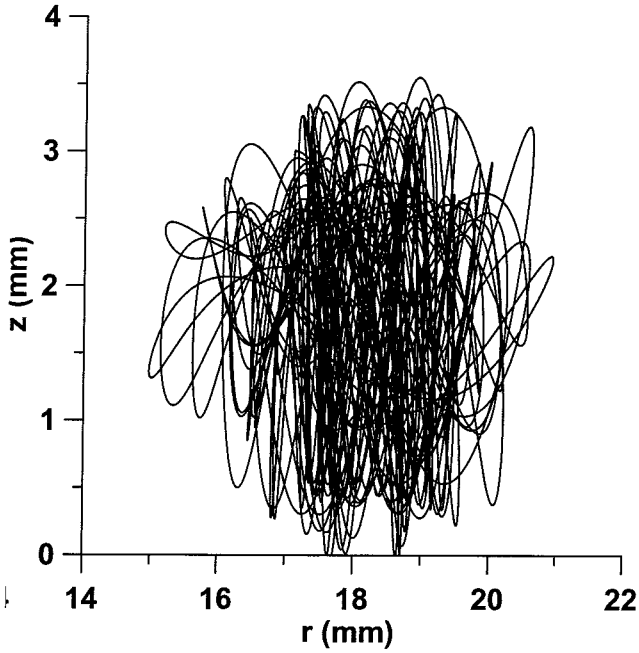

Figure 5.3 Trajectory of a sample electron emitted from the cathode for $RC = 1$.

5.3.2 Sheath architecture

More reflection means more electrons in front of the cathode and more negative space charge created there. An illustration of this statement is shown in Figure 5.4, where the potentials at $r = 18.2$ mm (*i.e.*, above the racetrack), normalized with respect to the cathode voltage, are plotted at $p = 4$ mtorr for different RC values.

The bigger the *RC*, the steeper the cathode fall and the more negative the space charge in the vicinity of the cathode. The latter leads to lower bombarding energies at the cathode, since the ionization maximum is situated at around 1.2 mm

from the cathode. Thus, the majority of the ions cannot gain the entire discharge potential difference.

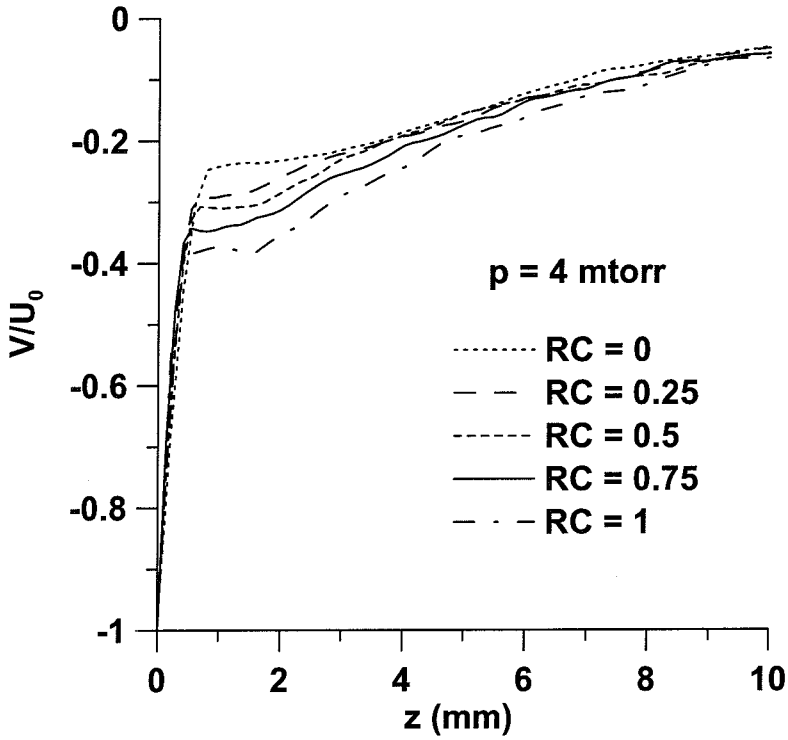

Figure 5.4 Calculated plasma potential V, normalized with respect to the cathode potential U_0, along $r = 18.2$ mm at $p = 4$ mtorr for different values of the reflection coefficient.

5.3.3 Ionization rate and plasma density

The steepness of the potential results in a stronger electric field, which creates a possibility for a denser population at the high-energy tail of the electron energy probability function (see Figure 5.5). All this inevitably causes an increased amount of ionization and higher electron density for higher values of the RC, as shown in Figure 5.6 and Figure 5.7 for $p = 4$ mtorr. Except in the sheath, the ion density profile (not shown here) is identical to the electron density profile, because the ions are electrostatically bound to the electrons, as it has been shown in Section 4.5.2.

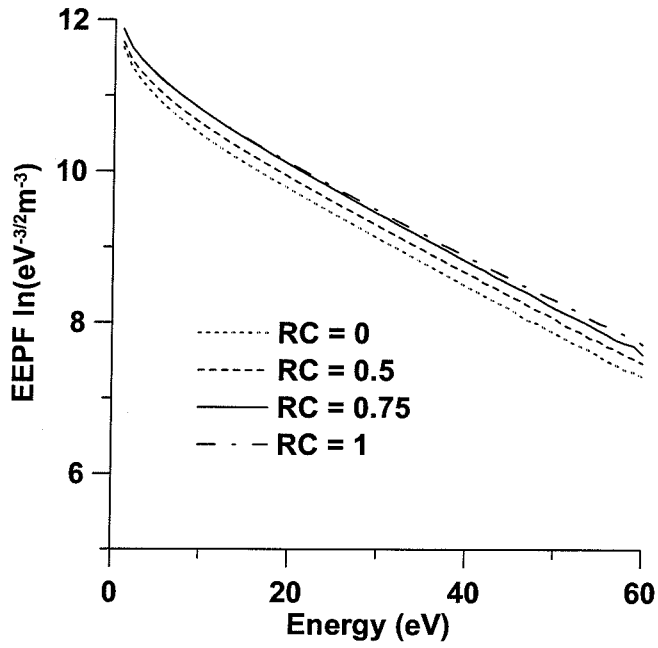

Figure 5.5 Calculated electron energy probability function at p = 4 mtorr for different values of the reflection coefficient.

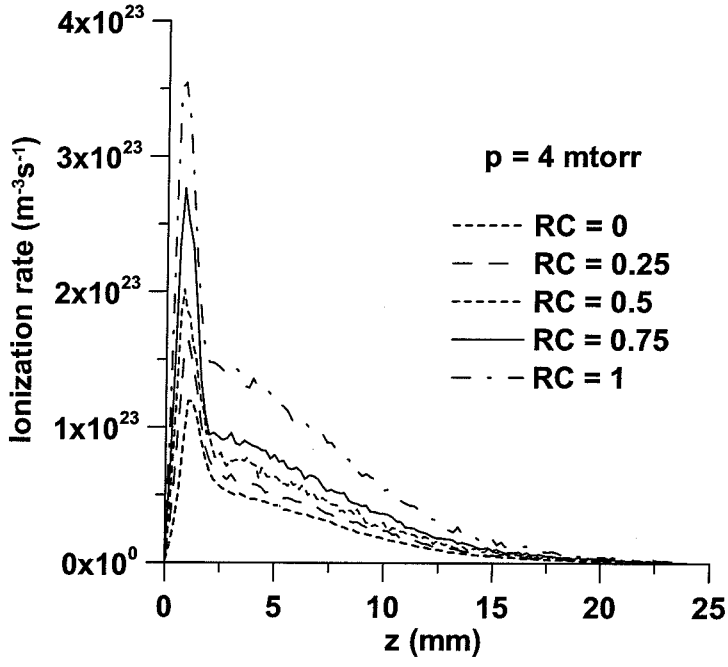

Figure 5.6 Calculated ionization rate along r = 18.2 mm at p = 4 mtorr for different values of the reflection coefficient.

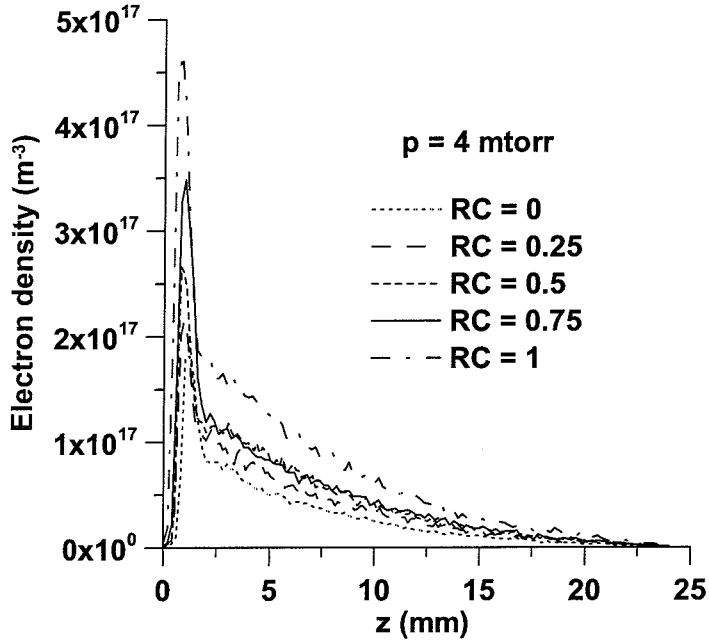

Figure 5.7 Calculated electron density along r = 18.2 mm at p = 4 mtorr for different values of the reflection coefficient.

The ionization rate for $p = 25$ mtorr for different values of the RC is presented in Figure 5.8. The same tendency as at $p = 4$ mtorr appears, but it is weaker, as might be expected (see below). The amplification factor, defined as the ratio of the maximum ionization rate at $RC = 1$ over the value at $RC = 0$, is 2.67 at the lower pressure, whereas at the higher pressure it is 1.67.

The weaker effect of the electron recapture at higher pressure is due to the increased probability for electron collisions. The higher probability decreases the possibility for return of the electrons back at the cathode. It also acts in a direction to weaken effectively the magnetic trap. This reduces the time that the electrons spend close to the cathode and therefore brings the space charge to less negative values, as it can be seen in Figure 5.9. The less effective confinement may be seen also in the radial expansion of the electron density, shown in Figure 5.10, when compared to the electron density distribution at p = 5 mtorr (Figure 4.9).

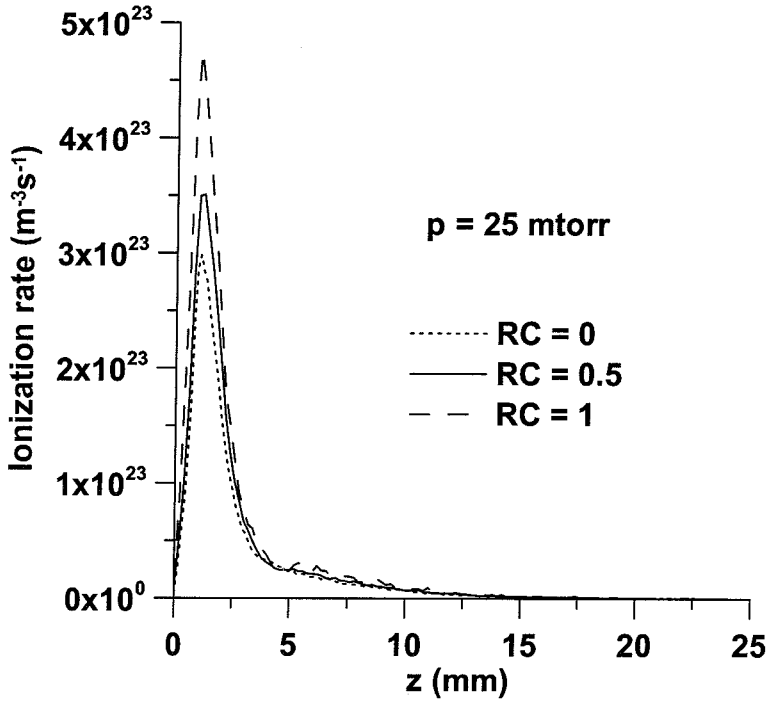

Figure 5.8 Calculated ionization rate along r = 18.2 mm at p = 25 mtorr for different values of the reflection coefficient.

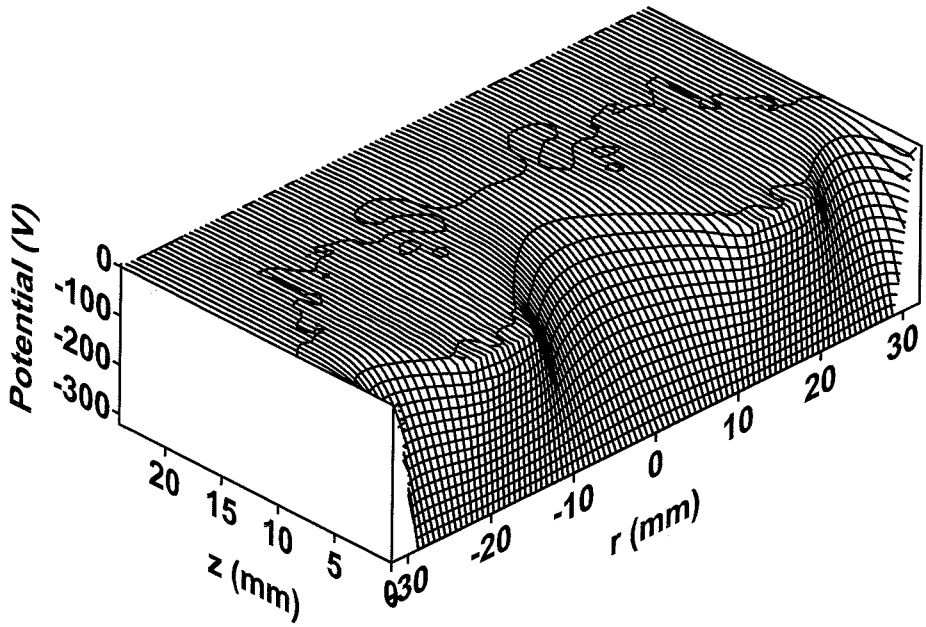

Figure 5.9 Calculated potential for p = 25 mtorr and RC = 0.5.

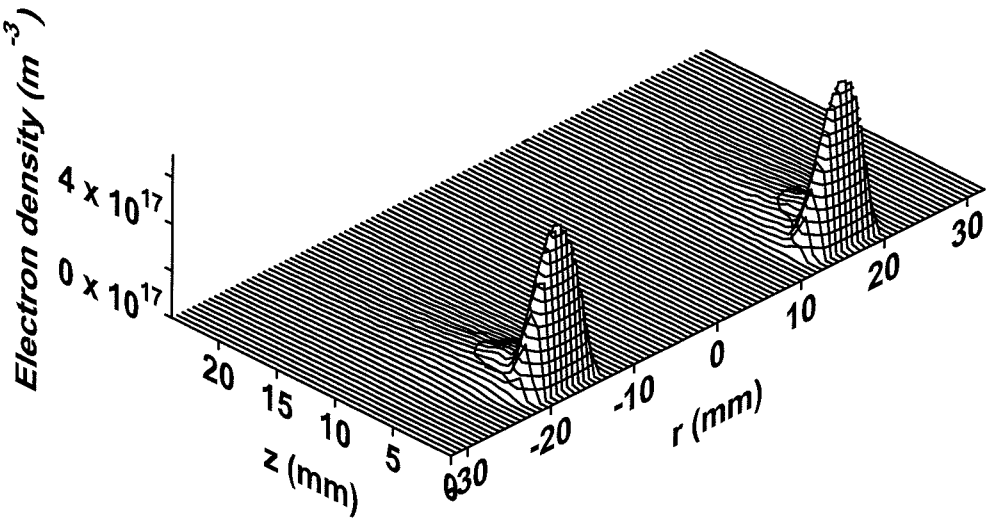

Figure 5.10 Calculated electron density for p = 25 mtorr and RC = 0.5.

5.3.4 Cathode potential and discharge current

To examine the influence of the RC upon the discharge potential and current, either the cathode voltage, U_0, or the external current, I_{ext}, should be kept constant, while changing the RC. This has proved to be not possible. The reason is, that the influence of the RC is so strong, that there is no single value of either U_0 or I_{ext} that can sustain the discharge throughout the whole range of RC values. If the converged U_0 for $RC = 0$, for example, is tried to be kept for higher RC, the discharge is overpumped and the simulation moves towards arc, becomes unstable, and eventually terminates. The instability is caused by a growth of the amount of ionization, strong enough to form a significant local space charge perturbation.

With an external circuit of the type used here, there are two ways to maintain a constant discharge voltage. Either the external voltage has to be increased, or the ballast resistance needs to be decreased, provided the discharge voltage has dropped and needs to be returned at its previous level. However, either of the two ways is essentially pumping more energy into the discharge, hence more ionization. More ionization means again a lower cathode voltage due to an increased positive charge deposition, which again calls for further power from the source.

The opposite situation happens when U_0, obtained for $RC = 1$, is attempted to be kept constant for lower RC. Then the discharge just extinguishes, because U_0 is

too low to maintain the discharge at low reflection rates. The process is gradual and passes through a condition close to a Townsend discharge – stable, but with extremely weak current. For this reason, all present simulations are performed with constant external parameters, allowing the discharge to achieve a steady state voltage and current. Their dependences on *RC* are shown in Figure 5.11 and Figure 5.12, respectively. The discharge current increases with the increase of the *RC*, while the discharge voltage drops. This simulation result is in a direct connection to the well-known fact, that glow discharges have a negative differential resistance. It can be easily explained by imagining a simple circuit consisting of a voltage source, a ballast resistor, and a variable resistor (representing the discharge) in series. When the resistance of the variable resistor is decreased, what exactly happens when the *RC* is increased, the current in the circuit increases, so does the voltage drop across the ballast resistor and to obey Kirchhoff's voltage loop law, the discharge voltage must decrease. As it can be seen in Figure 5.11 and Figure 5.12, at higher pressure, the change of U_0 and I_{disch} with *RC* is significantly weaker.

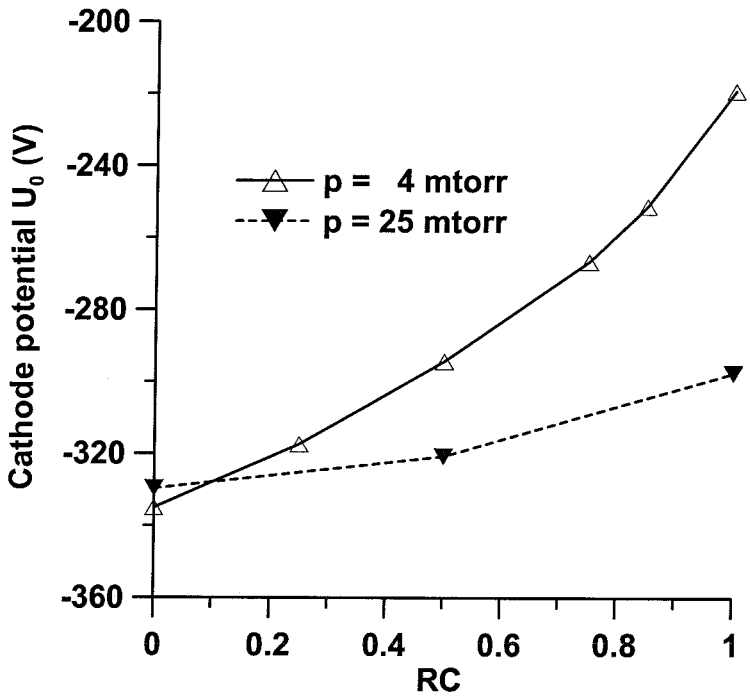

Figure 5.11 Calculated cathode potential, U_0, as a function of the reflection coefficient. The solid curve is for $p = 4$ mtorr; the dashed curve stands for $p = 25$ mtorr. The triangles represent the calculated values.

The dependence is non-linear, and becomes stronger when allowing more reflected electrons. This is in contradiction with the statement made in [25], where the authors, performing a 1d PIC/MCC simulation of a cylindrical dc magnetron, claim that no significant influence on the steady state results is observed for *RC* between 0.5 and 0.9.

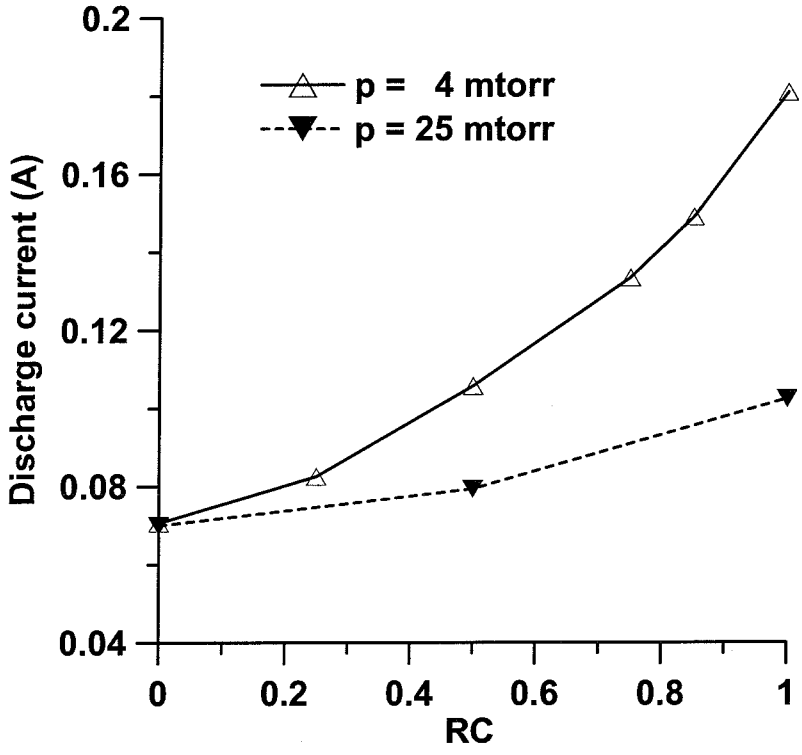

Figure 5.12 Calculated discharge current, I_{disch}, as a function of the reflection coefficient. The solid curve is for p = 4 mtorr; the dashed curve stands for p = 25 mtorr. The triangles represent calculated values.

5.3.5 Effective SEEC

It is interesting to assign a macroscopic parameter, which can be used in analysis, with respect to the electron recapture. Such a parameter is the *SEEC*, but in the way, the discharge sees it , *i.e.*, γ_{disch} , which can be defined as:

$$\gamma_{disch} = \left(N_{ej} - N_{rec}\right)/N_{ion}$$

Here, N_{ej} is the number of electrons produced by ion bombardment per unit time, N_{rec} is the number of electrons recaptured at the cathode during this time, and N_{ion} is the number of ions striking the cathode for the same period of time. γ_{disch} is, in fact, the effective *SEEC*, which should be used in estimates to account for the effect of electron recapture. The beam *SEEC*, γ_{beam}, that is what is normally available from the literature, will be

$$\gamma_{beam} = N_{ej}/N_{ion}$$

Both quantities are shown in Figure 5.13, calculated at $p = 4$ mtorr for different *RC* values.

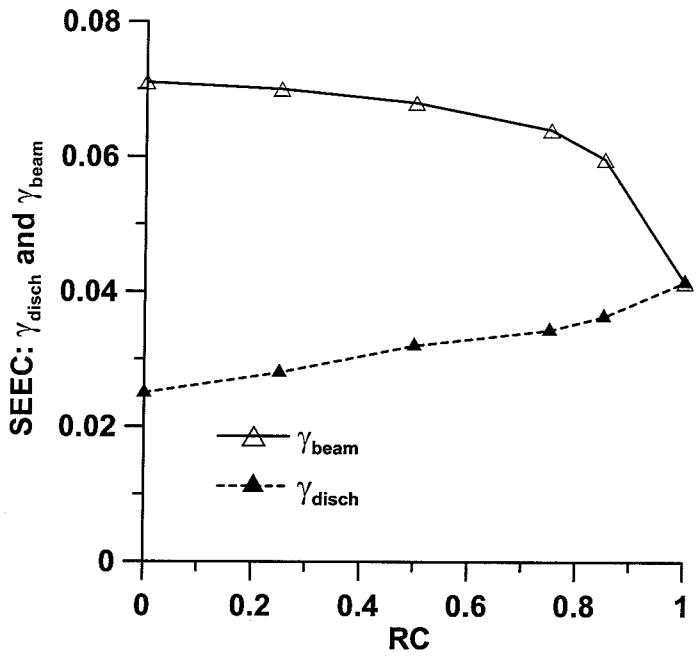

Figure 5.13 Calculated secondary electron emission coefficient at p = 4 mtorr as a function of the reflection coefficient. Solid curve: as seen by the cathode (SEEC from ion beam data). Dashed curve: as seen by the discharge (effective SEEC). The triangles represent to the calculated values.

As it can be seen, the effective *SEEC* is significantly reduced due to the existence of electron recapture. For $RC = 1$, γ_{disch} is equal to γ_{beam} because no electrons will be recaptured. For the intermediate value of $RC = 0.5$, γ_{disch} is found to be exactly the half of γ_{beam}. This result confirms the assumption made by Thornton in [19] and is in good agreement with the value $\gamma_{disch} = 0.46\gamma_{beam}$ for a pressure of 3.75 mtorr obtained in [40]. However, the exact value of γ_{disch} is always a function of the *RC* and the pressure.

5.3.6 Constant versus probabilistic recapture

As it has been mentioned in the Introduction (see Section 5.1), the recapture of the electrons at the cathode can be treated according to the procedure described in [197] and [198]. The model described there is fully compatible with the PIC/MCC technique and capable of dealing with different kinds of surfaces. The surface properties are implemented in a set of parameters, which are derived from experimental data. Therefore, primal knowledge of experimental data for electron induced secondary electron emission is needed, in order to apply the model. Beside this restriction, there exists a purely computational drawback. To obtain the probability for absorption, reflection or emission of each electron hitting the cathode and the velocity of the reflected and emitted electrons, computationally exhaustive calculations have to be performed. This includes, among others, a numerical evaluation of normalized incomplete gamma and beta functions [199], as well as, the functional inverse of both of them. In the present work, gamma and beta functions are calculated according to [148] and their functional inverse by applying the Newton-Raphson method [132].

A simulation with the above-mentioned algorithm has been run with the necessary parameters for Cu. Next, a simulation with a constant $RC = 0.39$ has been carried out. The value 0.39 has been obtained as an averaged value from the first simulation. The results of both simulations are practically identical. An illustration of this statement is Figure 5.14, where the temporal evolution of the cathode potential, U_0, for both cases is shown.

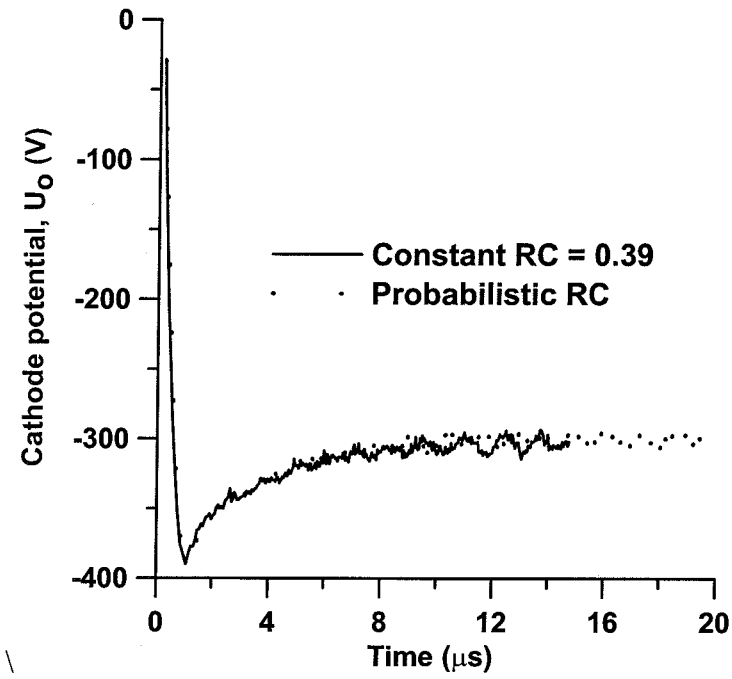

Figure 5.14 Time evolution of the calculated cathode potential. Dotted curve: recapture treated probabilistically, as in [197] and [198]. Solid curve: recapture treated with a constant $RC = 0.39$.

.As it can be seen, in both simulations U_0 converges to a value of $-303\ V$. The other discharge parameters (not shown here) exhibit also few differences. This is an expected result having in mind that the electrons hitting the cathode have a very narrow energy dispersion, which makes them beam-like and with a low mean energy (a few eV), which makes the probability for an emission of a truly secondary electron statistically insignificant

Therefore, using the probabilistic method for numerical simulation of dc magnetrons, although physically consistent and fully compatible with the PIC/MCC technique, could be successfully replaced by a constant RC value, provided that such a value is known from an experiment or theoretical calculations. The advantage of such a replacement is the computational efficiency.

5.4 Conclusion

The possible effect of the electron recapture at the cathode in planar dc magnetrons has been investigated by means of numerical simulations. The results of the simulations indicate that the electron recapture indeed happens when $RC \neq 1$ and

has a significant role in the processes in dc planar magnetrons. This role is manifested to be stronger at lower pressure (4 mtorr) than at higher pressure (25 mtorr). But since often magnetrons are operated at pressures, even lower than 4 mtorr, the question of how the recapture is dealt with in models, theories, and estimates is essential for the correct understanding and prediction of these systems. The effect is not only pressure dependent, but also nonlinear with respect to the *RC* value. The *RC* can be used as a fitting parameter in numerical simulations in order to bring the calculated volt-ampere characteristics and electron densities in closer agreement to the experimentally measured values. In addition, a simple approach based on the assumption of a constant *RC* has been tested against an approach based on a mathematically self-consistent, phenomenological, probabilistic model. The comparison shows that both approaches yield identical results and therefore, the important issue for a correct numerical simulation of a dc magnetron is the knowledge of the value of the *RC*.

Chapter Six

Calculation of gas heating in dc magnetron

6.1 Introduction

The volume in front of the cathode in a sputter magnetron has to be viewed as a highly dynamic region. Except for the main ingredients of the plasma, *i.e.*, charged particles and equilibrium gas atoms, there exist additional energetic species such as reflected, neutralized gas atoms, gas atoms born in charge exchange collisions, and non-thermal sputtered atoms. All of them can participate in momentum transfer collisions with the background gas, cold atoms. These collisions are expected to be highly effective, due to the similar masses of the colliding partners. In this way, significant energy and momentum can be deposited from the energetic species to the volume of the background gas, giving rise to a temperature increase of the gas, and consequently creating a density inhomogeneity through the ideal gas law. It is the density fluctuations that can influence the whole discharge, because of the dependency of the cross sections of all major collisions on the gas density. Most of the energetic species are created either at the cathode (sputtered atoms, reflected and neutralized ions) or in the sheath (atoms generated by charge exchange collisions). This brings a large amount of directionality to the energy and momentum transfer. In addition to that, the distribution of the bombarding fluxes at the cathode is nonuniform. Thus, there can be expected a large degree of nonuniformity in the dynamics of the gas and the sputtered atoms. This particularity of the magnetron operation has been referred to as sputtering wind, a name given first by Hofman [200].

The gas heating and the corresponding reduction of the gas density at a given pressure, also known as *gas rarefaction*, is a function of three factors. The first one is the available energy in the discharge. It depends on the power introduced in the discharge by the external power supply.

The second factor is the ability of the background gas to absorb the available energy. The absorption is via binary collisions and their rate is proportional to the

gas density. Therefore, the two main operating parameters upon which the gas heating depends are the applied power and the gas pressure. This claim has been experimentally confirmed by Rossnagel [115], who reports a maximum gas reduction of 85% at 3 kW input power and by the simulation reported in [201].

Besides the operating conditions, the gas heating is also a function of the type of atoms into consideration. This is the third factor and it is present, because the sputtering yield is material sensitive and so is the reflection coefficient. The latter determines what fraction of the energetic gas atoms will be reflected back into the discharge after hitting the cathode or the vessel walls. This is important, because the mean free path of the gas atoms at typical pressures is about two centimeters and they need several collisions before being thermalized [202].

The possible gas density fluctuations and corresponding energy exchange reactions are important for the energy flux at the substrate and therefore for the film growth quality. Despite that fact, the papers devoted to give a quantitative estimate of the extent and the effect of gas heating in magnetrons are limited. They include the combination of experiment and global energy balance modeling [115], non self-consistent Monte Carlo simulation [203], a theoretical approach [204], a and non self-consistent, fluid heat flow calculation [201]. Only the last work is not one-dimensional. The main uncertainties in these papers are the estimated (assumed) number of collisions, both in the volume and at the cathode, as well as their spatial distribution. This weakness is a direct result of the lack of a model that treats simultaneously and self-consistently the whole magnetron plasma. Such model should give the exact, spatially resolved source terms for the heat transfer, based on the real energy exchange processes. Three such models that fulfill this requirement have been reported. The first one is for sputtering in non-magnetized dc glow discharge [205]. It is a 1d3v PIC/MCC simulation with an incorporated heat module.

The other two are for analytical dc glow discharges in argon [129, 206]. They are, however, not applicable to magnetrons, because they are hybrid models, whereas a kinetic description is necessary to cope with the low pressure and high magnetic field typical for the sputtering magnetrons.

In the present work, a self-consistent PIC/MCC model, suitable for axisymmetric dc sputter magnetrons (cylindrical, 2d3v) and capable of calculating the gas heating and its effects is presented. The model is an expansion of the

PIC/MCC model described in Chapter Three. Calculated results for pressures in the range 1 -100 mtorr will be presented.

6.2 Description of the model

6.2.1 Included species in the model and their collision processes

The present model is based on the general PIC/MCC algorithm, shown in Figure 3.9. The necessity to account for the energetic neutrals requires the inclusion of the fast gas atoms and the sputtered atoms and their ions in the model. Thus the additional species are fast argon atoms (Ar^f), sputtered copper atoms (Cu), singly ionized copper ions (Cu^+), and argon metastable atoms (Ar_m^*). The last are included for their role in the production of copper ions (see Section 2.3.5.2). This brings a new set of collisions to be added to those listed in Table 4.1. They are given in Table 6.1.

Table 6.1 Included collisions (in addition to those given in Table 4.1) and the references for their cross sections or rate constants

Processes		Cross section or Rate (m^3s^{-1})	Ref.
$e^- + Ar \rightarrow e^- + Ar_m^*$	electron-impact excitation	σ(e)	[207]
$e^- + Ar_m^* \rightarrow 2e^- + Ar^+$	electron-impact ionization	σ(e)	[107]
$e^- + Ar_m^* \rightarrow e^- + Ar^*$	electron-impact excitation	σ(e)	[208]
$e^- + Ar_m^* \rightarrow e^- + Ar_r^*$	electron quenching	$k_q = 2 \times 10^{-13}$	[209]
$e^- + Ar^+ \rightarrow Ar_m^* + h\nu$	electron-ion recombination	$k_{rec} = 10^{-17}$	[210]
$e^- + Cu \rightarrow e^- + Cu^+$	electron-impact ionization	σ(e)	[106]
$Ar^f + Ar \rightarrow Ar^f + Ar_m^*$	atom-impact excitation	σ(e)	[108]
$Ar^+ + Cu \rightarrow Ar + Cu^+$	asymmetric charge transfer	$k_{ct}=1.75 \times 10^{-16}$	[110]
$Ar_m^* + Ar_m^* \rightarrow Ar + Ar^+ + e^-$	metastable-metastable	$k_m = 6.4 \times 10^{-16}$	[211, 212]
$Ar_m^* + Cu \rightarrow Ar + Cu^+ + e^-$	Penning ionization	σ(e)	[111]
$Ar_m^* + Ar \rightarrow Ar + Ar$	two-body collision	$k_{2b} = 2.3 \times 10^{-21}$	[113]
$Ar^f + Ar \rightarrow Ar^{(f)} + Ar^{(f)}$	elastic scattering	σ(e)	[213]
$Ar^f + Ar \rightarrow Ar + Ar^+ + e^-$	atom-impact ionization	σ(e)	[108]
$Cu^{(+)} + Ar \rightarrow Cu^{(+)} + Ar$	elastic scattering	σ(e)	[126]

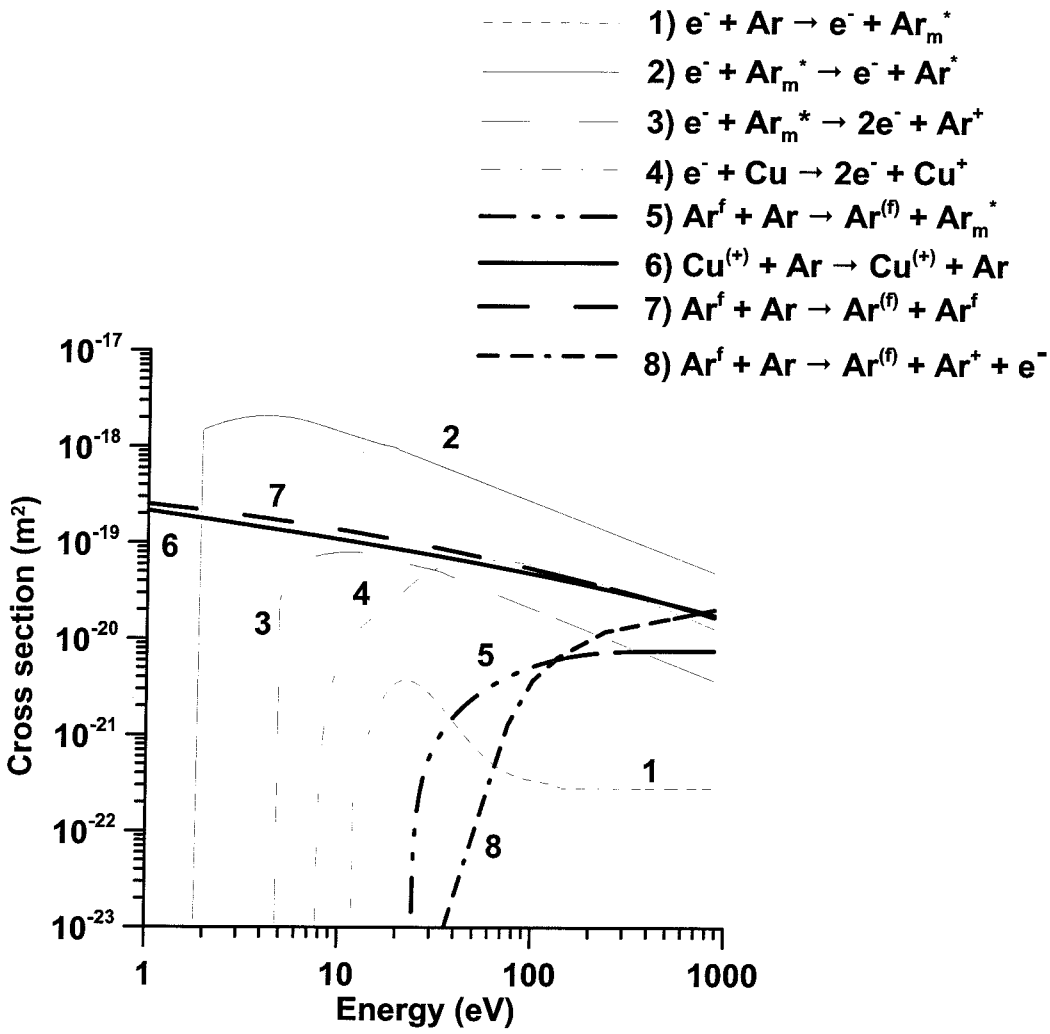

Figure 6.1 Cross sections of the additional collisions included in the model. The thin- line collisions involve electrons: 1) electron-impact excitation of the argon atom to the metastable level; 2) electron-impact transition from the metastable to the irradiative excited state of the argon atom; 3) electron-impact ionization of the metastable argon atom; and 4) electron-impact ionization of the copper atom. The bold-line collisions are between heavy particles: 5) argon atom-induced excitation to the metastable level of the argon atom; 6) elastic scattering of copper atoms and ions from argon atoms; 7) elastic scattering of fast argon atoms and ion with argon background gas atoms; and 8) argon atom-impact ionization of the argon atom.

A discussion about the cross section for Penning ionization has been given in Section 2.3.5.2. The rate constant for asymmetric charge transfer is subject to

significant uncertainty. The problem has been briefly discussed in [110] and latter on elaborated in [214].

The rest of the cross sections from Table 6.1 are plotted in Figure 6.1.

There are also additional surface interactions, taken into consideration. Sputtering caused by fast atoms and copper ions (Cu^+) is added. The process is treated in an analogous way to the sputtering caused by argon ions (Ar^+) (see Section 2.4.3). In addition, secondary electron emission (see Section 2.4.1) caused by the copper ions and the fast argon atoms is included. The deexcitation and the recombination of the metastable argon atoms and the argon ions, respectively, are treated as described in Section 2.4.4). The reflection and possible thermalization of the energetic argon atoms on the surfaces is also explained there. The velocity change in all these plasma surface interactions is given by (2.11) and (2.12). The coefficient of thermal accommodation, α, is defined as [205]

$$\alpha = \frac{E_{inc} - E_{refl}}{E_{inc} - E_{wall}},$$

where E_{inc} is the mean energy of the incident particles (the averaging is made after the incident energy has been reduced with the energy of the sputtered particle and the sputtering threshold energy, providing sputtering has taken place), E_{refl} is the mean energy of the reflected particles, and E_{wall} ($= 2kT_{wall}$) is the energy of the mean energy of the particles leaving the wall after thermal accommodation (k is the Boltzmann constant and T_{wall} is the wall temperature). The thermal accommodation coefficient has been assumed equal to 0.5. Therefore, the results are influenced by that choice. The choice has been made based on the following arguments. There are reported values of α of 0.6 for incident energies of 10 eV and $\alpha > 0.8$ for incident energies higher than 200 eV for Ar^+ ions on Au and Pt surfaces [215]. At low energies, α drops to 0.2 for the same materials. At the same time, thermal accommodation values have been found to be very similar for different metal surfaces [216]. A parametric study of the influence of the value of α on the calculated amount of gas heating in analytical glow discharges [129] has shown that the results are only slightly changed when varying α between 0.5 and 1.

6.2.2 Numerical procedure

As it has been explained in the previous chapters, the PIC/MCC simulation needs to be run until convergence is obtained. This numerical convergence must be correlated to the achieving of steady state by the real physical system that is the subject of the simulation. The time necessary for the physical system to reach a steady state is determined by the slowest processes in the system. When the heating of the gas is taken into consideration, the characteristic time, τ_H, for thermal equilibrium (*i.e.*, bringing the heat conduction to a steady state) is the longest - $\tau_H \sim 10^{-2}$ s. This estimate is based upon the relation [145]

$$\tau_H = \frac{L}{V_H} = \frac{c_p \rho L^2}{k}.$$

Here, L ($\simeq 0.1$ m [79]) is the characteristic diffusion length, V_H is the characteristic speed of heat transfer, c_p is the specific heat per unit mass at constant pressure, ρ ($= 7.97 \times 10^{-5}$ kg/m^3 [217]) is the argon mass density, k ($= 0.018$ Wm^{-1}K^{-1} [217]) is the thermal conductivity of argon.

At the same time, the characteristic time for bringing electrons and ions to steady state does not exceed 10^{-5} s [12]. All other important processes, like the relaxation time for thermalization of the energetic neutrals and pressure equalization are situated in between these two limits [12, 205]. Because of this big difference in the characteristic time steps of the electrons, ions, fast neutrals, and thermal conduction, some modifications in the general PIC/MCC algorithm are necessary to cope with this disparity. Not doing so would result in a huge amount of computational time. This is so, because of the general restriction for the time step (3.21) (see Section 3.2.6).

The procedure used here [205] is to advance the different sorts of particles with different time steps. The hierarchy being $\Delta t_e << \Delta t_i << \Delta t_n$ (e-electron, i-ion, and n-neutral). This difference in the time steps is accounted for by the weight, W of the produced energetic, charge-exchange neutrals and sputtered atoms, *i.e.*,

$$W_n = W_s = W_i \frac{\Delta t_n}{\Delta t_i}, \tag{6.1}$$

where s refers to the sputtered atoms. Electrons are subcycled inside the ion time step (see Section 3.5.1) and have $W_e = W_i$. In this way, it is assured that the production and loss rates of the real plasma particles are correctly represented, *i.e.*, the global mass conservation is obeyed.

The procedure separates the particles into two groups – fast and slow. The upper size of the superparticles from each group can be controlled independently from the corresponding value of the other group. When the upper limit is reached, only the members of the corresponding group are reduced twice, and their weight is doubled. The weight and number of the superparticles from the other group are not changed. However, a change in the time step is needed, in order to maintain (6.1) valid. Because Δt_i is coherent with the stability criterion, the time step that always changes is Δt_n ($= \Delta t_s$).

The heat transfer can occur by conduction or/and convection. Which of the two mechanisms is dominant, if any, is commonly determined by the Peclet number

$$Pe = \frac{V}{V_H} = \frac{c_p \rho V L}{k},$$

where V is the flow velocity and the other symbols have been explained above. A calculation of the flow velocity in conditions similar to those in the present work reads $V \approx 1$ m/s [79]. Based on that, the Peclet number is

$$Pe \approx 0.2.$$

Thus, it can be accepted with a sufficient accuracy that for the given operating conditions the heat transfer is governed by conduction. Deviations from this regime can be expected if the flow of the feeding gas is strong. This, however, is out of the scope of the present work.

The overall cycle consists of one ion time step. At the end of it, the power, P, transferred to and from the feeding gas is accumulated

$$P = \frac{m_g W_n}{V_{cell} \Delta t_n} \left[\sum_l \frac{v_l'^2 - v_l^2}{2} - \sum_l \frac{v_l^2}{2} + \sum_l \frac{v_l'^2}{2} \right], \tag{6.2}$$

where v_l' is the post- and v_l the pre- collision velocity of the l-th gas atom, m_g is the gas mass, and V_{cell} is the volume of the computational grid cell. The first sum is the contribution from all collisions between the feeding gas atoms from one side and the ions, fast atoms, metastable atoms, and sputtered atoms from the other side. Only collisions, in which the postcollision energy of gas atoms is less than some threshold, are counted. This threshold is chosen to be [205]

$$E_{th} = 9 \times 3/2 k_b T_g, \tag{6.3}$$

where k_b is the Boltzmann constant. The other collisions result in creation of fast gas atoms, which are incorporated by the second sum. The third sum is the contribution of the thermalized fast gas atoms. This calculated power is used as a source term in the heat conduction equation

$$\frac{\partial^2 T_g}{\partial z^2} + \frac{1}{r} \frac{\partial}{\partial} \left(r \frac{\partial T_g}{\partial r} \right) = -\frac{P}{k}, \tag{6.4}$$

which is solved once per 10^{-8} s (actually, after each number of time steps divisible exactly by one hundred and which sum is greater than or equal to 10^{-8} s) to calculate the gas temperature, T_g. In the above equation, k is the thermal conductivity of the gas.

It should be mentioned that T_g is a dynamic quantity dependent on the coordinates. Consequently the threshold energy given by (6.3) is also dynamic (changes with time) and is a function of the coordinates.

The sputtered atoms are followed as particles until being thermalized. Once that happens, they cannot anymore contribute to the gas heating directly; collisions between fast argon atoms and sputtered atoms are disregarded in the model, because of the statistical insignificance of the process. The overall copper density, however, is important for the processes of Penning ionization and asymmetric charge transfer. Therefore, a compromise between accuracy of the algorithm and its computational

efficiency is to treat the thermalized copper atoms as a fluid. Thus, the overall copper density is a sum of the density of the fast copper atoms and the slow copper atoms. The density of the slow (thermalized) copper atoms, n_{Cu}^{sl}, can be obtained by solving the diffusion equation, which in (r, z) cylindrical coordinates reads

$$D_{Cu}\Delta n_{Cu}^{sl}(r,z) = r_{loss}(r,z) - r_{prod}(r,z), \tag{6.5}$$

where D_{Cu} is the diffusion coefficient of copper atoms in argon, r_{loss} is the rate of loss of the slow copper atoms, and r_{prod} is their production rate. The diffusion coefficient is obtained from the value $D_{Cu} = 1.44\times10^{-2}$ cm^{2}s^{-1} [218], which is based on the rigid-sphere collision model and refers to a pressure of 1 torr and temperature of 300 K in argon. The recalculation of the diffusion coefficient for the simulation conditions (pressure, p and gas temperature, T_g) is done as

$$D_{Cu}(p) = D_{Cu}(p = 1\text{ torr})\frac{1000}{p[mtorr]}\frac{T_g[K]}{300}$$

The loss rate of the copper atoms, r_{loss} (r, z), is equal to the rate of ionization of the copper atoms, caused by all ionization mechanisms: electron-impact, Penning ionization, and asymmetric charge transfer.

The production rate of the copper atoms, r_{prod} (r, z), is equal to the rate of thermalization of the sputtered atoms.

Equation (6.5), as well as (6.4) is mathematically the same as the Poisson equation for the potential. Therefore, the same numerical technique, cyclic reduction [137], is used for their solution. The boundary conditions of (6.5) are $\nabla^2 n_{Cu}^{sl}\big|_{wall} = 0$ and $\nabla_r\left[n_{Cu}^{sl}(0,z)\right] = 0$. The latter represents simply the cylindrical symmetry of the system.

The procedure described above can be represented by the flowchart in Figure 6.2.

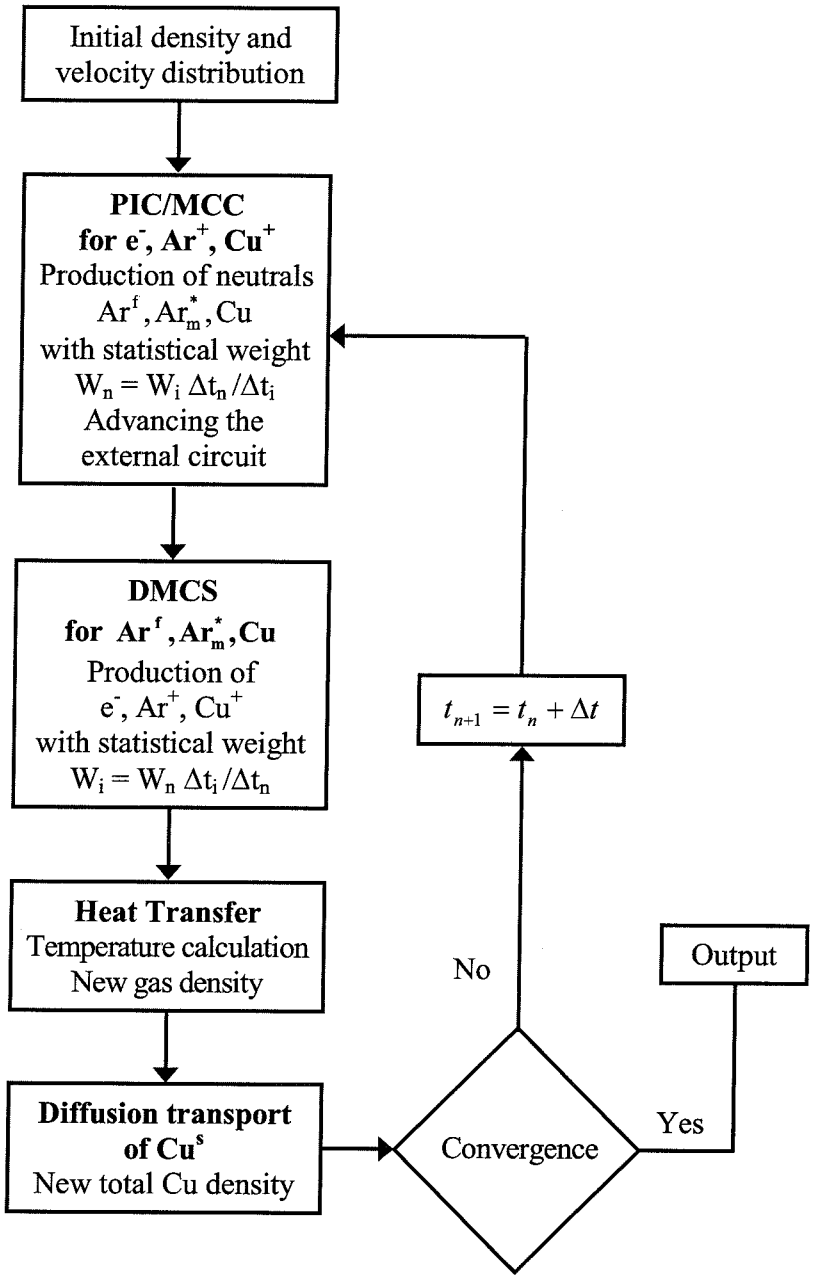

Figure 6.2 Flowchart of the simulation procedure for calculation of the gas heating. The abbreviation DMCS stands for "Direct Monte Carlo simulation".

6.2.3 Initial condition and operating conditions

The simulation procedure shown in Figure 6.2 is applied for the magnetron discharge presented in Figure 4.1. The maximum radial magnetic field above the

cathode reaches 1300 G. Simulations for pressures of 1, 4, 10, 25, 50, and 100 mtorr are performed. To verify the expected pressure dependence of the gas heating, the parameters of the external circuit (see 3.2.4) have been readjusted in the course of the runs to maintain a regime close to constant power. This is illustrated in Figure 6.3.

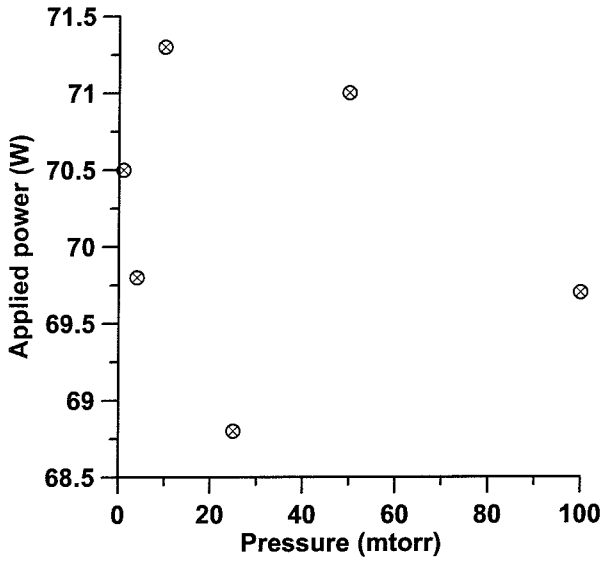

Figure 6.3 Illustration of the quasi-constant power regime. At all pressures, the applied power does not differ by more than 1.8% from the desired value of 70 W.

As it can be seen there, the power is 70 W ± 2%.

The maximum number of superparticles per type is 900000. Initially, only electrons and argon ions are assumed with a homogeneous and equal density of 1×10^{14} m^{-3}. The computational grid has 301 nodes in z-direction and 129 nodes in r-direction. The initial time step is set to 3×10^{-10} s. The number of electronic subcycles per ionic cycle is 40. The simulation is run until convergence is obtained in terms of discharge current and particles' densities. This is illustrated in Figure 6.4, where the time evolution of the discharge (plasma) and external currents is shown.

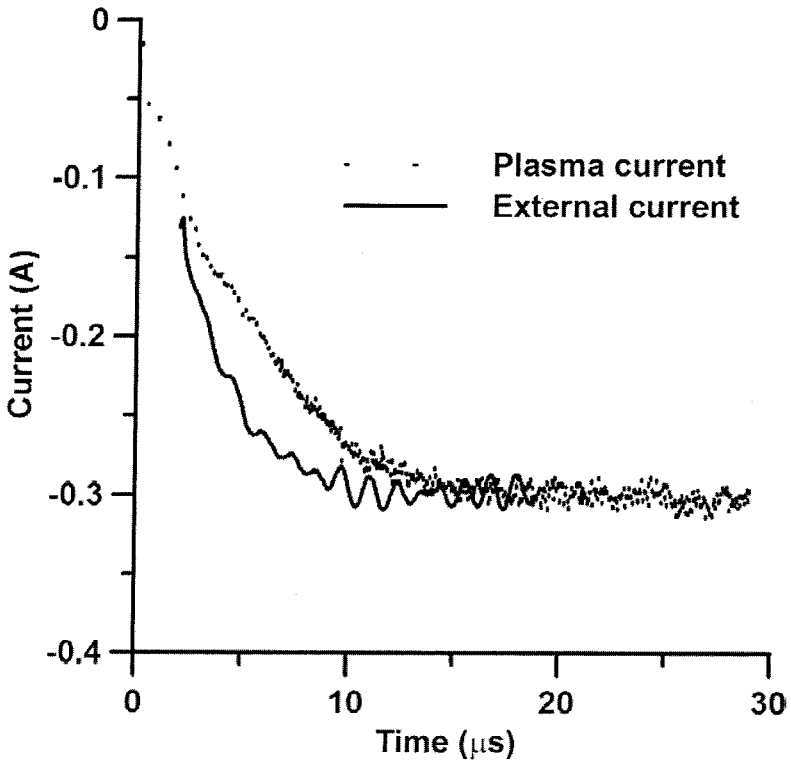

Figure 6.4 Time evolution of the calculated plasma (dotted line) and the external currents for the case of p = 10 mtorr. The steady state occurs at time, $t \approx 15\,\mu s$, when both currents equalize to a value of approximately 300 mA.

To ensure the convergence of the temperature distribution, the maximum gas temperature is traced in time. It is shown in Figure 6.5. It is clear that the relaxation of the maximum temperature occurs at approximately 2 ms. This is about 4 times earlier than the estimate made in the previous section. The difference is less than an order of magnitude and it should be mentioned that the estimate is for total thermal equilibrium, while Figure 6.5 presents only the value of the maximum temperature and not the spatial distribution of the temperature. Therefore, it can be concluded that Figure 6.5 is satisfactory for the purpose of checking for convergence. Note the different time scales in Figure 6.4 and Figure 6.5. This is in connection to (6.1).

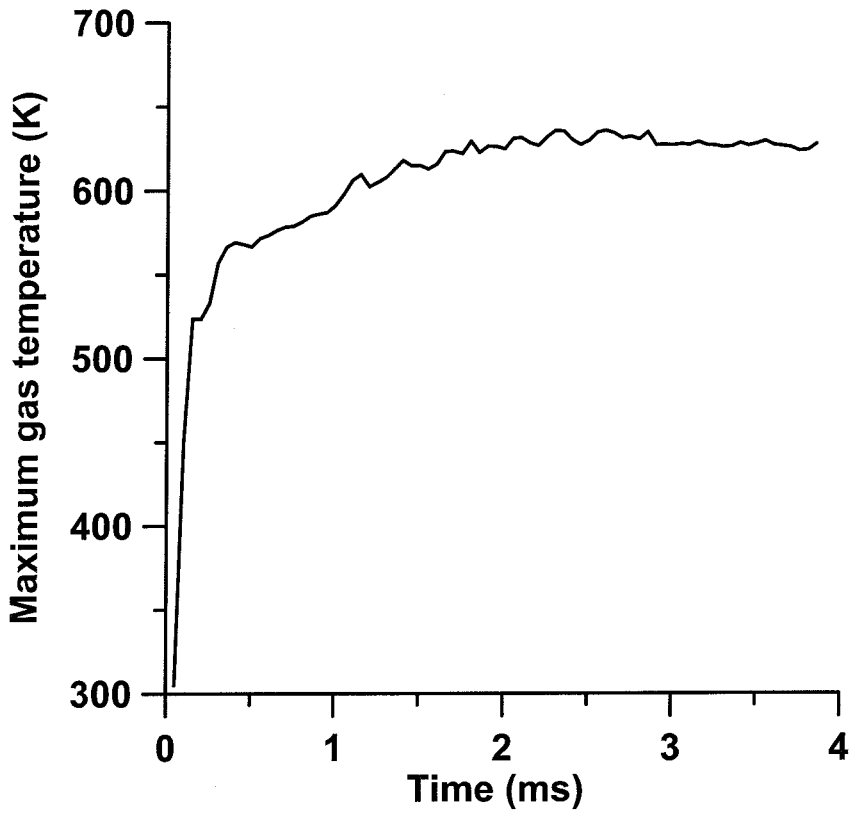

Figure 6.5 Relaxation of the maximum gas temperature with time for the case of $p = 50$ mtorr.

6.3 Results and discussion

6.3.1 Temperature distribution

Following the procedure from Figure 6.2 the temperature distribution of the gas has been obtained for the five different pressures. At 1 mtorr, there is practically no heating of the gas. The rise of the gas temperature is about 1K, which is within the limit of the expected errors. With the increase of the pressure, the gas begins to heat up. For $p = 10$ mtorr, the temperature increases to 316 K, which is about 5%, as can be seen in Figure 6.6. With the increase of the pressure, holding the input electrical power constant, the temperature strongly increases farther, being about 600 K at 50 mtorr, and reaching almost 1000 K at 100 mtorr (see Figure 6.7 and

Figure 6.8, respectively). The increase of the maximum gas temperature with pressure is also illustrated in Figure 6.9.

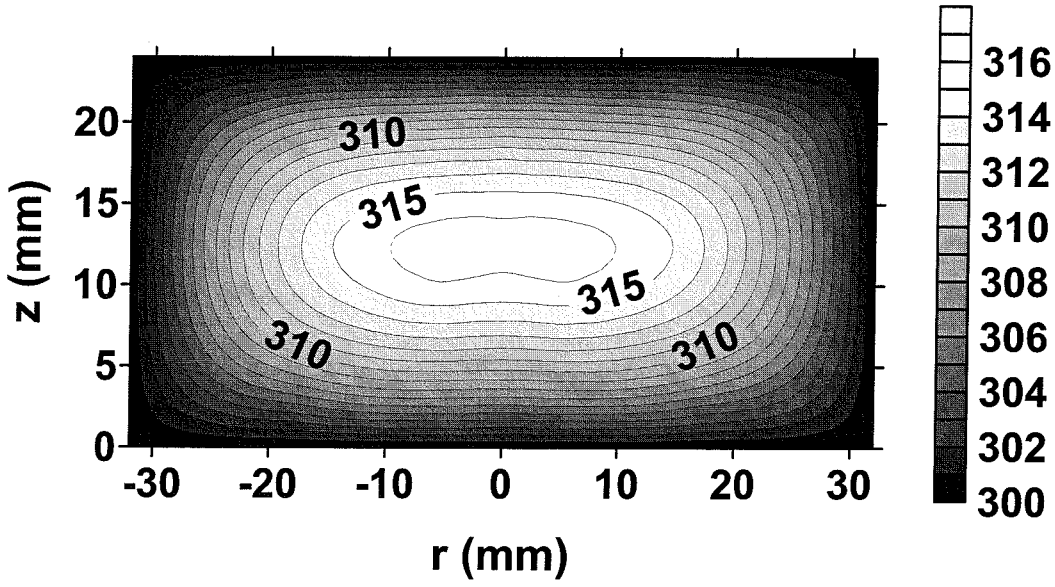

Figure 6.6 Contour plot of the calculated gas temperature distribution for the case of p = 10 mtorr.

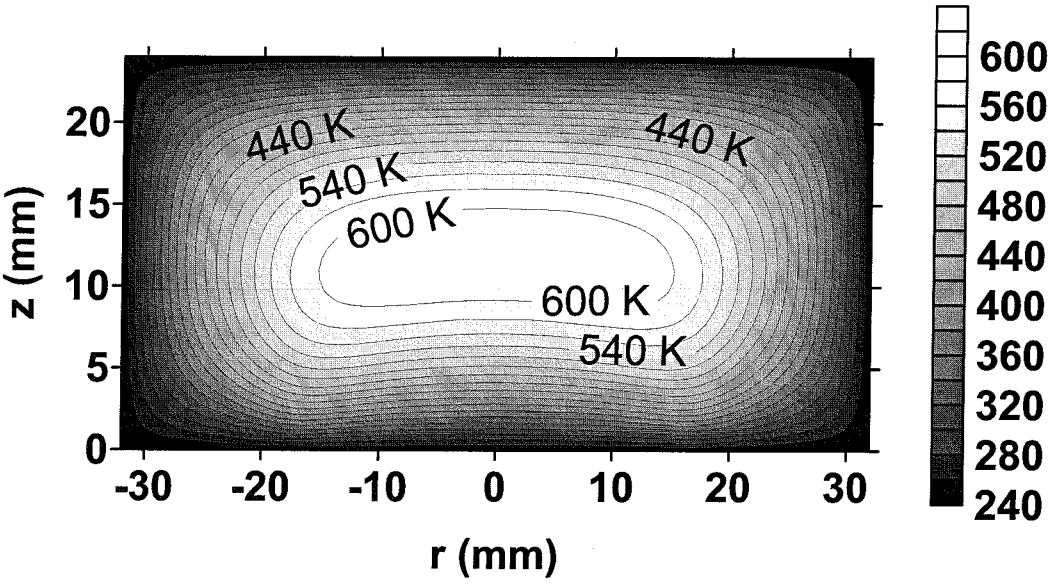

Figure 6.7 Contour plot of the calculated gas temperature distribution for the case of p = 50 mtorr.

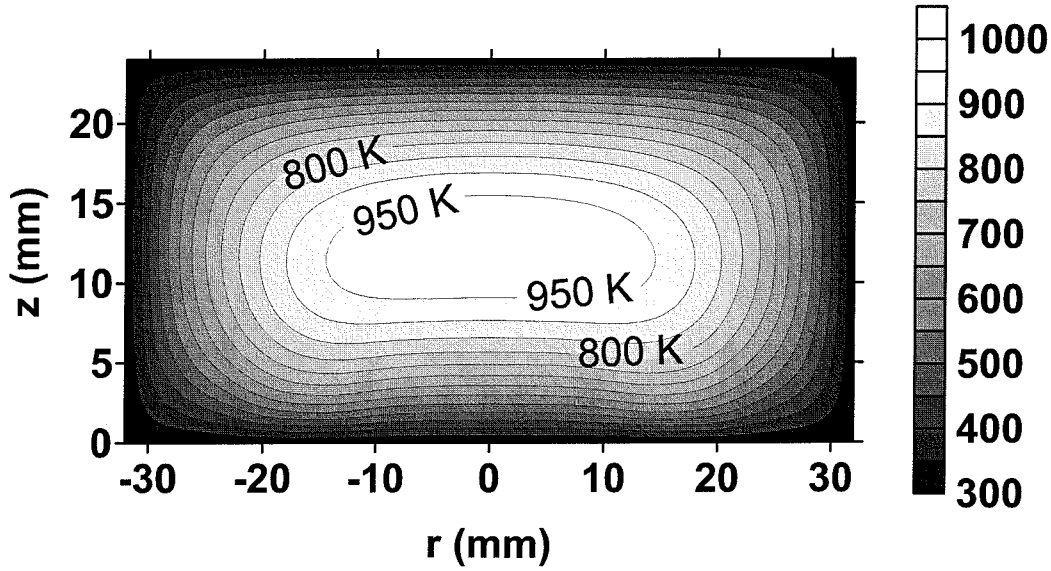

Figure 6.8 Contour plot of the calculated gas temperature distribution for the case of p = 100 mtorr.

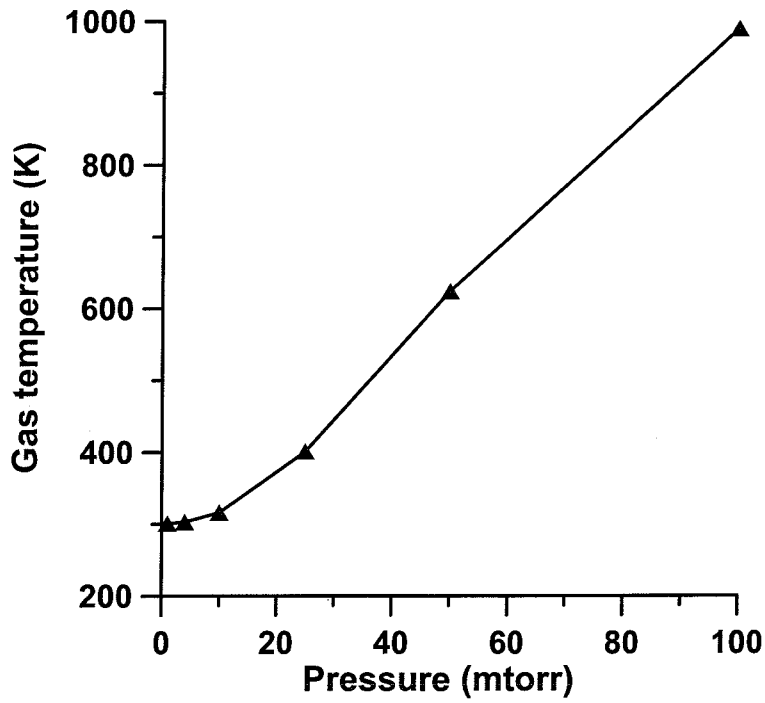

Figure 6.9 Calculated maximum gas temperature as a function of the gas pressure at constant electric power. The symbols demote the calculated values.

The presented results show that the gas heating is strongly pressure dependent. For the given operating conditions: feeding gas argon, copper cathode, and input power of 70 W, the gas heating is not significant for pressures of up to 10 mtorr. These are typical conditions for laboratory magnetrons. Commercial sputtering magnetrons may be up to 10 times bigger and with power supplies of several kW. These operating conditions, however, are outside the scope of this study.

It is interesting to compare the obtained results with other data from the literature. The results for p = 50 mtorr can be compared to [205], where the gas heating in a sputtering glow discharge is calculated for p = 42 mtorr and 40 mm electrode separation. The temperature profile obtained there for a copper electrode and three times higher cathode voltage agrees very well with the gas temperature profile calculated in the present study. The lower voltage in the present case can be easily explained with the magnetic trap leading to much higher discharge efficiency, and to some extent with the smaller volume of the gas discharge.

Another comparison can be made with [115]. It is the most often cited work in the literature about the gas heating in sputter magnetrons. The author reports a density reduction of about 37% for a pressure of 30 mtorr and a current of 300 mA. This corresponds reasonably well to our calculation results. Indeed, it can be deduced from Figure 6.9 that the gas temperature at 30 mtorr would be around 440 K, which is about 47% than 300 K.

More substantial is the difference with the calculations reported in the recent work of Epke and Dew [201]. The maximum temperature there is on average a factor of two higher than the values obtained in our study. In addition, the axial temperature profile is with a different shape. The values of the gas temperature in [201] are also higher than those in [115]. The shape of the profile in [201] resembles those obtained for analytical glow discharges in [129]. The common issue between these two models is that they are entirely or partially fluid. In addition, [201] is not a self-consistent simulation, but based on several assumptions, each of which brings uncertainties.

The resemblance in the profile shapes (see Figure 6.10) and the close correspondence of the absolute values of the present work with the kinetic simulation [205] and the early experimental work [115] indicate that a kinetic self-

consistent simulation represents more accurately the considered effect of gas heating in sputter magnetrons at typical operating conditions.

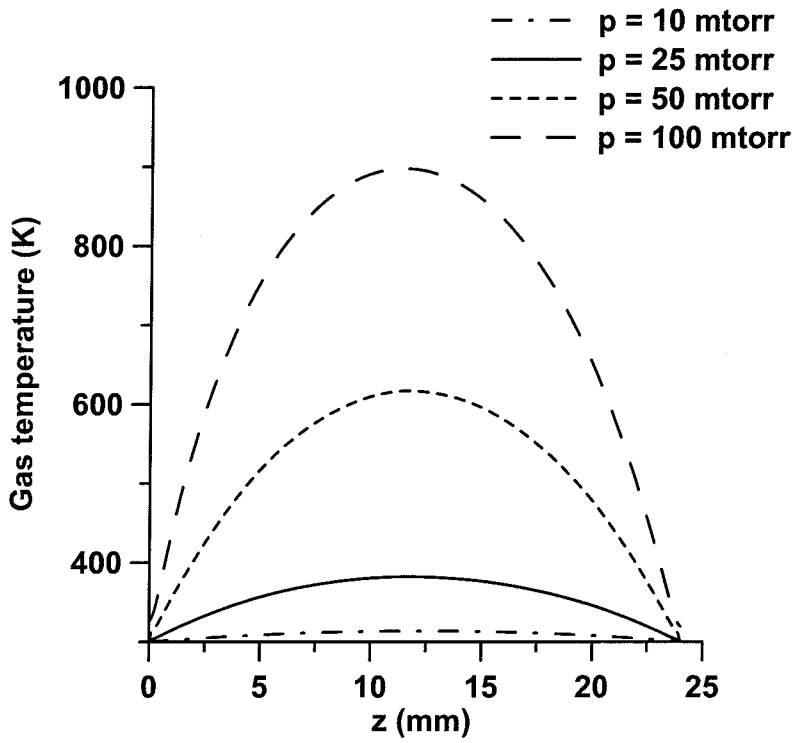

Figure 6.10 Calculated gas temperature profile above the racetrack along r = 18.2 mm for different values of the pressure.

6.3.2 Analysis of the power transferred to the gas

Each plasma particle that collides with the gas atoms can transfer power to the gas. Here, the power transfer is counted as positive with respect to the gas if it leads to increase of its temperature. This means that the power transferred to the gas, which results in the creation of energetic (non-thermal) gas atoms is counted as negative, because it actually absorbs thermal energy from the gas [see (6.2)] . As it has been discussed in Section 6.2.2, this separation is sensitive to the thermal limit, (6.3) above which the atoms are considered energetic. This formalism leads to the following consequences. A fast heavy particle needs several interactions with the background gas atoms before it can directly contribute to gas heating. This means

that during the first several collisions, the result will be not rising the gas temperature, but creating fast gas atoms. These fast atoms subsequently collide with the thermal atoms and contribute directly to the gas heating. This leads to enlargement of the region where the power is transferred effectively to the gas.

The total power input, summed over all contributors, is pressure dependent as can be seen in Figure 6.11. The power deposition is almost constant with respect to the distance from the cathode at low pressure, whereas with the increase of the pressure, more power is deposited near the cathode. This is explained with the change in the proportion that each type of plasma species has in the total power. For example, sputtered atoms thermalize much faster at higher pressure and their direct contribution to the total power increases (Figure 6.13). The same holds for the ions. When they accelerate in the sheath at low pressure, they mostly create energetic neutrals, which is counted as cooling of the gas (Figure 6.13). For the time of their fall to the cathode, the ions cannot suffer enough collisions to begin to contribute to the deposited power directly. At high pressure, however, more ions can directly contribute to the gas heating, as shown in Figure 6.14.

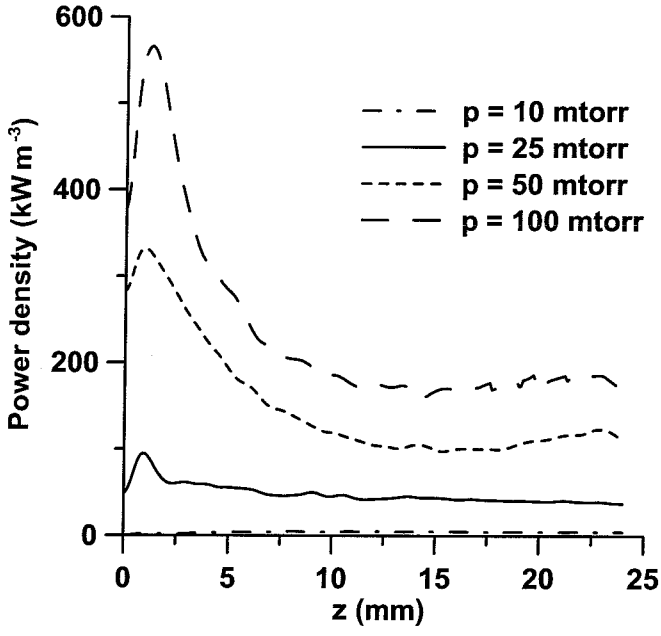

Figure 6.11 Calculated axial distribution of the total power density deposited in the gas along $r = 18.2$ mm for different values of the pressure.

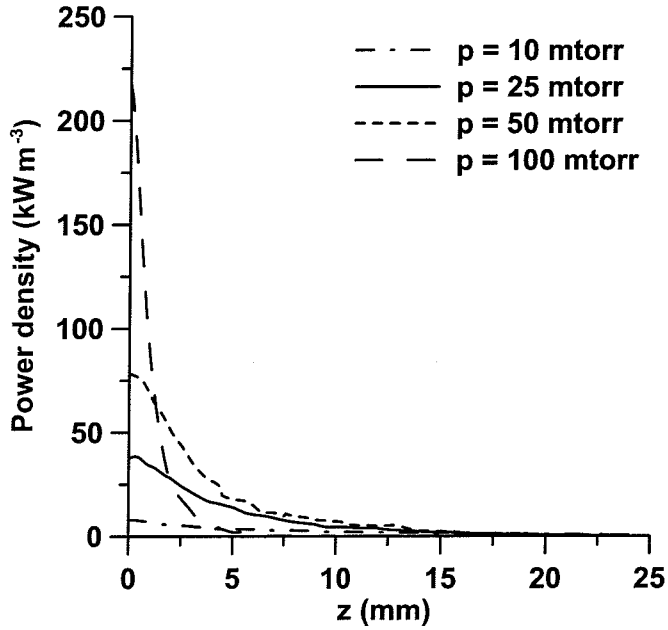

Figure 6.12 Calculated axial distribution of the power density deposited by sputtered copper atoms in the gas along r = 18.2 mm for different values of the pressure.

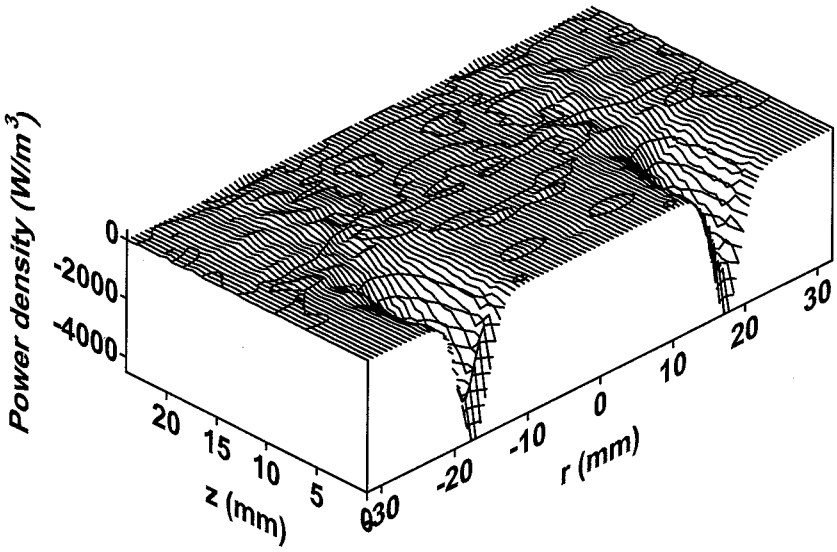

Figure 6.13 Calculated distribution of the power density transferred from the ions (Ar^+ and Cu^+) for the case of p = 10 mtorr. Note that the value is negative at this low pressure, indicating that the ions mostly create energetic atoms near the cathode, which is counted as cooling of the gas.

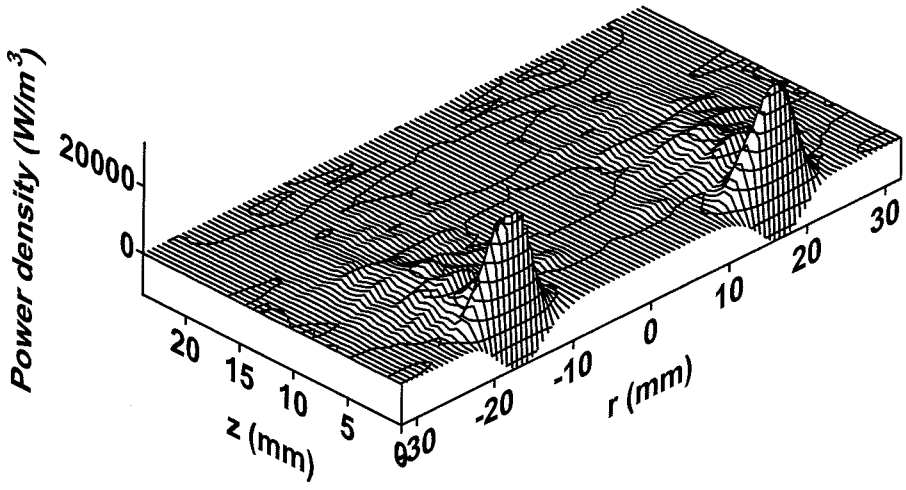

Figure 6.14 Calculated distribution of the power density transferred from the ions (Ar^+ and Cu^+) for the case of p = 100 mtorr. Now the value is mostly positive, indicating that the ions now directly contribute to gas heating in the sheath.

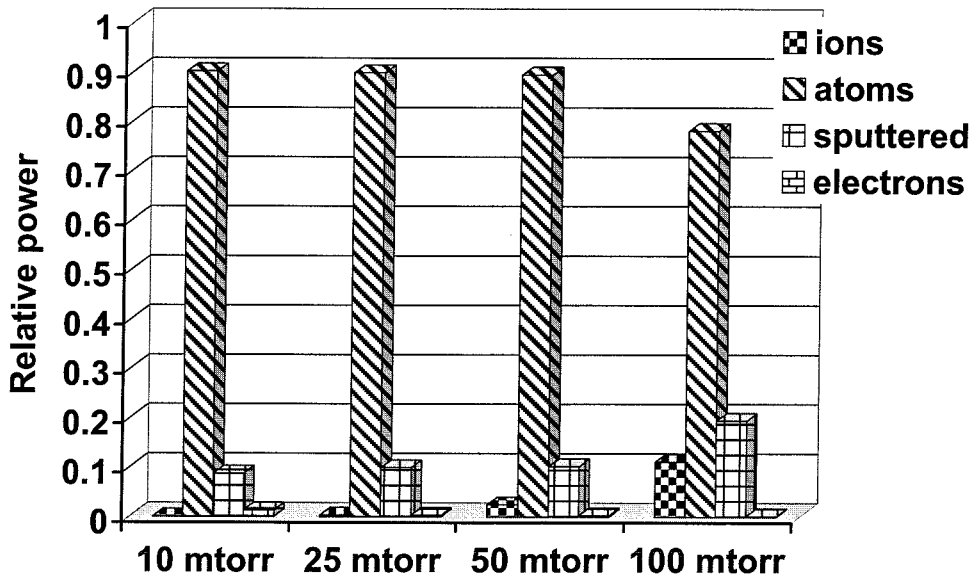

Figure 6.15 Calculated relative contribution to the total power transferred to the argon gas (integrated over the whole discharge) for ions, atoms, sputtered atoms, and electrons for different pressures.

The power, integrated over the whole discharge, deposited by the different plasma species as a function of the pressure is presented in Figure 6.15. It is clear that for all pressures the collisions between argon atoms are the main contributors to the gas heating. This means that ions and sputtered atoms transfer their energy to the thermal gas atoms mostly indirectly. At low pressure, the ions transfer more energy to energetic gas atoms than to the thermal gas atoms. That is why their relative contribution to the heating is lower than that of electrons, even though the mass of the latter is so much smaller. This result shows the necessity of the inclusion of the fast neutrals in models when the gas heating should be accounted for.

Chapter Seven

Numerical study of dc magnetron sputtering

7.1 Introduction

The process of sputtering – releasing of atoms and ions from a solid target by bombardment of energetic particles has been explained in detail in Section 2.4.3. Sputtering and more precisely its magnetically enhanced version is the main reason for the wide use of dc magnetrons as sputter sources. Sputter magnetrons, however, are not only sputter sources, but are also responsible for the deposition of thin films on different materials. Thus in one chamber, two opposite processes occur: sputtering and deposition. An efficient sputter magnetron, used for deposition, must provide high sputtering rate and high quality of the deposited film. Unfortunately, such important operating condition as the pressure influences the sputtering yield and the quality of the film in opposite ways. Generally, the higher the pressure, the higher the sputtering yield, though the increased pressure facilitates the return of part of the sputtered material back to the target (redeposition). The higher pressure, however, obstructs the transport of the sputtered material to the substrate where the film is deposited, because of the increased number of collisions between the sputtered atoms and the rest of the plasma species. This decreases the efficiency of the process of deposition. The magnetic confinement in magnetrons allows achieving a high sputtering yield at relatively low pressures, but brings the question of target utilization. Due to the magnetic confinement, only a small part of the target (the cathode) is bombarded intensively and the whole target must be replaced much more often than in the case of non-magnetic sputtering. The prediction of the life of the target at given operating conditions is of great importance for the industry as is the choice of these conditions. The above discussion shows that the achievement of optimal conditions for sputter deposition needs a quantitative estimation of all processes occurring in the magnetron chamber as a function of the operating conditions. A possible way to obtain such estimation is by means of numerical modeling. Most often, this is done by non self-consistent Monte Carlo simulations.

The drawbacks there are related to the fact that the spatially resolved energy distribution of the bombarding flux at the cathode is not known and needs to be estimated. Having in mind that this distribution is highly inhomogeneous, it can be expected that the estimate might not be very accurate. The rest of this Chapter presents the results of a PIC/MCC survey of a laboratory dc sputtering magnetron at various operating pressures for a copper target.

7.2 Description of the model

The model used to describe the behavior of the sputtered species is essentially the same as the one described in Chapter Six, but with some modifications. The included collisions and their cross sections or rate constants are given in Table 4.1 and Table 6.1. The cross sections are shown in Figure 4.2, Figure 4.3, and Figure 6.1. The sputtering yield is calculated according to (2.10) and the explanation of the quantities included there is given in Section 2.4.3. The flow chart of the simulation is as in Figure 6.2 with the following difference. The copper atoms are not split into two groups: fast and thermalized atoms, but are all considered particles. This is done to resolve the energy and angular distribution of the incident sputtered flow at the substrate. Thus, the transport of the copper atoms is solved entirely kinetically and the diffusion equation from Figure 6.2 (the bottom box on the left side) is not solved. The copper atoms are followed until they reach the substrate or sidewall, return to the cathode (redeposition), or are ionized.

As in Chapter Six, different weights are used for the charged and the neutral particles. The relation between the weights is given by (6.1) and the necessity to use different weights is discussed in Section 6.2.2.

Two phenomena influence the sputtered flux distribution at the substrate at given operating conditions. These are the initial energy and angular distribution at the cathode after sputtering and the scattering angle in the Cu - Ar elastic collisions. To investigate how important these factors can be, simulations with isotropic and anisotropic scattering are performed at different pressures. The anisotropic scattering is performed according to (3.69). All the discussion referring to (3.69) is given in detail in Section 3.4.3.

As it has been illustrated in Chapters Four through Six, the structure of the planar magnetron is highly inhomogeneous and with axial symmetry. The main processes occur in a segment distant enough from the center of the cathode (the

origin of the cylindrical coordinate system). As it is known, the use of an equidistant grid in r-direction may cause some problems in the region close to the origin. The nature of the problems is the rapid decrease of the volume of the grid elements, with decreasing r. The above-mentioned concentration of the main phenomena in the planar magnetrons away from the origin, however, allows the use of an equidistant grid in r-direction, which is computationally much less intensive.

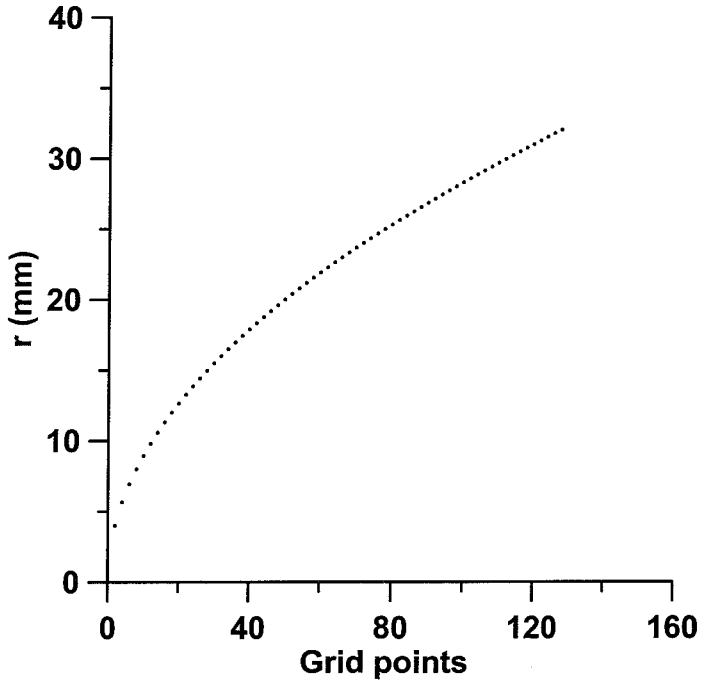

Figure 7.1 Illustration of the non-equidistant grid in r-direction. The surface between every two neighboring grid points is equal.

This situation changes when information on the distribution of the sputtered atoms, especially at the substrate, is desired. The reason for that is simply the neutrality of the atoms. They feel neither the electric, nor the magnetic fields, which create the inhomogeneity. Therefore, the sputtered atoms are not restrained to a region away from the origin. Using an equidistant grid then can distort significantly the statistics. That is why a non-equidistant grid is used in this simulation. The grid points are chosen so that the surface elements that fall between them have an equal surface. The distance between two grid points then decreases as $1/r^2$ when r increases. This is illustrated in Figure 7.1.

7.3 Results and discussion

All presented here results refer to the magnetron shown in Figure 4.1 (see Chapter Four). The simulations are performed in a constant power regime of about 160 W. The deviation from that value did not exceed 7%.

7.3.1 Bombarding fluxes at the cathode

All presented here results refer to the magnetron shown in Figure 4.1 (see Chapter Four).The heavy particles that bombard the cathode are the argon ions and atoms and the copper ions. Some copper atoms can also return to the cathode, but their energy is normally below the threshold for sputtering. In principle, all of the heavy particles can cause sputtering. Their relative contribution to the sputtering depends on the intensity of the corresponding bombarding fluxes and on their energies. The latter is a result of the existence of a threshold energy, under which the sputtering does not occur (see Section 2.4.3 and Figure 7.2). The dependence of the sputtering yield on the incident energy is shown in Figure 7.2, calculated according to (2.10).

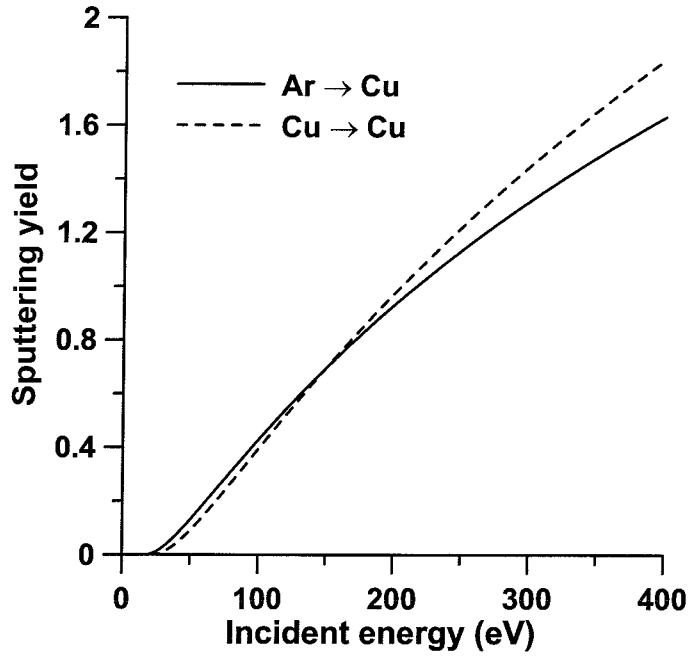

Figure 7.2 Sputtering yield for a copper target as a function of the incident energy according to [125]. Dashed line: Cu atoms; solid line: Ar atoms.

As seen there, significant sputtering occurs for incident energies from about 150 eV, for which the value of the sputtering yield is above 0.6.

The calculated bombarding fluxes of the Ar atoms, Ar^+ ions, and Cu^+ ions as a function of the pressure at constant power of 160 W (*please give also the corresponding voltage and current; this information is really interesting to include!)* are shown in Figure 7.3, Figure 7.4, and Figure 7.5, respectively. Note that only fast argon atoms are considered, *i.e.* with kinetic energies above the thermal threshold defined in (6.3) (see Section 6.2.2). This is not a limitation, because the thermal threshold energy is lower than the sputtering threshold energy.

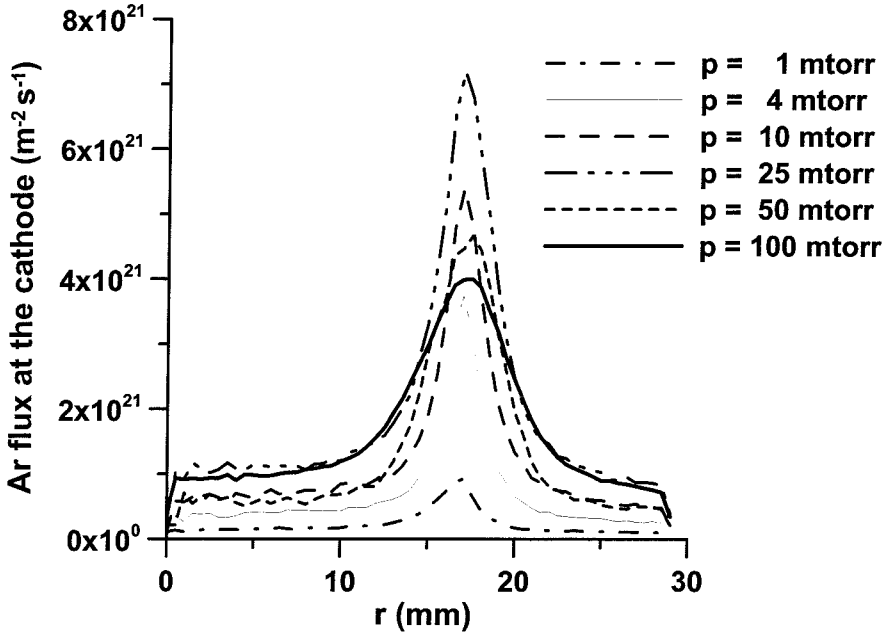

Figure 7.3 Calculated fast Ar atom flux at the cathode for different values of the gas pressure. As fast atoms are considered those, which energy is above the thermal threshold energy, discussed in Chapter Six [see equation (6.3)].

The bombarding fluxes of all types of particles are localized in the region, where the radial component of the magnetic field is strongest, *i.e.*, around $r = 18$ mm. The flux of the Ar^+ ions is most localized in the radial direction, followed by those of the Cu^+ ions. The flux of Cu^+ ions is more spread, because of the fact that a fraction of the Cu^+ ions is produced by Penning ionization, which is

not as localized as the electron-impact ionization. The latter is almost entirely responsible for the creation of the Ar^+ ions.

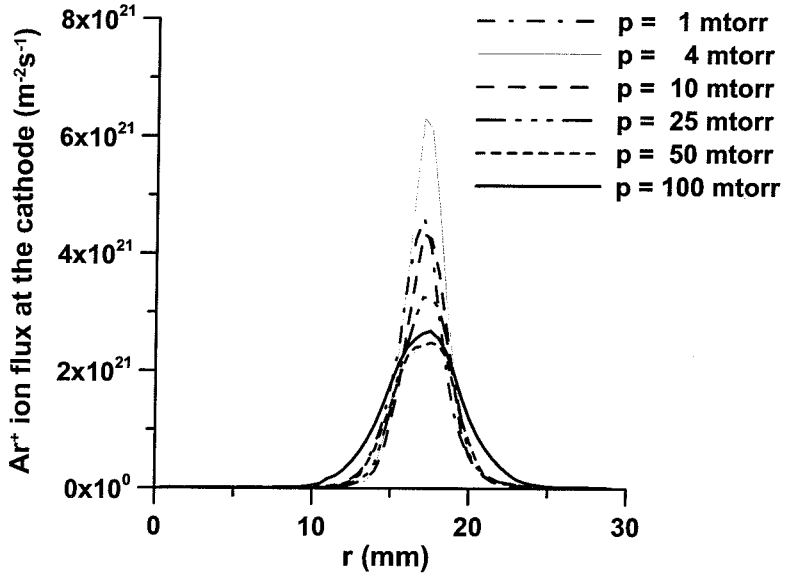

Figure 7.4 Calculated Ar^+ ion flux at the cathode for different values of the gas pressure.

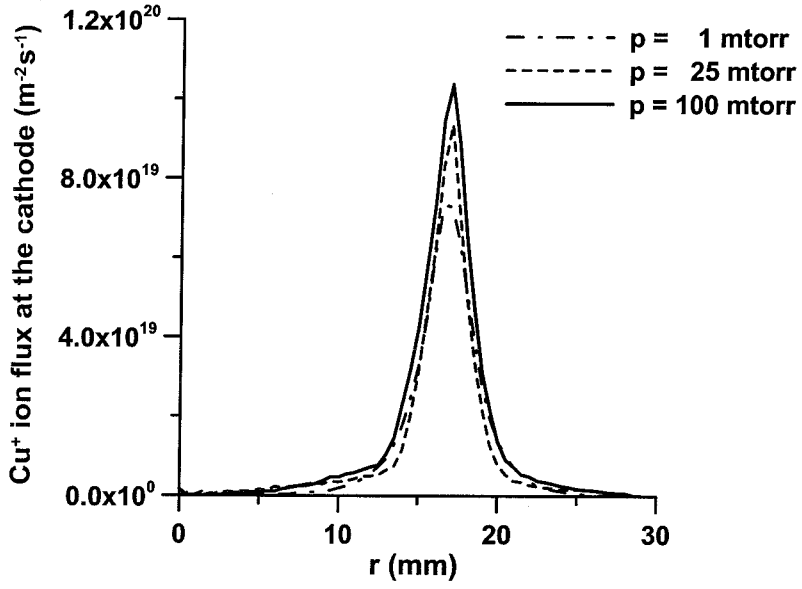

Figure 7.5 Calculated Cu^+ ion flux at the cathode for different values of the gas pressure. The fluxes corresponding to pressures of 4, 10, and 50 mtorr lie within the limits of the graph and are omitted for clarity.

The flux of Ar, although with a maximum approximately identical to the Ar^+ flux, spreads over the entire cathode (the target). The localized part of the flux originates from symmetric charge transfer collisions (see Section 2.3.4.1.2), whereas the part that is located outside of the maximum is related to Ar – Ar elastic collisions.

The magnitudes of the Ar^+ and Ar fluxes are very close, whereas the magnitude of the Cu^+ flux is almost two orders of magnitude lower. The latter corresponds to the ratio of the densities of the argon gas and the copper atoms in the discharge.

The maximum of the Ar^+ flux first increases with pressure (the maximum calculated value corresponds to $p = 4$ mtorr) and then decreases, while at the same time the flux becomes more spread in the radial direction (see Figure 7.4). This trend can be explained with the increase of the ionization rate with pressure at low pressures. At higher pressures, the rate of the symmetric charge exchange collisions plays a more significant role and neutralizes the effect of the increased ionization.

Similar is the picture for the Ar atom flux (see Figure 7.3). The maximum of their flux at the cathode, however, corresponds to $p = 25$ mtorr.

For both Ar^+ and Ar fluxes, their magnitude at higher pressures is also influenced by the gas density reduction caused by the gas heating (see Chapter Six and Figure 6.10).

As it has already been mentioned, the sputtering is also a function of the energies of the bombarding fluxes. For that reason, the calculated mean energies of the bombarding Ar atoms and Ar^+ ions are presented in Figure 7.6 and Figure 7.7, respectively. The mean energy of the Cu^+ ions (not presented here) has a similar radial distribution. However, its maximal values are only slightly lower than the applied potential. This is in accordance with the results obtained for a hollow cathode discharge [219] and represents the difference in the cross section of the elastic scattering of Ar^+ and Cu^+ from Ar (see Figure 4.3 and Figure 6.1, respectively) as well as the difference in mass between Cu+ and Ar^+.

The mean Ar atom energy decreases from about 100 eV at $p = 1$ mtorr to about 16 eV at pressures above 25 mtorr, above the racetrack. It is natural to expect that the mean energy will decrease more or less monotonically with the rise of pressure due to the increasing probability for elastic collisions. The fact that the

mean energy is approximately the same in the pressure range 25 – 100 mtorr can be attributed to the increase of the symmetric charge transfer rate with pressure as well as to the gas density reduction.

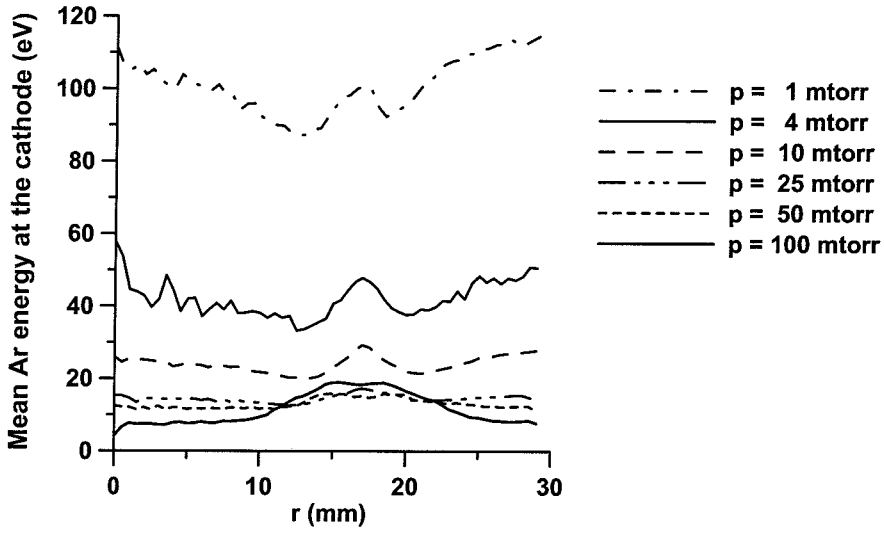

Figure 7.6 Calculated distribution of the mean Ar atom energy at the cathode for different values of the pressure.

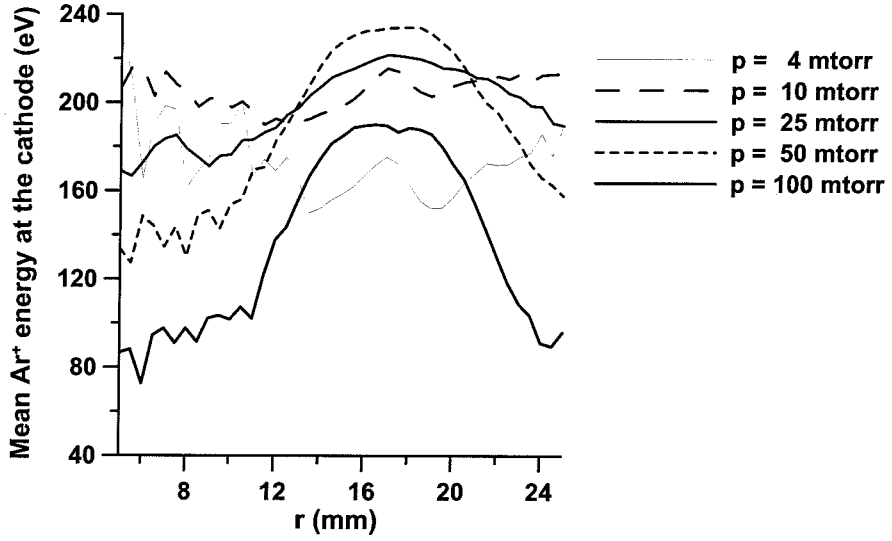

Figure 7.7 Calculated distribution of the mean Ar^+ ion energy at the cathode for different values of the pressure. The mean energy for p = 1 mtorr is very similar to that for p = 4 mtorr and is omitted for clarity[1].

[1]In the region $r < 5$ mm, due to the very low Ar^+ flux, the results are statistically not relevant and for this reason are not presented,

Thus at higher pressure, the Ar atoms are not expected to have a significant influence on the sputtering (see Figure 7.2), although their flux at the cathode is approximately of the same magnitude as that of the Ar^+ ions (see Figure 7.3 and Figure 7.4).

The Ar^+ ions, however, possess enough energy at all pressures studied here for efficient sputtering of the target. The same is true for the Cu^+ ions, but since their flux is about 100 times lower than the Ar^+ flux, it is expected that the Cu^+ ions will have very little importance for the sputtering at the studied operating conditions.

In our model, the sputtering events are calculated based on the computing of the sputtering yield according to (2.10), each time when a heavy particle strikes the cathode. The yield computed in this way is considered as the probability for sputtering and it is compared to a uniformly distributed random number. If the random number is lower than the sputtering yield, an atom is sputtered from the target. As it follows from Figure 7.2, the sputtering yield can be larger than one. In this case, there is always one sputtered atom. In addition, the sputtering yield is reduced by one, and the remainder is compared to a random number to check whether a second sputtered atom is being released. This approach is fully consistent with the principle of detailed equilibrium.

7.3.2 Sputtered flux from the cathode

When calculating the sputtering flux from the cathode, the Cu atoms that return at the cathode as a result of elastic collisions are considered absorbed and counted with a minus sign in the sputtered flux. Therefore, the calculated sputtered flux is the net flux equal to the number of the sputtered atoms minus the number of the returned (redeposited) atoms. It is shown in Figure 7.8 for different values of the pressure. The net flux is at maximum at $p = 4$ mtorr and has a maximum value of 6.3×10^{23} $m^{-2}s^{-1}$, which is about 50% more than the maximum value at $p = 1$ mtorr. With further increase of the pressure, the maximum of the sputtered flux decreases and at $p = 100$ mtorr it is one third of that at $p = 4$ mtorr. With the increase of the pressure, the sputtered flux becomes more spread in the radial direction, which can lead to better utilization of the target. However when the choice is for most intensive sputtering, the optimal pressure range appears to be 1 – 10 mtorr.

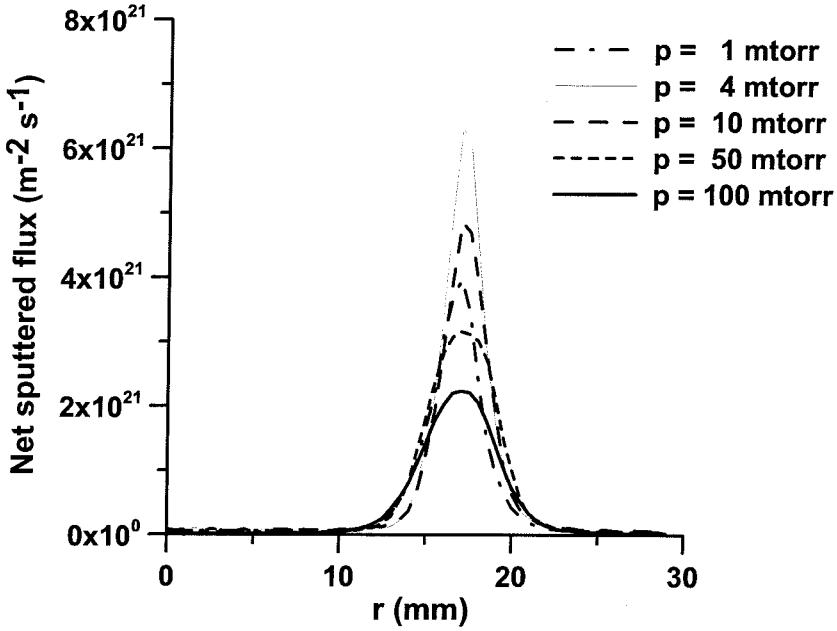

Figure 7.8 Calculated net sputtered flux from the cathode for different values of the gas pressure. The data for p = 25 mtorr is omitted for clarity.

Having the value of the net sputtered flux from the cathode, the erosion profile can be calculated, based on the relation [220]

$$EP = J_{sput}^{net} \frac{M}{N_A \rho} t, \tag{7.1}$$

where EP [cm] is the depth of the erosion profile , J_{sput}^{net} [cm^{-2}s^{-1}] is the net sputtered flux , M [g/mol] is the atomic weight and ρ [g/cm^3] is the mass density of the target, and finally t [s] is the period of sputtering. The copper density is equal to $\rho_{Cu} = 8.92$ g/cm^3 [221].

To validate the calculated results, the erosion profile at $p = 10$ mtorr is calculated according to (7.1) and compared to the experimentally measured erosion profile for similar pressure ($p_{exp} = 10.65$ mtorr) [181]. The latter has been obtained after 4.5 hours of sputtering at constant current regime. The present simulation is

performed in constant power regime, but the maintained power is the same as in the experiment. Both normalized profiles are shown in Figure 7.9.♦

The comparison shows very reasonable agreement. The location of the measured and calculated erosion craters coincides within 0.3 mm. This can easily be attributed to the possible error in the measurement of the magnetic field, which is an input for the model. The central part of the crater agrees also very well. Some deviation in the erosion depth is observed at the periphery of the crater. The measurements show some net redeposition in the region, $r < 8$ mm. Our results do not show redeposition in this region. This fact, as well as the generally smaller agreement in the periphery of the crater provokes a discussion about the collision cross section of the Cu – Ar elastic collisions and the scattering angle in the Ar – Ar collisions, which may influence the directionality of the argon atoms. As a whole, the agreement can be considered enough for validating the model.

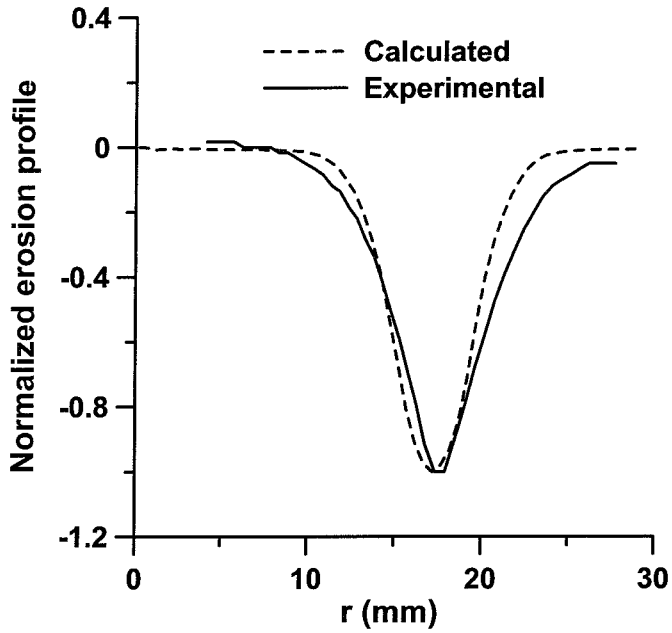

Figure 7.9 Calculated (dashed line) and measured (solid line) normalized erosion profiles [181] for p = 10 mtorr.

♦ Experimental data were available as normalized values. For this reason, the comparison here is of the normalized erosion profiles.

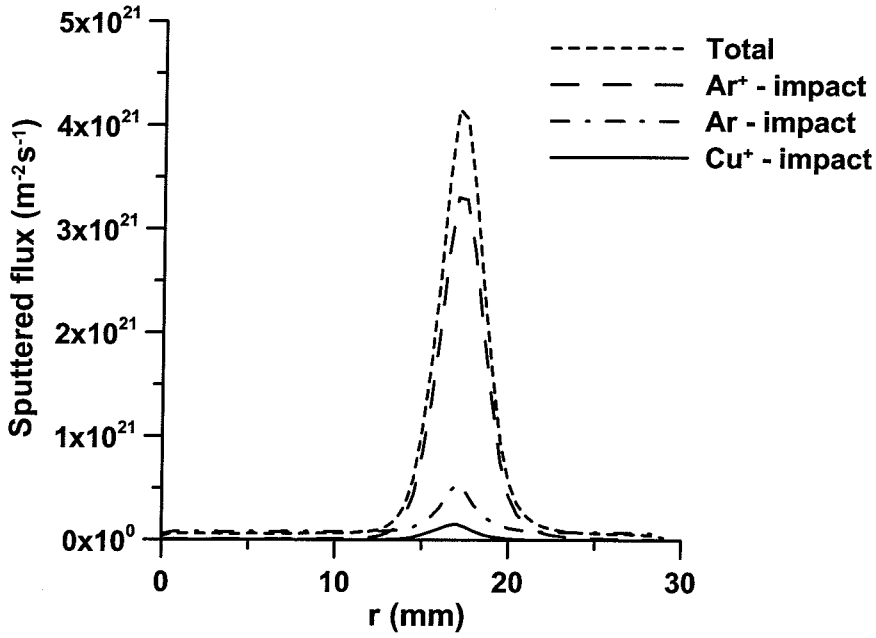

Figure 7.10 Calculated contribution of the different species to the sputtering flux from the cathode for p = 10 mtorr.

The calculated contribution of the different bombarding species is presented in Figure 7.10 for $p = 10$ mtorr. These results are representative for all pressures. The most efficient sputtering is caused by the Ar^+ ions, which are responsible for 83% of the sputtered copper atoms. The contribution of Ar atoms is about 13%, whereas the Cu^+ ions contribute only for about 4% of the total sputtering

In other types of discharges, like analytical glow discharges and hollow cathode discharges, where sputtering also takes place, it has been reported that significant redeposition of the sputtered atoms can occur. In the first group of discharges, a redeposition of 57% has been calculated [47] at a pressure of 75 Pa. In the second group, the redeposited atoms have been calculated even to exceed the sputtered atoms at given areas of the cathodes [222] at a pressure of 300 mtorr. At our operating conditions (*i.e.*, p < 100 mtorr), the rate of redeposition, caused by backdiffusion, is much lower. It is at maximum at p = 100 mtorr, where it is about 7% of the total sputtered flux. At p = 1 mtorr, it is only 0.1 %. Therefore, redeposition can be neglected at typical operating conditions for sputtering magnetrons, according to our calculations.

The calculated rate of redeposition for three different pressures is shown in Figure 7.11.

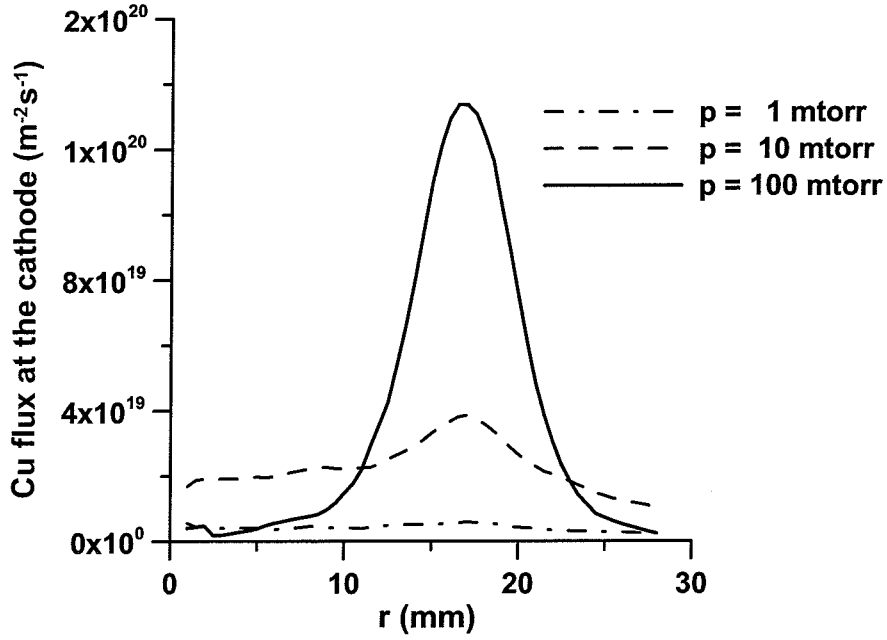

Figure 7.11 Calculated rate of redeposition of Cu atoms at the cathode for different values of the pressure.

7.3.3 Calculated density profiles of the sputtered atoms

After being sputtered from the cathode, the copper atoms are transported towards the substrate and the sidewall of the magnetron chamber. Their movement is inertial, with changes in the velocity only due to collisions. The initial speed at the cathode is obtained from the initial energy, calculated according to (3.97) (see Section 3.4.5). The direction of the initial velocity is given by (3.95), which represent a cosine distribution. The copper atoms are followed until they reach the substrate, the sidewall, or the cathode or until they are ionized.

The calculated density profiles for pressures of 4, 25, and 100 mtorr are presented in Figure 7.12, Figure 7.13, and Figure 7.14, respectively. At $p = 4$ mtorr, the distribution of the sputtered atoms in the volume of the discharge, away from the cathode, is relatively homogeneous, because the pressure is too low for enough collisions that can act as an obstruction for the Cu transport. The maximum near the cathode simply represents the ejection source. The situation at $p = 1$ mtorr (not shown here) is identical. This is in full agreement with other simulation works for magnetron sputtering at the same pressure range [70, 81].

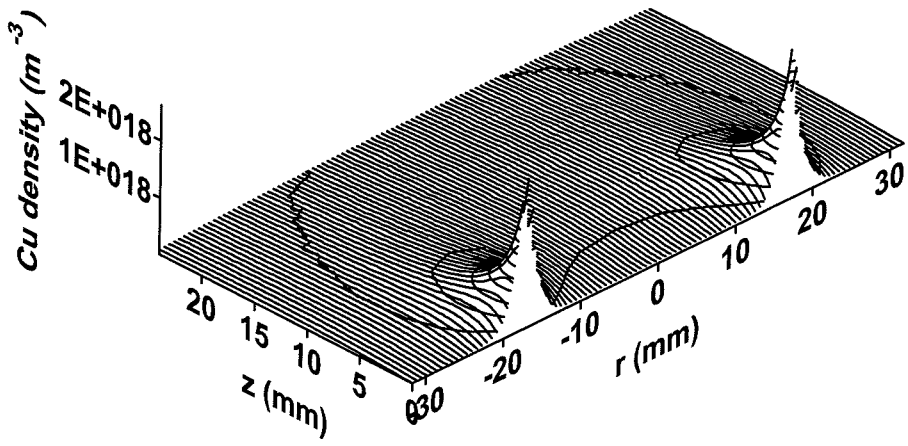

Figure 7.12 Calculated Cu atom density profile for p = 4 mtorr.

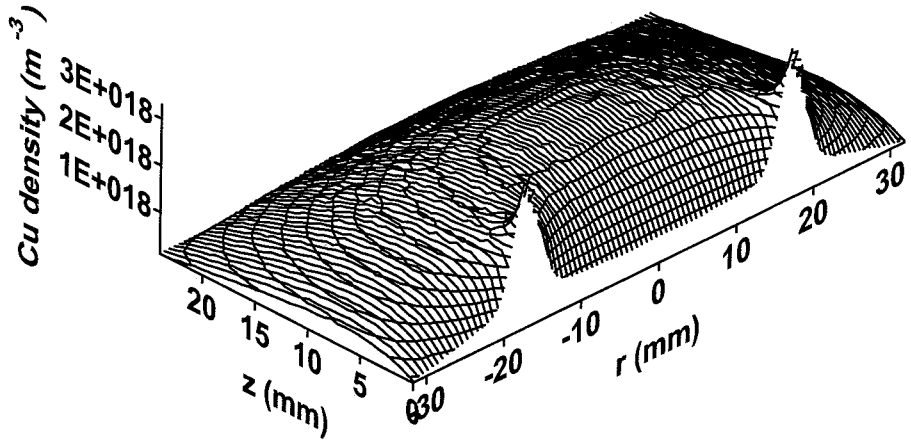

Figure 7.13 Calculated Cu atom density profile for p = 25 mtorr.

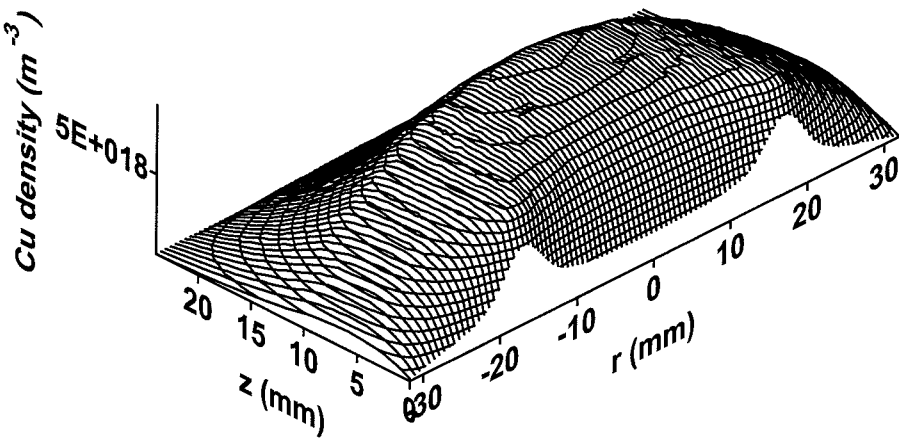

Figure 7.14 Calculated Cu atom density profile for p = 100 mtorr.

At $p = 25$ mtorr, the copper transport is already influenced by the collisions (see Figure 7.13), but the peak density in the volume is still lower than the density near the target. This situation is changed at $p = 100$ mtorr, where the peak density inside the discharge is higher than the density near the target, as illustrated in Figure 7.14. At this pressure, the transport of the sputtered atoms is already collision-dominated. The pictures at $p = 10$ mtorr and $p = 50$ mtorr, both not shown here, are transitional with respect to the results presented here.

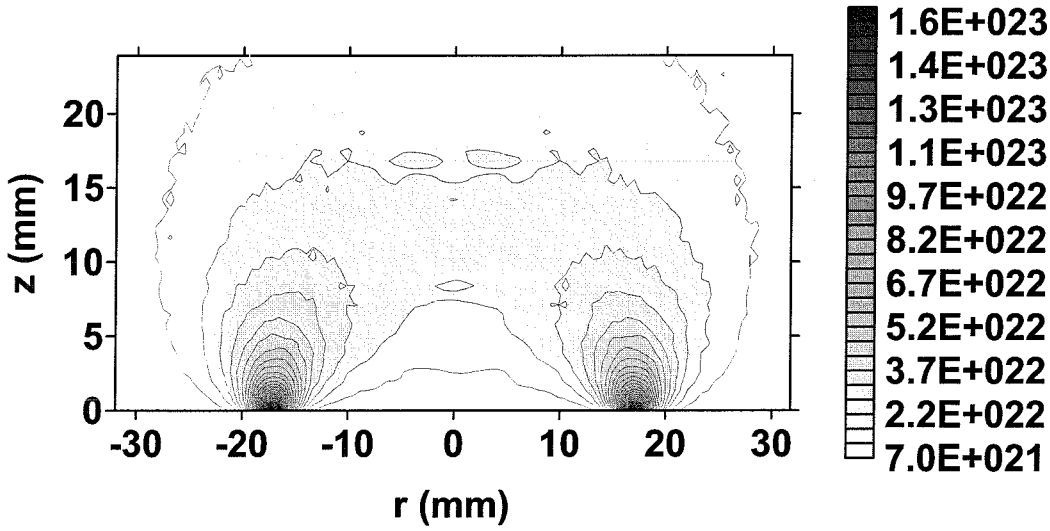

Figure 7.15 Calculated rate of the elastic Cu-Ar collisions for p = 1 mtorr.

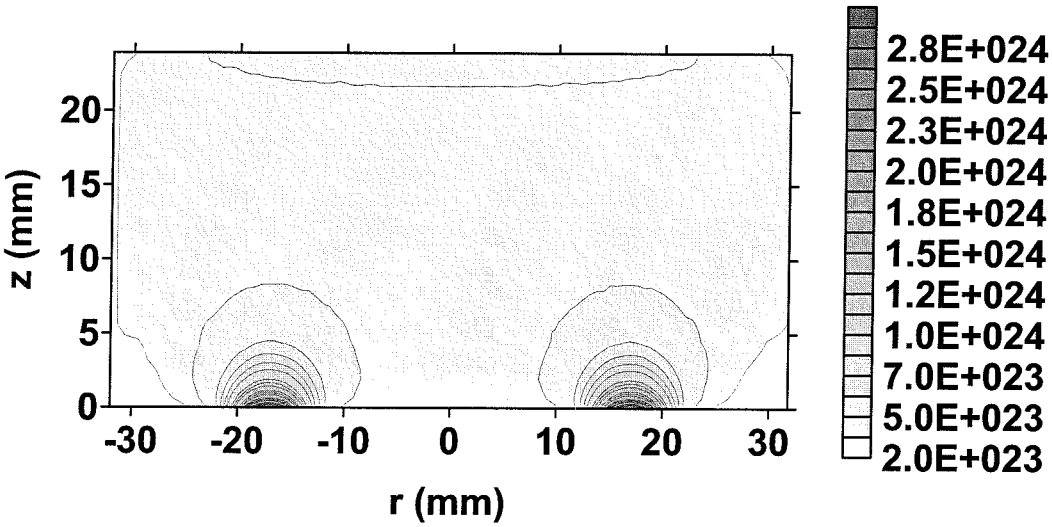

Figure 7.16 Calculated rate of the elastic Cu-Ar collisions for p = 100 mtorr.

The rate of the elastic Cu - Ar collisions in the volume differs with 1.5 orders of magnitude between $p = 1$ mtorr and $p = 100$ mtorr as shown in Figure 7.15 and Figure 7.16. This is logical, because the increase of the pressure increases the probability of collisions. The more collisions result in the more diffuse density profile, as it is at $p = 100$ mtorr (see Figure 7.14).

7.3.4 Deposition flux at the substrate

The sputtered flux at the substrate (the deposition flux) calculated for several values of the gas pressure is plotted in Figure 7.17. As seen there, it is pressure dependent. An increase of the pressure leads to a decrease in the flux. The maximum values of the flux, which are located in the middle of the substrate for all pressures, differ by a factor of 3, for a pressure difference of two orders of magnitude (1 – 100 mtorr). At the same time, the spatial inhomogeneity of the flux with respect to the radial coordinate, defined as the ratio of the flux in the center of the substrate and in its periphery, does not change with pressure, except for the case of $p = 100$ mtorr, which appears to be less inhomogeneous.

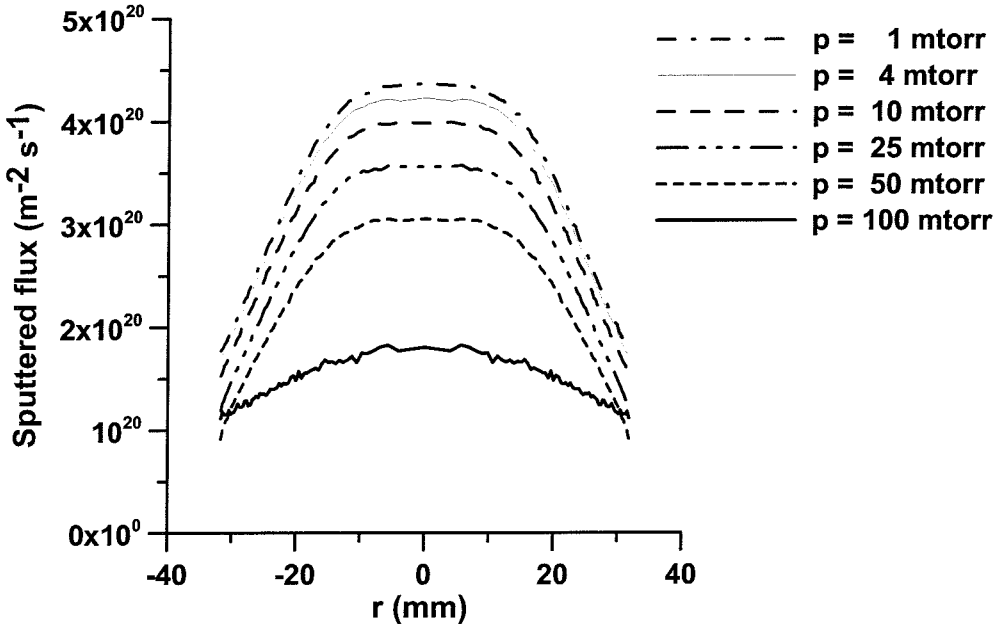

Figure 7.17 Calculated sputtered flux arriving at the substrate for different values of the gas pressure.

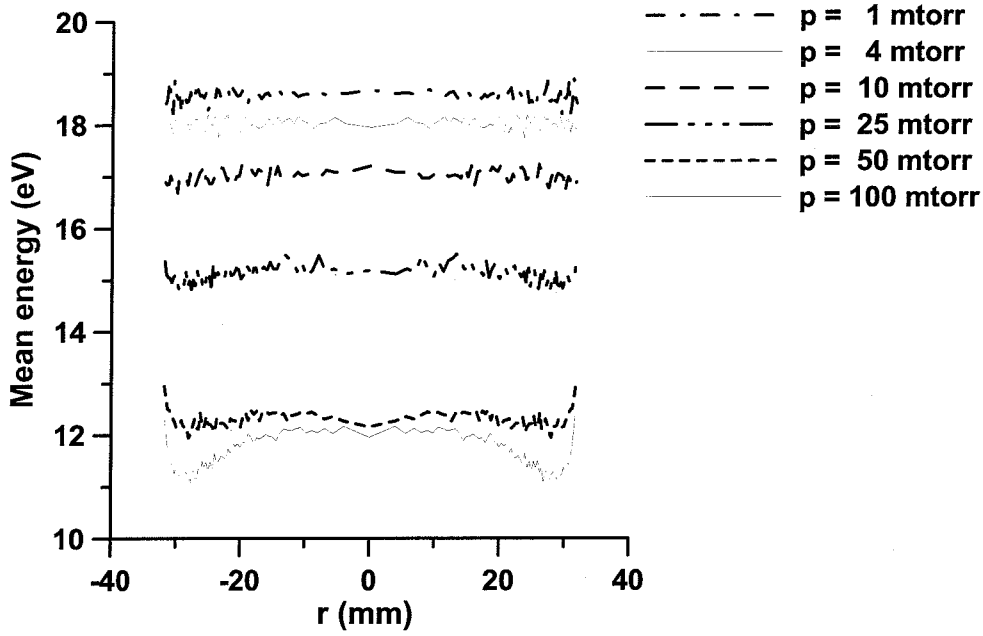

Figure 7.18 Calculated mean energy of the sputtered atoms at the substrate for different values of the gas pressure.

The mean energy of the arriving particles also decreases with increasing pressure, as can be seen in Figure 7.18. The value of the mean energy drops from 18.3 eV at $p = 1$ mtorr to 12 eV at $p = 100$ mtorr, where also a spatial distribution of the mean energy with respect to the r-direction is observed. The relatively high values of the mean energy arise from the asymmetry of the energy distribution of the sputtered atoms. This means that there is a small fraction in the energetic tail of the distribution, whereas the majority of the sputtered atoms have much lower energies. This is illustrated in Figure 7.19, where the normalized energy distribution of the sputtered atoms at the substrate is plotted for $p = 10$ mtorr. The plot is representative for the rest of the pressure values under study. As seen in Figure 7.19, the maximum of the distribution is around 3 eV, but there are also atoms arriving at the substrate with energies up to 200 eV.

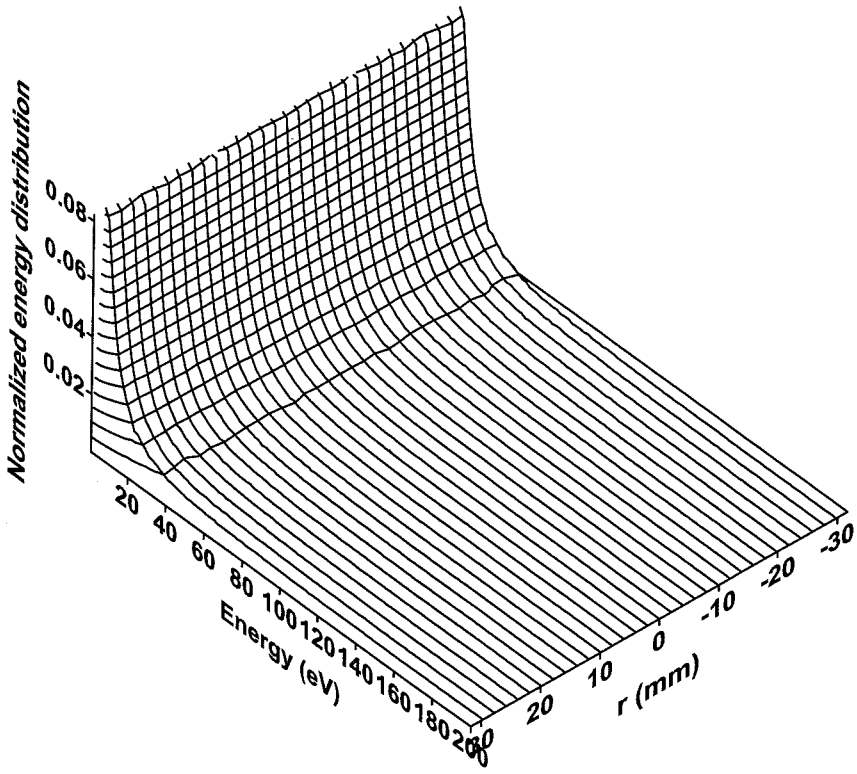

Figure 7.19 Calculated normalized energy distribution of the sputtered atoms at the substrate at $p = 10$ mtorr.

7.3.5 Influence of the target - substrate distance

The distance between the target and the substrate can affect the quality of the deposited film, by the number of collisions, and hence energy and velocity distribution, of the sputtered atoms. To investigate how important this effect is, simulations for four distances (*i.e.*, 24, 50, 100, and 150 mm) are performed for different values of the pressure. The calculated sputtered flux at the cathode for the four distances at $p = 4$ mtorr is presented in Figure 7.20. As it can be seen there, when enlarging the distance from 24 to 150 mm, the magnitude of the sputtered flux decreases from 4×10^{20} $m^{-2}s^{-1}$ to about 2.4×10^{19} $m^{-2}s^{-1}$, *i.e.*, more than an order of magnitude. The radial homogeneity of the flux, however, improves by a factor of 1.8. The mean energy (Figure 7.21) also decreases, but only by about 20%. From all this it follows that the target – substrate distance acts similarly to the change of the gas pressure.

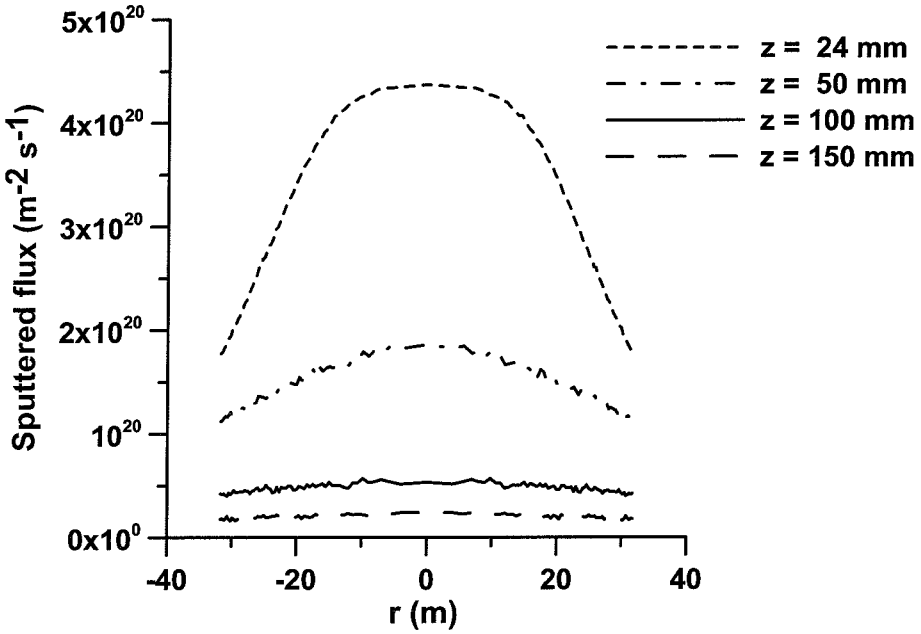

Figure 7.20 Calculated sputtered flux arriving at the substrate for different target – substrate separations at $p = 4$ mtorr.

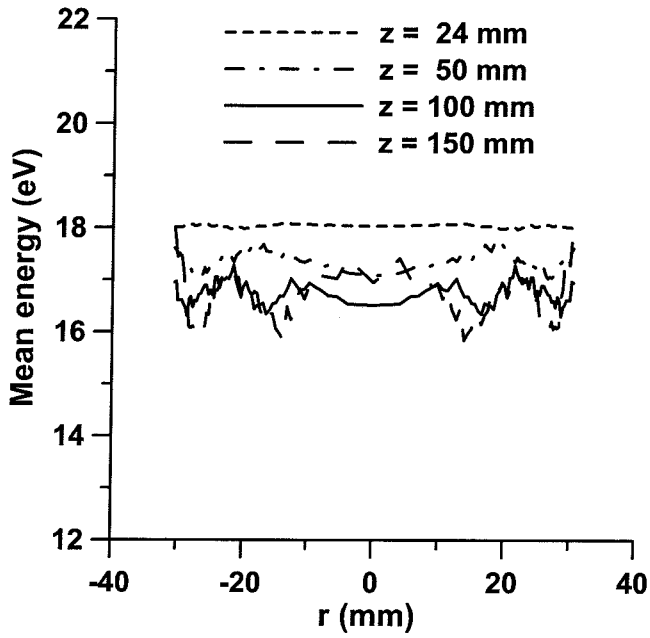

Figure 7.21 Calculated mean energy of the sputtered atoms at the substrate for different target – substrate separations at p = 4 mtorr.

The same trend holds for all pressures. However, the effect of increasing distance on the magnitudes of the sputtered fluxes increases with the pressure. At $p = 100$ mtorr, the difference in flux for a target – substrate distance of 150 vs. 24 mm is already more than 3 orders of magnitude. In addition, at separation $z = 150$ mm, the deposited sputtered flux is only 0.01% of the originally sputtered flux from the target. It means that almost all sputtered atoms have been scattered towards the sidewall and deposited there, instead of on the substrate.

7.3.6 Influence of the scattering angle

The scattering of argon and copper atoms is subject to uncertainty. Not only is the total cross section not precisely known, but also the differential cross section that determines the scattering angle. In our study, the scattering angle is considered energy dependent and is calculated according to (3.69). The whole procedure behind (3.69) has been discussed in detail in Section 3.4.3. A possible alternative is to consider the scattering to be isotropic. This is often applied in simulations when reliable data is not available. In our study, the effect of the scattering angle is investigated by performing three sets of simulations for pressures of 4, 25, and 100 mtorr for a target – substrate separation of 50 mm. Each set consists of two

simulations – one with isotropic Cu – At scattering and one with scattering treated according to (3.69). The results for 4 and 100 mtorr are presented in Figure 7.22 and Figure 7.23, respectively.

The two ways of treating the scattering lead to a difference in the calculated sputtered flux at the substrate. This difference is calculated to be only 6% at low pressure (4 mtorr), but at higher pressure (100 mtorr) it is already above 100%. At $p = 25$ mtorr, it is calculated to be 63% (the results are not shown here).

Therefore, when sputtering is considered at low pressures (below 10 eV) the issue of how the scattering angle in the elastic Cu – Ar collisions is treated is of limited importance for the calculation of the sputtered flux at the substrate. At higher pressures, however, the issue should be dealt with carefully.

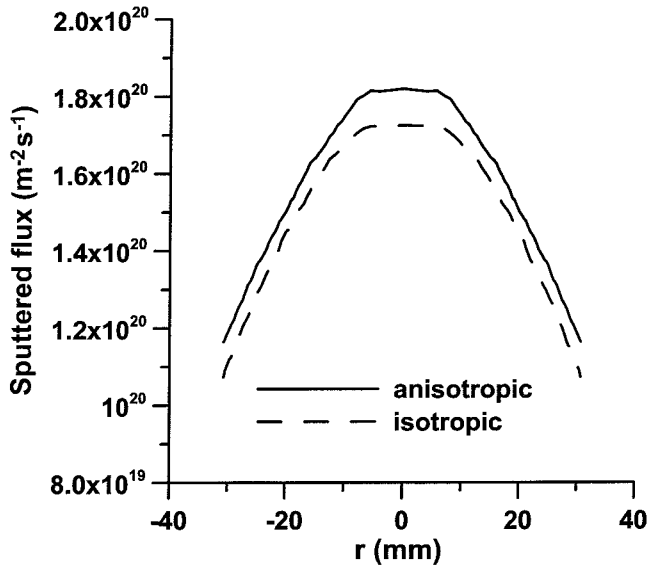

Figure 7.22 Calculated sputtered flux at the substrate at $p = 4$ mtorr and distance between the cathode and the substrate of 50 mm. The solid line represents anisotropic scattering, according to (3.69). The dashed line represents isotropic scattering.

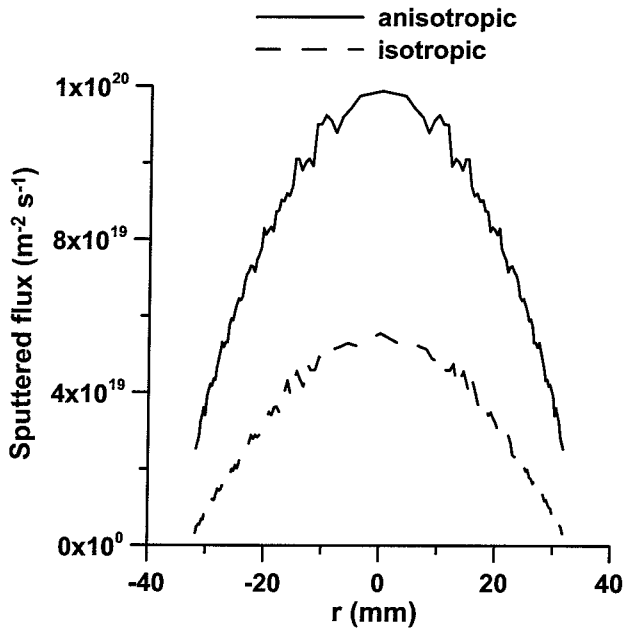

Figure 7.23 Calculated sputtered flux at the substrate at p = 100 mtorr and distance between the cathode and the substrate of 50 mm. The solid line represents anisotropic scattering, according to (3.69). The dashed line represents isotropic scattering.

7.4 Conclusion

The performed study of a laboratory magnetron Von Ardenne PPS 50 by means of a two-dimensional numerical model, based on the PIC/MCC method, has revealed the generation, transport, and deposition of the sputtered atoms from a copper cathode. The calculated erosion profile agrees very reasonably with the experimentally measured one. The results of the study show that the main sources of sputtering at the examined pressure range, 1 – 100 mtorr, are the Ar^+ ions. They are responsible for at least 80% of the sputtered atoms at all pressures. The second contributor to the sputtering are the fast argon atoms, created in symmetric charge transfer between the Ar^+ ions and their parent atoms. The role of self-sputtering (caused by Cu^+ ions) is found to be negligible.

The sputtering and deposition efficiency is highest at p = 4 mtorr. Hence, the most favorable pressure window for sputtering and deposition is found to be within 1 and 10 mtorr.

The distance between the target and the cathode plays a significant role for the efficiency of the deposition, *i.e.*, the radial homogeneity of the deposited film

and the deposition speed. The effect of the distance is present at all studied pressures but it is stronger at the highest pressure.

The effect of how the Cu –Ar elastic scattering is treating has been investigated by comparing an energy dependent scattering angle to isotropic scattering. It has been calculated that at lower pressures the difference in the deposited flux is below 10 %, whereas at higher pressures it can be above 100% (*i.e.*, a factor of two).

Chapter Eight

Conclusions

8.1 Summary

The *overall goal of this research* has been to develop a numerical model of a dc planar magnetron:

based on as little as possible approximations and assumptions;
including as many as possible plasma species;
accounting for all important processes occurring in the discharge;
being as general as possible.

Magnetrons are a special class of glow discharges, able to operate at pressures as low as 1 mtorr with applied voltages lower than 400 – 500 V. This operating regime is possible due to the strong external magnetic field applied to the discharge by powerful magnets located behind the cathode. This magnetic field acts as a trap for the electrons in the discharge plasma and prevents them from leaving the discharge at the anode. It is this magnetic confinement that sustains the discharge at low pressures and moderate applied power, because the electrons can produce enough ionization events of the feeding gas for the self-sustained operation of the discharge.

Magnetrons are widely used for sputter deposition of thin films on plates, known as substrates, made by various materials. The usefulness of the magnetrons comes precisely from their ability to operate at low pressures – low enough to allow the sputtered flux to reach the substrate (often located at the anode) and to form a thin film.

Being gas discharges, magnetrons are described by the physics of plasma. Plasma is formed in any gas, in which two oppositely charged electrodes are submerged, providing that the potential difference between the two electrodes is sufficient for initiating the discharge. Plasma is a quasi electroneutral mixture of charged and neutral particles (electrons, ions, and atoms, as well as molecules and

radicals, in a molecular gas). Its unique property is the ability to exhibit collective behavior. An example for such behavior are the plasma waves. Magnetrons, therefore, can be regarded as magnetized low-temperature plasma.

The interest in studying magnetrons is driven by both practical (industry-related) and fundamental issues. The industrial reasons are to develop more and more efficient sputter magnetrons. The fundamental issues are related mainly to the abnormal electron diffusion at high reduced magnetic fields (*i.e.*, the ratio of the magnetic field and the background gas density). A high reduced magnetic field in combination with the low pressure limits severely the use of the well-developed fluid models for plasmas. An additional obstruction is the complicated form of the equation of magnetohydrodynamics that describes such systems. On the other hand, many of the structure-determining phenomena in magnetrons take place in a region very closely located to the cathode (as close as 1 mm or even less), in the plasma sheath or near its edge. This limits drastically some of the most popular experimental techniques, such as Langmuir probe measurements. All this plus the need for a better insight of the processes occurring in the magnetrons has provoked the development of kinetic numerical methods for studying magnetrons. Kinetic, because only kinetic models can cope with the low pressures and strongly inhomogeneous structure of the magnetrons, especially the planar ones. Several models have been developed and reported in the literature in the last decade. Each of them has built up further knowledge for the processes in magnetrons and for the numerical techniques themselves. Our model exceeds the existing models in several ways. First, it incorporates an external electric circuit in a self-consistent manner to a two-and-a-half-dimensional simulation (two-dimensional in the coordinate and three-dimensional in the velocity space). In this way, not only the model is made more physical, but also, as it is explained throughout the thesis, the issue with the convergence of the simulation is sorted out. Note, that the convergence problem of Particle-in-Cell/Monte Carlo Collisions (PIC/MCC) simulations of dc devices is almost completely untouched in the literature.

Second, the model includes the effect of the gas heating, also in a self-consistent way. This has not been done before for magnetrons.

Third, the model incorporates the sputtered atoms and all their relevant interactions, again in a self-consistent way. The difficulties in the last two issues are

related to the problem of combining processes with characteristic times that differ as much as six orders of magnitude in a single simulation.

Fourth, the model deals with the Coulomb collisions, which is a necessary elaboration to secure that the electron transport is resolved as realistically as possible. This has to do with the fundamental property of the magnetrons, namely that all sorts of electron collisions contribute to their mobility and consequently to the discharge current. This is just the opposite of the situation in unmagnetized discharges, where the collisions restrict the current.

For all these reasons, the model developed in this work can be regarded as a novel step in the direction of better understanding of the magnetron discharges.

The typical calculation results of the model include, among others:

- density profiles of the electrons, gas ions and fast atoms, sputtered ions and atoms;
- profiles of the rates for all relevant collision processes in the plasma such as ionization of the feeding gas and sputtered material, charge-exchange collisions, excitation of the feeding gas, etc.;
- distribution of the electric field and potential;
- discharge current;
- distribution of the gas temperature;
- erosion profile due to sputtering, deposition fluxes at the substrate, and angular and energy distribution of the deposited particles at the substrate;
- energy probability functions of all included species.

The model has been applied to a laboratory magnetron Von Ardenne PPS 50. The calculations have been verified by a comparison of the calculated and the experimentally measured erosion profile, which has shown very good agreement. The whole structure of a dc planar magnetron used for sputtering has been investigated. Some important results include the appearance of a negative space charge region and the fact that the ions do not have a Maxwellian velocity distribution as is often accepted in models and estimates.

The results of the model have shown the importance of the effect of electron recapture at the cathode. All aspects of the influence of this effect have been investigated and two ways of including it in models have been applied and

compared. The results can be of help to other simulators, as well as, to experimentalists.

The study of the gas heating has revealed at which operating conditions the gas heating is important and how this influences the other processes taking place in sputter magnetrons.

The study of the sputtering has revealed the sputtered atom density distribution as a function of the gas pressure. For low pressures, the distribution is relatively homogeneous, whereas for higher pressures it has a maximum that is related to the increased amount of elastic collisions with the gas atoms. The contribution of all types of bombarding particles for sputtering has been studied. It has been shown that the largest amount of sputtered material is produced by argon ions. The role of the self-sputtering has been shown to be negligible, and no significant redeposition of the sputtered material back to the cathode has been observed. The influence of the target-substrate separation has been investigated at different pressures. Finally, it has been shown how the way, in which the scattering of the sputtered atoms from the gas atoms is treated, can change the sputter deposition at the substrate. An added value of the results concerning sputtering is that they have been obtained in a completely self-consistent way (not done before for dc planar sputtering magnetrons).

In conclusion, the model has shown the entire physical picture in a dc planar magnetron. The influence of different processes and factors has been enlightened. Methodological issues about convergence of a PIC/MCC simulation have been addressed and solved. The model results can be used as a reference to compare results obtained by both simpler models and experimental measurements.

8.2 Future possibilities

The future work can go in two directions. The first one is computational - to find a way for further speedup of the code. Here, the main thing to be done is to parallelize the code, *i.e.*, to rewrite the code in such a way that different groups of instructions (machine operations) are assigned to different processors, in order to complete these instructions simultaneously and not sequentially, as it is now. The PIC/MCC algorithm is naturally suitable for that. The challenge is, however, the solver of Poisson's equation. Parallelization will allow bigger number of particles to

be simulated, and hence, larger geometries that are closer to the industrial magnetrons.

The second direction is to expand the model to cope with different applications, e.g., reactive sputtering or pulsed magnetrons. It will be interesting to combine the model with molecular dynamics modules that can treat the sputtering or/and deposition in a more accurate way.

Conclusies

9.1 Samenvatting

Het doel van dit onderzoek was het ontwikkelen van een numeriek model voor een dc planaire magnetron ontlading. Het model dient:

gebaseerd te zijn op zo weinig mogelijk benaderingen en veronderstellingen;
zoveel mogelijk plasma deeltjes te omvatten;
alle belangrijke plasma processen te beschrijven;
zo algemeen mogelijk te zijn.

Magnetrons zijn een bijzondere vorm van glimontladingen, waarbij het mogelijk is te werken bij lage drukken, tot 1 mtorr, en bij aangelegde spanningen lager dan 400 – 500 V. Dit regime is mogelijk dankzij het sterke magneetveld dat wordt aangelegd d. m. v. magneten die achter de kathode zijn aangebracht. Dit magneetveld "vangt" de elektronen in de ontlading, zodat deze de ontlading niet kunnen verlaten aan de anode. Dankzij deze magnetische insluiting kan de ontlading onderhouden worden bij lage drukken en matig vermogen, omdat de elektronen hierdoor in voldoende ionizatie van het ontladingsgas kunnen voorzien.

Magnetrons worden veel gebruikt voor sputter-depositie van dunne films op substraten van verschillende materialen. Het nut van magnetrons komt voort uit de mogelijkheid om te werken bij lage druk – voldoende laag zodat de flux van gesputterde deeltjes het substraat (dat vaak op de anode geplaatst is) bereikt en zo de film vormt.

Vermits magnetrons gas ontladingen zijn, kunnen ze beschreven worden door de wetten van de plasma fysica. Een plasma kan gevormd worden in een gas waarin twee elektroden met tegengestelde lading zijn aangebracht, vooropgesteld dat het potentiaalverschil tussen beide elektroden voldoende groot is om de ontlading op te starten. Een plasma is een quasi elektroneutraal mengsel van geladen en neutrale deeltjes (elektronen, ionen en atomen, en in een moleculair ontladingsgas bovendien ook moleculen en radicalen). Een unieke plasma-eigenschap is het vertonen van

collectief gedrag, zoals bv. plasma-golven. Magnetrons kunnen dan ook beschouwd worden als gemagnetiseerde lage-temperatuursplasma's.

De blijvende interesse in het bestuderen van magnetrons wordt zowel door praktische (industrie gerelateerde) als fundamentele factoren bepaald. De belangrijkste industriële reden is het ontwikkelen van meer en meer efficiënte sputter-magnetrons. De fundamentele redenen zijn voornamelijk gerelateerd aan de abnormale elektronendiffusie bij hoge gereduceerde magnetische velden (d.i. de verhouding van het magnetisch veld en de dichtheid van het achtergrondgas). Een hoog gereduceerd magnetisch veld in combinatie met de lage werkingsdruk beperkt zeer sterk de toepasbaarheid van zgn. fluid modellen voor plasmas. Een bijkomende moeilijkheid is de complexe vorm van de magnetohydrodynamische vergelijkingen die dergelijke systemen beschrijven. Anderzijds is het zo dat veel structuurbepalende fenomenen in magnetrons plaatsvinden in een regio nabij de kathode (tot een afstand van 1 mm of zelfs minder), in de plasma sheath of nabij de plasma sheath grens. Dit beperkt drastisch de toepasbaarheid van enkele van de meest gebruikte experimentele technieken, zoals Langmuir probe metingen. Deze redenen, en de noodzaak om een beter inzicht in de processen die optreden in magnetrons te verkrijgen, hebben de ontwikkeling van kinetische numerieke methoden om magnetrons te bestuderen in de hand gewerkt. Enkel kinetische modellen zijn in staat om de combinatie van lage druk en de sterk inhomogene structuur van magnetrons (en meer in het bijzonder, de planaire magnetrons) te beschrijven. In de laatste 10 jaar zijn er verschillende modellen ontwikkeld en gepubliceerd in de literatuur. Elk van deze modellen heeft een beter inzicht opgeleverd, zowel in de processen die optreden in magnetrons, als in numerieke technieken. Het in dit werk ontwikkelde model overtreft de bestaande modellen op verschillende vlakken. Ten eerste omvat het huidige model een extern zelf-consistent elektrisch circuit in een twee-en-een-half dimensionele simulatie (twee dimensioneel in de ruimte en drie dimensioneel in de snelheden). Op deze manier is het model niet alleen meer fysisch verantwoord, maar wordt er ook een oplossing geboden voor het convergentieprobleem, zoals in detail uitgelegd in dit werk. Hierbij dient opgemerkt te worden dat het convergentieprobleem in Particle-in-Cell / Monte Carlo Collisions (PIC/MCC) simulaties van gelijkstroom bronnen nagenoeg onbesproken is gebleven in de literatuur.

Ten tweede omvat het model ook het effect van gas verhitting, opnieuw op zelf-consistente wijze. Dit was tot nu toe niet eerder gedaan voor magnetrons.

Ten derde omvat het model de gesputterde atomen en al hun relevante interacties, opnieuw op een zelf-consistente manier. De moeilijkheden, geassocieerd met deze laatste twee elementen, zijn een gevolg van het combineren van processen met karakteristieke tijdsschalen die tot zes grootte-ordes van elkaar kunnen verschillen in een enkele simulatie.

Ten vierde omvat het model ook Coulomb botsingen, hetgeen noodzakelijk is om elektronentransport zo realistisch mogelijk te beschrijven. Deze noodzaak is een gevolg van een fundamentele eigenschap van magnetrons, nl. dat alle soorten elektronenbotsingen bijdragen tot de elektronenmobiliteit en bijgevolg tot de ontladingsstroom. Dit fenomeen is precies het omgekeerde van de situatie in niet-gemagnetiseerde ontlading, waarin de stroom beperkt wordt door de botsingen.

Omwille van deze redenen, kan het model, zoals ontwikkeld in dit werk, gezien worden als een nieuwe stap in de riching van een beter inzicht in en begrip van magnetron ontladingen.

De typische resultaten van het model omvatten o.m.:

- dichtheidsprofielen van de elektronen, ionen en snelle atomen van het ontladingsgas, alsook van de gesputterde ionen en atomen;
- snelheidsprofielen van alle relevante botsingsprocessen in de ontlading, zoals ionizatie van het ontladingsgas en van het gesputterde materiaal, ladingsoverdracht botsingen, excitatie van het ontladingsgas, enz.;
- verdeling van het elektrische veld en potentiaal;
- ontladingsstroom;
- verdeling van de gas temperatuur;
- erosieprofielen ten gevolge van sputtering, depositiefluxen op het substraat, en hoek- en energieverdelingen van de afgezette deeltjes op het substraat;
- energie probabiliteitsfuncties van alle deeltjes.

Het model werd toegepast op een laboratorium magnetron "Von Ardenne PPS 50". De berekeningen werden geverifieerd door de berekende en gemeten erosieprofielen te vergelijken, hetgeen een uitstekende overeenkomst vertoont. De

volledige structuur van een dc planaire magnetron, gebruikt voor sputtering, werd onderzocht. Enkele belangrijke resultaten omvatten het optreden van een regio met negatieve ladingsdichtheid, en het feit dat de ionen geen Maxwelliaanse snelheidsverdeling vertonen, in tegenstelling tot wat vaak aangenomen wordt in modellen en schattingen.

De resultaten van het model tonen ook het belang aan van het effect van elektronen recapture aan de kathode. Alle aspecten van de invloed van dit effect zijn onderzocht en twee verschillende manieren van implementeren werden vergeleken. De resultaten kunnen nuttig zijn zowel voor andere simulatoren als voor experimentatoren.

De studie van de gasverhitting heeft aan het licht gebracht onder welke onladingsvoorwaarden gasverhitting van belang is, en hoe dit andere processen die plaatsvinden in sputter magnetrons beïnvloedt.

Bij de studie van de sputtering werd o.m. de dichtheidsverdeling van de gesputterde atomen in functie van de gasdruk bekomen. Bij lage druk is de verdeling relatief homogeen, terwijl bij hogere druk de dichtheidsverdeling seen maximum vertoont dat gerelateerd is aan het toegenomen aantal elastische botsingen met de gas atomen. Ook de bijdrage van alle types van bombarderende deeltjes tot sputtering werd onderzocht. Er werd aangetoond dat de grootste hoeveelheid gesputterd materiaal geproduceerd wordt door argon ionen. De rol van zgn. zelf-sputtering is verwaarloosbaar, en er werd geen significante redepositie van gesputterd materiaal op de kathode waargenomen. De invloed van de target-substraat afstand werd onderzocht bij verschillende drukken. Tenslotte werd ook aangetoond dat de wijze waarop de verstroiing van gesputterde atomen door gas atomen wordt behandeld, de sputter depositie aan het substraat kan beïnvloeden. Een toegevoegde waarde van de resultaten betreffende de sputtering is dat deze resultaten bekomen zijn op een zelf-consistente manier, hetgeen niet eerder gedaan is voor dc planaire sputter-magnetrons.

Samenvattend: het model geeft het volledige fysische beeld van een dc planaire magnetron. De invloed van verschillende processen en factoren is opgehelderd. Methodologische problemen betreffende convergentie in een PIC/MCC simulatie zijn aangepakt en opgelost. De resultaten van het model kunnen gebruikt worden als referentie om resultaten bekomen met eenvoudigere modellen alsook om experimentele metingen mee te vergelijken.

9.2 Toekomst mogelijkheden

Het toekomstig werk kan in twee richtingen verder gezet worden. De eerste is computationeel: hoe kan de code verder versneld worden? Het belangrijkste dat in dit gebied gedaan kan worden is het parallelliseren van de code, d.i. de code zodanig te herschrijven dat verschillende groepen van instructies (machine operaties) toegekend worden aan verschillende processoren, zodat deze instructies gelijktijdig ("parallel") kunnen uitgevoerd worden in plaats van sequentieel, zoals nu het geval is. De aard van het PIC/MCC algorithme maakt dit mogelijk. De uitdaging echter is het oplossen van de Poisson vergelijking.

Parallellisatie zal toelaten een groter aantal deeltjes te simuleren, en dus ook om grotere geometrieën te simuleren, die dichter aanleunen bij de industriële magnetrons.

De tweede mogelijkheid is het uitbreiden van het model naar andere toepassingen, zoals reactieve sputtering of gepulste magnetrons. Een interessante piste zou ook het combineren van het model zijn met een moleculair dynamica model dat de sputtering en/of depositie op een meer accurate manier kan beschrijven.

Appendix

List of publications, contributions to international conferences, and invited talks

Published articles

1. *Modeling of magnetron and glow discharges*
   A. Bogaerts and I. Kolev
   Le Vide: Science, Technique et Applications **2/4**, 296 - 307 (2002)

2. *Numerical models for dc magnetrons*
   I. Kolev and A. Bogaerts
   Contributions to Plasma Physics **44**, 582 – 588 (2004)

3. *Numerical modeling for a better understanding of gas discharge plasmas*
   A. Bogaerts, K. De Bleecker, V. Georgieva, D. Herrebout, I. Kolev, M. Madani, and E. Neyts
   Journal of High Temperature Material Processing **9**, 321 – 344 (2005)

4. *Modeling of gas discharge plasmas: what can we learn from it?*
   A. Bogaerts, K. De Bleecker, I. Kolev, and M. Madani
   Journal of Crystal Growth Surface & Coatings Technology **200**, 62 – 67 (2005)

5. *Influence of the electron recapture by the target on the discharge characteristics in dc planar magnetrons*
   I. Kolev, A. Bogaerts, and R. Gijbels
   Physical Review E **72**, 05642 (2005)

6. *Computer simulation for processing plasmas*
   A. Bogaerts, K. De Bleecker, V. Georgieva, I. Kolev, M. Madani, and E. Neyts
   Plasma Processes and Polymers **3**, 110 – 119 (2006)

7. *PIC-MCC numerical simulation of a dc planar magnetron*
   I. Kolev and A. Bogaerts
   Plasma Processes and Polymers **3**, 127 – 134 (2006)

8. *Detailed numerical investigation of a dc sputter magnetron*
   I. Kolev and A. Bogaerts
   IEEE Transactions on Plasma Science **34**, 886 – 894 (2006)

9. *Modeling of the magnetron discharge*
   A. Bogaerts, I. Kolev, and G. Buyle
   Chapter in *Reactive Sputter Deposition*, ed. by D. Depla and S. Mahieu (Springer), to be published

Contributions to international conferences

1. *Reactive sputtering in dc magnetrons*
   A. Bogaerts, I. Kolev, Z.Chen, and V. Ignatova
   Oral presentation at the symposium "Reactive Sputter Processes and Related Phenomena", Ghent, Belgium, 19 October, 2002

2. *Hybrid fluid - MC model for dc magnetrons*
   I. Kolev and A. Bogaerts
   Oral presentation at the 5-th Euregional WELT-PP, Workshop on the Exploration of Low Temperature Plasma Physics, Kerkrade, The Netherlands, 4 November 2002

3. *Numerical investigation of the electron recapture at the cathode in dc magnetrons*
   I. Kolev and A. Bogaerts
   Poster at the XXVI International Conference on Phenomena in Ionised Gazes, Greifswald, Germany, 15 July 2003

4. *2D PIC/MCC simulation of magnetized plasmas*
   I. Kolev and A. Bogaerts
   Oral presentation at the 5-th International Workshop on Electrical Probes in Magnetized Plasmas, Greifswald, Germany 17 July 2003

5. *Numerical investigation of planar magnetrons via PIC/MC method*
   I. Kolev and A. Bogaerts
   Oral presentation at the 6-th Eurogional WELT-PP, Workshop on the Exploration of Low Temperature Plasma Physics, Kerkrade, The Netherlands, 11 November 2003

6. *EEPF as a function of the magnetic field strength in dc magnetrons: numerical simulation*
   I. Kolev and A. Bogaerts
   Oral presentation at the International Scientific Meeting of the Belgian Physical Society, Mons, Belgium, 25 May 2004

7. *2D numerical investigation of dc magnetrons: influence of the pressure and the magnetic field*
   I. Kolev and A. Bogaerts
   Poster at the Gordon Research Conference on Plasma Processing Science, Plymouth, New Hampshire, The USA, 20 August 2004

8. *Detailed numerical investigation of a dc planar magnetron*
   I. Kolev and A. Bogaerts
   Oral presentation at the International Symposium: Reactive Sputter Processes and Related Phenomena III, Ghent, Belgium, 10 December 2004

9. *Calculation of the Gas Heating in Planar Magnetrons*
   I. Kolev and A. Bogaerts
   Poster at the XXVII International Conference on Phenomena in Ionized Gases, Veldhoven, The Netherlands, 20 July 2005

10. *Comprehensive PIC-MC model for planar magnetron discharges*
    I. Kolev and A. Bogaerts
    Invited talk at the International Workshop: "Nonlocal, Collisionless Electron Transport in Plasmas", Princeton Plasma Physics Laboratory, Princeton, The USA, 4 August 2005

11. *Numerical modeling of dc sputter magnetrons*
    I. Kolev and A. Bogaerts
    Poster at the XIV International Summer School on Vacuum, Electron and Ion Technologies, Sunny Beach, Bulgaria, 12 September 2005

Invited talks and seminars

1. *Numerical Modeling of Planar Magnetrons – State of the Art and Perspectives*
   I. Kolev
   Invited seminar at Bekaert Technology Center, Deerlijk, Belgium, 31 March 2004

2. *Comprehensive PIC-MC model for planar magnetron discharges*
   I. Kolev and A. Bogaerts
   Invited talk at the International Workshop: "Nonlocal, Collisionless Electron Transport in Plasmas", Princeton Plasma Physics Laboratory, Princeton, The USA, 4 August 2005

Scientific prizes

Travel grant award by National Science Foundation (USA) for the Gordon Research Conference on Plasma Processing Science, Plymouth, New Hampshire, The USA, 20 August 2004

Bibliography

1 J. A. Thornton and A. S. Penfold, *Chapter: Cylindrical Magnetron Sputtering* in *Thin Film Processes*, J. Vossen and W. Kern, eds. (Academic: New York, 1978).
2 F. M. Penning, *Physica* **3**, 873 (1936).
3 R. K. Waits, *J. Vac. Sci. Technol.*, **15**, 179 (1978).
4 J. W. Bradley, S. Thompson, and Y. Aranda Gonzalvo, *Plasma Sources Sci. Technol.* **10**, 490 (2001).
5 F. F. Chen, *Introduction to Plasma Physics and Controlled Fusion* (Plenum Press: New York, 1964).
6 M. A. Lieberman and A. J. Lichtenberg, *Principles of Plasma Discharges and Materials Processing* (John Wiley & Sons: New York, 1994).
7 A. V. Phelps and Z. Lj. Petrovic, *Plasma Sources Sci. Technol.* **8**, R21 (1999).
8 J. D. Cobine, *Gaseous Conductors* (Dover: New York, 1958).
9 J. S. Townsend, *Electricity in Gases* (Oxford: Clarendon, 1915).
10 H. Raether, *Electron Avalanches and Breakdown in Gases* (Butterworths Advanced Physics Series, Butterworth Inc.: Washington, D.C., 1964).
11 F. Paschen, *Wied. Ann.* **37**, 69 (1889).
12 Y. P. Raizer, *Gas Discharge Physics* (Nauka: Moscow, 1987; Springer-Verlag: Berlin, 1997).
13 B. Chapman, *Glow Discharge Processes* (Wiley: New York, 1980).
14 R. K. Waits, *Chapter: Planar Magnetron Sputtering* in *Thin Film Processes*, J. Vossen and W. Kern, eds. (Academic: New York, 1978).
15 L. T. Lamont, Jr. and F. T. Turner, *J. Vac. Sci. Technol.* **11**, 47 (1974).
16 J. C. Sellers, *Vak. Forsch. Prax.* **3**, 193 (1998).
17 V. Kirchhoff, T. Kopte, T. Winkler, M. Schulze, and P. Wiedemuth, *Surf. Coat. Technol.* **98**, 828 (1998).
18 J. W. Bradley, H. Bäcker, P. J. Kelly, and R. D. Arnell, *Surf. Coat. Technol.* **135**, 221 (2001).
19 J. A. Thornton, *J. Vac. Sci. Technol.* **15**, 171 (1978).
20 J. A. Thornton, *SAE Trans.* **82**, 1787 (1974).
21 J. A. Thornton, *Thin Solid Films* **80**, 1 (1980).
22 F. A. Green and B. N. Chapman, *J. Vac. Sci. Technol.* **13**, 165 (1976).
23 J. S. Chapin, *Res. Develop.* **25**, 37 (1974).
24 S. Schiller, U. Heisig, and K. Goedicke, *Thin Solid Films* **40**, 327 (1977).

25 T. A. van der Straaten, N. F. Cramer, I. S. Falconer, and B. W. James, *J. Phys. D: Appl. Phys.* **31**, 177 (1998).
26 I. Kolev, A. Bogaerts, and R. Gejbels, *Phys. Rev. E* **72**, 056402 (2005).
27 I. Kolev and A. Bogaerts, *IEEE Trans. Plasma. Sci.* **34**, 886 (2006).
28 I. Kolev and A. Bogaerts, *Plasma Processes and Polymers*, **3**, 127 (2006).
29 L. Gu and M. A. Lieberman, *J. Vac. Sci. Technol. A* **6**, 2960 (1988).
30 A. E. Wendt and M. A. Lieberman, *J. Vac. Sci. Technol. A* **8**, 902 (1990).
31 K. Wasa and S. Hayakawa, Handbook of Sputter Deposition Technology: Principles, Technology, and Applications (Noyes Publications: Park Ridge, NJ, 1992).
32 L. Pekker, *Plasma Sources Sci. Technol.* **4**, 31 (1995).
33 N. F. Cramer, *J. Phys. D: Appl. Phys.* **30**, 2573 (1997).
34 T. A. van der Straaten, N. F. Cramer, I. S. Falconer, and B. W. James, *J. Phys. D: Appl. Phys.* **31**, 191 (1998).
35 J. W. Bradley and G. Lister, *Plasma Sources Sci. Technol.* **6**, 524 (1997).
36 J. W. Bradley, *Plasma Sources Sci. Technol.* **7**, 572 (1998).
37 J. W. Bradley, R. D. Arnell, and D. G. Armour, *Surf. Coat. Technol.* **97**, 538 (1997).
38 J. W. Bradley, *Plasma Sources Sci. Technol.* **5**, 622 (1996).
39 A. Palmero, E.D. van Hattum, W. M. Arnoldbik, F. H. P. M. Habraken, *Surf. Coat. Technol.* **188-189**, 392 (2004).
40 G. Buyle, W. De Bosscher, D. Depla,K. Eufinger,J. Haemers, and R. De Gryse, *Vacuum* **70**, 29 (2003).
41 G. Buyle, D. Depla, K. Eufinger, and R De Gryse, *J. Phys. D: Appl. Phys.* **37**, 1639 (2004).
42 R. Krimke and H. M. Urbassek, *Plasma Sources Sci. Technol.* **5**, 389 (1996).
43 G. Lister, *J. Vac. Sci. Technol. A* **14**, 2736 (1996).
44 S. T. Surzhikov and J. S. Shang, *J. Comp. Phys.***199**, 437 (2004).
45 B. Kuvshinov, E. Westerhof, T. J. Schep, and M. Berning, *Phys. Lett. A* **241**, 287 (1998).
46 C. Costin, L. Marques, G. Popa, and G. Gousset, *Plasma Sources Sci. Technol.* **14**, 168 (2005).
47 A. Bogaerts, *Mathematical Modeling of a Direct Current Glow Discharges in Argon*, PhD Thesis (University of Antwerp: Antwerp, 1996).
48 R. K. Porteous and D. B. Graves, *IEEE Trans. Plasma Sci.* **19**, 204 (1991).
49 R. K. Porteous, H.-M. Wu, and D. B. Graves, *Plasma Sources Sci. Technol.* **3**, 25 (1994).
50 E. Shidoji, N. Nakano, and T. Makabe, *Thin Solid Films* **351**, 37 (1999).
51 E. Shidoji, H. Ohtake, N. Nakano, and T. Makabe, *Jpn. J. Appl. Phys.* **38**, 2131 (1999).
52 E. Shidoji, K. Ness, and T. Makabe, *Vacuum* **60**, 299 (2001).
53 E. Shidoji, E. Ando, and T. Makabe, *Plasma Sources Sci. Technol.* **10**, 621 (2001).

54 I. Kolev and A. Bogaerts, *Contrib. Plasma Phys.* **44**, 582 (2004).
55 K. Ness and T. Makabe, *Phys. Rev. E*, **62**, 4083 (2000).
56 E. Shidoji and T. Makabe, *Thin Solid Films*, **442**, 27 (2003).
57 E. Passoth, J. F. Behnke, C. Csambal, M. Tichý, P. Kudrna, Yu. B. Golubovskii, and I. A. Porokhova, *J. Phys. D: Appl. Phys.* **32**, 2655 (1999).
58 I. A. Porokhova, Yu. B. Golubovskii, J. Bretagne, M. Tichy, and J. F. Behnke, *Phys. Rev. E* **63**, 056408 (2001).
59 I.A. Porokhova, Yu.B. Golubovskii, C. Csambal, V. Helbig, C. Wilke, and J.F. Behnke, *Phys Rev. E* **65**, 046401 (2002).
60 I. A. Porokhova, Yu. B. Golubovskii, M. Holík, P. Kudrna1, M. Tichý, C. Wilke, and J. F. Behnke, *Phys. Rev. E* **68**, 066407 (2003).
61 I. A. Porokhova, M. Holík, O. Bilyk, P. Kudrna, Yu. B. Golubovskii, M. Tichý, J. F. Behnke, *Contrib. Plasma Phys.* **44**, 319 (2004).
62 I. A. Porokhova, Yu. B. Golubovskii, and J. F. Behnke, *Phys. Rev. E* **71**, 066406 (2005).
63 I. A. Porokhova, Yu. B. Golubovskii, and J. F. Behnke, *Phys. Rev. E* **71**, 066407 (2005).
64 Yu. B. Golubovskii, I. A. Porokhova, V. P. Sushkov, M. Holík, P. Kudrna, and M. Tichý, *Plasma Sources Sci. Technol.* **15**, 228 (2006).
65 T. E. Sheridan, M. J. Goeckner, and J. Goree, *J. Vac. Sci. Technol. A* **8**, 30 (1990).
66 T. E. Sheridan, M. J. Goeckner, and J. Goree, *J. Vac. Sci. Technol. A* **8**, 1623 (1990).
67 J. E. Miranda, M. J. Goeckner, J. Goree, and T. E. Sheridan, *J. Vac. Sci. Technol. A* **8**, 1627 (1990).
68 M. J. Goeckner, J. Goree, and T. E. Sheridan, *IEEE Trans. Plasma Sci.* **19**, 301 (1991).
69 J. Li, Q. Chen, and Z. Li, *J. Phys. D: Appl. Phys.* **28**, 681 (1995).
70 J. Li, Q. Chen, and Z. Li, *J. Phys. D: Appl. Phys.* **28**, 1121 (1995).
71 J. Li, Q. Chen, W. Zhang, Z. Li, and J. J. Pan, *J. Phys. D: Appl. Phys.* **29**, 1624 (1996).
72 C. Heise, K. Lemke, and M. Kock, *Contrib. Plasma Phys.* **37**, 431 (1997).
73 E. Shidoji, M. Nemoto, and T. Nomura, *J. Vac. Sci. Technol. A* **18**, 2858 (2000).
74 Q. H. Fan, L. Q. Zhou, and J. J. Gracio, *J. Phys. D: Appl. Phys.* **36**,244 (2003).
75 A. M. Myers, J. R. Doyle, J. R. Abelson, and D. N. Ruzic, *J. Vac. Sci. Technol A* **9**, 614 (1991).
76 E. Shidoji, M. Nemoto, T. Nomura, and Y. Yoshikawa, *Jpn. J. Appl. Phys.* **33** 4281 (1994).
77 Y. Yamamura and M. Ishida, , *J. Vac. Sci. Technol. A* **13**, 101 (1995).
78 C. Eisenmenger-Sittner, R. Beyerknecht, A. Bergauer, W. Bauer, and G. Betz, *J. Vac. Sci. Technol. A* **13**, 2435 (1995).
79 V. Serikov and K. Nanbu, *J. Vac. Sci. Technol. A* **14**, 3108 (1996).
80 S. Ido, M. Kashiwagi, and M. Takahashi, *Jpn. J. Appl. Phys.* **38**, 4450 (1999).

81 K. Macàk, P. Macàk, U. Helmersson, *Comp. Phys. Communic.* **120**, 238 (1999).
82 O. Yamazaki, K. Iyanagi, S. Takagi, and K. Nanbu, *Jpn. J. Appl. Phys.* **41**, 1230 (2002).
83 B. Feddes, J. G. C. Wolke, J. A. Jansen, and A. M. VredenbergB. Feddes, *J. Appl. Phys.* **93**, 662 (2003).
84 A. Kuzmichev and I. Goncharuk, *IEEE Trans. Plasma Sci.* **31**, 994 (2003).
85 U. H. Kwon and W. J. Lee, *Jpn. J.Appl. Phys.* **45**, 8629 (2006).
86 K. Nanbu, S. Segawa, and S. Kondo, *Vaccuum* **47**, 1013 (1996).
87 K. Nanbu and S. Kondo, *Jpn. J.Appl. Phys.* **36**, 4808 (1997).
88 S. Kondo and K. Nanbu, *J. Phys. D: Appl. Phys.* **32**,1142 (1999).
89 S. Kondo and K. Nanbu, *J. Vac. Sci. Technol. A* **19**, 830 (2001).
90 T. M. Minea, J. Bretagne, G. Gousset, L. Magne, D. Pagnon, and M. Touzeau, *Surf. Coat. Technol.* **116-119**, 558 (1999).
91 C. H. Shon, J. K. Lee, H. J. Lee, Y, Yang, and T. H. Chung, *IEEE Trans. Plasma Sci.* **26**, 1635 (1998).
92 Y. Kusumoto and K. Iwata, *Vaccuum* **74**, 359 (2004).
93 S. Kuroiwa, T. Mine, T. Yagisawa, and T. Makabe, *J. Vac. Sci. Technol. B* **23**, 2218 (2005).
94 T. Yagisawa and T. Makabe, *J. Vac. Sci. Technol. A* **24**, 908 (2006).
95 Ch. Popov, *Electrodynamics* (Nauka i Izkustvo: Sofia, 1989)
96 L. D. Landau and E. M. Lifshitz, *Course of Theoretical Physics, volume 1: Mechanics* (Butterworth-Heinemann: Burlington MA, 2003).
97 R. O. Dendy, *Plasma dynamics* (Clarendon Press: Oxford, 1990)
98 L. D. Landau and E. M. Lifshitz, *Course of Theoretical Physics, volume 2: The Classical Theory of Fields* (Butterworth-Heinemann: Burlington MA, 2003).
99 E. W. McDaniel, *Collision Phenomena in Ionised Gases* (Wiley: New York, 1993)
100 D. Cvejanovic and A. Geowe, *J. Phys. B: At. Mol. Opt. Phys.* **30**, 2873 (1997).
101 W. C. Fon, K. A. Berrington, P. C. Burke, and A. Hibbert, *J. Phys. B: At. Mol. Opt. Phys.* 16, 307 (1983).
102 Y. Tzeng and E. E. Hunhardt, *Phys. Rev. A,* **34**, 2148 (1986).
103 P. S. Ganas and A. E. S. Green, *Phys. Rev A* **4**, 182 (1971)
104 S. Trajmar, W. Williams and S. K. Srivastava, *J. Phys. B: Atom. Molec. Phys.* **10**, 3323 (1977).
105 D. H. Madison, R. P. McEachram, M. Ismail, and P. J. O. Teubner, *J. Phys. B: At. Mol. Opt. Phys.* **31**, 1127 (1998).
106 L. Vriens, *Phys. Lett.* **8**, 260 (1964).
107 H. A. Hyman, *Phys. Rev. A* **20**, 855 (1979).
108 A. V. Phelps, *J. Phys. Chem. Ref. Data* **20**, 557 (1991).
109 A. V. Phelps, *J. Appl. Phys.* **76**, 747 (1994).
110 A. Bogaerts and R. Gijbels, *J. Appl. Phys.* **79**, 1279 (1996).
111 L. A. Riseberg, W. F. Parks, and L. D. Schearer, *Phys. Rev. A* **8**, 1962 (1973).
112 S. Inaba, T. Goto, and S. Hittori, *J. Phys. Soc. Jpn.* **52**, 1164 (1983).

113 K. Tachibana, *Phys. Rev. A* **34**, 1007 (1986).
114 M. Bourène and J. Le Calve, *J. Chem. Phys.* **58**, 1452 (1973).
115 S. M. Rossnagel, *J. Vac. Sci. Technol. A* **6**, 19 (1988).
116 D. B. Medved, P. Mahadevan, and J. K. Layton, *Phys. Rev.* **129**, 2086 (1963).
117 A. A. Kruithof, *Physica* **7**, 519 (1940).
118 W. R. Grove, *Philos. Trans. R. Soc. London* **142**, 87 (1853).
119 W. R. Grove, *Philos. Mag.* **5**, 203 (1853).
120 P. Sigmund, *Chapter Sputtering by Particle Bombardment* in *Topics in Applied Physics*, Vol. 47, I. R. Berhrisch, ed. (Springer: Berlin, 1981).
121 P. Sigmund, *Phys. Rev.* **184**, 383 (1969).
122 G. Falcone, *Phys. Rev. B* **38**, 6398 (1988).
123 M. W. Weissmann and P. Sigmund, *Radiat. Eff.* **19**, 7 (1973).
124 Y. Yamamura, N. Matsunami and N. Itoh, *Radiat. Eff.* **77**, 65 (1983).
125 N. Matsunami, Y. Yamamura, Y. Itikawa, N. Itoh, Y. Kazumata, S. Miyagawa, K. Morita, R. Shimizu and H. Tawara, *Atom. Data and Nucl. Data Tables* **31**, 1 (1984).
126 J. Lindhard, M. Scharff and H. E. Schiøtt, *Mat. Fys. Medd. Dan. Vid. Selsk.* **33**, 3 (1963).
127 H. A. Oechsner, *Physics (N. Y.)* **261**, 37 (1973).
128 V. Serikov and K. Nanbu, *Rep. Inst. Fluid Sci.* **6**, 43 (1994).
129 A. Bogaerts, R. Gijbels and V. Serikov, *J. Appl. Phys.* **87**, 8334 (2000).
130 A. Matveev, *Molecular Physics* (Vyshaya Shkola: Moscau, 1987)
131 R. W. Hockney and J. W. Eastwood, *Computer Simulations Using Particles* (Adam Hilger: Bristol, 1988).
132 F. S. Acton, *Numerical Methods That Work* (Mathematical Association of America: Washington, 1990).
133 J. P. Boris, *Proc. Fourth Conf. Num. Sim. Plasmas,* Naval Res. Lab. Wash. DC, 3 (1970).
134 C. K. Birdsall and D. Fuss, *J. Comput. Phys.* **3**, 494 (1969).
135 P. K. MacKeown and D. J. Newman, *Computational Techniques in Physics* (Adam Hilger: Bristol, 1987).
136 E. Brigham, *Fast Fourier Transform and Its Applications* (Prentice – Hall, Inc.: Upper Saddle River, NJ, 1988).
137 P. N. Swartztrauber, SIAM *J. Numer. Anal.* **11**, 1136 (1974).
138 C. K. Birdsall and W. B. Bridges, *Electron Dynamics of Diode Regions* (Academic: New York, 1966).
139 C. K. Birdsall and A. B. Langdon, *Plasma Physics via Computer Simulations* (Adam Hilger: Bristol, 1991).
140 J. P. Verboncoeur, M. V. Alves, V. Vahedi and C. K. Birdsall, *J. Comput. Phys.* **104**, 321 (1993).
141 V. Vahedi and G. DiPeso, *J. Comput. Phys.* **131**, 149 (1996).
142 R. W. Hamming, *Digital Filters* (Dover Publications: Mineola, NY, 1998).

143 D. Schlichthärle, *Digital Filters: Basics and Design* (Springer – Verlag: Berlin, 2000).
144 E. Kawamura, C. K. Birdsall and V. Vahedi, *Plasma Sources Sci. Technol.* **9**, 413 (2000).
145 I. P. Bazarov, *Thermodynamics* (Pergamon Press: New York, 1964).
146 K. Nanbu, *IEEE Trans. Plasma Phys.* **28**, 971 (2000).
147 H. Babovsky and R. Illner, *SIAM J. Num. Anal.* **26**, 45 (1989).
148 W. H. Press, S. A. Teukolsky, W. T. Vetterling, and B. P. Flannery, *Numerical Recipes in Fortran, The Art of Scientific Computing* (Cambridge University Press: Cambridge, 1992).
149 K. Nanbu, *J. Phys. Soc. Jpn.* **49**, 2042 (1980).
150 W. Feller, An Introduction to Probability Theory and Its Applicatins, Volume 2 (Wiley: NY, 1971).
151 H. R. Scullerud, *Brit. J. Appl. Phys. ser. 2* **1**, 1567 (1968).
152 V. Vahedi and M. Surendra, *Comput. Phys. Commun.* **87**, 179 (1995).
153 K. Nanbu, *Jpn. J. Appl. Phys.* **33**, 4752 (1994).
154 W. G. Vincenti and Ch. H. Kruger, Jr., *Introduction to Physical Gas Dynamics* (Wiley: NY, 1965).
155 J. H. Jeans, *The Dynamical Theory of Gases*, 4th ed. (Dover, 1954).
156 A. Okhrimovskyy, A. Bogaerts, and R. Gijbels, *Phys. Rev. E*, **65**, 037202 (2002).
157 K. Nanbu and S. Uchida, *Proc. 19th Int. Symp.: Rarefied Gas Dynamics* (Oxford, UK), **1**, 601 (1995).
158 Y. Nakamura and K. Kurachi, *J. Phys. D: Appl. Phys.* **21**, 718 (1988).
159 C. B. Opal, W. K. Peterson, and E. C. Beaty, *J. Chem. Phys.* **55**, 4100 (1971).
160 L. R. Peterson and J. E. Allen, Jr., *J. Chem. Phys.* **56**, 6068 (1972).
161 A V Phelps, private communications.
A review of the existing measurements and calculations of the cross-sections for symmetrical charge transfer is available at:
ftp://jila.colorado.edu/collision_data/ionneutral/symmchgtransnote.txt
162 J. Sielanko, *Rad. Eff. Lett.* **86**, 185 (1984).
163 I. M. Torrens, *Interatomic Potentials* (Academic: New York, 1972).
164 O. B. Firsov, *Zh. Eksp. Teor. Fiz.* **33**, 696 (1957).
165 Z. Wronski, *Vacuum* **42**, 635 (1991).
166 R. W. Hockney, S. P. Goel, and J. W. Eastwood, *Chem. Phys. Lett.* **21**, 589 (1973).
167 J. W. Eastwood and R. W. Hockney, *J. Comp. Phys.* **16**, 342 (1974).
168 J. W. Eastwood, *J. Comp. Phys.* **18**, 1 (1975).
169 M. N. Rozenbluth, W. M. McDonald, and D. L. Judd, *Phys. Rev.* **107**, 1 (1957).
170 T. Takizuka and H. Abe, *J. Comput. Phys.* **25**, 205 (1977).
171 M. E. Jones, D. S. Lemons, R. J. Mason, V. A. Thomas, and D. Winske, *J. Comput. Phys.* **123**, 169 (1996).
172 K. Nanbu, *Phys. Rev.E* **55**, 4642 (1997).

173 K. Nanbu, *Phys. Rev.E* **56**, 7314 (1997).
174 K. Nanbu and S. Yonemura, *J. Comput. Phys.* **145**, 639 (1998).
175 M. W. Thompson, *Philos. Mag.* **18**, 377 (1968).
176 D. P. Jackson, *Can. J. Phys.* **53**, 1513 (1975).
177 B. J. Garrison, N. Winograd, D. Lo, T. A. Tombrello, M. H. Shapiro, and D. E. Harrison, Jr., *Surf. Sci.* **180**, 129 (1987).
178 H. Gades and H. M. Urbassek, *Nucl. Instrim. Methods B* **69**, 232 (1992).
179 K. J. Bowers, *J. Comput. Phys.* **173**, 393 (2001).
180 T. H. Cormen, C. E. Leiseron, and R. L. Rivest, *Introduction to Algorithms* (MIT Press: Cambridge, MA, 1990).
181 G. Buyle, University of Gent, Belgium, private communications (May 2004).
182 E. Eggarter, *J. Chem. Phys.* **62**, 883 (1975).
183 M. Hayashi, *IPPJ - AM Research Rep. 19 (unpublished).* Available on: ftp://jila.colorado.edu/collision_data/electronneutral/hayashi.txt
184 A. Bogaerts, University of Antwerp, Belgium, private communications, (2000).
185 D. J. Field, S. K. Dew, and R. E. Burrell, *J. Vac. Sci. Technol. A* **20**, 2032 (2002).
186 F. F. Chen, in *Plasma Diagnostics Technics,* R. H. Huddlestone and S. L. Leonard, eds. (Academic: New York, 1965).
187 P. Spatenka, J. Vlcek, and J. Blazek, *Vacuum* **55**, 165 (1999).
188 T. E. Sheridan, M. J. Goeckner, and J. Goree, *J. Vac. Sci. Technol. A* **9**, 688 (1991).
189 H. D. Hagstrum, *Phys. Rev.* **104**, 672 (1956).
190 J. Li and Z. Li, *J. Phys. D: Appl. Phys.* **28**, 1121 (1995).
191 V. Serikov and S. Kawamoto, poster at*XXIV ICPIG*, Warsaw, Poland, P-410, (1999).
192 S. Anderson and B. Kasemo, *Solid State Commun.* **8**, 961 (1970).
193 E. G. McRae and C. W. Caldwell, *Surf. Sci.* **57**, 77 (1976).
194 A. J. Hatch and H. B. Williams, *Phys. Rev.* **112**, 681 (1958).
195 R. A. Kishek, Y. Y. Lau, L. K. Ang, A. Valfells, and R. M. Gilgenbach, *Phys. Plasmas* **5**, 2120 (1998).
196 R Reimer, *Scanning Electron Microscopy: Physics of Image Formation and Microanalysis*, 2nd edition (Springer-Verlag: Berlin, 1998).
197 M. A. Furman and M. T. F. Pivi, *PRST-AB 5*, 124404 (2002).
198 M. A. Furman and M. T. F. Pivi, LBNL report No. LNBL-52807, SLAC-PUB-9912 (2001).
199 M. Abramovitz and I. A. Stegun, *Handbook of Mathematical Functions, Applied Mathematical Series* (National Bureau of Standards: Washington, 1968).
200 D. W. Hoffman, *J. Vac. Sci. Technol. A* **3**, 561 (1985).
201 S. D. Epke and S. K. Dew, *J. Phys. D: Appl. Phys.* **39**, 1413 (2006).
202 R. S. Robinson, *J. Vac. Sci. Technol.* **16**, 185 (1979).
203 G. M. Turner, *J. Vac. Sci. Technol. A* **13**, 2161 (1995).

204 A. Palmero, H. Rudolph, and F. H. P. M. Habraken, *Appl. Phys. Lett.* **87**, 071501 (2005).
205 V. Serikov and K. Nanbu, *J. Appl. Phys.* **82**, 5948 (1997).
206 I. Revel, L. C. Pitchford, and J. P. Boeuf, *J. Appl. Phys.* **88**, 2234 (2000).
207 N. J. Mason and W. R. Newell, *J. Phys. B* **20**, 1357 (1987).
208 H. A. Hyman, *Phys. Rev. A* **18**, 441 (1978).
209 D. P. Lymberopoulos and D. J. Economou, *J. Appl. Phys.* **73**, 3668 (1993).
210 M. A. Biondi, *Phys. Rev.* **129**, 1181 (1963).
211 C. M. Ferreira and A. Ricard, *J. Appl. Phys.* **54**, 2261 (1983).
212 C. M. Ferreira, J. Loureiro and A. Ricard, *J. Appl. Phys.* **57**, 82 (1985).
213 A. V. Phelps, C. H. Greene, and J. P. Burke, Jr., *J. Phys. B* **33**, 2965 (2000).
214 A. Bogaerts and R. Gijbels, *J. Anal. At. Spectrom.* **11**, 841 (1996).
215 H. F. Winters, H. Coufal, C. T. Rettner, and D. S. Bethune, *Phys. Rev. B* **41**, 6240 (1990).
216 H. Coufal, H. F. Winters, E. Bay, and W. Eckstein, *Phys. Rev. B* **44**, 4747 (1991).
217 R. L. Powell G. E. Childs, *in American Institute of Physics Handbook,* D. E. Grey, ed. (McGraw – Hill: New York, 1972).
218 J. O. Hirschfelder, C. F. Curtiss, and R. B. Bird, *Molecular Theory of Gases and Liquids* (Wiley: New York, 1964).
219 N. Baguer, *Numerical modeling of a hollow cathode discharge*, PhD Thesis (University of Antwerp: Antwerp, 1996)
220 M. van Straaten, *Analytical Glow Discharge Mass Spectrometry: Physical Aspects and Applications*, Ph. D. Dissertation (University of Antwerp: Antwerp, 1996).
221 R. C. Weast and M. J. Astle, *CRC Handbook of Chemistry and Physics, 63rd Edition* (CRC Press: Boca Raton, 1982 – 1983).
222 N. Baguer and A. Bogaerts, *J. Appl. Phys.* **88**, 033303 (2005).